Photocatalytic valorization of biobased alcoholic wastes: a sustainable approach for the generation of green products

Thèse

Mahmoodreza Karimiestahbanati

Doctorat en génie chimique
Philosophiæ doctor (Ph. D.)

Québec, Canada

Valorisation photocatalytique des résidus alcooliques: approche durable pour la production de produits verts

Thèse

Mahmood Reza Karimi Estahbanati

Sous la direction de :

Maria Cornelia Iliuta, research director
Mehrzad Feilizadeh, research codirector

Résumé

Ces dernières années, une attention croissante a été portée à la valorisation de différents types de résidus en produits chimiques à valeur ajoutée. La valorisation des résidus peut non seulement résoudre les problèmes environnementaux croissants et actuels, mais elle peut contribuer également au développement durable de la société. Les résidus alcooliques constituent une catégorie à fort potentiel de valorisation en différents types de produits chimiques. Dans ce contexte, la valorisation photocatalytique des résidus alcooliques est une approche prometteuse du point de vue du développement durable.

L'objectif principal de la thèse était d'étudier la valorisation photocatalytique de différents résidus alcooliques biosourcés en produits à valeur ajoutée. À cet égard, ces travaux ont principalement porté sur (i) l'analyse des effets individuels et d'interaction des paramètres opératoires et l'optimisation de la production d'hydrogène à partir de glycérol (ii) l'étude de la cinétique de la production d'hydrogène à partir de glycérol et d'éthanol, (iii) la mise au point de catalyseurs nanocomposites au TiO_2 utilisant des biomatériaux à base de carbone (nanotubes de carbone et sphères de carbone) pour la production d'hydrogène à partir de glycérol, et (iv) l'étude du mécanisme et de la cinétique de la valorisation photocatalytique du cyclohexanol en cyclohexanone.

Pour la production d'hydrogène à partir du glycérol, les modèles « Réseau de neurones artificiels » ainsi que « Méthode des surfaces de réponses » ont été utilisés pour évaluer l'effet et l'importance des principaux paramètres opératoires (pourcentage de glycérol, catalyseur, et Pt (co-catalyseur), ainsi que pH). La comparaison de ces modèles a révélé une meilleure précision du premier, qui a été par la suite sélectionnée pour une optimisation basée sur un algorithme génétique. La plus grande quantité d'hydrogène produite s'est révélée être à 50% de glycérol dans l'eau (v/v), à une masse de catalyseur de 3,9 g/L, à 3,1% de Pt et à un pH de 4,5. Finalement, une analyse basée sur la méthode de Garson pour évaluer l'importance relative des paramètres opératoires a montré que les pourcentages de glycérol et de catalyseur affectent de façon différente la production d'hydrogène.

L'effet des plus importants paramètres opératoires (catalyst loading, glycerol%, intensité de la lumière, and temps) sur la valorisation photocatalytique du glycérol en hydrogène a été analysé et un modèle cinétique a été développé sur la base d'un mécanisme proposé. La capacité du modèle à prédire le taux de production d'hydrogène pour différents substrats, photocatalyseurs et paramètres opératoires a été confirmée en comparant les valeurs calculées avec des données expérimentales de la littérature.

Le rôle des composants carbonés (CT) biosourcées en tant que matrice, cocatalyseur et adsorbant dans les composites TiO_2@CT a été étudié en utilisant des nanotubes de carbone et des sphères de carbone. L'analyse morphologique a permis d'examiner le rôle de la matrice et d'évaluer la formation uniforme du TiO_2 sur le CT. Les expériences photocatalytiques ont été ensuite utilisées pour analyser les rôles du co-catalyseur et de l'adsorbant. Fait intéressant, les résultats ont révélé que l'incorporation de CNT dans un composite de TiO_2 pouvait presque doubler le taux de production d'hydrogène (i) en l'absence de Pt ou (ii) à faible concentration en glycérol. Par conséquent, il a été constaté qu'en plus d'être une matrice, le CNT peut jouer deux autres rôles importants, comme co-catalyseur et adsorbant.

Pour évaluer la valorisation des résidus alcooliques en produits liquides à valeur ajoutée, la conversion photocatalytique sélective du cyclohexanol en cyclohexanone a été investiguée par des études cinétiques et spectroscopiques. Un mécanisme de réaction a été proposé sur la base des résultats de l'analyse in situ ATR-FTIR et un modèle cinétique a été développé pour prédire le taux de production de cyclohexanone. Une très grande sélectivité de la cyclohexanone a été confirmée à la fois par des analyses spectroscopiques que chromatographiques (HPLC et GC-MS), démontrant que l'approche photocatalytique est une alternative prometteuse pour la production sélective de cyclohexanone.

En résumé, les résultats de cette thèse ont montré que la photocatalyse est une alternative prometteuse pour la valorisation des résidus alcooliques biosourcés en produits à valeur ajouté. La conversion photocatalytique de ces résidus peut conduire à la production d'hydrogène comme carburant vert prometteur pour l'avenir. D'autre part, la photocatalyse peut être appliquee pour produire des composes liquides avec une sélectivité élevée.

Abstract

In the recent years, increasing attention has been paid to valorizing different types of waste materials to valuable chemicals. Waste valorization not only reduces the growing modern environmental issues, but also contributes to the sustainable development of the society. The alcoholic waste is an important category with high potential to be valorized into different types of valuable chemicals. As example, glycerol is a substantial alcoholic waste of biodiesel production process whose generation increased significantly during the recent years. In this context, photocatalytic valorization of alcoholic wastes is a promising approach from a sustainable development point of view.

The main objective of the thesis was to study the photocatalytic valorization of different biobased alcoholic wastes to value-added products. In this regard, this work focused on (i) analyzing individual and interaction effect of operating parameters and optimization of hydrogen production from glycerol (ii) studying the kinetics of hydrogen production from glycerol and ethanol, (iii) developing TiO_2 nanocomposite catalysts using biobased carbonaceous materials (carbon nanotubes and carbon spheres) and studding the roles of carbonaceous materials in hydrogen production from glycerol, and (iv) investigating the mechanism and kinetics of the photocatalytic valorization of cyclohexanol to cyclohexanone.

For hydrogen production from glycerol, Artificial Neural Network (ANN) as well as Response Surface Methodology (RSM) models were employed to evaluate the effect and importance of the main operating parameters (glycerol%, catalyst loading, Pt (cocatalyst)%, and pH). Comparison of these models revealed that the ANN model had a better accuracy and it was therefore selected for a Genetic Algorithm-based optimization. The highest amount of hydrogen production was found to be at 50% glycerol in water (v/v), 3.9 g/L catalyst loading, 3.1% Pt, and pH of 4.5. Finally, a Garson's method-based analysis of the relative importance of the operating parameters showed that the glycerol% and catalyst loading are, respectively, the least and most influential parameters on hydrogen production.

The important operating parameters (catalyst loading, substrate%, light intensity, and time) of the process of photocatalytic valorization of glycerol and ethanol to hydrogen were analyzed and a kinetic model was developed based on a proposed mechanism. The ability of the model to predict the rate of hydrogen production for different substrates, photocatalysts,

and ranges of operating parameters was confirmed by comparing the model predictions with the experimental data from literature.

Carbon nanotube (CNT) and carbon sphere (CS) were used to prepare carbonaceous TiO_2 composites and then the role of these biobased carbonaceous materials (CT) as template, cocatalyst, and adsorbent was investigated. The morphology analysis helped in examination of the template role and find the uniformity of the formed TiO_2 on the template. On the other hand, the photocatalytic experiments assisted in the analysis of the cocatalyst and adsorbent roles of CT. Interestingly, the results revealed that CNT incorporation in TiO_2 composite can almost double the rate of hydrogen production (i) in the absence of Pt or (ii) at low glycerol concentrations. Consequently, it was found that in addition to being a template, the CNT can play two important roles as cocatalyst and adsorbent.

To evaluate the valorization of alcoholic wastes to valuable liquid product, photocatalytic selective conversion of cyclohexanol to cyclohexanone was analyzed kinetically and spectroscopically. A reaction mechanism was proposed based on the *in-situ* ATR-FTIR analysis results and a kinetic model was developed to predict the rate of cyclohexanone production. Experimental data were used to evaluate the kinetic parameters using genetic algorithm method and confirm the accuracy of model predictions. A very high selectivity of cyclohexanone was confirmed by both spectroscopic and chromatographic (HPLC and GC-MS) analyses, demonstrating that the photocatalytic approach is a promising alternative for selective production of cyclohexanone.

In summary, the results of this thesis showed that photocatalysis is a promising alternative for valorization of biobased alcoholic wastes to value-added products. Photocatalytic conversion of alcoholic wastes can lead to the production of hydrogen as a promising green fuel for the future. On the other hand, the conversion of alcoholic wastes can be engineered to produce valuable liquid product with high selectivity.

Table of Contents

List of Figures

List of Tables

To my lovely wife Bahareh,

Sharing our life and love along this journey together is a blessing beyond words.

Acknowledgment

I would like to express my deepest appreciation to my supervisor, Prof. Maria Cornelia Iliuta, for her continuous guidance during my Ph.D. study. I am deeply indebted for her support not only for thesis work, but even different aspects of academic and personal life. I would like to also express my sincere gratitude to Dr. Mehrzad Feilizadeh for his endless advisement and mentorship through my Ph.D. research project. Many of the challenges in this path would not be solved without their creative ideas and supports.

I am very grateful to the Ministry of Education and Higher Education of Quebec, The Fonds de recherche du Québec - Nature et technologies (FRQNT), TELUS, Laval University, The Natural Sciences and Engineering Research Council of Canada (NSERC), and FQRNT Centre in Green Chemistry and Catalysis (CGCC) for their financial support.

I sincerely acknowledge all members of the Prof. Iliuta research group and my friends, who gave me the motivation and devoted their support and friendship in tough times. I am especially grateful to Farid Attar, Marziehossadat Shokrollahi Yancheshmeh, Alexandre Babin, Mustapha Aissaoui, Mohammad Reza Gholipour, Shahab Boroun, Ommolbanin Ali Zadeh Sahraei, and Antonin Paquet who assisted me during my research work.

I would like to greatly thank my parents, my brothers and my parents-in-laws for their love and supports. Without such a family behind me, I doubt I would accomplish this doctorate today.

Last, but not least, I thank with love to my dear wife, Bahareh, for her support, patience, and encouragement. Bahareh has been with me all these years and has made them the best years of my life. But most of all, thank you for being my best friend.

Foreword

This thesis comprises five chapters. An introduction on of photocatalytic valorization of alcoholic wastes is first presented and then an literature review is conducted in Chapter 1. Chapter 2 explains the methodology of material preparation and characterization, photocatalytic experiments and product analyses, preparation of statistical and kinetic models, and model optimization and analysis. Chapter 3 deals with statistical analysis and development of statistical models for the photocatalytic hydrogen production process from glycerol. Accordingly, the individual and interaction effects of main operating parameters of the process is studied. In the next stage, in Chapter 4 an intrinsic kinetic model was developed to predict the rate of hydrogen production as a function of the most important parameters obtained based on previous chapter. This chapter presents an intrinsic kinetic model for photocatalytic production of hydrogen in liquid phase that is valid for different substrates and photocatalysts. As the catalyst load was found to be the most effective operative parameter for hydrogen production from glycerol (Chapter 3), Chapter 5 deals with the incorporation of carbon nanotubes and carbon sphere (as carbonaceous templates) in the preparation of composite photocatalysts. The role of support, cocatalyst, and adsorbent of carbonaceous templates was studied. Following the kinetic study on the photocatalytic valorization of alcoholic wastes to hydrogen (Chapter 4), a spectroscopic and kinetic study was performed in Chapter 6 on photocatalytic selective valorization of alcoholic wastes to liquid product (cyclohexanol to cyclohexanone). This chapter presents a mechanism of reaction that is confirmed by *in-situ* ATR-FTIR experiments as well as an intrinsic kinetic model. Finally, the general conclusions and suggestions for future work are presented.

The articles representing Chapters 1 and 3-6 are listed below:

1. **M.R. Karimi Estahbanati,** Mehrzad Feilizadeh, Farid Attar, M.C. Iliuta., Photocatalytic glycerol valorization. Part I: Photocatalyst development. submitted (Chapter 1).
2. **M.R. Karimi Estahbanati,** Mehrzad Feilizadeh, Farid Attar, M.C. Iliuta., Photocatalytic glycerol valorization. Part II: Process analysis. submitted (Chapter 1).

3. **M.R. Karimi Estahbanati,** Mehrzad Feilizadeh, M.C. Iliuta. Photocatalytic valorization of glycerol to hydrogen: Optimization of operating parameters by artificial neural network, *Applied Catalysis B: Environmental*, 209 (2017), 483–492 (Chapter 3).

4. **M.R. Karimi Estahbanati,** Mehrzad Feilizadeh, M.C. Iliuta. An intrinsic kinetic model for liquid phase photocatalytic hydrogen production, *AIChE Journal*, https://doi.org/10.1002/aic.16724 (Chapter 4).

5. **M.R. Karimi Estahbanati**, Mehrzad Feilizadeh, Marziehossadat Shokrollahi Yancheshmeh, Maria C. Iliuta. Effects of carbon nanotube and carbon sphere templates in TiO_2 composites for photocatalytic hydrogen production, *Industrial & Engineering Chemistry Research, 58* (2019), 2770–2783 (Chapter 5).

6. **M.R. Karimi Estahbanati**, Mehrzad Feilizadeh, Alexandre Babin, Bastian Mei, Guido Mul, Maria C. Iliuta. Selective photocatalytic oxidation of cyclohexanol to cyclohexanone: a spectroscopic and kinetic study, *Chemical Engineering Journal*, https://doi.org/10.1016/j.cej.2019.122732 (Chapter 6).

The candidate has main contribution in all stages of the work presented in the current papers, including design of the experimental set-up, design of experiment, synthesis of materials, analysis of the characterization of materials, development of kinetic and statistical models, planning and performing experiments, as well as writing the papers by considering the supervisor's comments.

In addition, some parts of the obtained results during this research work were presented by the candidate in the following academic national conferences:

1- **M.R. Karimi Estahbanati**, Mehrzad Feilizadeh, Marziehossadat Shokrollahi Yancheshmeh, Maria C. Iliuta. Carbonaceous templates for TiO_2 nanocomposites: Preparation, characterization and photocatalytic activity for hydrogen production. *20^{th} International Conference on Emerging Materials and Nanotechnology*, Vancouver British Columbia (2018).

2- **M.R. Karimi Estahbanati**, Maria C. Iliuta and Mehrzad Feilizadeh. Photocatalytic valorization of alcoholic wastewaters to valuable products. *9th CGCC Annual Conference Meeting*, Quebec, Quebec (2018).

3- **M.R. Karimi Estahbanati**, M. Feilizadeh, M.C. Iliuta. Simultaneous photocatalytic treatment of biodiesel wastewater and production of hydrogen. *Congrès Eau Terre Environnement "Un environnement, plusieurs visions"*, Quebec, Quebec (2017).

4- **M.R. Karimi Estahbanati**, M. Feilizadeh, M.C. Iliuta. Statistical analysis of photocatalytic glycerol valorization into hydrogen. *66th Canadian Chemical Engineering Conference*, Quebec, Quebec (2016).

5- **M.R. Karimi Estahbanati**, M. Feilizadeh, M.C. Iliuta. Green hydrogen production by photocatalytic glycerol valorization: analysis of operating parameters. *ICCE2016: International Conference & Exhibition on Clean Energy*, Montreal, Quebec (2016).

6- **M.R. Karimi Estahbanati**, Mehrzad Feilizadeh, Maria C. Iliuta. Analysis of operating parameters for photocatalytic green hydrogen production from an industrial residue. *7th CGCC Annual Conference*, Montreal, Quebec (2016).

Introduction

Sustainable development is a set of principles that are essential to meet development goals of societies while preserving the natural systems to retain their ability of providing natural resources that the life cycle is dependent on them [1]. A society that adheres to the sustainable development principles contributes to supply of present generation needs without any negative effect in providing requirements of future generations. Sustainable development can be described in terms of three domain: environment (or ecology), economy, and society [2]. The ecological stability is connected to human and its natural, social and built environments [3]. The quality of human fundamental needs in life such as air, water, food and shelter are related to ecological stability [4]. By implementation of the sustainable development principles, the society has a continuous access to natural resources without deterioration of the integrity and stability of the ecosystem [5]. After industrial revolution, environment deteriorating human activities accelerated rapidly, caused a series of ecological and *environmental issues*.

Damages that affect the natural environment by human activities is known as environmental issues. These damages can be occurred in terms of climate change, pollution, environmental degradation, and resource depletion [6]. Resource depletion occur because of the activities that lead to natural resources depletion in higher rate than their replenishment. The depletion of resources can be categorized into depletion of minerals, water, wetlands, oil resources, renewable resources, and deforestation. Depletion of oil resources is an important issue of societies, which is creating big concerns as a result of expanding population of earth. It is predicted that the global human population will reach around 10 billion by year 2050 [7], raising current environmental issues. As a result, efficient management of resources is essential for sustainable development of societies. In this regard, reusing, recycling, and valorization of wastes should be considered. As depletion of oil resources will considerably affect provision of energy and organic resources for living, finding *renewable resources* have gained a lot of attentions in the last years.

A renewable resource is a resource in the nature that reproduces naturally or through recurring processes in a limited time in comparison to human time scale. Renewable

chemicals that are related to carbon atoms from biomass are important class of renewable resources according sustainable development goals. Renewable energies are another important type of renewable resources that refers to the kind of energies that naturally replenished with an acceptable rate as are being harvested. Based on the experiences related to renewable energy production from biomass in the recent years, utilization of food feedstocks for production of renewable chemicals and energy is not desirable due to the issues related to provision of human food needs in long term. Non-food feedstocks, lignocellulosic, and waste streams are the most important renewable sources for generation of renewable chemicals and renewable energy [8]. Using renewable waste streams as renewable resources is considered as a green approach in the last years. Renewable wastes can be categorized into municipal, agricultural, forestry, and industrial [9]. *Alcoholic wastes* discharged from industries are important source of renewable chemicals that can be valorized into a vast variety of valuable chemicals.

The rapid human population growth in parallel with changing the lifestyle toward consumerism considerably increased global waste production, causing serious environmental issues. The growth of waste generation by various industries (e.g., agricultural, food, chemical) is a nowadays global issue, especially in the developing countries. Waste produced by food processing companies is a typical example of large scale production of pre-consumer type of waste. This source of waste is significant in many societies as may compose more than half of the total waste production, around 60% belonging to organic wastes [10]. Alcoholic wastes are a kind of organic waste that can easily contaminate the environment and surface water. Many simple alcohols can be produced through fermentation of saccharides, ethanol is the most common [11, 12]. By pyrolysis of biofuels, different alcohols such as methanol, ethanol or other alcohols may be produced [13].Cyclohexanol is another example of alcoholic wastes that could be produced during transformation of biomass-derived feedstocks [14, 15]. As this cyclic alcohol is used as precursor for nylon production, cyclohexanol is an important feedstock in the polymer industry. Glycerol is one of the most well-known alcoholic wastes that is produced through production of biodiesel process [16]. United States Department of Energy analyzed the top value added chemicals from biomass, glycerol was selected as one of top carbohydrate-derived building blocks for production of

renewable chemicals [17]. Because of the significance of glycerol and its economic and technical potentials for valorization to valuable products, it is well discussed in the following.

Approximately 22.7 million tons of biodiesel was produced in 2012 and the 2020 production is estimated at 36.9 million tons [18]. This rapid development of biomass industries causes a vast production of glycerol as a waste (crude glycerol) [19]. The amount of glycerol in the biodiesel wastes can vary from about 1% to 85% (v/v) [20]. On average, around one volume of crude glycerol is formed for every 10 volumes of biodiesel [21]. As the glycerol market is limited, its overproduction led to a glut and significant decrease of its price in the recent years [15, 22]. As it can be seen from Fig. I. 1, the glycerol price in the market has surprisingly reduced around fivefold from 2004 to 2006. It is predicted that in 2022 glycerol oversupply would be twenty-fold [23], which will decrease its price more than ever [24].

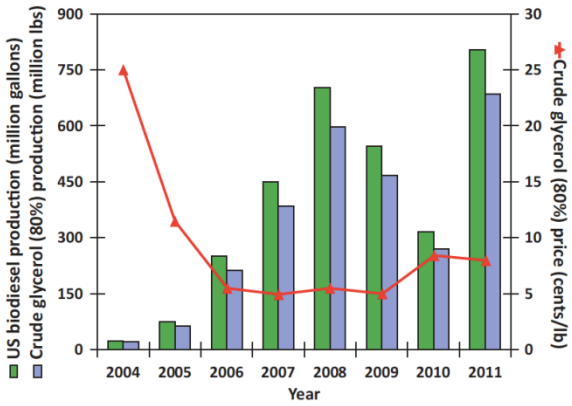

Fig. I. 1. The amount of glycerol production and its price in the market in the recent years [25].

Glycerol has diverse applications such as cosmetic, paint, food, tobacco, pharmaceutical, pulp and paper, leather, and textile industries [26, 27]. On the other hand, crude glycerol contains impurities like methanol, soap, salts, oils, and solid organic materials [28]. These impurities restrict applications of glycerol in most of the industries mentioned above and glycerol purification implies excessive cost [29]. As a result, the research on alternative technologies to convert glycerol to value-added products has been considerably increased in the recent years.

The present thesis will focus on the valorization of *glycerol, ethanol,* and *cyclohexanol,* as three promising biobased alcoholic wastes for value-added products generation. The literature review related to the present thesis will therefore be limited to these substrates.

Because of depleting the petroleum sources, some efforts are necessary to develop new technologies for production of valuable chemicals from alternate sources to mitigate the forthcoming social and economic influences of this issue. By considering the sustainable development approach, alcoholic wastes are valuable resources for the production of chemicals and fuels [10, 30]. Valorization of alcoholic wastes not only takes advantage of low cost of provision, but even contributes to protection of environment by consumption of polluting wastes. This approach will enhance the profit of industries through achievement of a zero waste economy.

In the recent years, an increasing interest has been devoted to biomass valorization technologies and contributed in creation of "biorefinery" concept. The concept of biorefinery is similar to conventional refineries, but (i) biomass and waste are used as feedstocks instead of crude oil, and (ii) valorization of feedstocks to valuable products is performed by employing sustainable and environmentally friendly technologies [31]. In this way, modern approaches should be followed in resource management to valorize residues, byproducts, and wastes in an economic order. It is expected that unlike traditional petrochemical refineries which are mostly dependent on thermal processes, employment of novel approaches such as fermentation, enzymatic and photocatalytic conversions will be dominant in future biorefinery industry. In a biorefinery, the alcoholic wastes can be valorized to value-added products, both in liquid and gas phases [32, 33]. This valorization process can be performed through oxidation, hydrogenolysis, dehydration, pyrolysis, gasification, transesterification, esterification, etherification, and carboxylation reactions [34, 35].

Ethanol, as an important biobased alcohol, can be valorized to various gas and liquid products. Dehydrogenation of ethanol occurs in two-electron transfer steps and leads to production of hydrogen and acetaldehyde [36]. Radical coupling of 1-hydroxyethyl species formed by dehydrogenation of ethanol towards C−C bond formation generates 2,3-

butanediol [37]. By partial or complete ethanol photoreforming, different gaseous products such as H_2, CH_4, C_2H_4, C_2H_6, CO and CO_2 can be obtained [15].

One-step dehydrogenation of cyclohexanol leads to production of hydrogen and cyclohexanone, as gas and liquid phase products, respectively. Cyclohexanone is an key feedstock in polymer industry for caprolactam production [38]. Caprolactam is a principal monomer for production of nylon-6. Around 90% of caprolactam produced in the polymer industry is generated from cyclohexanone [39]. A significant amount of energy is consumed during production of caprolactam, since it is mainly produced through thermal routes at high temperatures and pressures [40]. Analysis of 12 different alcohols revealed cyclohexanone ranks 10th in rate of photocatalytic hydrogen production through photo-reforming, suggesting that it is not a good substrate for photocatalytic hydrogen production [41]. Liquid phase analysis of cyclohexanol photocatalytic oxidation demonstrated a 100% selectivity for cyclohexanone production [42, 43]. Photocatalytic conversion of cyclohexanol to cyclohexanone for subsequent caprolactam production seems a sustainable approach for production of bioplastics.

As already mentioned, glycerol seems the most promising alcoholic wastes because of its overproduction in the recent years. Glycerol molecule is highly functionalized in comparison to other hydrocarbons derived from crude oil [44]. A vast range of potential chemicals can be generated through partial oxidation of glycerol: C3 (dihydroxyacetone, hydroxypyruvic acid, mesoxalic acid, glyceraldehydes, glyceric acid, tartronic acid, and hydroxymethyl glyoxal), C2 (oxalic acid and hydroxyethanoic acid) and C1 (formic acid and COx). Moreover, by hydrogenolysis of glycerol, the chemicals like 1,2-propanediol, 1,3-propanediol, and ethylene glycol can be produced [45]. The production of hydrogen from glycerol has although received the highest attention, as a promising green fuel of tomorrow.

Although different chemicals can be produced from the valorization of alcoholic wastes, the present thesis will focus only on the production of *hydrogen* (from glycerol and ethanol) and *cyclohexanone* (from cyclohexanol), as sample gas and liquid products. The literature review will therefore be limited to these subject.

Energy security has ever been one of the concerns of human beings. Since industrial revolution in the 18th century, exploration of fossil fuels accelerated rapidly, raised concerns

regarding risks of its depletion in the near future. The concerns related to energy crises as well as environmental issues forced countries to invest in renewable energies. Hydrogen is a type of renewable energy (provided that it is produced from renewable sources) that is considered as a promising alternative energy source for the future [46, 47]. Hydrogen production from biobased alcoholic wastes is indeed a proper approach from the sustainable development point of view.

Steam reforming of methane (derived from natural gas) to produce synthesis gas followed by water gas shift reaction is currently the most conventional and economical method for hydrogen production. The price of every kg of hydrogen produced by this process is around 1.5–3.75 US$ [48]. On the other hand, for the case of glycerol as an alcoholic waste example, the cost of hydrogen produced based on glycerol steam reforming is in the range of 2.6–3.8 US$ per kg [49]. It seems that by increasing the price of fossil fuels (because of diminishing fossil fuel reservoirs) as well as decreasing glycerol price (due to more glycerol glut in the market), production of hydrogen from glycerol will be more economically viable than methane.

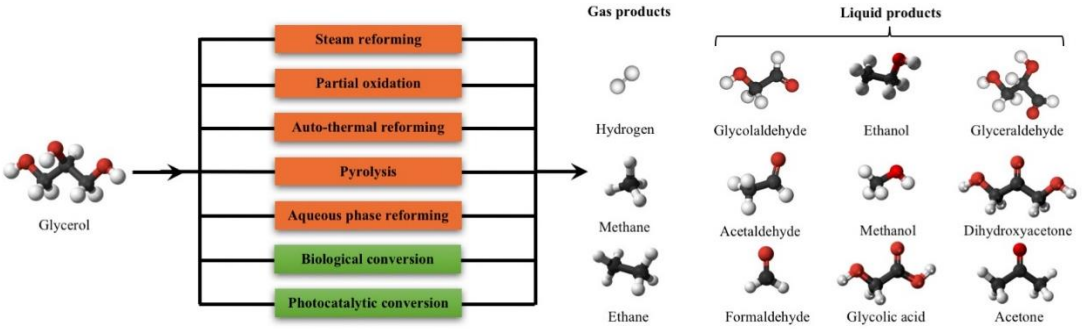

Fig. I. 2. Summary of most common methods for glycerol valorization and most common gas and green liquid products.

Different thermal [50, 51], biological [52, 53], and photocatalytic [54] technologies can be employed for valorization of wastes. Fig. I. 2 shows different methods for glycerol valorization to the most important value-added gas and liquid products. Thermal technologies usually convert waste to valuable products in a process that usually working at high temperature. The most common thermal methods for alcoholic wastes conversion to hydrogen or liquid products are steam reforming, partial oxidation, auto-thermal reforming, pyrolysis, aqueous phase reforming [55]. In catalytic steam reforming process, alcohol reacts

with water at a high temperature of 600–800 K [56]. In partial oxidation, alcohol reacts with oxygen in sub-stoichiometric ratios at even higher temperatures of around 1000-1100 K [57]. Auto-thermal reforming is a combination of partial oxidation and steam reforming, during which a defined ratio of alcohol, water and air are fed into reactor simultaneously [27]. Pyrolysis is thermal decomposition of alcohol in the absence of oxygen to produce bio-oils for subsequent conversion to other feedstocks. Aqueous phase reforming is a new and non-conventional approach which operates at moderate temperatures (200–250 °C) and pressures (2–2.5 MPa) [58, 59].

Although in thermal processes the rate of reaction is high, they impose high energy consumption and may not be suitable from sustainable development point of view. Biological processes are ecofriendly approaches that take advantage of low temperature and pressure, low waste generation, and low energy consumption, however, suffers from long operating time (about 3–5 months), feedstock loss, and low conversion efficiency [60].

Photocatalytic waste valorization is a new alternative that takes advantage of operating at ambient temperature and pressure, utilizing clean solar energy for the driving force, and low operating cost. However, photocatalysis suffers from low rate of conversion and high capital cost [61]. From an environmental point of view, photocatalytic valorization of biobased alcohols is a very attractive process; from a technological point of view, however, there are several restrictions due to its low reaction rate and the presence of impurities in alcoholic wastes such as the case of crude glycerol. As a result, more intensive research is compulsory to reduce these limitations and improve the process efficiency towards an economically viable process. For example for the case of hydrogen production, such a process should be capable to produce hydrogen with price of 2.0–4.0 US$ per kg H_2 [62].

The present thesis concerns *photocatalytic* valorization of alcoholic wastes. The literature review will therefore be limited to the works performed based on the photocatalysis approach.

Photocatalysis is a reaction that uses a catalyst which is activated in the presence of light. This process mimics natural photosynthesis which directly harvests photons of solar radiation to drive chemical reactions. The idea of photocatalysis was first developed in 1912 by

Ciamician [63], however, it was called photocatalysis after Fujishima and Honda [64] who discovered water photolysis on a TiO_2 electrode.

In a photocatalytic reaction, the semiconductor absorbs a photon of light to produce a pair of photogenerated electron and hole and utilizes them in redox reactions. The energy of incident photon must be equal or higher than the band gap energy of semiconductor to be absorbed. In other words, the wavelength of light must be shorter than the band gap of the semiconductor. In this case, an electron can be promoted from a filled valence band to an empty conduction band of the photocatalyst. The photogenerated electron tends to recombine rapidly (as fast as ~10 ps [65]) with a hole, unless an electron scavenger is available to absorb it. Fig. I. 3 represents the main processes during a photocatalytic reaction.

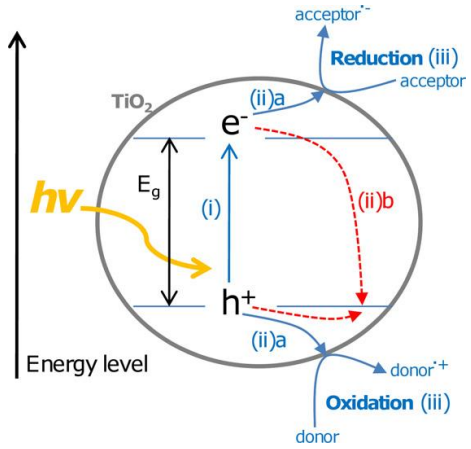

Fig. I. 3. Schematic representation of (i) production of photogenerated electrons and holes by a photon of light; (ii) consumption of photogenerated species towards surface reaction cites (a) or recombination and conversion to thermal energy (b); (iii) performance of oxidation and reduction reactions at active sites [66].

In spite of extensive research on photocatalytic processes, rarely a visible light driven semiconductor can reach more than 5% efficiency, mainly because of recombination reactions [67, 68]. However, that a benchmark efficiency of 10% is required for commercialization purposes [69]. Although the rate of overall water splitting for hydrogen production is extremely low, some semiconductors can perform one of half reactions in the presence of some substrates to increase the rate. For example, the substrate can react with photogenerated holes, not only contribute in production of hydrogen, but also facilitate

hydrogen production through water splitting. In general, the substrates are more readily oxidized than water to react with photogenerated holes.

Although extensive research has been performed on photocatalytic reactions in the recent years, most of them focused on degradation of pollutants (photocatalytic degradation) [70] and only recently, targeted conversion of chemicals (photocatalytic synthesis) attracted some attention. While the photocatalytic degradation considers the substrate as pollutant and aims to eliminate it, in photocatalytic synthesis the substrate is considered as feedstock to selectively convert it to valuable chemicals. As a result, in photocatalytic synthesis the reaction is engineered to not only produce higher value products, but also increase their selectivity. Table. I. 1 compares photocatalytic degradation and photocatalytic synthesis approaches. As can be seen, although photocatalytic synthesis seems a promising approach, a limited attention has been devoted to this area in comparison to photocatalytic degradation.

Table. I. 1. Comparison of photocatalytic degradation and photocatalytic synthesis approaches.

	Photocatalytic degradation	**Photocatalytic synthesis**
Target	Environmental treatment	Synthesis of chemicals
Role of substrates	Pollutant	Feedstock
Products	Not controlled	Engineered
No. of papers[1]	6,031	104

[1] The number of papers with "photocatalytic degradation" or "photocatalytic synthesis" in their title. Data collected from "Web of Science" on Apr. 25, 2019.

Chapter 1 : Literature review

1.1. Operating conditions

In order to perform the experiments for this work, a comprehensive literature review was first conducted to find a suitable range of operating conditions, as summarized in Table 1.1. Accordingly, most of the works used a UV source of light to conduct the photocatalytic experiments, which can be attributed to higher activity of photocatalysts under UV radiation in most cases. Some experiments were also performed under visible or solar radiations, as visible light forms an important fraction of solar radiation. The power of light source is an important factor that must be considered for comparison of different experiments, as most of the reviewed works did not provide quantum yield. According to Table 1.1, a power in the range of 100-500 W is used for most of the reviewed works, which is approximately the sum of visible, UV, and infrared energies emitted by sun to 0.1-0.5 m^2 at ground level in the noon [71]. To investigate efficiency of photocatalyst at a limited range of light spectrum, some works used a filter (mainly 365, 418, or 420, nm) to control the spectrum of emitted light. The amount of photocatalyst loading used to conduct the photocatalytic experiments were selected in the range of 0.1-3 g/l. Around 10% alcohol solution in water was used in most of the works that is equal to the average percentage of glycerol in crude glycerol [21]. The solution volume was selected in the range of 10-200 ml and its temperature was controlled to be fixed around ambient in most of the works. According to Table 1.1, the reviewed works mostly did not report quantum yield, which makes it difficult to compare different works.

Table 1.1. Operating condition of different research on photocatalytic alcohol valorization.

Photocatalyst	Light source	Power (W)	Filter	Photocatalyst loading (g/l)	Alcohol concentration (v/v)%	Solution volume (ml)	Reaction temperature	Quantum yield (%)	Ref.
TiO_2 nanorod	Solar	-	-	0.1	5	50	ambient	-	[72]
TiO_2 nanorod	Solar, UV LED	300	400 nm	0.2	5	5	-	-	[73]
Pt/TiO_2	Xe	450	Water	0-2.7	0.00073–7.9	60	40 °C	-	[74]
Pt/TiO_2	UV-visible	125	-	0.38	6	260	ambient	-	[75]
Pt/TiO_2	Hg, Halogen	250, 300	420 nm	0.06	20	80	-	-	[76]
Pt/TiO_2	Xe	300, 450	water filter	1.3	0.00073–0.01	60	ambient	1.8 (Pure water), 70 (Glycerol) @ λ=365 nm	[77]
Pt/TiO_2	Hg, Halogen	250, 300	420 nm	0.6	10	80	-	-	[78]
Pt/TiO_2	Hg	250	-		10	200	-	-	[79]
Pt/TiO_2	Hg	250	-	0.4	0-20	100	ambient	-	[80]
Pt/TiO_2	Osram	450	-	1.3	0, 0.0027-0.01	60	40 °C	-	[81]
Pt/TiO_2	Hg	125	-	0.25	0.02	200	30 °C	-	[33]
Pt/TiO_2	Xe	150	-	0.6	7.3	80	25 °C	-	[82]
Pt/TiO_2	Fluorescent, Sun	4×15	-	1	-	75	25 °C	-	[83]
Pt/TiO_2	Xe	300	-	0.6	3.2	155	ambient	-	[84]
$rGO/Pt/TiO_2$	Hg, LED	450, 230	-	0.1-1	5-80	300	30-40	-	[85]
M/TiO_2 (M=Au, Pt, Pd)	Hg	125	-	1	10	85	-	-	[86]
M/TiO_2 (M=Au, Pt, Pd)	Xe	(2-4)×75	-	0.09-8.75	4.5	16	25-55 °C	-	[87]

M/TiO_2 hollow sphere (M=Cu, Cr, Ag, Co, Ni)	solar	-	-	2	5	50	-	-	[88]
M/TiO_2 (M= Pd, Pt, Au)	UV-A	200	365 nm	0.3	10	20	-	-	[89]
M/TiO_2 (M=Pt, Cu)	Xe	300	-	0.5	10	100	-	-	[90]
M/TiO_2 (M=Pt, CuO)	UV-A	-	-	2.3	1.04-0.73	250	40 °C		[91]
$Pt/B,N,TiO_2$	Xe	300	-	1	2-10	50	-	-	[92]
$Pt/Cu_xTi_{1-x}O_{2-\delta}$	Solar, Hg	450	water filter	6.7	33	15	-	7.5% @ λ=300–600nm	[93]
$Cu_{0.02}Ti_{0.98}O_{2-\delta}$	Solar, Hg	-	-	3.3-10	20	15	-	-	[94]
$Pt/N/TiO_2$ nanotube	Hg	250	-	1	50	400	-	37% @ λ=365	[95]
Cu/TiO_2	Sun, Hg	400	-	2	5	50	-	-	[96]
Cu/TiO_2	Hg, Xe	125	atmospheric	2.1	7.3	240, 80	-	-	[97]
Cu/TiO_2	Hg	125	-	0.1-0.19	0.75-18	-	25 °C	-	[98]
Cu/TiO_2 nanosheets	Xe	300	-	0.5	5	100	-	-	[99]
Cu/TiO_2 nanotube	Solar	-	-	0.06-2	5	50	ambient	-	[100]
CuO_x/TiO_2	Osram	250	water	1.3	0.0027-7.3	60	ambient	-	[101]
CuO_2/TiO_2	Metal halide	400		0.5	5	200	-	-	[102]
$Cu_3(PO_4)_2/TiO_2/CuO$	Solar	-	-	0.05-0.4	5	50	ambient	-	[103]
Cu/TiO_2 nanorod	Solar	-	-	0.1	5	50	ambient	-	[104]
M/TiO_2 (M=Cu, Ni)	Halogen	500	-	12.5	0-50	8	ambient	-	[105]
CP-1/TiO_2*	UV-A	-	-	0.2	5	25	-	-	[106]
Au/TiO_2	UV-A	100	365 nm	6.5	10-90	20	-	-	[107]
Au/TiO_2 nanorod	UV-A	100	365 nm	0.3	10-90	20	-	-	[108]
M/TiO_2 (M= Au, Pd, Au-Pd)	UV-A	100	365 nm	0.325	10	20	-	-	[109]
M/TiO_2 (M= Au, Pd)	Xe	400	-	2	0.1	100	ambient	-	[110]
Pd/TiO_2	Xe	400	-	2	0.1	100	-	-	[41]
Ag/TiO_2 nanotube	Solar	-	-	0.1	5	50	ambient	-	[111]

Co/TiO_2	Hg, sun	400	-	2	5	50	-	-	[112]
NiO/TiO_2	Hg	500	-	1.7	0-25	12	50 °C	-	[113]
$Ni(OH)_2/TiO_2$ nanotube	Solar	-	-	0.1	5	50	-	-	[114]
NiO_x/TiO_2	Hg	500	-	1.7	16.6	12	50 °C	-	[32]
TiO_2, CuO_x/TiO_2	Hg	125	-	2.1	7.3	240	20 °C	29% @ λ=365 nm	[115]
Cu/TiO_2	Halogen	-	-	1	10	100	24 °C	-	[116]
$N/M/TiO_2$ (M=Cr, Co, Ni, Cu)	Hg	450	-	2	10	10	30 °C	-	[117]
TiO_2/CNT	Solar	-	-	0.06-2	5	50	ambient	-	[118]
$La/CNTs/TiO_2$	UV-visible	35	-	0.83	10	120	-	-	[119]
Montmorillonite/ TiO_2/CNTs	Xe	335	-	0.625	1-10	80	-	-	[120]
TiO_2/CNTs	Hg	-	-	-	5	-	-	-	[121]
Pt/TiO_2/Graphene	Xe	500	-	0.1	10	800	Ambient	-	[122]
$rGO/CuFe_2O_4/TiO_2$	Xe (UV-vis)	250	-	0.2	5.2	50	-	-	[123]
$rGO/g\text{-}C_3N_4/TiO_2$	Xe (UV-vis)	250		0.2	5.2	50	-	-	[124]
$Fe/g\text{-}C_3N_4/TiO_2$	Solar	-	-	0.2	10	50	-	-	[125]
Cu_2O/TiO_2/Graphene oxide	Xe	250	-	0.1	5	-	-	-	[126]
HPA/TiO_2 (HPA= $H_3PW_{12}O_{40}$,	UV-A	4×8	-	1	-	100	35 °C	-	[127]
M/TiO_2(M=Ag_2O, Bi_2O_3, ZnO)	UV-vis	350	-	0.2	10	100	ambient	3.2%@ λ=320–780nm	[128]
Pt/CdS, Pt/TiO_2	Hg–Xe	500	IR, 418 nm	1	30	60	-	-	[129]
Pt/CdS	Hg-Xe	500	IR, 418 nm	1-2	30-70	60	-	-	[130]
Ni/CdS	Hg	500	400 nm	0.04	0.15-32.85	10	-	12.2% @ λ=410	[131]
Zn_2TiO_4	Solar	-	-	0.2	5	50	ambient	-	[132]
$Cd_{0.5}Zn_{0.5}S$	Hg	250	420 nm	0.5	10	100	-	-	[133]
$Pt/Cd_{1-x}Zn_xS$	Hg-Xe	500	IR, 418 nm	1.2	50	100	-	-	[134]

$Pt/Cd_{1-x}Zn_xS$ /ZnO /$Zn(OH)_2$	Hg	1000	420 nm	0.8	0.365-7.3	-	20 °C	9.6% @ λ>420 nm	[135]
ZnO/ZnS	Xe	350	-	0.02-4	10	50	25 °C	13.90%	[136]
ZnO/ZnS	Hg, Xe	125, 500	-	30	7	10	-	22% (UV), 13% (Solar) @ λ=365 nm	[137]
ZnO/ZnS/graphene	Hg	300	-	0.5	1-50	100	30 °C	-	[138]
Pd/PdS-ZnO/ZnS	Hg, Xe	125, 500	water filter	6	5	10	-	-	[139]

*CP-1: ($[\{Cu^{II}(4,4'\text{-dipy})_2\}\{Ni(CN)_4\}]_n 0.7(C_2H_6O_2)1.6(H_2O)$ polymer)

1.2. Reaction mechanism

1.2.1. Photocatalysis in water

The photocatalytic reaction is triggered by absorption of a photon of light to generate a pair of electron and hole as follows:

$$TiO_2 \xrightarrow{h\upsilon} e^- + h^+ \quad (1–1)$$

The photogenerated species could initiate a series of reactions. H^+ ions can be produced by water ionization (Eq. (1–2)) or reaction of water molecule with a photogenerated hole (Eq. (1–3)):

$$H_2O \rightarrow OH^- + H^+ \quad (1–2)$$

$$H_2O + h^+ \rightarrow OH^\bullet + H^+ \quad (1–3)$$

In the absence of oxygen, two H^+ ions can produce a hydrogen molecule using two photogenerated electrons:

$$2H^+ + 2e^- \rightarrow H_2 \quad (1–4)$$

On the other hand, in the accessibility of molecular oxygen, it can be reduced by photogenerated electrons to form a superoxide radical:

$$e^- + O_2 \rightarrow O_2^{\bullet -} \quad (1–5)$$

Moreover, the generated superoxide radicals may be protonated as follows:

$$O_2^{\bullet -} + H^+ \rightarrow HO_2^\bullet \quad (1–6)$$

$$O_2^{\bullet -} + H^+ + HO_2^\bullet \rightarrow H_2O_2 + O_2 \quad (1–7)$$

Afterward, photoreforming of hydrogen peroxide can also generate free hydroxyl radicals [140]:

$$H_2O_2 + hv \rightarrow 2OH^{\bullet} \quad (1–8)$$

These free radicals have a great potential to react with other species in the solution, like alcohol molecule [141].

Even in the absence of alcohol, hydrogen can be produced by photocatalytic water splitting process.

$$2H_2O \rightarrow 2H_2 + O_2 \quad (1–9)$$

During this reaction, protons are reduced by photogenerated electrons (Fig. 1.1 (a)) and on the other hand, water molecules are oxidized by photogenerated holes (Fig. 1.1 (b)).

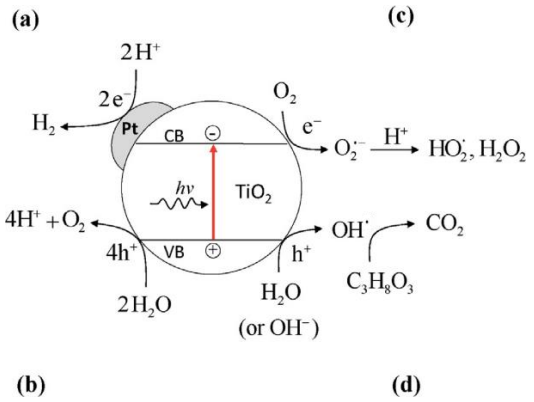

Fig. 1.1. Schematic representation of water splitting (a+b), glycerol photo-oxidation (c+d) and glycerol photoreforming (a+d) over Pt/TiO_2 photocatalyst [69].

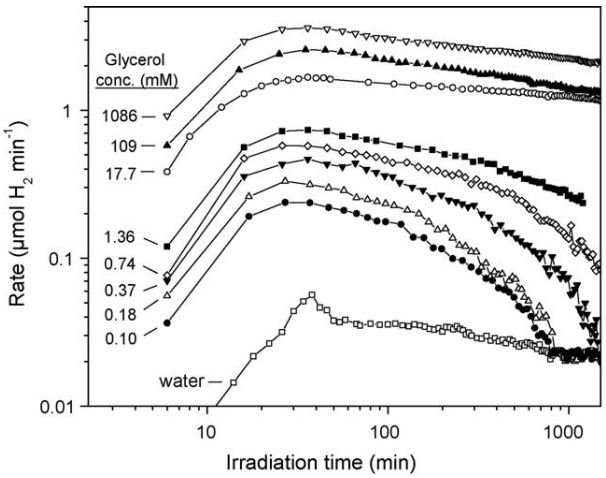

Fig. 1.2. Correspondence of hydrogen production rate from solutions containing low concentration of glycerol with hydrogen production rate from pure water at prolonged time [74].

1.2.2. Alcohol valorization

The photocatalytic valorization of alcohol can be performed through its direct reaction with photogenerated holes (hole-mediated mechanism) or indirect reaction with photogenerated hydroxyl radicals (radical-mediated mechanism). Apart from the mechanism of reaction, deep oxidation of alcohol leads to the generation of hydrogen and carbon dioxide. Addition of alcohol to the solution can significantly increase the rate of hydrogen production by water splitting. At low alcohol concentrations, by passing irradiation time, the rate of hydrogen

production approaches the rate of hydrogen production from water splitting, indicating the water splitting mechanism governs after alcohol consumption (Fig. 1.2) [74].

The photocatalytic valorization of alcohol can be performed in the presence of oxygen (photo-oxidation) or its absence (photo-reforming). Table 1.2 illustrates the comparison of water splitting, alcohol photoreforming and alcohol photo-oxidation reactions. Accordingly, only in the alcohol photo-oxidation process, oxygen molecule is present to play the role of oxidant and in the alcohol photoreforming process the water molecule plays the role of oxidant. As water is not an effective oxidant in comparison to oxygen, the rate of alcohol photo-oxidation is much greater than alcohol photoreforming [69]. In addition, only in the absence of oxygen alcohol can be valorized to hydrogen as in the alcohol photo-oxidation reaction protons are oxidized to water and no hydrogen may be produced. It is worth to mention that of alcohol can be valorized to green liquid chemicals by both photo-oxidation and photoreforming processes, however, the rate of the former one is higher [69].

Table 1.2. Comparison of water splitting, alcohol photoreforming and alcohol photo-oxidation reactions.

	Water splitting	**Alcohol photoreforming**	**Alcohol photo-oxidation**
Presence of oxygen	×	×	✓
Oxidant	-	Water	Oxygen
Reaction rate	Very low	Low	High
H_2 production	✓	✓	×
Green liquid chemicals production	×	✓	✓

The mechanisms of water splitting (a+b), alcohol photo-oxidation (c+d) and alcohol photoreforming (a+d) over Pt/TiO_2 photocatalyst are schematically represented in Fig. 1.1. In the photo-oxidation process, alcohol is oxidized by O_2 to produce CO_2 and H_2O (Eq. (1–10)). On the other hand, in the anaerobic condition, alcohol is oxidized by H_2O to produce protons which in turn convert to hydrogen molecule. For the case of glycerol as an example, the overall photo-oxidation and photoreforming reactions are illustrated in Eqs. (1–10) and (1–11), respectively [69].

$$C_3H_8O_3 + (7/2)O_2 \rightarrow 3CO_2 + 4H_2O \quad (1–10)$$

$$C_3H_8O_3 + 3H_2O \rightarrow 3CO_2 + 7H_2 \quad (1–11)$$

According to Eq. (1–11), during the photoreforming of glycerol, hydrogen molecules are produced both from glycerol and water; however, the share of glycerol is more. It could be verified by observation of a significant amount of hydrogen production from glycerol solution in D_2O as the solvent, suggesting that glycerol is the main source of hydrogen [113]. In addition, a stoichiometric amount of hydrogen based on Eq. (1–11) was detected by complete photo-decomposition of dilute glycerol solutions [84].

Table 1.3. Summary of the range and optimum values (in the parenthesis) of various parameters investigated in different research on alcohol valorization to hydrogen.

Photocatalyst	Cocatalyst wt%	Calcination Temp. (°C)	Alcohol % (vol/vol)	pH	Photocatalyst loading (g/L)	Duration (hr)	Hydrogen source	No. of cycles	Reaction temperature (°C)	Ref.
TiO_2 nanorod	-	200-400 (250)	-	-	-	-	-	5	-	[72]
Pt/TiO_2	0.05-5 (2)	-	0.00073–7.9 (7.9)	3-10 (8)	0–2.66 (2.66)	-	-	-	40-80 (60)	[74]
Pt/TiO_2	-	-	-	-	-	5	-	-	-	[76]
Pt/TiO_2	-	-	0-8 (8)	-	-	27	LAC>CBO> MALE>ST>CL	-	-	[77]
Pt/TiO_2	0-2 (0.5)	-	-	1-4.5 (1)	-	-	-	-	-	[78]
Pt/TiO_2	-	-	0-20 (20)	0-13 (6.4)	-	5	-	-	-	[80]
Pt/TiO_2	-	-	0-0.01 (0.01)	-	-	70	-	-	-	[81]
Pt/TiO_2	-	-	-	-	-	14	GLY>PPG>IPA	-	-	[33]
Pt/TiO_2	-	-	-	-	-	24	-	-	-	[82]
Pt/TiO_2	-	-	8.9-73.9 (62.3)	-	-	3.5	-	5	-	[83]
Pt/TiO_2	-	200-500 (400)	0.006-9.7 (9.7)	-	-	5	-	4	-	[84]
CP-1/TiO_2*	2.5-7.5 (5)	-	-	-	-	-	-	-	-	[106]
M/TiO_2 (M=Au, Pt, Pd)	0.5–3 (3)	-	-	-	-	16.7	-	-	-	[86]
M/TiO_2 (M= Au, Pd, Au-Pd)	-	500-700 (600)	-	-	-	3	GLY>MEG>ETOH	-	-	[109]
M/TiO_2 (M=Au, Pt, Pd)	0.1-0.5 (0.1)	-	-	-	0.09-8.75 (0.09)	3.5	GLY>MEOH>ETOH> IPA>1-BOH>GLC	-	-	[87]

M/TiO_2 (M= Pd, Pt, Au)	-	-	-	-	-	6	GLY>MEG>PPG >MEOH>ETOH> IPA> TBA	-	-	[89]
M/TiO_2 (M=Pt, Cu)	-	-	-	-	-	3	-	-	-	[90]
M/TiO_2 (M=Pt, CuO)	-	-	-	-	-	-	GLY>crude GLY	-	-	[91]
$Pt/B,N,TiO_2$	-	-	2-10 (10)	-	-	-	GLY>GLC≈SUC	-	-	[92]
$Pt/Cu_xTi_{1-x}O_{2-\delta}$	-	-	-	-	-	12	MEOH>GLY	-	-	[93]
$Pt/N/TiO_2$ nanotube	-	-	0-70 (50)	-	-	5	-	-	-	[95]
Pt/TiO_2/Graphene	-	-	-	-	-	6	GLY>MEG> MEOH> PPG ETOH>PA	4	-	[122]
$rGO/Pt/TiO_2$	1.5-3.8 (3.8)	-	5-80 (20)	5-11 (7)	0.1-1 (0.25)	-	-	2	30-40(30)	[85]
$rGO/CuFe_2O_4/TiO_2$	1-4 (3) for rGO	-	-	-	-	4	-	4	-	[123]
$rGO/g\text{-}C_3N_4/TiO_2$	0.5-1.5 (1.5)	-	-	-	-	4	GLY>MEOH> TETA	4	-	[124]
$CuFe_2O_4/TiO_2$	10-40 (20)	-	-	-	-	4	-	-	-	[123]
$Cu_3(PO_4)_2/TiO_2$/CuO	0.5-3 (1)	500-800 (500)	0-20 (5)	-	0.05-0.4 (0.2)	-	-	5	-	[142]
Cu/TiO_2	0.2-5 (0.5)	-	0-20 (5)	-	-	-	-	6, 8	-	[96]
Cu/TiO_2	1, 2.5 (2.5)	-	-	-	-	-	-	-	-	[97]
Cu/TiO_2	-	-	0.75-18 (18)	-	-	-	-	-	-	[98]
Cu/TiO_2 nanosheets	0-2.65 (1)	200-450 (350)	-	-	-	3	-	5	-	[99]
Cu/TiO_2 nanotube	0.1-2 (1.5)	-	-	-	0.06-2 (0.1)	-	-	-	-	[100]

CuO_x/TiO_2	0.01–2.8 (2.8)	-	0.0027-7.3 (7.3)	-	-	16.7	-	-	-	[101]
Cu/TiO_2 nanorod	0.5-2(1.5)	400-550 (500)	-	-	-	-	-	3	-	[104]
M/TiO_2 (M=Cu, Ni)	0-15 (10)	-	0-50 (20)	-	-	-	-	-	-	[105]
Au/TiO_2	-	-	-	-	-	3	GLY>MEG>MEOH>ETOH	-	-	[107]
Au/TiO_2 nanorod	0.5-2 (1.5)	200-1000 (600)	-	-	-	-	Triol (GLY)>diol (MEG≈PPG)>ETOH> NPA	-	-	[108]
M/TiO_2 (M=Au, Pd)	-	-	-	-	-	3.3	GLY>MEOH	-	-	[110]
Pd/TiO_2	-	-	-	-	-	-	GLY>DALC> SUC> CyOH>BA	-	-	[41]
Ag/TiO_2 nanotube	0.3-2.0 (1.5)	-	-	-	-	4	-	-	-	[111]
$Ni(OH)_2/TiO_2$ nanotube	0.5-4 (2)	-	-	-	-	2	-	-	-	[114]
Co/TiO_2	0.2-5 (2)	-	0-20 (5)	2-12 (6)	-	10	GLY>MEG> MEOH>ETOH >IPA	7	-	[112]
NiO/TiO_2	0-5 (2)	-	0-25 (25)	2-11 (6.6)	-	-	-	-	-	[113]
NiO_x/TiO_2	-	250-650 (450)	-	-	-	12	-	-	-	[32]
TiO_2, CuO_x/TiO_2	-	-	-	-	-	-	-	-	-	[115]
Cu/TiO_2	-	-	-	-	-	5	-	-	-	[116]
$N/M/TiO_2$ (M=Cr, Co, Ni, Cu)	-	-	-	-	-	-	-	-	-	[117]

TiO_2/CNT	-	-	-	-	0.06-2 (0.1)	-	GLY>MEOH>ETOH	4	-	[118]
TiO_2/CNT	-	300-450 (350)	-	-	-	4	-	-	-	[143]
Fe/g-C_3N_4/ TiO_2	-	-	0-30 (10)	-	0.1-1 (0.2)	10	-	-	-	[125]
La/CNT/TiO_2	3-7 (5)	-	0-20 (10)	-	-	-	GLY>MEG> MEOH>ETOH	3	-	[119]
TiO_2/CNT	0-1 (0.1)	350-500 (450)	-	-	-	-	-	5	-	[121]
Montmorillonite/ TiO_2/CNT	3-7 (5)	-	1-10 (5)	-	-	-	GLY>MEG> MEOH>ETOH> PA	4	-	[120]
TiO_2/CNT	-	300-450 (350)	-	-	-	4	-	-	-	[143]
Cu_2O/TiO_2/GO	0-2 (1)	-	-	-	-	2	-	4	-	[126]
Cu_2O/TiO_2	-	-	-	-	-	8	-	2	-	[144]
Pt/CdS, Pt/TiO_2	-	-	-	-	-	7	-	-	-	[129]
Pt/CdS	-	-	30-70	4-10	-	3-7	-	-	-	[130]
Ni/CdS	-	-	0.15-55(33)	3-13 (6)	-	10	-	-	-	[131]
$Cd_{0.5}Zn_{0.5}S$	-	-	0-11 (7)	2-14 (14)	-	-	-	3	-	[133]
Pt/$Cd_{1-x}Zn_xS$	-	-	-	-	-	5	-	3	-	[134]
Pt/$Cd_{1-x}Zn_xS$ /ZnO /$Zn(OH)_2$	-	-	0.365-7.3 (2.2)	-	-	2	-	-	-	[135]
ZnO/ZnS	-	-	-	-	0.2-4 (1)	-	-	4	5-25 (25)	[136]
ZnO/ZnS	-	-	-	-	-	-	-	-	40-80 (80)	[137]
ZnO/ZnS/graphene	0.01-0.1 (0.05)	-	1-50 (40)	-	-	-	-	3	-	[138]

Pd/PdS-ZnO/ZnS	0-0.48 (0.24)	-	-	-	-	-	-	-	40-80 (80)	[139]

GLY(glycerol), MEOH (methanol), ETOH (ethanol), PA (propanol), IPA (isopropanol), NPA (Propyl alcohol), PPG (1,2-propanediol), MEG (ethylene glycol), TBA (tert-butanol), 1-BOH (1- butanol), BA (benzyl alcohol), CyOH (cyclohexanol), LAC (lactose), GLC (glucose), DALC (d-glucose), SUC (sucrose), CBO (cellobiose), MALE (maltose), CL (cellulose), ST (starch), TETA (Triethanolamine).

1.3. Parametric study of photocatalytic alcohol valorization

In this section, a comprehensive review is conducted on the effect of synthesis and operating parameters in photocatalytic alcohol conversion to hydrogen. In the first step, effects of the cocatalyst percentage and calcination condition are explained as two synthesis parameters. Afterward, the review focuses on the effects of operating parameter such as alcohol concentration, initial pH of solution, photocatalyst loading, duration of reaction, hydrogen source, photocatalyst deactivation, source and intensity of light, and reaction temperature are discussed as the most effective operating parameters. Table 1.3 summarize the range and optimum values of the operating parameters investigated in different research on valorization alcoholic wastes.

1.3.1. Synthesis parameters

1.3.1.1. Cocatalyst percentage

The photocatalytic activity of photocatalyst can be significantly enhanced by incorporation of cocatalyst, especially for alcohol photoreforming condition. By increasing the amount of cocatalyst deposition, hydrogen production rate can increase due to higher availability of reaction sites. On the other hand, an excessive amount of cocatalyst can (i) make a barrier against the incidence of photons to the semiconductor, (ii) impede access of substrate to semiconductor surface, and (iii) increase the rate of electron-hole recombination [145]. Moreover, excessive deposition of cocatalyst not only leads to agglomeration of its clusters that decreases the accessible active sites, but also prevents appropriate dispersion of particles on photocatalyst surface [104, 146]. This phenomenon negatively affects the rate of reaction as reduces the number of active sites (which is the contact line of photocatalyst and cocatalyst [146]).

As it can be seen from Table 1.3, generally between 1-3wt.% of cocatalyst produced optimal amount of hydrogen. Deposition of 2% Pt [74], Co [112] and NiO [113] as cocatalyst on TiO_2 was found to produce highest amount of hydrogen. In addition, 1.5, 1 and 1.5 weight percentages of Cu were obtained as optimum values for TiO_2 nanorod [104], TiO_2 nanotube [100] and TiO_2 nanosheet [99], respectively. The optimum amount of cocatalyst can decrease by highly dispersing it. Finely dispersed copper in both of Cu^+ and Cu^{2+} forms represents a

decreased value of 0.5% as the optimum amount of cocatalyst for TiO_2 [96]. Babu *et al*. [126] reported that the incorporation of 1% Cu on the reduced graphene oxide supported TiO_2 is the optimum amount, while by deposition of 1.5% and 0.5% of Cu, the rate of hydrogen production decreased more than three times (Fig. 1.3). Deposition of 1.5% of Au on P25 was found to be optimum; however, when it was deposited on TiO_2 nanorods, a lower Au percentage (i.e. 0.5%) made the highest hydrogen evolution [108]. Deposition of 0.1% of Pd and Pt produced more hydrogen than 0.5%, however, almost no difference was observed for the case of Au, which may be attributed to the size of nanoparticles [106]. 1.5% of Ag deposited on TiO_2 nanotube produced the highest amount of hydrogen [111]. In the case of loading bimetallic Cu-Ni cocatalyst on TiO_2, the high amount of 10% (Cu:Ni mass ratio of 9:1) was optimum. An addition of 0.24% Pd on the surface of ZnO/ZnS nanorods was found as optimum to produce the maximum amount of hydrogen both under UV and solar radiation [139]. Deposition of 5% Cu/Ni based polymer ($[\{Cu^{II}(4,4'\text{-dipy})_2\}\{Ni(CN)_4\}]_n$ $0.7(C_2H_6O_2)1.6(H_2O)$(CP-1)) on TiO_2 as cocatalyst was optimum for hydrogen generation under both UV and visible light irradiation [106]. Reddy et al. [121] found that deposition 0.1% CNT (in the range of 0-1%) as optimum because of formation of Ti-O-C in the boundary of TiO_2 and CNTs leads an effective charge transfer between. They reported that CNT could not effectively disperse in when its content is less than 0.1 wt% and on the other hand solution is opaque in higher content. As CNT can play different roles other than the cocatalyst role, this optimum value can be the outcome of different phenomena.

1.3.1.2. Calcination condition

A sample is usually calcined to (i) produce or change a crystalline phase during semiconductor preparation, (ii) form metallic particles or reduce them after impregnation of cocatalyst on the semiconductor surface, and (iii) doping the formed cocatalyst on the surface with the semiconductor bulk. The temperature and duration of calcination can control and/or change the crystal phase structure of photocatalysts. By calcination of amorphous TiO_2, crystalline structure phase is obtained. Calcination at low temperature can lead poor crystallinity and as a result, less active sites would be accessible for photocatalytic reactions. On the other hand, calcination at high temperature can cause particle agglomeration (decreasing the number of surface active sites) [72, 142], phase transformation [142], and formation of inactive phases through mixing with other phases or impurities[121].

For titanate nanorods, 250 °C was obtained as the optimum calcination temperature [72]. Kumar *et al*. [104] showed that Cu decorated titanate nanorods calcined at 500 °C produced the highest amount of hydrogen. They attributed less hydrogen production of samples calcined at lower temperatures to their single-crystalline TiO_2 (B) phase which exhibits a high rate of recombination of photogenerated charge carriers. However, the sample which calcined at 500 °C was a bicrystalline of TiO_2 (B)/anatase phases with approximately equal ratios. As the level of conduction band edge of TiO_2 (B) is higher, the excited electrons are transferred to anatase phase and this phenomenon can reduce the rate of electron-hole recombination [104]. As seen in Fig. 1.4, non-calcined Au decorated titanate nanorods and the ones that calcined at 1000 °C exhibited almost no hydrogen production, and the highest amount of hydrogen was produced when the sample calcined at 600 °C as had the smallest average Au particle size [108]. In addition, the optimum calcination temperature for Pt/TiO_2 and titanate nanosheets was found to be respectively 400 °C [84] and 350 °C [99]. For both of TiO_2 and NiO_x/TiO_2, 450 °C was obtained as the optimum calcination temperature for maximizing hydrogen production rate [32]. In addition, it was found that although increasing calcination temperature to 600 °C did not significantly affect hydrogen production by TiO_2, the hydrogen production rate under NiO_x/TiO_2 was decreased around ten times. It reveals that the calcination temperature has different effects on the pure and doped semiconductors, as the analysis of samples illustrated that the calcination temperature affected the formation of n-type (NiO_x) and p-type (TiO_2) junction [32].

The calcination condition may change the path of reaction by formation of different active sites on the semiconductor. It was reported that the oxidation state of copper is +2 when calcined at 350 °C and +1 when calcined at 450 °C [96]. Calcined NiO_x/TiO_2 at 450 °C produced the lowest amount of CO, and just under the sample that calcined at 600 °C, production of CH_4 was observed [32]. Despite this, Petala *et al*. [101] showed that the calcination temperature had no effect on the photocatalytic activity of CuO_x/TiO_2 in glycerol conversion to hydrogen.

Time duration of the calcination also affects the structure of the photocatalyst and its hydrogen production rate. Reddy *et al*. [72] showed that the time duration of calcination might be more effective than the calcination temperature. Titanate nanorods calcined at 250 °C for 2 hr produced around 2.5 and 7 times more hydrogen in comparison to the ones

calcined at the same temperature for 1 and 3 hr, respectively [72]. Time duration of calcination can also affect the bonding between different components of composite photocatalyst. Reddy *et al*. [143] indicated that 2 h is the optimum for calcination of CNT/TiO_2 because of formation of more effective carbon and titanium oxide bonds and therefore enhancement of charge transfer between TiO_2 and CNT.

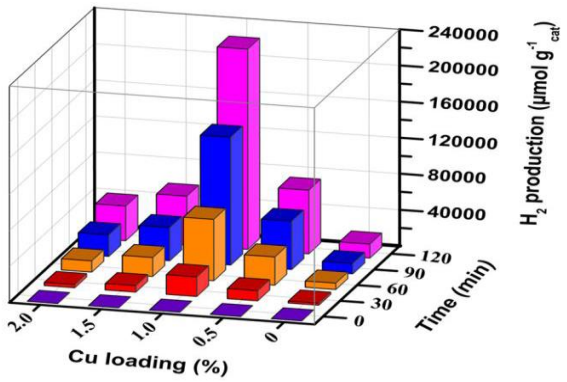

Fig. 1.3. The effect of Cu deposition as a cocatalyst on the rate of hydrogen evolution by reduced graphene oxide supported TiO_2 [126].

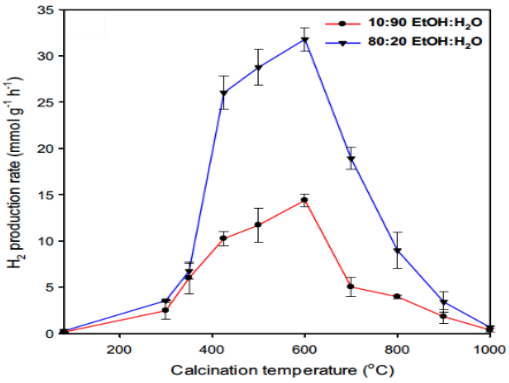

Fig. 1.4. The effect of calcination temperature on hydrogen production by Au decorated titanate nanorods [108].

1.3.2. Operating parameters

1.3.2.1. Hydrogen source

In water splitting, water molecules are the sole source of the produced hydrogen. On the other hand, no photocatalyst have been yet found to generate an acceptable amount of hydrogen from pure water [15]. Utilization of alcohols (dissolved in water) as the secondary source of hydrogen can increase the rate of hydrogen evolution 1 to 2 orders of magnitude [89]. In this situation, water and alcohol may have synergistic effect to produce more hydrogen, as it can be seen in Eq. (1–11) for the case of glycerol. Comparison of the potential of different alcohols to be valorized to hydrogen is an interesting area of research to discover alcohol valorization potentials. Different factors such as substrate polarity, number of α-H, number of OH bond, position of OH in the molecule, number of carbons in the alcohol, and oxidation potential of substrate can affect their photocatalytic transformation [109, 119]. Lower oxidation potential of alcoholic substrate generally leads to a better hole scavenging and therefore higher rate of photocatalytic reaction [109].

Fu *et al*. [33] compared the amount of produced hydrogen from C3-polyols (glycerol, propylene glycol and isopropanol) over Pt/TiO_2 and found the ratios of hydrogen production are approximately proportional to the alcohols' number of OH groups, *i.e*. 3, 2, and 1, respectively. As a result, it can be concluded that hydrogen atoms that are connected to hydroxyl carbon (α-H) can be easily valorized to hydrogen, and this hydroxyl carbon would be converted to CO_2. In the presence of tertiary butanol (as a sacrificial agent with no α-H), the rate of hydrogen production was around one order of magnitude lower than the alcohols containing α-H [107]. Chen *et al*. [107] reported the rate of hydrogen production (over Au/TiO_2) from glycerol is higher than other alcohols with a different number of carbons in the following order: glycerol > ethylene glycol > methanol > ethanol. By plotting the rate of hydrogen production from these alcohols as a function of the number of α-H or OH groups, a linear trend can be obtained (Fig. 1.5). In addition, the polarity of these alcohols is in the order of glycerol > ethylene glycol > methanol > ethanol > 2-propanol [122]. Glycerol also produced the higher amount of hydrogen using Au/titanate nanotube: glycerol > 1,2-ethanediol ≈ 1,2-propanediol > ethanol > 1-propanol [108]. These results illustrates the order of triols > diols > 1° aliphatic alcohols > 2° aliphatic alcohols for the rate of hydrogen production, that not only confirms the results of previous work, but also suggests a relation for the situation that the number of OH groups is equal. Almost the same result was obtained by using Pt and Pd as cocatalyst, where by applying M/TiO_2 photocatalysts (M = Pd, Pt, Au), the hydrogen production rate increased as: glycerol > 1,2-ethanediol > 1,2-propanediol > methanol > ethanol > 2-propanol > tert-butanol [89]. It is worth mentioning that making a binary glycerol solution with ethanol or methanol reduced the rate of hydrogen production [87]. By increasing the number of OH groups of C3-polyols (glycerol, propylene glycol and isopropanol), the quantity of generated CH_4 and C_2H_6 significantly reduced [33], which reveals that this increase tends more to valorize the alcohols in the form of an alkane. Bahruji *et al*. [41] showed in addition to the presence of α-H, the feasibility of dissociation of α-C-C bond is another determinative factor. For example, hydrogen production from cyclohexanol (a ring alcohol) and benzyl alcohol (an aromatic alcohol) was not significant in comparison to glycerol.

One reason for the enhancement of the rate of hydrogen evolution by increasing the number of OH groups can be ascribed to the adsorption of alcohols on the surface of photocatalyst

from their OH groups which serve as anchor for hydrogen bonding [33]. Using a TiO_2/CNT composite that contains much more surface OH groups than pure TiO_2, it was revealed that glycerol produced much more hydrogen in comparison to methanol and ethanol (respectively 10 and 14 times more) [118], confirming the determinative role of the number of alcohol OH groups for an effective alcohol adsorption on the catalyst surface.

Comparison of pure and crude glycerol as hydrogen source revealed that pure glycerol produced 2.5 and 4 times more hydrogen under Pt/TiO_2 and CuO_x/TiO_2 photocatalysts, respectively [91]. It was reported that millimolar concentrations of NaCl, Na_2SO_4 or $NaNO_3$ reduced the rate of hydrogen production nearly 20 %. The presence of NaH_2PO_4 had a more negative effect as reduced the reaction rate by approximately 60 %. These negative effects can be attributed to the competitive adsorption of the anions and glycerol molecule on the active catalyst sites. A part of the lower hydrogen production from crude glycerol would be because of foam generation from the residual soaps, while defoamers could not be effective as they degrade under photocatalyst. The rate of hydrogen production from crude glycerol was found to be 9-fold less than pure glycerol using Ni deposited TiO_2 nanotubes [114]. The lower oxidation potential of pure glycerol than the impurities present in crude glycerol can be another reason for its higher photocatalytic efficiency [114]. Rawool et al. [94] concluded the rate of hydrogen production from crude glycerol was around half of methanol, however, it is a potential candidate to replace methanol which is industrially important.

The presence of impurities in crude glycerol can have an interaction effect on the operating parameters. Ribao *et. al* [85] reported that the optimum value of catalyst loading (rGO/Pt/TiO_2) for crude and synthetic glycerol conversion to hydrogen was 0.5 and 0.25 gL^{-1}, respectively. It means that more catalyst is required to achieve an optimum amount for crude glycerol which can be attributed to inactivation of active catalyst sites by impurities. On the other hand, 1 and 20% solution was found as optimum for crude and synthetic glycerol, respectively. By noting that almost no hydrogen was produced using 20% crude glycerol solution, it can be concluded that the impurities can have a detrimental effect on the photocatalytic activity [85].

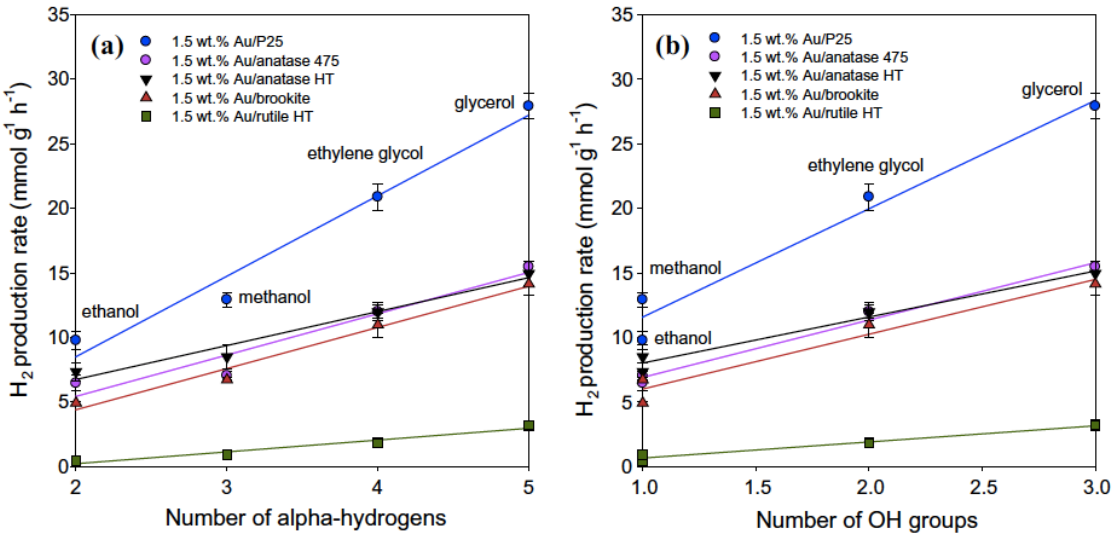

Fig. 1.5. Increase of the hydrogen evolution by Au on different photocatalysts versus augmentation of the number of (A) α-H, and (B) OH groups [108].

1.3.2.2. Time duration of reaction

The photocatalytic hydrogen evolution can perform continuously as long as alcohol or water are remained and reaction conditions are appropriate to convert them, even though the reaction rate can change during the reaction. Most of the works reported an approximately linear trend for amount of hydrogen production during a few hours of experiment [84, 108, 110, 134]. However, by extending the reaction time, a plateau would be observed after several hours [112, 131]. A few works investigated the rate of hydrogen production at low concentrations of alcohol for prolonged exposure to irradiation, to reach a 100% conversion of the alcohol. In this condition, at the beginning of photoreforming reaction, the rate of hydrogen production increased very sharply to a maximum and then decreases gently towards the rate of hydrogen production from pure water, due to depletion of alcohol [81]. For these cases, CO_2 production rate also varied with approximately the same manner of hydrogen production, indicating deep oxidation of alcohol and conversion of intermediates to CO_2 and H_2 [81]. By accumulating the total amount of produced H_2 and CO_2, it was found that they are in good agreement with stoichiometric amounts of Eq. (1–11) [69]. However, at high concentrations of alcohol, the rate of hydrogen evolution did not tend to the rate of hydrogen production from pure water even after several days [86].

It is worth mentioning that the conversion of alcohol may not start exactly after the triggering photocatalytic reaction. For example, for *in situ* photodeposition of cocatalyst on the semiconductor, the earlier photogenerated electrons is used for metallic cocatalyst formation. Petala *et al*. [101] showed that in low concentrations of glycerol and using CuO_x/TiO_2 as photocatalyst, CO_2 was appeared just after start of illumination, however hydrogen was detected after a delay. This observation could be attributed to alteration of oxidation state of copper particles from Cu (II) to Cu(I) or metallic Cu. It can be due to this fact that formation of CuO is more thermodynamically favorable that reduction of hydronium ions. This assumption could also be justified by noting that the delay increased in high Cu load, in such a way that by increasing Cu load from 0.04 to 2.8%, hydrogen detection time also started from 25 to 120 minutes (see Fig. 1.6) [101].

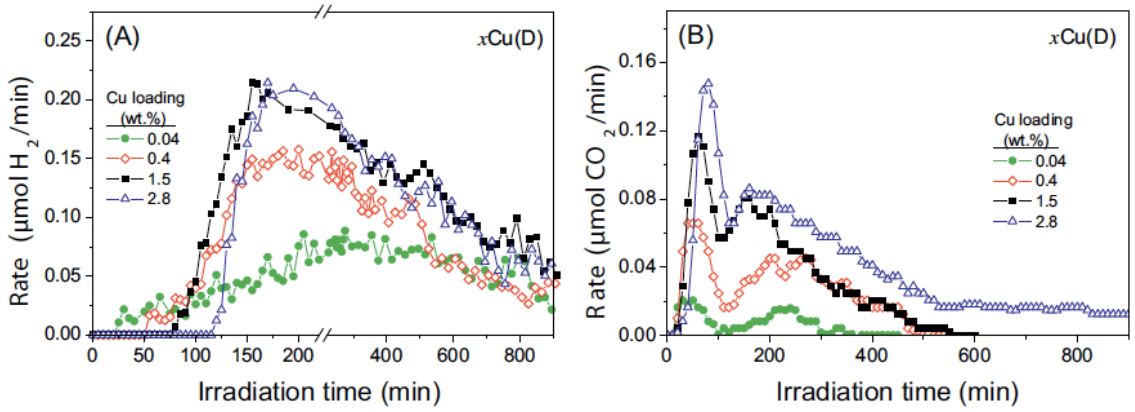

Fig. 1.6. Time variation of the production rate of (A) hydrogen and (B) CO_2 in different Cu loadings [101].

1.3.2.3. Alcohol concentration

As discussed earlier, based on the current photocatalyst technology, the presence of alcohol in water is vital to increase the rate of photocatalytic hydrogen production, and consequently, shift the process towards an economically viable one. On the other hand, discovering the effect of alcohol concentration in the solution is interesting from mechanism development point of view, and also its optimization is of interest to commercialize the process. Bastos *et al*. [130] made a parametric study on some operating parameters of photocatalytic glycerol valorization using Pt/CdS photocatalyst based on a statistical approach and reported that glycerol concentration had the most positive effect on the rate of hydrogen production. By

increasing alcohol concentration (i) it is more accessible by the photocatalyst to be converted to products, and (ii) the probability of recombination (which is usually the controlling step) reduces. Nevertheless, hydrogen production is reduced after an optimum point of alcohol concentration, as a result of blockage of water molecules as well as restriction of hydronium cations adsorption at active sites of the photocatalyst [120, 125, 142, 147].

Under Pt/TiO_2 photocatalyst, an addition of only 0.073% (vol./vol.) glycerol to water enhanced the rate of hydrogen production around 3 times and its further increase up to 7.93% improved the rate of hydrogen evolution [74]. In another work on Pt/TiO_2, glycerol concentration increased more, and it was found that rising glycerol concentration up to 5.48% sharply enhanced the rate of hydrogen evolution, and reached a plateau at higher concentrations (than 5.48%) up to 29.2% [80]. This behavior resembles Langmuir-Hinshelwood kinetic model and suggests Langmuir type alcohol adsorption which causes hydrogen production rate to obey Eq. (1–12):

$$r_{H_2} = \frac{k_1 K_a C_0}{1 + K_a C_0} \qquad (1–12)$$

where r_{H2}, C_0, k_1, and K_a respectively represent H_2 evolution rate, initial alcohol concentration, the reaction rate constant and the equilibrium constant of alcohol adsorption/desorption [113]. Langmuir–Hinshelwood reaction mechanism is expected to be observed only in low or medium alcohol concentrations. For Pt/TiO_2 photocatalyst, the maximum hydrogen production was obtained at 53.6% in study of a wider range of glycerol concentration [148], while at 74.0% of glycerol, hydrogen production decreased meaningfully. Other work by the using Pt-decorated commercial Kronos vlp7000 (KR) photocatalyst also showed an optimum for glycerol concentration at 62.3% [83]. Moreover, an optimum around 45% was suggested by Slamet *et al*. [95] for P25 (Fig. 1.7). Interestingly, these optimums are near 3:1 stoichiometric molar ratio which can be inferred from Eq. (1–11). For the case of using Cu [96] and Co [112] as cocatalyst, 5% of glycerol was suggested as optimum, suggesting another mechanism using these cocatalysts. It can be justified by this fact that the rate of reaction is high using platinum an active cocatalyst and therefore a high alcohol concentration on the surface is required. However, using Cu and Co as less active cocatalysts, the rate is controlled by another parameter.

As the amount of adsorbed alcohol on the surface differs for other types of photocatalyst, the optimum value of alcohol concentration may also be different. A volume percent of 55 was suggested as optimum glycerol amount for CdS based photocatalyst [130]. Despite this, an optimum around 33% glycerol was reported for CdS quantum dots, which can be attributed to their high amount of surface to volume ratio and size-dependent spectroscopic properties [131]. For $Cd_{0.5}Zn_{0.5}S$ [133] solid solution and $Pt/Cd_{0.2}Zn_{0.8}S/ZnO/Zn(OH)_2$ multiphase photocatalyst [135], respectively 7 and 2.2% glycerol were reported as optimum.

In addition to hydrogen production rate, alcohol concentration can affect other parameters like the stability of photocatalyst, as is reported in the case of Pt/hex-CdS [130]. Minero et al. [149] showed glycerol concentration changed initial rate of glycerol conversion, and they found that the rate enhanced by increasing glycerol concentration.

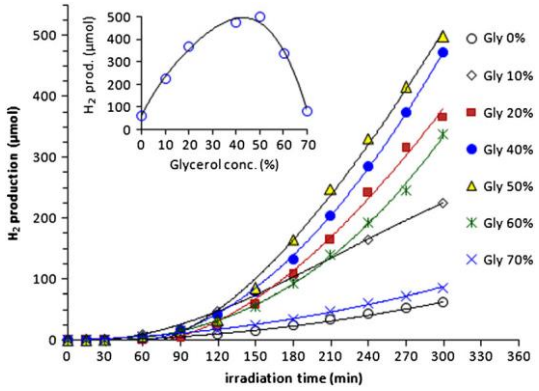

Fig. 1.7. The effect of glycerol concentration on hydrogen production [95].

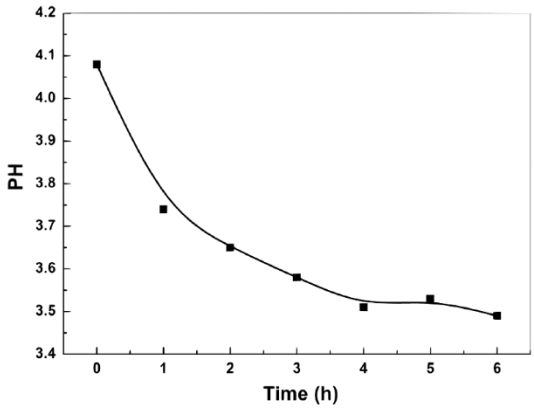

Fig. 1.8. Variation of solution pH during reaction [84].

1.3.2.4. Initial pH of solution

The acidity or basicity of solution is one of the most effective operating parameters on alcohol valorization [130, 150]. This determinative role is attributed to the influence of pH on various factors such as catalyst particle agglomeration, surface functional groups of photocatalyst, the stability of intermediates and final products, band gap of the photocatalyst, and surface charge of photocatalyst which in turn affects the adsorption/desorption of the chemicals on the photocatalyst surface [15, 151]. It should be noted that pH of the solution is not constant during the reaction due to continuous generation and consumption of hydronium ions and hydroxide anions. Jiang *et al*. [84] reported reduction of the pH of glycerol solution and its

approach to a stable value around 3.5 during the reaction under Pt/TiO_2 photocatalyst (Fig. 1.8); and attributed that to the generation of intermediate carboxylic acids.

For the cases of using platinum [74, 80], cobalt [112] and nickel [113] as cocatalyst for TiO_2, initial pH around neutral (i.e. pH≈7) was found to be optimal. It can be ascribed to this fact that at neutral pH that is near the point of zero charge (PZC) of photocatalyst (6.3 for anatase TiO_2 [80, 152]), glycerol can be adsorbed more easily on the photocatalyst surface. Li *et al*. [80] investigated this phenomenon, and reported that the maximum glycerol adsorption was at PZC of the photocatalyst, when surface charge of the photocatalyst was neutral.

For nickel-hybrid CdS quantum dots also neutral pH was suggested to be optimum [131] that is near PZC of the CdS (7.5 [153]). On the contrary, for $Cd_{0.5}Zn_{0.5}S$ photocatalyst, hydrogen production under acidic or neutral solutions was found to be negligible while it was improved by increasing alkalinity [133]. Only at high concentrations of NaOH (C_{NaOH}=4 $mol.L^{-1}$), the production rate was decreased and hydrogen evolution was maximum in initial pH of 14. This observation can be ascribed to relatively high isoelectric point of this photocatalyst which is in the pH range of 8.1-11.

For using heteropoly blue sensitized Pt/TiO_2, it is reported that hydrogen was produced in pH less than 3 and no hydrogen was detected in initial pH of 3-4.5 [78]. This observation can be explained by the effect of increasing pH on the degradation of $H_3PW_{12}O_{40}$ to other heteropoly anions that have less photocatalytic activity [154], and finally, as $H_3PW_{12}O_{40}$ can be completely decomposed at pH higher than 2.5[155].

1.3.2.5. Photocatalyst loading

Accessibility of the photocatalyst for the absorption of light photons and adsorption of substrates play a major role in all of photocatalytic reactions. Although many works showed the effectiveness of photocatalyst by reporting a negligible activity in its absence (as control experiments), limited works dealt with optimization of photocatalyst loading. For Pt/P25, it is reported that by increasing the photocatalyst loading to 2.66 g/L, the hydrogen production rate increased [74]. However, 0.1 g/L of photocatalyst was found to produce maximum hydrogen from glycerol using TiO_2 nanotube, which can be attributed to its high specific surface area (200 m^2/g) in comparison to P25 (48 m^2/g) [100]. Similarly, for the case of CNT/TiO_2 that generally can have a surface area of more than 100 m^2/g, a low photocatalyst

loading of 0.1 g/L was reported as optimal that can be due to its capability to strongly adsorb glycerol. On the other hand, for ZnO/ZnS heterostructured nanorod, an optimum photocatalyst loading of 1 g/L was observed [136]. Then observation of an optimum for alcohol load can be justified by taking into consideration that by increasing the photocatalyst loading, absorption of light as well as the number of active sites can increase [152, 156]. On the other hand, in very high photocatalyst loadings, photocatalyst agglomeration tendency increases, as a result (i) a part of photocatalyst surface would be unavailable for absorption of photons [157, 158], and (ii) the light can scatter because of solution opaqueness [125].

1.3.2.6. Photocatalyst deactivation

To evaluate the recyclability and durability of photocatalysts, their photocatalytic activities can be compared in several cycles by repeating the experiment after purging the reactor. As the alcohol concentration does not usually change significantly in a cycle, the photocatalytic activity variations can be considered as a result of the photocatalyst deactivation. The deactivation of photocatalyst is mainly because of accumulation of partially oxidized intermediates on active sites. A kinetic study on the deactivation process showed that the adsorption of poisonous intermediates is almost irreversible if take place in the initial stage of reaction [159]. By purging the reactor, the gasses species produced during the reaction and adsorbed on the catalyst active surface sites can be removed to regenerate the photocatalyst.

The deactivation of photocatalyst may be different under UV or visible range radiation. Co/TiO_2 showed a better stability under radiation in the solar spectrum in comparison to UV illumination [112]; however, for Cu/TiO_2, photocatalyst stability was found to be better under UV irradiation, as 3% and 16% of Cu was leached under UV and solar radiations, respectively [97]. Bi_2WO_6 was stable under visible light illumination, and the glycerol conversion as well as product selectivity were approximately the same after six runs [160].

Cu_2O/TiO_2 nanorod was found to be stable under solar irradiation [104], however Cu_2O/TiO_2/reduced graphene oxide did not illustrate a good stability under Xe lamp irradiation after 4 cycles [126]. $rGO/CuFe_2O_4/TiO_2$ illustrated a great stability without leaching and deactivation [123], which may be attributed to the high stability of $CuFe_2O_4$ [161, 162]. Cu_2O/TiO_2 showed a good stability as Cu_2O did not oxidize during reaction and no Cu^{2+} was detected on the surface of TiO_2 [144]. ZnO/ZnS/graphene was not entirely stable

under Hg lamp after 3 cycles [138]. Activity of titanate nanorods [72] and TiO_2/CNT [118] was slightly decreasing under solar illumination. The rate of hydrogen generation using La/CNT/TiO_2 in the 2nd and 3rd cycles decreased because of deactivation of catalyst active site by intermediate products [119]. CNTs/TiO_2 also did not show a good activity after three cycles because of the generation of intermediates which affected the light penetration and the interaction of alcohol and photocatalyst [121]. However, montmorillonite/TiO_2/CNT could enhance the stability of hydrogen production [120]. $Cd_{0.5}Zn_{0.5}S$ was more deactivated under UV irradiation [133]. In addition, $Cd_{1-x}Zn_xS$ were deactivated meaningfully after their exposure to air, which could be attributed to metal sulfide oxidation by atmospheric oxygen [134]. ZnO/ZnS heterostructured nanorod arrays showed almost a stable photocatalytic activity under visible light illumination after four cycles [136].

It was shown that the rate of hydrogen production from alcohol solution decreased in consecutive cycles; however, addition of a little amount of fresh alcohol solution increased the rate to its initial amount [104]. This observation suggests that at least a part of hydrogen evolution rate decrease can be because of less reactivity of the intermediates or their lower tendency to be adsorbed on the active sites. In spite of this, for Ag_2O/TiO_2 nanotubes, the amount of deactivation was found to be the same in pure water and glycerol solution and no silver was detected in the effluent [111], suggesting another reason (like changing the photocatalyst characterization or deactivation by water molecule [163]) for the decrease of H_2 evolution for this material.

Pt/TiO_2 (Kronos vlp7000) photocatalyst exhibited less deactivation under fluorescent for glycerol valorization, in comparison to Pt/P25 [83]. It can be attributed to higher surface area of the former (around five times) which causes less sensitivity to blockage of the active sites. TiO_2 nanosheets doped with quantum Cu (II) nanodots showed higher activity in the second run in comparison to the first one [99]. Less hydrogen evolution in the first cycle could be attributed to the reduction of Cu (II), the assumption is confirmed by the observation of higher CO_2 evolution rate in the first run.

1.3.2.7. Source and intensity of the light

Solar radiation is a sustainable, clean and renewable source of energy and light, and consequently it is considered as a promising source for photocatalysis in the future [164].

Around 3-5% of the total solar energy is in UV spectra (<400 nm) and the rest is in the range of visible and infrared [15]. As the number of photons is important in photocatalytic reactions, by considering a photon basis, even less percentage of solar radiation is in UV range [71]. As absorption range of TiO_2 photocatalyst is mainly in the UV spectrum, numerous research focused on extending its absorption range to visible spectrum. In some research, solar radiation was provided using a solar simulator, usually using Xe arc lamp coupled with some filters [101, 130]. However, some others used natural solar radiation as the light source to valorize alcohol [104, 112]. Despite this, most works focused on other aspects of research and usually utilized UV lamps (Table 1.1).

A work on the photocatalytic valorization of alcohol under P25 and H_2O_2 showed that the most effective parameter on conversion of alcohol and the selectivity of products is irradiation time [140]. Regarding the power of the light source, most of the research utilized 100-500 W lamps (Table 1.1), which is comparable with 1000 w/m^2 that reported by American Society for Testing and Materials (ASTM) for the average solar radiation at ground level in the noon [71]. The rate of glycerol to hydrogen valorization by Pd/P25 under the visible light was found to be enhanced around 25%, by 30% increasing the light intensity [165].

There is some work in the literature on the comparison of photocatalytic activity under UV and visible radiations. However, it is very challenging to develop a consensus on the effect of light type as usually in these studies the intensity of light is different. It is worth mentioning that the solar spectrum generated by solar simulator may not supply the exact range of solar radiation [142]. Hydrogen production under UV light was found to be around 3.4 times more than solar light using TiO_2 nanorods [73]. Cu/TiO_2 illustrated around 1.5 times more photocatalytic activity under UV radiation in comparison to solar radiation [97], however, for Co/TiO_2 this difference was reported to be around 2 times more [112]. Wang *et al*. [137] showed ZnO/ZnS–PdS core/shell nanorods produced around nine times more hydrogen under UV radiation in comparison to solar radiation. Ternary rGO/ Pt/TiO_2 photocatalyst can produced about 95% more hydrogen under UV light than visible [85].

1.3.2.8. Reaction temperature

The rate of photocatalytic reactions is dependent upon the temperature like other chemical reactions. As the band gap of photocatalysts is too large to undergo thermal excitation around ambient temperature, usually the influence of temperature cannot be attributed to light-driven reaction steps. However, the solution temperature influences on the net rate of hydrogen production by affecting the individual reaction steps (i.e. conversions of chemicals), the adsorption/desorption of substrates/products and their diffusivity in the solution [166-168]. Rising temperature (especially till 80 °C) usually increases the hydrogen production.

Under Pt/TiO_2 photocatalyst, the rate of hydrogen production from glycerol enhanced around twice by increasing the reaction temperature from 40 °C to 60 °C; however, an increase from 60 °C to 80 °C did not affect the rate significantly [74]. By increasing reaction temperature from 5 to 25 °C, ZnO/ZnS and ZnS photocatalysts illustrated around two-fold increase in the hydrogen production, while ZnO showed an increase of about three times [136]. By increasing the reaction temperature of ZnO/ZnS in a higher range (40 °C to 80 °C), it was revealed that the positive effect of increasing temperature was around 1.5 times more for 0.2 molar ratio of ZnO/ZnS in comparison to other ratios in the range of 0.3-0.8 [137]. Moreover, it was found that the effect of increasing temperature from 40 °C to 80 °C enhanced the rate of hydrogen evolution using ZnO/ZnS–PdS photocatalyst around two times more than ZnO nanorods [139].

1.4. Photocatalyst development for alcoholic waste valorization

Most of the photocatalysts developed for alcoholic waste valorization are solid semiconductors decorated by a cocatalyst. In addition, the research has also been devoted to composites composed of more than one semiconductor (Z-scheme systems). In this section, different photocatalysts developed for alcoholic waste valorization are reviewed. As TiO_2 is the most commonly used photocatalyst [156], a dedicated sub-section focuses on TiO_2 based photocatalysts and describes their properties as well as different methods for their enhancement. The incorporation of cocatalyst, as the most common methods to improve the activity of photocatalysts, is also reviewed in detail.

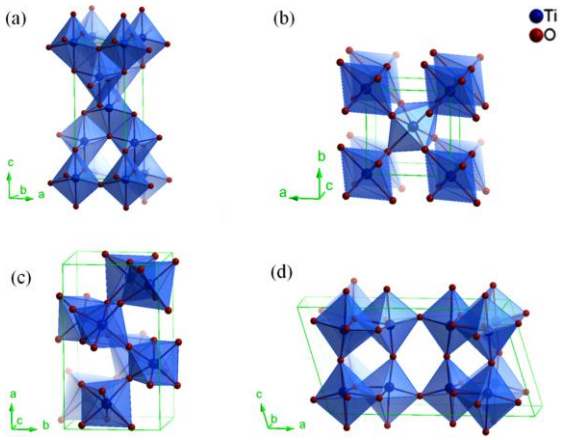

Fig. 1.9. Three-dimensional representation of different TiO_2 phase structures: (a) anatase, (b) rutile, (c) brookite and (d) TiO_2(B) [169].

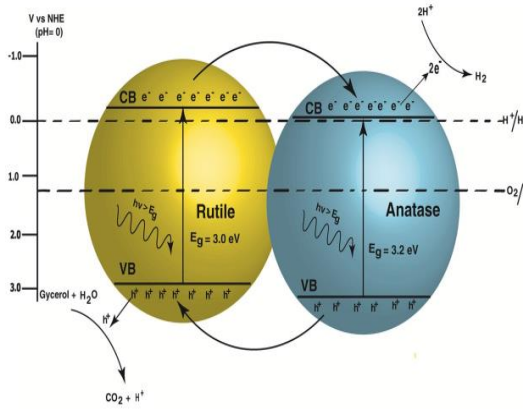

Fig. 1.10. The pictorial representation of charge transfer between anatase and rutile phases in mixed phase TiO_2 [73].

1.4.1. TiO_2 based photocatalysts

TiO_2 is the most commonly used semiconductor for alcoholic waste valorization which benefits from various advantages like significant photoactivity, non-toxicity, low cost, accessibility, and thermal stability [164, 170, 171]. As it can be revealed from Table 1.3, most of the works utilized TiO_2 as the semiconductor. TiO_2 can be found in nature in different polymorphs such as anatase, rutile, brookite, and TiO_2(B). All these structures consist of TiO_6 octahedra but differ in the shared edges and corners. In anatase polymorph the octahedra have four shared edge, in rutile two shared edge exist, in brookite both edge and corners are connected, and TiO_2(B) structure is made of titanium layers [172]. Three-dimensional representation of each of these structures that exhibit different electronic band structures and mass densities are presented in Fig. 1.9. Heating the metastable anatase phase up to high temperatures causes its transformation to more thermodynamically stable rutile phase. Anatase phase is usually preferred due to higher stability and photocatalytic activity [173, 174], however, each of the polymorphs can be attractive because of their unique characteristics. Regarding the hydrogen production rate from alcohol, when normalized in respect to the surface area was enhanced by increasing the brookite percentage; however, when the normalization was based on the weight of the catalyst, the increase of anatase phase showed a better improvement [82].

Mixed phase TiO_2 anatase–rutile demonstrates unique features such as fast dispersion of photogenerated species to the surface, which can improve its photocatalytic efficiency. Fig. 1.10 shows electron and hole transfer between the anatase and rutile phases of TiO_2. As it can be seen, the photoexcited electrons transfer from the conduction band of rutile to anatase, and on the other hand the photoexcited holes move from the valence band of anatase to rutile, because of the different anatase and rutile phase band-edge energies. Consequently, hydrogen can be generated on the anatase phase and alcohol can be transformed on the rutile phase [73]. Hafeez et al. [124] prepared a mixed anatase-brookite TiO_2 and showed its photocatalytic activity can be around one order of magnitude higher than pure anatase TiO_2.

Composed of around 75–80% anatase and 25–20% rutile, P25 is known as the most common commercial photocatalyst [175] and it is the case for its application for alcohol valorization, as Table 1.3 confirms. It is therefore usually considered as a standard to study the mechanism of alcoholic waste valorization photocatalytic reactions and evaluate the prepared quality of prepared photocatalysts [76, 77, 106, 176]. It was found to have the highest photocatalytic activity under simulated solar light irradiation among a series of 20 commercial TiO_2 based photocatalysts [177]. Phase junctions in P25, because of the simultaneous presence of anatase and rutile, is a key factor for its high photoactivity. Comparison of the photocatalytic glycerol valorization using P25 and Merck TiO_2 commercial photocatalysts revealed that at glycerol concentrations less than 0.3 mM, the initial rate of glycerol conversion using P25 is more probably because of its higher surface area; however, at glycerol concentrations higher than 0.3 mM, the rate was approximately the same as the concentration of adsorbed glycerol did not control the rate of reaction [149]. Augugliaro *et al*. [178] compared the photocatalytic activity of P25 and Sigma–Aldrich TiO_2 (pure rutile) commercial photocatalysts with two home-made photocatalysts (pure rutile and pure anatase) and concluded that both of the commercial photocatalysts demonstrated a higher photocatalytic activities, probably because of higher crystallite sizes.

As it can be seen from Table 1.3, most of the works used a commercial photocatalyst to study process of alcoholic waste valorization. The commercial photocatalysts can be treated to tailor their characteristics, modify their shapes, and increase the activity and durability [95]. However, usually the favored photocatalyst characteristics were achieved through their synthesis from photocatalyst precursors, mainly using sol-gel [33, 97, 115] and hydrothermal

[92, 108] methods (Table 1.3). Sol-gel is a well-known method for preparation of porous materials by their solidification in the solution. In this method, after formation of a stable colloidal solution (sol), an anisotropic condensation of the formed colloidal particles occurs to generate a polymeric chain which results in the formation of a "gel". After drying the obtained gel, a aerogel or xero-gel forms. Hydrothermal synthesis of photocatalyst is mainly conducted at high temperature in an autoclave. Enhancement of crystallization as well as control on the crystal composition is an advantage of hydrothermal synthesis [179]. Beltram *et al.* [82] developed an urea assisted hydrothermal method to tailor the phase composition of TiO_2, by alteration of urea/Ti molar ratio. They showed that while in the absence of urea, 100% rutile phase was formed, the addition of small amounts of urea leads to the formation of anatase phase. The increase of urea/Ti ratio to values higher than 3.5 caused the formation of brookite phase (Fig. 1.11). In brief, in urea/Ti ratios of 0, 3.25, and 19.5, respectively, pure rutile, anatase, and brookite phases were formed. Moreover, it was found that crystalline size of rutile, anatase and brookite were around 70, 35, and 15 nm, respectively (Fig. 1.11). This method seems an interesting approach to tailor the phase composition of TiO_2 and study the effect of phase composition on different aspects of photocatalysis. Chen *et al.* [107] compared the behavior of synthetic (sol-gel and hydrothermal) and commercial (P25 and Sigma–Aldrich brookite) TiO_2 photocatalysts and reported the rate of surface area normalized hydrogen production from glycerol in the following order: Au/P25>Au/sol-gel anatase≈Au/Sigma–Aldrich brookite>Au/hydrothermal anatase≈Au/hydrothermal rutile. It shows that P25 has generally a better activity than home-made photocatalysts.

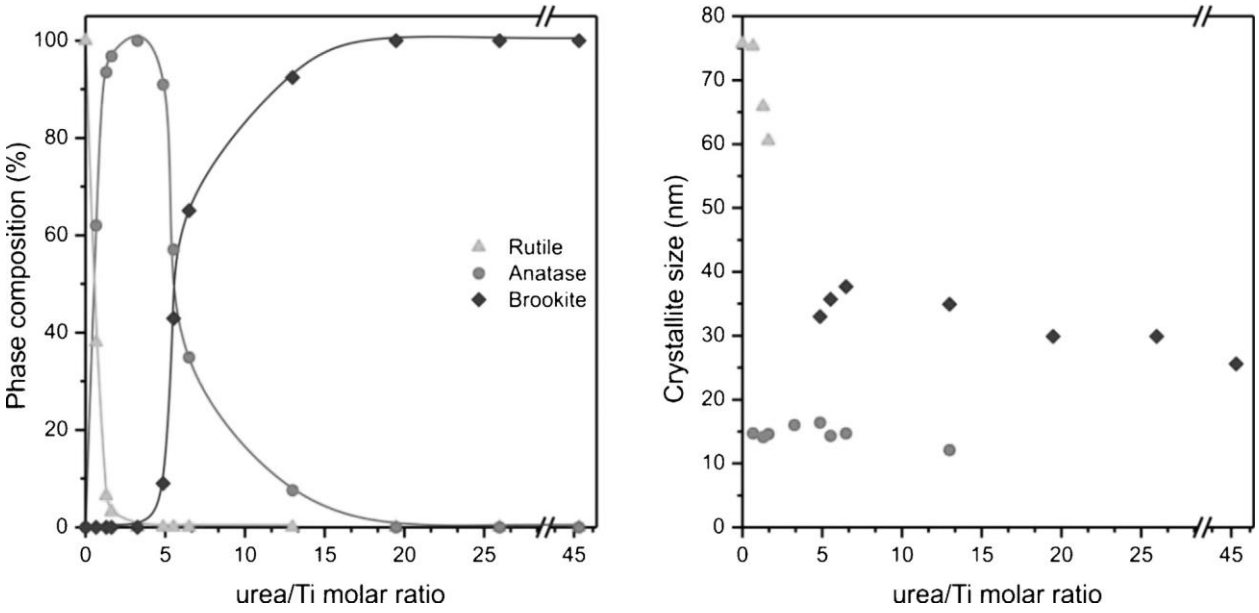

Fig. 1.11. Control of rutile, anatase, and brookite phase compositions (left) as well as crystallite sizes (right) in a urea-assisted hydrothermal TiO_2 synthesis method [82].

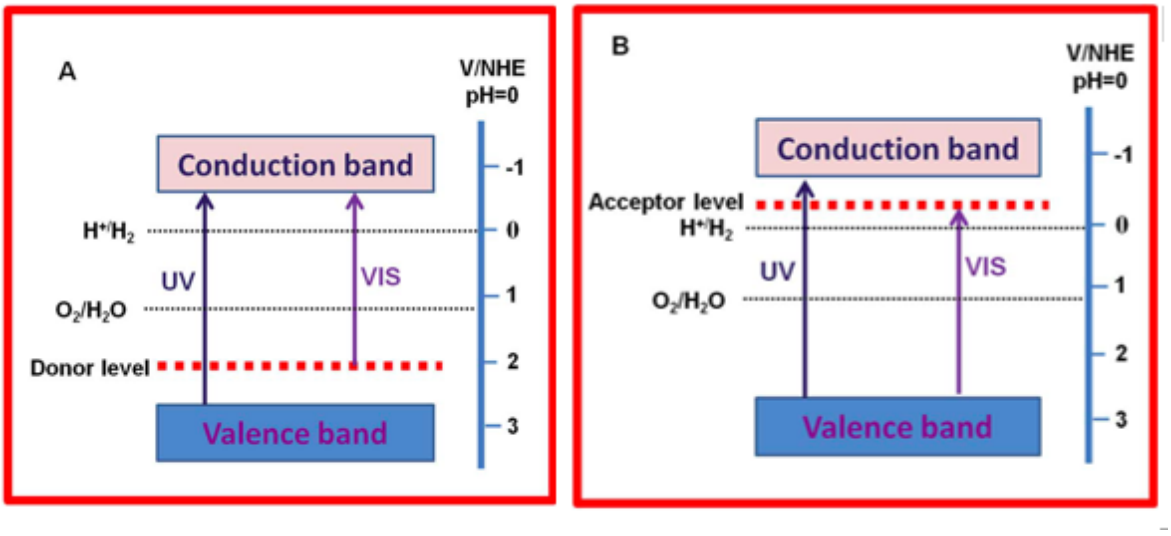

Fig. 1.12. Narrowing the bandgap to increase the visible light absorption of photocatalyst by ion doping on semiconductor to create a donor level (A) and an acceptor level (B) [180].

Synthesis of the photocatalyst also offers the tools to tailor its band gap through doping the semiconductor with metallic (such as V, Cr, Mn, Fe, and Ni) and non-metallic (like N, C, and S) ions, to shift the adsorption of light towards visible range and increase the photocatalytic activity under solar light [158, 181]. This method is characterized by addition of the ions into solution during the synthesis to form a uniform mixture of ions in semiconductor in the first step followed by calcination of the obtained amorphous catalyst to transfer the ions into the semiconductor crystal. Doping both of transition metal cations or

non-metals leads appearance of a donner level above valance band, however, formation of an acceptor level below the conduction band is usually observed by metal cation doping (Fig. 1.12). Different methods such as solid state reaction, hydrothermal and sol–gel auto-combustion could be utilized to insert an element to host metal oxide.

Investigation of the effect of Fe as a metallic dopant on g-C_3N_4/TiO_2 revealed that the co-existence of g-C_3N_4 can reduce the optimum amount of Fe to obtain the highest rate of hydrogen generation (2% and 1% at the absence and presence of g-C_3N_4, respectively) [125]. Fujita *et al*. [113] showed that by increasing the content of doped NiO, the band gap energy of photocatalyst decreases, leading to the increase in the rate of H_2 evolution under UV radiation (Fig. 1.13) [113]. Typically, non-metal ion doping is more suitable as metal ion doping increases recombination of photogenerated electrons and holes by providing recombination centers [180]. N-doped Pt/TiO_2 nanotube illustrated 20% improvement in the rate of hydrogen evolution compared to undoped Pt/TiO_2 [95]. Utilization of $CuFe_2O_4$ and reduce graphene oxide (rGO) with TiO_2 could approximately halve the band gap from 3.20 eV to 1.51 eV [123].

Codoping of semiconductor with two metals, two nonmetals, or a metal and a nonmetal can be an promising approach for taking advantage of synergistic effects of the doping agents. Investigation of simultaneous non-metal and metal doping as N-M-TiO_2 photocatalyst (M=none, Cr, Co, Ni and Cu) under near-UV or visible light revealed that N-Cu-TiO_2 and N-Ni-TiO_2 illustrated the highest enhancement and produced, respectively, 44 and 5 times more hydrogen than undoped P25 [117]. The photoluminescence measurements revealed a lower radiative charge recombination rate codoped samples in the near-UV or visible range. Luo *et al.* [92] investigated codoping of metalloid and nonmetal and showed that (N, B)-TiO_2 co-doped photocatalyst could improve hydrogen production rate under visible light from glycerol even more than single-doped N-TiO_2 photocatalyst. (N, B)-TiO_2 was characterized to have a lower band gap, due to a synergistic effect of B and N which causes the formation of defects.

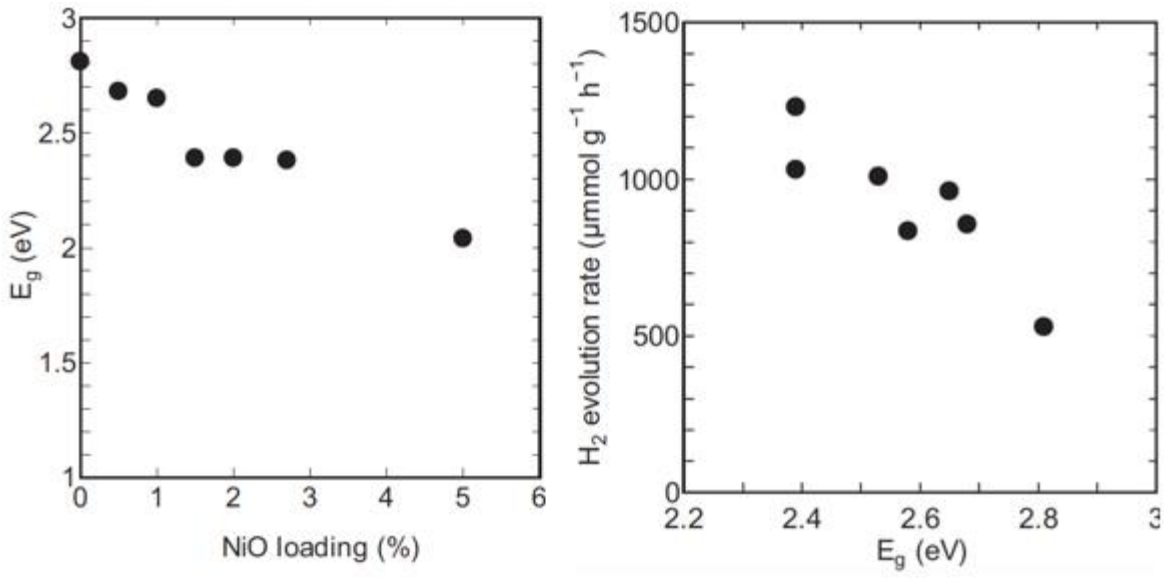

Fig. 1.13. The effect of NiO loading as cocatalyst on band gap energy (Eg) of NiO/TiO_2 photocatalyst as well as the influence of Eg on the rate of glycerol to H_2 conversion [113].

Segovia-Guzman et al. [102] used new method of synthesis of Cu_2O/TiO_2 using glucose and onion skin waste as reducing and stabilizing agents, and indicated that green synthesized catalyst with onion skin waste had higher performance. Moreover, the comparison of Cu/TiO_2 and Cu_2O/TiO_2 showed that the latter was more active.

Some investigations have been also made for the preparation of TiO_2 in different shapes such as nanorod [72], nanotube [79, 111], hollow sphere [88], and nanosheets [99]. Titania nanotubes can be prepared by hydrothermal treatment of commercial P25 according to Fig. 1.14 [95, 114]. As can be seen, TiO_2 is first converted to $Na_2Ti_3O_7$ nanosheets and after its transformation to $H_2Ti_3O_7$ nanotube, TiO_2 nanotube was obtained by calcination. By calcination of hydrogen titanate ($H_2Ti_3O_7$) nanotubes at 1000 °C, or incorporation of 1-(2-methoxyethyl)-3-methylimidazolium methanesulfonate in ionothermal synthesis, titania nanorods can be synthesized [73, 108]. Hydrogen trititanate ($H_2Ti_3O_7$) nanorods were prepared by hydrothermal method and its transformation to single-crystalline and bicrystalline TiO_2 (B) was observed by calcination at 400-450 and 500-550 °C, respectively [104]. Seadira *et al.* [88] investigated the effect of reflux temperature and Ti/ethanol ratio for preparation of TiO_2 hollow sphere (THS) using hydrothermal method. High Ti/ethanol ratio caused the agglomeration of particles, and on the other hand non-uniform spherical shapes were generated at low ratios, suggesting Ti/ethanol ratio plays an important role. Moreover,

the particle size raised by increasing the reflux temperature. The prepared THS had some specific characteristics (such as large surface area and enhanced recombination of photogenerated species) that can deeply affect the rate of hydrogen production.

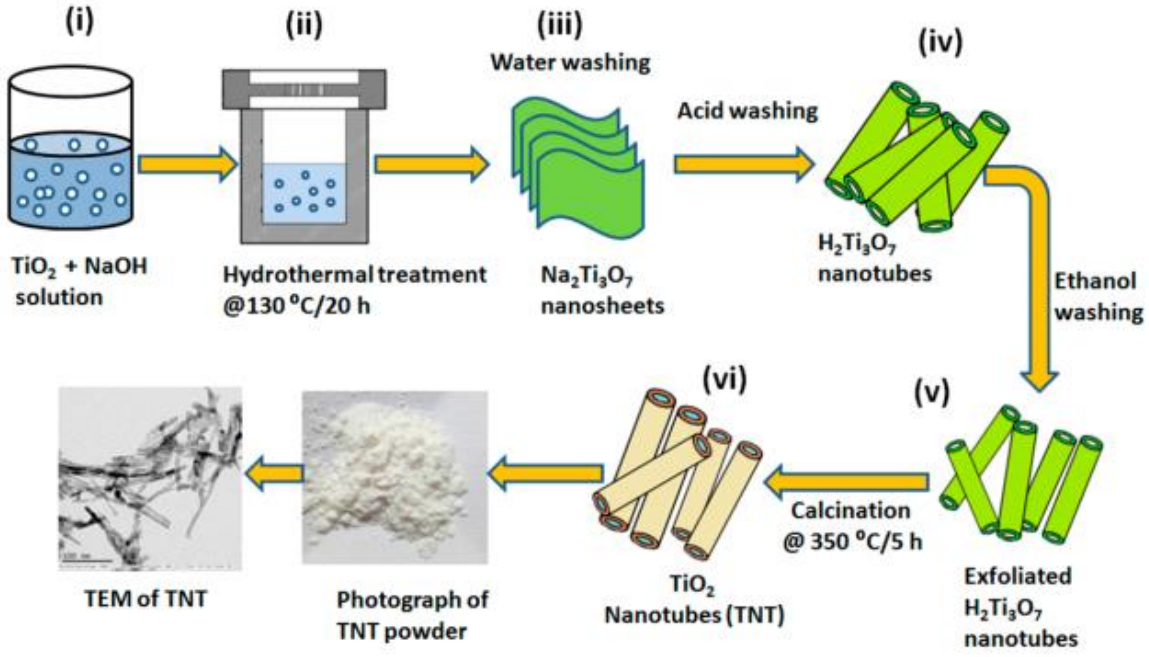

Fig. 1.14. Preparation of TiO_2 nanotube by hydrothermal method [114].

Incorporation of carbonaceous materials like nanotubes, graphene, activated carbon, fullerenes, and nanodiamonds to make a carbon-semiconductor composite is a promising technique to not only increase the photocatalytic activity, but even change the path of reaction towards the production of higher value products. Carbon materials usually benefit from attractive characteristics such as high specific surface area, inertness, high stability and tunable surface chemistry [175]. Photocatalytic activity enhancement by carbonaceous materials can be attributed to adsorption of molecules, enhancement of charge separation and decrease of bandgap energy of the composite [121, 132, 143]. It was shown that graphene oxide plays the role of cocatalyst as has a synergistic effect with platinum and its presence reduced the amount of required pt [85]. Moreover, CNT is shown to be able to play as either a cocatalyst or sensitizer or both [121]. It is shown that CNT can suppress the recombination of electron/hole as has a unique 1D-nanostructure that the photo excited charges can easily be transferred through the tubes [143]. For TiO_2/CNTs composite which was prepared using a mixture of multi-wall carbon nanotubes, single-wall carbon nanohorns and multi-walled carbon nanohorns, it was revealed that the composite could produce 3 times more hydrogen

than pristine TiO_2. This photocatalytic activity enhancement may be attributed to TiO_2 oxygen defects (formed during calcination) that caused better transfer of photogenerated species between surface interface. A composite containing 10 wt% CNT showed the highest activity to convert glycerol to hydrogen, as higher percentage could increase the suspension opaqueness [118]. Babu *et al*. [126] introduced a novel ultrasonic assisted method for preparation of reduced graphene oxide with simultaneous reduction of Cu^{2+} to Cu^{+} and graphene oxide to reduced graphene oxide (rGO) without employing an additional reducing agent. It was revealed that rGO increased the carrier mobility and enhanced the hydrogen production from glycerol under visible light by a factor 7. This enhancement can be attributed to decrease of photogenerated charge recombination, as proved by photoluminescence spectra. At least 3% rGO loading was required for an considerable photocatalytic activity enhancement, however, higher loading decreased the rate of hydrogen production probably because of its detrimental effect on light absorption (Fig. 1.15).

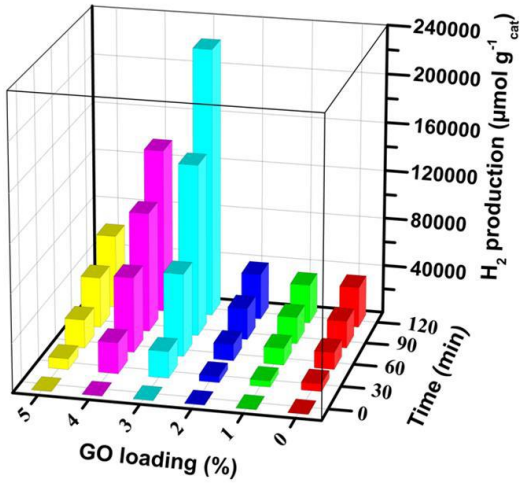

Fig. 1.15. Enhancement of H_2 production from glycerol using different amounts of graphene oxide in carbonaceous Cu_2O-TiO_2 composite [126].

Tahir [119] used CNT as a template to prepare La-doped TiO_2 nanorods. To do so, La/ TiO_2 nanoparticle was first prepared on CNT by sol-gel assisted hydrothermal method and then converted to La/TiO_2 nanorodes by addition of NaOH and calcination, as can be seen in Fig. 1.16. The obtained CNTs/La/TiO_2 nanorodes enhanced the rate of hydrogen production around 14% in comparison to CNTs/La/TiO_2 nanoparticles, that can be attributed to its capability in quickly transmitting the photogenerated charges along the axis. It is also proposed that CNTs not only can play the role of sensitizer by adsorbing the light, but also

can play the role of cocatalyst with capturing the generated electrons by TiO_2 (Fig. 1.17). In the presence of CNT, hydrogen can be produced on the surface of TiO_2 and CNT. By addition of La into the composite, it can capture the photogenerated electrons either by CNT or TiO_2, therefore, both of hydrogen production and glycerol conversion reactions can be performed on the surface of La.

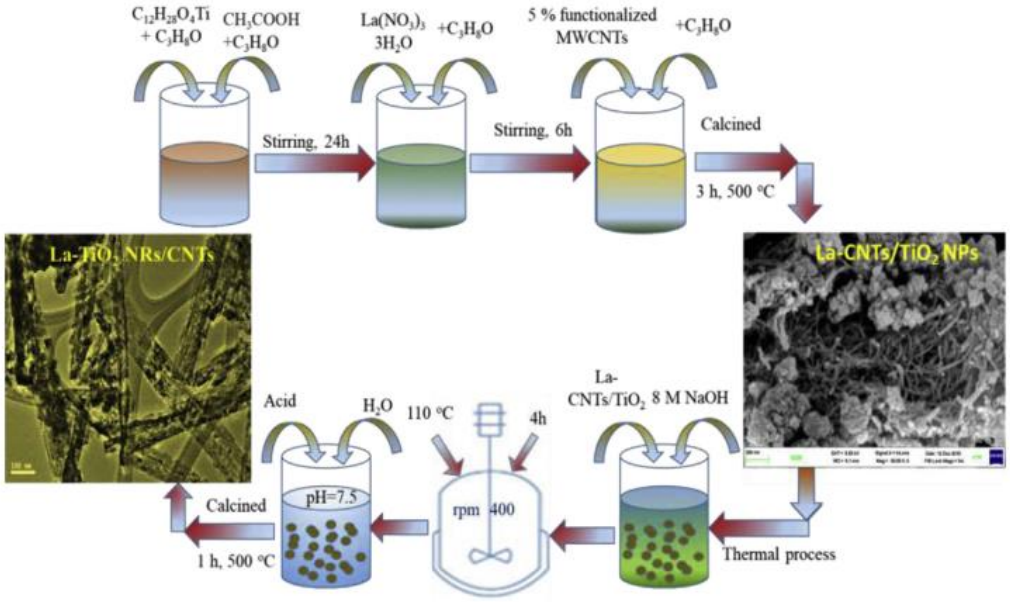

Fig. 1.16. Preparation of La-modified TiO_2 composite using CNT as template [119].

Simultaneous incorporation of CTNs and montmorillonite with TiO_2 illustrated a synergic effects for higher efficiency of hydrogen generation because of promotion of visible light absorption and separation of charge carrier. As depicts, Fig. 1.18 it is suggested that the electrons can move from the valence band of montmorillonite to that of CNT. On the other hand, the photoexcited electrons which are located in the conduction band of TiO_2 transfer to the montmorillonite conduction band because of its less potential energy than TiO_2. Eventually, the electron is caught by CNT as electron acceptor to generate hydrogen[120].

TiO_2 could be sensitized using a series of heteropoly blues, to absorb the light in the range of visible. Heteropoly blue sensitized Pt/TiO_2 photocatalyst was used to valorize glycerol to hydrogen under visible light, and it was found that 0.62 $mmol.L^{-1}$ of heteropoly acid is optimal [78].

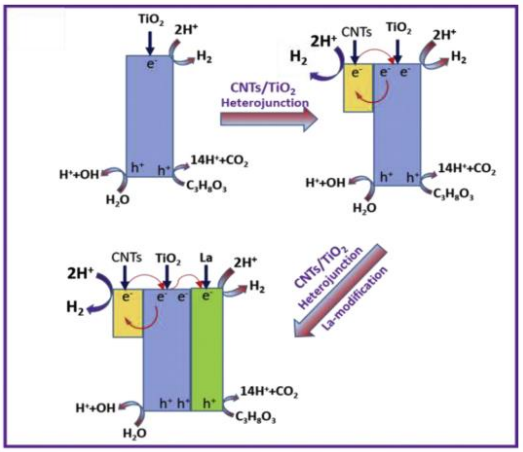

Fig. 1.17. Scheme of synergistic effects of CNTs/La towards enhanced photo-activity of TiO_2 for H_2 production [119].

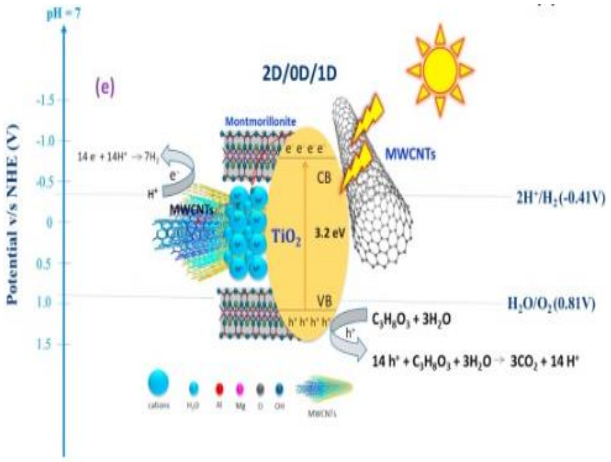

Fig. 1.18. mechanism of photocatalytic hydrogen production using montmorillonite and CTN [120].

The most attention for increasing activity of the photocatalysts has been devoted to the incorporation of cocatalysts. Because of the larger work function of noble metals than most of semiconductors, photogenerated electrons would be readily transferred from the conduction band of the semiconductor to the metal. Although diverse research has been performed on noble metals as the best cocatalysts, their high price directed scientists towards earth-abundant materials [15]. In the following section, different research on photocatalytic alcoholic waste valorization enhanced by cocatalyst incorporation is discussed.

1.4.1.1. Cocatalyst-enhanced TiO_2

Cocatalyst is an auxiliary compound incorporated in the photocatalyst to improve its photocatalytic activity. It can form a Schottky junction with a semiconductor to improve charge separation by the formation of an electric field that separates excited electrons and holes. When the work function of cocatalyst matches the semiconductor's conduction band-edge, the photogenerated electron can migrate to the cocatalyst to perform reduction half reaction (Fig. 1.19) [173].

In 1983 Honda *et al.* [182] introduced platinum as an active site for hydrogen production in Pt/TiO_2 photocatalyst. In fact, Pt plays the role of active site where two hydronium ions combine to form an H_2 molecule. More precisely, a photocatalytic reaction takes place at the boundary between photocatalyst and cocatalyst [146]. Among the noble metals, Pt possesses

the largest work function and the lowest activation energy for proton reduction [169]. As a result, it is the most powerful proton reduction cocatalyst for hydrogen production.

Incorporation of cocatalyst in TiO_2 can significantly enhance the rate of photocatalytic reaction (Fig. 1.20) [69]. By incorporation of only 0.05 wt.% Pt on TiO_2 as cocatalyst, the rate of hydrogen production increased significantly [74]. Although Pt is the most common cocatalyst for hydrogen production from alcoholic wastes [33, 69, 74-76, 78, 80-86, 89-91, 93, 95, 165, 183], other metals like Cu [90, 91, 96, 97, 99-101, 104, 105, 115, 116, 126], Au [86, 89, 107-110, 165], Pd [41, 86, 89, 109, 165, 183], Ni [32, 88, 105, 113, 165], Co [88, 112, 165], Ag [88, 111, 165], Mn [165], Ru [183], Rh [183], Cr [88, 165], and W [165] have also employed to enhance the photocatalytic activity.

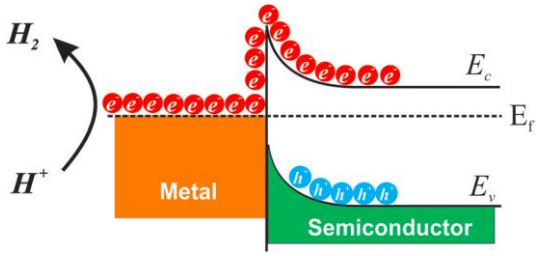

Fig. 1.19. Schematic illustration of energy band model of a Schottky junction [173].

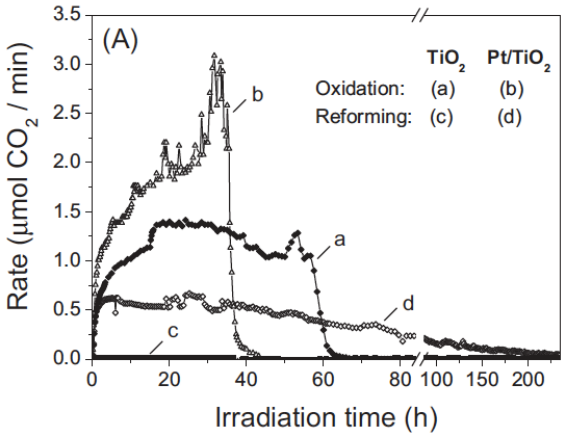

Fig. 1.20. Comparison of the rate and duration of glycerol photo-oxidation and photoreforming [69].

Modifying TiO_2 with noble metals such as Pt, Pd, Au, or Ag cocatalysts illustrated the most positive effect on its photocatalytic activity. Deposition of Ag_2O on TiO_2 nanotubes increased the rate of hydrogen production under solar radiation 13 times because of Ag_2O sensitization property. Al-Azri *et al*. [89] compared the effect of cocatalyst type and reported the order of Pd > Pt ≈ Au for the rate of glycerol to hydrogen using TiO_2. This observation can be attributed to higher difference between the work function of Pd, Pt, Au and TiO_2 (5.6, 5.7, 5.3 and 4.2 eV, respectively). By growing the difference between the work function of metal and TiO_2, the height of formed Schottky barrier at the surface of TiO_2 increases. Superior photocatalytic activity of Pd in comparison to Pt in spite of lower work function can be

justified by higher the density of states in the vicinity of the Fermi level. In addition, the lower electron affinity of Pd in comparison to Pt and Au facilitates electron transfer from Pd to donor species. [111]. Co-presence of noble metals can show a synergic effect as Au and Pd deposited TiO_2 produced more hydrogen that Au or Pd deposited TiO_2 samples [109].

Although noble metals are the most effective and common cocatalysts to improve the photocatalytic activity, their high price restricted their application. Recently researchers took much attention to earth abundant metals to be used as cocatalyst. Deposition of $Ni(OH)_2$ QD as cocatalyst on TiO_2 nanotube improved the hydrogen generation 12 fold in comparison to bare TiO_2 nanotube [114]. Table 1.3 shows that after platinum, Cu is the most investigated cocatalyst for alcoholic waste valorization. Jung *et al*. [90] compared individual- and co-deposition of Cu and Pt and reported that (i) Cu deposition has almost no significant effect, (ii) Pt deposition enhanced the photocatalytic activity around 3 times, and (iii) Cu and Pt co-deposition increased the activity around 4.5 times. This result demonstrates a synergistic effect of Cu and Pt co-deposition. The XPS and TPR analyses of these samples also revealed the CuO_x–PtO_2 interaction caused an enhanced electron density on the Pt. The maximum rate of glycerol to hydrogen conversion using bimetallic Cu-Ni/TiO_2 photocatalyst was reported to be at Cu:Ni mass composition of 9:1 [105]. Metal containing polymer can also act as cocatalyst as it was shown that incorporation of a Cu/Ni based polymer ($[\{Cu^{II}(4,4'\text{-dipy})_2\}\{Ni(CN)_4\}]_n 0.7(C_2H_6O_2)1.6(H_2O)$(CP-1)) as cocatalyst could improve the efficiency of hydrogen production [106]. The impact of various metals as cocatalyst was compared and the efficiency of hydrogen production was found to follow the order of Cu > Ag > Ni > Co > Cr [88]. The lower activity of Cr deposited sample can be attributed to the tendency of deposited Cr particles to have bright color when immersed in water, which can decrease their light adsorption capability. Furthermore, although the existence of Ni as cocatalyst reduces its band gap, it had less impact on preventing the e^-/h^+ recombination, as showed by Photoluminescence test. Using Cu not only narrowed the band gap, but also had no effect on the crystallinity of photocatalyst, in contrast with other cocatalysts as confirmed by XRD.

The size of cocatalyst particles deposited on semiconductor surface affect the photocatalytic activity. As the boundary between cocatalyst and semiconductor is the active site [146], generally low particle size of cocatalyst is favorable to generate more active site per mass of cocatalyst. Despite this, it seems that the particle size has an optimum as it is reported that in

the range of 2-5 nm, the photocatalytic activity enhances by increasing the average particle size [86]. Other than the size of Pt particles, their chemical state, and interaction with semiconductor affect the rate of H_2 production [84].

The most common methods for cocatalyst deposition on semiconductors are photo-deposition [83, 92, 97, 130], wet impregnation [74, 91, 104], dry impregnation [110], and chemical reduction [33, 135] (Table 1.3). The photodeposited method usually exhibits a higher rate of hydrogen production as yields a well dispersed and in elemental state cocatalyst. In this method, the dissolved cocatalyst precursor is decreased using the photogenerated electrons and deposit on the photocatalyst surface. As the electrons migrate from the semiconductor to surface trapping sites, the cocatalyst particles forms with the minimum distance from the trapping sites, decreasing the electron migration path during the photocatalytic reaction and therefore the probability of charge recombination. As the electrons are provided from the semiconductor side, the reduced cocatalyst transfers the electrons to outer layer of the formed cocatalyst particles to grow uniformly. This method is therefore the most commonly used method, as can be seen from Table 1.3. In the impregnation method, the precursor is first randomly loaded on the surface by impregnation and drying which forms non-uniform particles. The elemental state particles then form by the reduction using an external reducing agent like H_2 or $NaBH_4$. As in contrast with the photodeposition method, the reduction occurs from the outer layer of the deposited particles, the reduction of balk cocatalyst is prevented after the reduction of outer layer. As a result, as confirmed by XPS analysis, both elemental and oxidized states of cocatalyst can be available in the sample prepared by the impregnation method [84]. The oxidized cocatalyst can hinder the charge transfer between the semiconductor and protons during photocatalytic reaction [184]. Fig. 1.21 represents the mechanism of photodeposition and impregnation deposition methods. The cocatalyst deposition method can significantly influence its chemical state; however, it might exhibit less effect on the cocatalyst particles size [84]. Photodeposition may perform through (i) a separate process and then the photodeposited photocatalyst is used to perform the photocatalytic reaction (*ex-situ* photodeposition) [93] or (ii) adding cocatalyst precursor to the solution just before starting the photocatalytic reaction (*in situ* photodeposition) [82]. The hydrogen production rate using *in situ* photodeposition method is usually higher compared to *ex-situ* photodeposition or impregnation method [84].

Gunlazuardi *et al.* [79] compared Pt-doped TiO_2 nanotubes (CRA) and Pt-deposited ones by chemical reduction (CRC) and photodeposition (PDC) methods and showed the amount of hydrogen production was in the order of PDC>CRA>CRC (Fig. 1.22). This result can be attributed to the fact that the content of Pt in the surface or structure of TiO_2 was found to be in the same order by Energy-dispersive X-ray spectroscopy and Atomic Absorption Spectrometry analysis. Moreover, the distribution of Pt was better in the sample prepared by the CRA method in comparison to CRC.

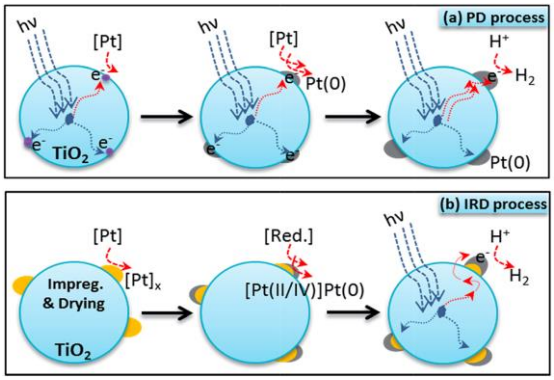

Fig. 1.21. The process of platinum deposition on TiO_2 using photodeposition and impregnation methods [84].

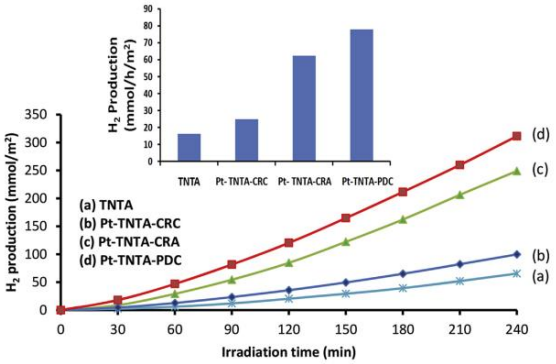

Fig. 1.22. The amount of hydrogen production by Pt-doped and deposited TiO_2 samples using chemical reduction and photodeposition methods [79].

It is worth mentioning that the deposition of cocatalyst may also incorporate in its doping with semiconductor. The deposition of metal by a method that contain a calcination step (like impregnation) can lead to the transfer of into the semiconductor crystal. In this case, the metal can also contribute in the band gap modification. Deposition of metal using co-precipitation method followed by calcination at even low temperature of 200 °C not only enhanced the absorption of visible light region, but also increased the UV range absorbance [105]. Zhang *et al.* [99] deposited Cu on the surface of photocatalyst by photodeposition method and then calcined the sample. They reported that Cu gradually permeated into the surface during the preparation in a way that the its concentration on the surface is maximum and decreased by element depth (Fig. 1.23).

Table 1.4. Summary of the developed photocatalysts for alcohol valorization to hydrogen.

Semiconductor type	Crystalline phase	Semiconductor source	Calcination condition	Cocatalyst type	Cocatalyst deposition method	Cocatalyst wt%	Ref.
TiO_2 nanorod	-	hydrothermal	200, 250, 300, 400 °C/1, 2, 3 h	-	-	-	[72]
TiO_2	anatase, rutile	commercial P25	-	Pt	wet impregnation	0.05-5	[74]
TiO_2	anatase, rutile	commercial P25	-	Pt	photoreduction	0.5	[76]
TiO_2	anatase, rutile	commercial P25	-	Pt	impregnation	0.5	[77]
TiO_2	anatase, rutile	commercial P25	-	Pt	wetness impregnation	1	[75]
TiO_2	anatase, rutile	commercial P25	-	Pt	photodeposition	0-2	[78]
TiO_2	anatase	commercial	-	Pt	photodeposition	0.5	[80]
TiO_2	anatase, rutile	commercial P25	-	Pt	impregnation	0.5	[81]
TiO_2	anatase, rutile, brookite	sol-gel	300 °C/3 h	Pt	impregnation	1	[33]
TiO_2	anatase, rutile, brookite	hydrothermal	400 °C/3 h	Pt	photodeposition	0.2	[82]
TiO_2	anatase, rutile	commercial P25 and Kronosvlp7000	-	Pt	photodeposition	2.1	[83]
TiO_2	anatase, rutile	commercial P25	-	Pt	photodeposition, impregnation	1	[84]
TiO_2	anatase, rutile	commercial P25	400 °C/2 h	Au, Pt, Pd	deposition-precipitation, impregnation, photodeposition	0.5–3	[86]
TiO_2	anatase, rutile	commercial P25	350 °C/2 h, 500 °C/2 h	Pd, Pt, Au	deposition–precipitation	0.5-1	[89]
TiO_2	anatase, rutile	commercial P25	-	Cu_2O	impregnation	2	[102]
TiO_2	anatase, rutile	commercial P25	300 °C/0.5 h	Pt, Cu	wet impregnation	0.04-0.08	[90]
TiO_2	anatase, rutile	commercial P25	450 °C/6 h	Pt, CuO	wet impregnation	1.25	[91]
Au/ TiO_2	anatase	sol-gel	400 °C/2h	Au, Pt, Pd	photodeposition	0.1-0.5	[87]

B,N,TiO_2	anatase	hydrothermal	450 °C/1 h	Pt	photodeposition	0.44	[92]
$Cu_xTi_{1-x}O_{2-\delta}$	anatase	sol-gel	500 °C/5 h	Pt	photodeposition	1	[93]
$Cu_{0.02}Ti_{0.98}O_{2-\delta}$	anatase	sol-gel	500 °C/4 h	-	-	-	[94]
N/TiO_2 nanotube	anatase, rutile	hydrothermal	500 °C/1 h	Pt	photodeposition	1	[95]
TiO_2	anatase, rutile	commercial P25	350, 450 °C/5 h	Cu	impregnation	0.2-5	[96]
TiO_2	anatase, rutile, brookite	sol-gel	450 °C/6 h	Cu	photodeposition	1-2.5	[97]
TiO_2	anatase, rutile	commercial P25	-	Cu	photodeposition	-	[98]
TiO_2 nanosheets	anatase	hydrothermal	350 °C/2 h	Cu	photodeposition	0-2.65	[99]
TiO_2 nanotube	anatase, rutile	hydrothermal	350 °C/5 h	Cu	impregnation	0.1-2	[100]
TiO_2 nanotube	anatase	sol-gel	500 °C/3h	Pt	chemical reduction, photodeposition	0-3	[79]
TiO_2 hollow sphere	anatase	hydrothermal	450 °C/5 h	Cu, Cr, Ag, Co, Ni	impregnation	-	[88]
TiO_2	anatase, rutile	commercial P25	450 °C/2.5 h	CuOx	equilibrium deposition filtration	0.01–2.8	[101]
TiO_2 nanorod	anatase	hydrothermal	350-550 °C/5 h	Cu	wet impregnation	0.5-2	[104]
TiO_2 nanorod	anatase, rutile	ionothermal	400 °C/3 h	-	-	-	[73]
TiO_2 nanorod	anatase	Sol-gel	500-700 °C/0.16-4 h	Pd, Au, Pd-Au	deposition precipitation with urea	0.5	[109]
TiO_2	anatase, rutile	commercial P25	200 °C/1 h	Cu, Ni	coprecipitation	0-15	[105]
TiO_2	anatase, rutile	sol-gel, hydrothermal	475 °C/4 h	Au	deposition–precipitation	1.5	[107]
TiO_2 nanorod	anatase, rutile	hydrothermal	150-1000 °C/2 h	Au	deposition–precipitation	0.5-2	[108]
TiO_2	anatase, rutile	commercial P25	500 °C/2 h	Au, Pd	incipient wetness	0.5-2	[110]
TiO_2	anatase, rutile	commercial P25	500 °C/3 h	Pd	wetness impregnation	0.5	[41]
TiO_2 nanotube	anatase, rutile	hydrothermal	350 °C/5 h	Ag	wet impregnation	0.3-2	[111]
TiO_2 nanotube	anatase	hydrothermal	350 °C/5 h	$Ni(OH)_2$	wet impregnation	0.5-4	[114]
TiO_2	anatase, rutile	commercial P25	400 °C/5 h	Co	impregnation	0.2-5	[112]

TiO_2	anatase, rutile	commercial, solvothermal	250, 400 °C	NiO	impregnation	0-5	[113]
TiO_2	anatase, rutile	commercial	250, 450, 650 °C/3 h	NiOx	impregnation	7.85	[32]
TiO_2	anatase, rutile	commercial P25	-	CP-1*	impregnation	2.5-7.5	[106]
TiO_2, CuO_x/TiO_2	anatase, rutile, brookite	sol-gel	450 °C/6 h, 1 h	-	-	2.5	[115]
$Cu_3(PO_4)_2$ /TiO_2/CuO	anatase, rutile	sol-gel	500 °C/2 h	-	-	-	[142]
Cu/TiO_2	anatase	sol-gel, hydrothermal	-	-	-	-	[116]
$N/M/TiO_2$ (M=Cr, Co, Ni, Cu)	anatase	modified sol-gel	450 °C/4 h	-	-	-	[117]
TiO_2/CNT	anatase, rutile	commercial P25, arc discharge, wet impregnation	400 °C/2 h	-	-	-	[118]
$Cu_3(PO_4)_2$ /TiO_2/CuO	anatase, rutile	sol-gel	500 °C/2 h	-	-	-	[122]
TiO_2/Graphene oxide	anatase, rutile	hydrolysis and peptization, hummers	400 °C/2 h, 500 °C/5 h	Cu_2O	ultrasound assisted wet impregnation	0-2	[126]
Fe/g-C_3N_4/ TiO_2	anatase, rutile	solid-state	450 °C/4 h	-	-	-	[125]
Montmorillonite/ TiO_2	anatase	sol-gel	500 °C/5 h	-	-	-	[120]
TiO_2/CNT		commercial P25	300-450 °C/1-3 h		wet impregnation	0.3	[143]
TiO_2/MWCNT	anatase	hydrothermal	350-500 °C/2 h	-	-	-	[121]
Montmorillonite/ TiO_2/MWCNTs	anatase	wet impregnation	500 °C/1 h	-	-	-	[120]
La-CNTs/ TiO_2	anatase	modified sol-gel	500 °C/3 h	-	-	-	[119]
TiO_2/Graphene oxide	anatase, rutile	hydrothermal	-	Pt	photodeposition	0-3.8	[85]
M/TiO_2(M=Ag_2O, Bi_2O_3, ZnO)	anatase, rutile	sol-gel	500 °C/4 h	-	-	-	[128]

Zn_2TiO_4	-	solid-state	1000 °C/2 h	-	-	-	[132]
CdS, TiO_2	anatase, hex-CdS wurtzite	heat-treatment, sol-gel, commercial P25	400 °C/2 h	Pt	photodeposition	0.3	[129]
CdS	-	heat-treatment	700 °C	Pt	photodeposition	-	[130]
CdS	-	precipitation	-	Ni	photodeposition	0.11-21.66	[131]
$Cd_{0.5}Zn_{0.5}S$	-	hydrothermal, coprecipitation	-	-	-	-	[133]
$Cd_{1-x}Zn_xS$	-	sonochemical	-	Pt	photodeposition	-	[134]
$Cd_{1-x}Zn_xS$ /ZnO/$Zn(OH)_2$	-	solid solution formation from hydroxide mixture	-	Pt	soft chemical reduction	1	[135]
ZnO/ZnS	-	anion-exchange	-	-	-	-	[136]
ZnO/ZnS	-	a low temperature route	-	-	-	-	[137]
PdS-ZnO/ZnS	-	hydrothermal, cation exchange	-	Pd	copricipitation	0-0.48	[139]

*CP-1: ($[\{Cu^{II}(4,4'\text{-dipy})_2\}\{Ni(CN)_4\}]_n 0.7(C_2H_6O_2)1.6(H_2O)$ polymer)

1.4.2. Other photocatalysts

Other than TiO_2, some other photocatalysts have also been utilized in alcohol valorization. Among them, CdS is one of the most active photocatalysts under visible light with band gap energy of 2.4 eV. This n-type semiconductor is therefore the most common non-titanium based photocatalyst for alcohol conversion (Table 1.4). Although the hexagonal structured CdS (wurtzite) exhibits a high activity, its cubic structure's activity is insufficient [185]. Drawback of CdS is related to its tendency to photooxidation which leads to cadmium leaching [130]. One approach to increase the stability of CdS is to form a solid solution and modify the crystalline phase by replacing Cd with Zn [186]. Lopes *et al*. [134] utilized a simple sonochemical procedure to synthesize $Cd_{1-x}Zn_xS$ solid solutions and found that up to 20% Zn can be incorporated in CdS wurtzite matrix and higher Zn content leads to the formation of γ-$Zn(OH)_2$ on surface. They reported that the highest amount of hydrogen is produced at Cd:Zn:S molar ratio of 1:8:4, where excess γ-$Zn(OH)_2$ was formed on surface. The most common methods for $Cd_{1-x}Zn_xS$ photocatalyst synthesis are co-precipitation and hydrothermal [134]. For hydrogen production, Peng *et al*. [133] used $Cd_{0.5}Zn_{0.5}S$ solid solutions synthesized by co-precipitation and hydrothermal methods. The sample prepared by co-precipitation method with glycerol as solvent (S_{BET}= 95.3 m^2g^{-1}) produced around two times hydrogen compared to the one produced by hydrothermal method (S_{BET}= 77.9 m^2g^{-1}) which can be attributed to its higher surface area. The photocatalytic activity of multiphase $Pt/Cd_{1-x}Zn_xS/ZnO/Zn(OH)_2$ photocatalyst was found to be around 2.1 times more than single-phase $Pt/Cd_{1-x}Zn_xS$ photocatalyst [135]. Sang *et al*. [137] coated ZnO nanorod with a layer of porous ZnS shell to produce more active ZnO/ZnS core/shell nanorods. They reported that a 0.6 molar ratio of ZnS/ZnO produced the highest amount of hydrogen because of have higher surface areas (S_{BET}= 34 m^2g^{-1}) and absorption based on UV-Vis analysis. This sample exhibited the quantum efficiencies of 22% and 13%, under UV and solar-simulated light, respectively. Polygonal Zn_2TiO_4 was synthesized using citric assisted solid state method and showed a higher hydrogen generation than Zn_2TiO_4, ZnO and TiO_2 because of more surface area and less e^-/h^+ recombination [132]. On the other hand, although the band gap of these samples is similar, the protons can more easily be reduced to hydrogen by Zn_2TiO_4 as its conduction band is more negative than ZnO and TiO_2.

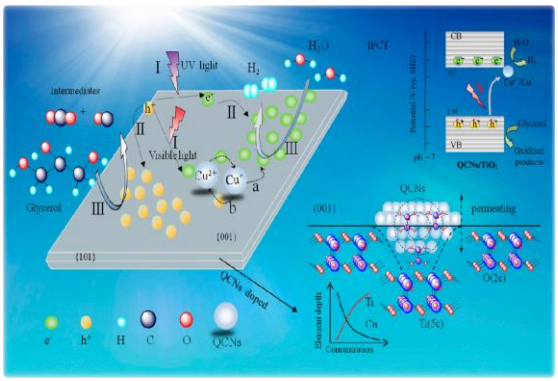

Fig. 1.23. The mechanism of hydrogen production from glycerol using Cu(II)-QD/ultrathin-TiO_2-nanosheet [99].

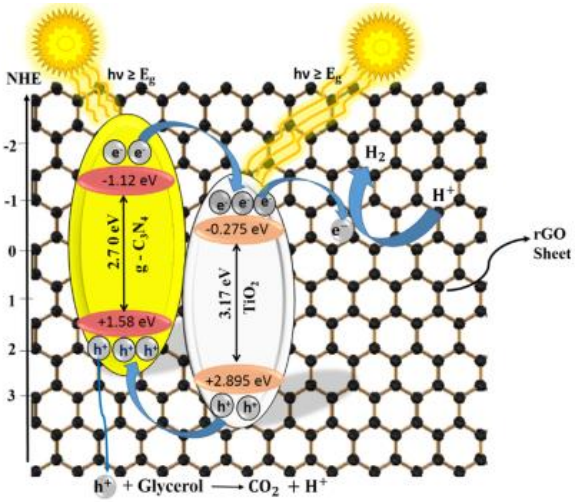

Fig. 1.24. Charge transfer between TiO_2, g-C_3N_4, and rGO for hydrogen generation [124].

Semiconductor nanocrystals (quantum dots; QD) are such tiny particles that their optical and electronic properties are different from their properties in their bulk form. Wang *et al*. [131] compared nickel-hybrid CdS QDs, CdTe QDs and CdSe QDs and reported that the first one illustrated the highest affinity toward Ni^{2+} ions to convert glycerol to hydrogen under visible-light irradiation and its quantum efficiency reached 12.2%. The higher photocatalytic activity of CdS can be attributed to its more positive valence band (E_{vb}=1.6 V) [187] than those of CdSe (E_{vb}=1.1 V) [188] and CdTe (Evb=0.54 V) [187], which provides a higher driving force for water or alcohol oxidation. Cu(II) QDs deposited *in situ* on ultrathin TiO_2 nanosheets (Fig. 1.23) exhibited 25 times more hydrogen production from glycerol in comparison to pure TiO_2 [99]. The sample decorated by 1% Cu (molar basis) was found to produce the highest amount of hydrogen and illustrated the highest surface area (S_{BET}= 54.4 m^2g^{-1}) and the most efficient rate of photoinduced e^-–h^+ pairs separation. For Cu(II) QDs deposited ultrathin TiO_2 nanosheets, it is reported that the conversion of Cu^+ to Cu^{2+} permitted two different paths of charge transfer for hydrogen production (route a) and h^+ consumption (route b, see Fig. 1.23). Therefore, the charge-transfer rate was enhanced because of increasing the number of generated e^-.

Mixing two or more semiconductors to produce composite semiconductors is a promising approach to improve the photocatalytic activity, as mixed semiconductors exhibit enhanced charge separation, light absorption and stability. The dual photocatalysts (also called Z-

scheme systems or electron mediator systems [173]) utilize two different photocatalysts, one is responsible for the reaction of photogenerated electrons, and the other provides the photogenerated holes in the other half reaction. As an example, binary Pt/hex-CdS hybrid photocatalyst and also ternary Pt/CdS/TiO_2 and Pt/TiO_2/hex-CdS hybrid photocatalysts were synthesized based on two approaches: (i) deposition of TiO_2 on a commercial CdS and (ii) deposition of CdS on a commercial P25 [129]. In the later approach, TiO_2 hindered the aggregation of CdS by playing the role of support and also improve the charge separation. The photocatalytic activity towards hydrogen varied in the order Pt/hex-CdS > Pt/CdS/TiO_2> Pt/TiO_2/hex-CdS. This may be attributed to creation of a potential gradient at the interface of CdS and TiO_2 because of more positive conduction band edge potential of TiO_2 (−0.43 V) compared to that of CdS (−0.75 V).

It is shown that the sequence of performing different steps during the synthesize pathway of ternary photocatalyst can significantly affect its efficiency, as affects their junctions. Hafeez et al. [124] compared g-C_3N_4-TiO_2/rGO and TiO_2-g-C_3N_4/rGO ternary catalysts and showed that the former had more efficiency for hydrogen generation. It can be therefore concluded that the junction between TiO_2 and rGO is more desirable than that of g-C_3N_4 and rGO. In g-C_3N_4-TiO_2/rGO the photo-excited electron can conveniently move from g-C_3N_4 to TiO_2 and then transfer to rGO for reducing the H^+ according to the energy of band edges of g-C_3N_4 and rGO (Fig. 1.24). On the other hand, the photogenerated holes can be transferred from TiO_2 to g-C_3N_4 and then react with glycerol.

1.5. Modelling of photocatalytic processes

Although photocatalytic process is less harmful than traditional thermal processes, it is important to engineer this process to decrease the harmful impacts on the environment. Optimization of the photocatalytic process to enhance the conversion, selectivity, and loss of energy and material is an approach to limit the environmental damages. In this way, using semi-experimental models is a sophisticated approach which is not well studied. Another approach is using catalyst supports to decrease consumption of photocatalysts (which are mainly non-renewable metallic oxides) and enhance the efficiency of photocatalytic reaction (to save energy and material). Carbonaceous templates are promising alternatives for this purpose, as are renewable, economical, and non-hazardous [189].

Many work has focused on the photocatalyst synthesis and studying the feasibility of photocatalytic reactions nevertheless, this field suffers from the lack of modeling studies. The previous research performed to develop a model for photocatalytic reactions focused on statistical and kinetic methods. As the fundamentals of photocatalytic processes are not well known to researchers, most of the developed models have been established based on statistical analysis of experimental data [130, 150, 190-192].

A statistical model utilizes particular statistical assumptions to develop a relation between independent variables with one or more dependent variables. This type of model can be applied to mathematically model complex processes like photocatalytic hydrogen production because it does not need knowledge about the photocatalysis fundamentals [193]. RSM is a statistical method to design experiments, develop a model, investigate effects of parameters, assess the interaction effect of the parameters, and optimize the desired responses [70, 151]. The idea behind RSM is to use experimental data to approximately find the optimum value of response. This method which is introduced by George E. P. Box and K. B. Wilson employs a second-degree polynomial function to model and find the polynomial constants using the experimental data. One advantage of RSM over conventional 'one-variable-at-a-time' (OVAT) approaches is the ability to determine the interaction effects of operating parameters that permits discussion on the effect of each operating parameter on the optimum value of other operating parameters. Only a single study on development of statistical models for photocatalytic valorization of alcoholic wastes was found in the literature. Bastos et al. [130] studied the valorization of alcohol to hydrogen with a simple factorial design statistical model. The obtained critical point in this work was corresponded to a minimum, i.e., it is not possible to perform an optimization using this model. No work using RSM approach was found in this area to optimize the process and find the interaction effects of operating parameters.

Artificial Neural Networks (ANN) is another useful modeling methods that was inspired by biological neural networks taking advantage of some simple and non-linear models [194]. An ANN model is a framework of machine learning algorithms that is trained using some examples from practice. Because of the ability of ANN in modeling of non-linear processes, this method has used in many disciplines. An ANN model uses a series of processing units that are usually arranged in three sections: an input layer that contains the units related to

independent variables, one or more hidden layers, and an output layer that represents one or more units related to dependent variables (responses). The units in an ANN model are connected with a value that is called weight. After development of a ANN model, optimization methods like genetic algorithm (GA) are required to optimize the developed model. There is no publication in this field using ANN approach to model photocatalytic valorization of alcoholic wastes.

Kinetics modelling is another technique that can model the rate of chemical processes as a function of different operating parameters. This modeling approach enables us to analyze chemical and physical reactions and unravel basic reaction mechanisms. Regarding photocatalytic valorization of alcoholic wastes, all of the observed studies simply used the Langmuir-Hinshelwood (L-H) model to develop a kinetic model [98, 195-202]. Therefore, the developed models in previous works are only valid under the specific conditions that the experiments were carried out. Moreover, the models developed based on L-H are limited because of being only a function of substrate concentration.

1.6. Conclusions on the available literature

Valorization of alcoholic wastes into renewable chemicals and fuels is a sustainable approach for value-added products generation. As a significant waste of bio-diesel production process, glycerol is introduced as one of the most challenging alcoholic wastes due to its overproduction in the recent years. Other biobased alcoholic wastes like ethanol and cyclohexanol are also promising alternatives for valorization process. Valorization of alcoholic wastes approach not only takes advantage of low-value or negative value wastes as feedstock, but even contributes to preservation of the environment by transformation of polluting compounds. Photocatalytic valorization of alcoholic wastes is a novel approach that benefits from several advantages that are in line with sustainable development guidelines.

Although a lot of research was performed on the synthesis of photocatalyst and feasibility of photocatalytic reaction, this field suffers from the lack of optimization of operating parameters. On the other hand, it is challenging to make a consensus on the optimum value of operating parameters because of substantial differences and contradictions in previous work. The observed conflicts may be due to employing OVAT approach and to a neglecting the effect of interaction between parameters. RSM and ANN methods are two practical

modeling approaches that can analyze the interaction effect of operating parameters. Possibility of incorporating design of experiment approach is an advantage for these modeling techniques to minimize the number of required experimental data for studying complex processes like photocatalytic valorization of alcoholic wastes. No research work using ANN or RSM modeling approaches was found in this area to optimize the process and find the interaction effects of operating parameters.

Regarding photocatalytic valorization of alcoholic wastes, all of the observed works simply employed the L-H model to develop a kinetic model. The L-H based models are limited as they are only a function of substrate concentration. Therefore, the available L-H-based models are not appropriate for a comprehensive modelling of photocatalytic valorization of alcoholic wastes. The single intrinsic kinetic models observed in the literature regarding photocatalytic valorization of alcohols is developed for gas phase [203]. Since the photocatalytic reactions are interesting due to being performed at ambient temperature and pressure, it is necessary to develop a comprehensive kinetic model for liquid phase photocatalysis. To overcome the issue related to OVAT approach, the statistical design of experiment can be used as a smart approach that considers the interaction effect of variables and minimizes the number of required experiments.

Incorporation of biobased carbonaceous templates to prepare TiO_2@CT composites is a sustainable alternative to enhance the photocatalytic activity. CNT and CS are two important CTs with unique structural, chemical, thermal, and electrical properties. These characteristics suggest these CTs for TiO_2@CT composites preparation. Several works have studied the photocatalytic activity of carbonaceous TiO_2 composites for valorization of alcoholic waste. Although many research reported the effectiveness of CNT and CS for enhancing photocatalytic activity of TiO_2@CT composites, some others illustrated that carbonaceous materials may not be beneficial in some cases. Thus, a thorough investigation is essential to elucidate the roles of CT in photocatalytic activity enhancement. CTs can play different roles, such as support, cocatalyst, and adsorbent. In spite of the importance of this subject, no study focussed on the individual effects and roles of CTs in the photocatalytic valorization of alcoholic wastes.

Photocatalytic production of value-added liquid chemicals is a promising approach for chemical synthesis as can achieve a higher selectivity in comparison to conventional thermal oxidation processes. Since the photocatalytic processes operate at ambient temperature and atmospheric pressure, photocatalytic synthesis of sensitive chemicals is a point of interest. The photocatalytic production of cyclohexanone from cyclohexanol and subsequent production of caprolactam is a key reaction in production of bioplastics. Lignin-sourced cyclohexanol is a biobased alcohol. A high selectivity of photocatalytic cyclohexanol transformation to cyclohexanone exhibits the potential of this reaction in future bioplastic production. A very limited study has been performed and no model is developed for this process.

1.7. Objective of the work

The conventional developed photocatalytic waste valorization processes mainly considered organic substances as pollutant and focussed on their complete degradation to non-hazardous molecules for the environment. From sustainable development point of view, these organic substances are valuable feedstocks and could be valorized to valuable liquid and gas products. This area of research requires sophisticated expertise to control the reaction conditions and maximize the selectivity of desired products. In this way, thorough parametric, mechanistic and kinetic studies should be performed to engineer the path of reactions.

In this context, the following objectives were defined based on the conclusion on the literature review:

1.7.1. General objective

The main objective of the current PhD thesis is to investigate the photocatalytic valorization of different alcoholic wastes to value-added products, by:

- Analyzing individual and interaction effect of operating parameters and optimization of hydrogen production from glycerol;
- Studying the kinetics of hydrogen production from glycerol and ethanol;
- Developing TiO_2 nanocomposite catalysts using biobased carbonaceous materials (carbon nanotubes and carbon spheres) for hydrogen production from glycerol;

- Investigating the mechanism and kinetics of the photocatalytic valorization of cyclohexanol to cyclohexanone.

To achieve this goal, the following specific objectives were defined:

1.7.2. Specific objectives

- Comparison of RSM and ANN modeling methods to statistically model the photocatalytic glycerol valorization to hydrogen based on the design of experiment approach.
- Optimization of four key operating parameters of glycerol%, catalyst loading, Pt%, and pH using the selected model, based on GA method.
- Finding the most critical operating parameters based on Garson's method for further investigation using kinetic modelling.
- Development of a novel and intrinsic kinetic model for photocatalytic valorization of liquid substrates to hydrogen.
- Development of a kinetic model to predict the rate of hydrogen production.
- Finding the kinetic parameters of the developed kinetic model for glycerol and ethanol.
- Incorporation of biobased carbonaceous templates in composite photocatalyst preparation in order to enhance the effect of catalyst loading (as the most influential operating parameter).
- Comparison of CS and CNT incorporation as carbonaceous template for carbonaceous TiO_2 nanocomposite preparation.
- Comparison of hydrothermal, alcohol phase sol-gel, and aqueous phase sol-gel synthesis methods for nanocomposite photocatalyst preparation.
- Investigation of CNT roles in TiO_2 nanocomposite photocatalyst for photocatalytic hydrogen production from glycerol.

- Development of a mechanism and kinetic model for photocatalytic cyclohexanone production from cyclohexanol and its validation based on *in-situ* ATR-FTIR analysis of photocatalytic experiment.

In the next chapter, the materials used in the current work, the synthesis procedure of template, photocatalyst, and composite as well as the material characterization techniques are explained. In addition, the methods of conducting photocatalytic experiments as well as the chromatographic and spectroscopic analyses of products procedures are presented. Finally, the methodology of the design of experiment, the statistical and kinetic modeling, and the model optimization and its statistical analysis are clarified.

Chapter 2 : Methodology

In this chapter, the methodology of performing the current work is explained in detail. The aim is to associate the methodologies of different chapters and present an overall view on the individual steps. Figure 2.1 and Figure 2.2 present the schematic of photocatalytic experiments procedure to produce hydrogen and cyclohexanone, respectively. These steps generally include material preparation, photocatalytic reaction, product analysis, and process modelling. In the following sections, each of these steps are explained in detail.

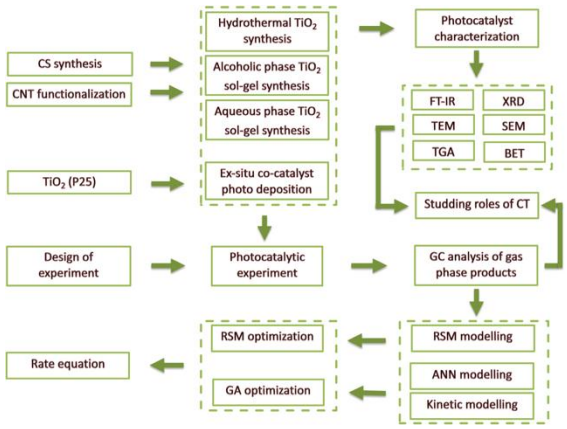

Figure 2.1. The schematic of photocatalytic hydrogen production experiments procedure.

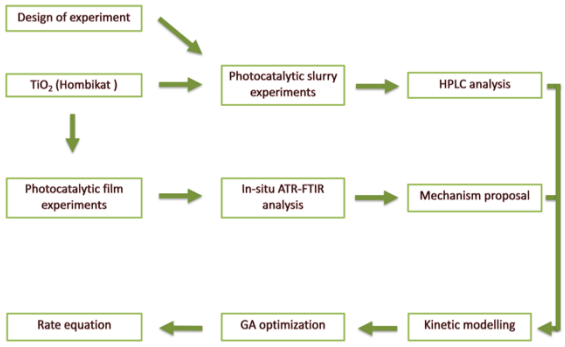

Figure 2.2. The schematic of photocatalytic cyclohexanone production experiments procedure.

Table 2.1. List of name, supplier, and purity of the materials employed in this work.

Chemical	Supplier	Purity	Notes
TiO_2 Aeroxide P25	Evonik Industries	≥99.5%	
TiO_2 Hombikat UV-100	Sachtleben Chemie GmbH	99%	100% anatase
Graphistrength C100 multiwalled CNT	ARKEMA	≥90%	10−15 nm diameter, 5−10 walls, 1−10 μm length
Titanium (IV) isopropoxide (TTIP)	Acros Organics	≥98%	
Titanium (IV) n-butoxide (TBOT)	Acros Organics	≥99%	
Hexachloroplatinic acid (IV) ($H_2PtCl_6 \cdot 6H_2O$)	Sigma–Aldrich	≥37.50% Pt	
Glycerol	Caledon, VWR	≥99.5%, ≥99.7%	
Ethanol	Commercial Alcohols	99.99%	
2-propanol	Fisher Scientific	≥99.9%	
Benzyl alcohol	Alfa Aesar	≥99%	
Cyclohexanol	Sigma Aldrich	99.0%	
Cyclohexanone	Sigma Aldrich	≥99.0%	
Sodium hydroxide	VWR	≥97%	
Hydrochloric acid	VWR, Anachemia	36.5-38.0%	
Acetic acid	Caledon	≥99.7%	
Nitric acid	Anachemia	68.0−70.0%	
Sulfuric acid	Anachemia	95.0−98.0%	
Potassium bromide	Oakwood Chemicals	≥99%	
D−(+)−glucose anhydrous	Alfa Aesar	≥99%	

2.1. Materials

The materials employed for conducting the experiments in the current work can be categorized into (i) commercial TiO_2 photocatalysts such as Aeroxide P25 and Hombikat

UV-100, (ii) commercial CNT of Graphistrength C100 as photocatalyst template, (iii) titanium isopropoxide and titanium n-butoxide for TiO_2 synthesis (iv) hexachloroplatinic acid as cocatalyst, (v) different alcohols such as glycerol, ethanol, 2-propanol, benzyl alcohol, and cyclohexanol, to be used as substrate, linking agent, and solution for material synthesis, (vi) cyclohexanone for HPLC calibration, (vii) sodium hydroxide and hydrochloric acid for pH adjustment, (viii) other acids such as acetic acid, nitric acid, and sulfuric acid for TiO_2 synthesis and CNT functionalization, (ix) potassium bromide for FTIR analysis, and (x) glucose for carbon sphere synthesis. The specifications of these materials such as supplier and purity are listed in Table 2.1.

2.2. Material preparation

2.2.1. Template preparation

2.2.1.1. Carbon sphere synthesis

Carbon sphere (CS) was prepared and employed as template for TiO_2 composite synthesis. Glucose was employed as a sustainable carbon source to prepare CS [204]. For CS synthesis, first 36 g of glucose was added into 200 mL deionized water and stirred for 30 min at ambient temperature. The prepared solution was heated in an oven at 180 ºC for 18 h using a 460-mL autoclave. The prepared CS was then separated by a centrifuge and washed 3 times using distilled water. The obtained brownish powder was finally dried at 80 ºC for 24 h. The schematic of carbon sphere synthesis procedure is illustrated in Figure 2.3.

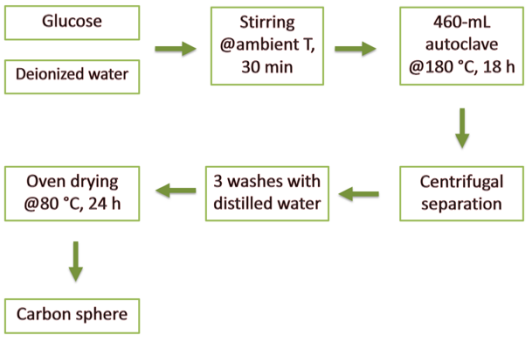

Figure 2.3. The schematic of carbon sphere synthesis procedure.

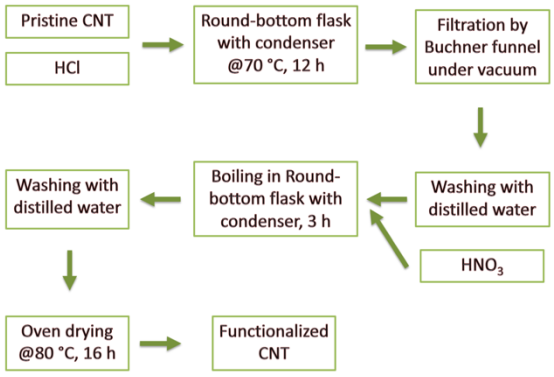

Figure 2.4. The schematic of carbon nanotube functionalization process.

2.2.1.2. Carbon nanotube functionalization

The purchased CNT was first added into 32 wt% HCl solution at heated in a round-bottom flask equipped with a condenser at 70 ºC for 12 h, to remove the metallic impurities and amorphous carbon. The obtained powder was filtered by a Buchner funnel under vacuum, and washed with distilled water. The sample was then boiled for 3 h in a 10 M nitric acid solution, to form oxygen-containing groups such as hydroxyl, carboxyl, carbonyl, and epoxy on the surface of CNT. The functional groups provide nucleation sites and play the role of anchor toward the reagents for attachment of TiO_2 particles during TiO_2 composite synthesis [205]. The functionalized CNT was washed using distilled water to reach a neutral pH of the filtrate. The obtained powder was then dried using an oven at 80 ºC for 16 h. The schematic of carbon nanotube functionalization procedure is depicted in Figure 2.4.

2.2.2. Synthesis of photocatalyst

2.2.2.1. Hydrothermal synthesis

Hydrothermal synthesis method was employed for preparation of TiO_2 photocatalysts. For each synthesis, TTIP was dissolved in propanol and then benzyl alcohol was added to play the role of linking agent and facilitate the attachment of TiO_2 particles on the template surface. The ratio of TTIP:BA:PrOH was adjusted equal to 10:17.5:150. The obtained solution was stirred for 30 min and then required amount of CT (CS or HCl-treated CNT) was added to form a 5% CS or 20% CNT composite. In order to detach CNT particles, the suspension was ultrasonication by a Hielscher UP400S Ultrasonic Processor for 1 h. The suspension was then transferred into an autoclave and heated using an oven at 180 ºC for 48 h. A 460 mL Teflon-lined stainless-steel autoclave was used for hydrothermal synthesis. The obtained composite was then separated using a centrifuge and washed three times with ethanol to remove impurities and unreacted TTIP. The powder was dried at 90 ºC overnight and then was ground into a fine powder and calcined in air for 2 h at different temperatures of 300, 400, 500, 600, or 800 ºC (a heating ramp of 5 ºC min^{-1}). Pure TiO_2 was also prepared using the same procedure, but without adding CT. The schematic of hydrothermal synthesis procedure is illustrated in Figure 2.5.

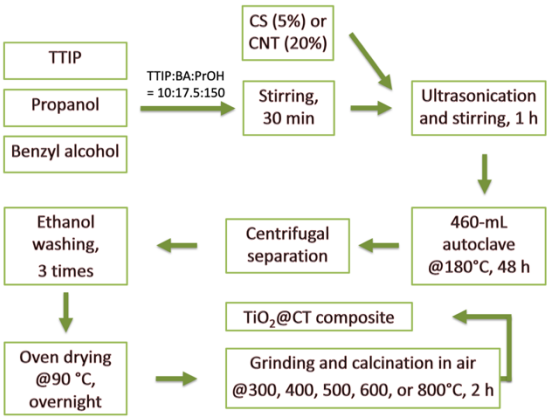

Figure 2.5. The schematic of hydrothermal synthesis procedure.

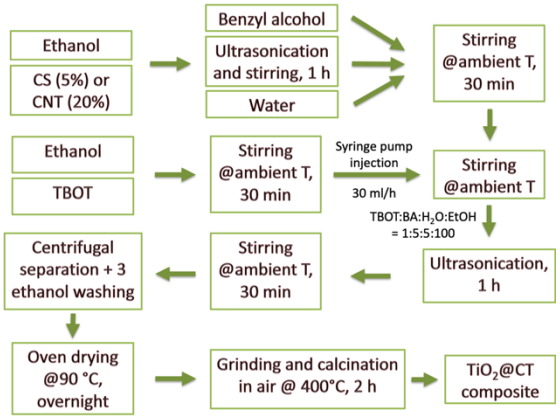

Figure 2.6. The schematic of alcoholic phase sol−gel synthesis procedure.

2.2.2.2. Alcoholic phase sol−gel synthesis

TiO_2 samples were also prepared using alcoholic phase sol−gel synthesis method. For each sample, required amount of CT (CS or HCl-treated CNT) to form a final 5% CS or 20% CNT composite was added into a beaker containing ethanol and then sonicated using a Hielscher UP400S Ultrasonic Processor to detach the CT particles. Benzyl alcohol was added into the suspension to play the role of linking agent and facilitate the attachment of TiO_2 particles on the CT surface. After addition of water, the suspension was then stirred for 30 min to form a homogeneous solution. In another beaker, TBOT was dissolved in ethanol and mixed for 30 min. The second beaker was added into the first one using a syringe pump with the rate of 30 ml/h. The amount of chemicals was adjusted in a way to have a molar ratio of TBOT:BA:H_2O:EtOH equal to 1:5:5:100. The suspension was ultrasonicated and then stirred for 1 h in order to completely hydrolyze the titanium precursor. The obtained powder was separated using a centrifuge and washed 3 times to separate and then dried in an oven at 90 ºC overnight. The dried powder was ground into a fine powder and calcined at 400 ºC for 2 h with a heating ramp of 5 ºC.min^{-1}. The same procedure was followed to synthesize pure TiO_2 (without CT). The schematic of alcoholic phase sol−gel synthesis procedure is provided in Figure 2.6.

2.2.2.3. Aqueous phase sol−gel synthesis

To prepared TiO_2 composites using aqueous phase sol−gel method, glacial acetic acid was added into a beaker and stirred in an ice bath to freeze. The beaker was covered with a

parafilm layer to avoid adsorption of ambient moisture. The beaker was removed from the ice bath and then TTIP was added into the beaker and stirred for 30 min to make a uniform solution. To start the hydrolysis process, deionized water was injected into the beaker using a syringe pump with a 30 ml/h rate. Required amount of nitric acid-treated CNT was then added into the solution and ultrasonicated to detach the agglomerated CNT, while keeping in the ice bath under magnetic mixing for 1 h. In order to completely hydrolyze TTIP, the suspension was stirred for 2 h without ice bath. Before aging the obtained suspension at room temperature in the absence of light for 24 h, the mixture was sonicated again in an ice bath for 15 min. The suspension was then heated at 75 ºC by an oven overnight, to form the gel. The obtained gel was dried in the oven at 120 ºC for 2 h. The dried gel was ground into a fine powder and then calcined in air at 400 ºC for 2 h with a heat ramp of 5 ºC/min. Pure TiO_2 was also prepared using the same procedure, without incorporating CT. Figure 2.7 shows the schematic of aqueous phase sol−gel synthesis procedure.

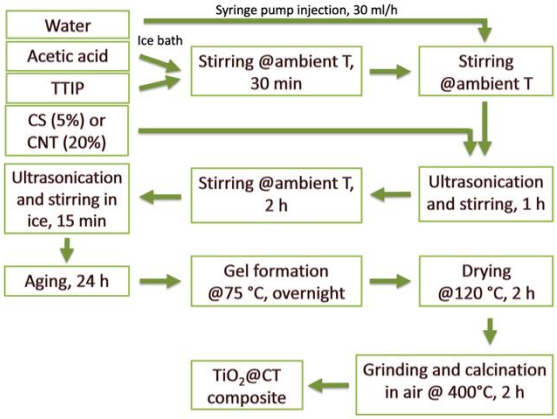

Figure 2.7. The schematic of aqueous phase sol−gel synthesis procedure.

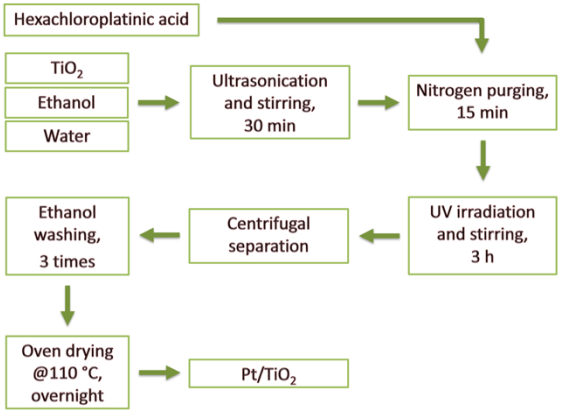

Figure 2.8. The schematic of ex-situ co-catalyst deposition procedure.

2.2.3. Co-catalyst deposition

2.2.3.1. Ex-situ photodeposition

Platinum was deposited on the surface of photocatalysts using photodeposition for some parts of this work (Chapter 3 and 4) [83]. For platinum deposition, 1 g TiO_2 was added into 120 ml of 10% ethanol solution in distilled water and then was sonicated for 30 min using a Hielscher UP400S Ultrasonic Processor. The required amount of hexachloroplatinic acid solution in distilled water (to obtain 0.02, 1, 2.51, or 5 wt% Pt loadings) was added to the

suspension and then purged with 50 ml/min of nitrogen for 15 min to remove the dissolved oxygen. The suspension was irradiated with four 20 W Black-Ray® mercury tubes (365 nm) for 3 h to form platinum particles on the surface of TiO_2. The nitrogen flow and magnetic stirring was kept during the photo deposition process. The platinum deposited TiO_2 was then separated by a centrifuge, washed 3 times, and dried in oven at 110 °C overnight. Figure 2.8 illustrates the schematic of ex-situ co-catalyst deposition procedure.

2.2.3.2. In-situ photodeposition

In-situ photodeposition was employed to deposit platinum on TiO_2 surface for another part of this work (Chapter 5). This method is based on the same principals of in-situ photodeposition, however, takes place at the same batch of photocatalytic hydrogen production experiments. For an in-situ photodeposition process, the required amount of hexachloroplatinic acid solution in distilled water was added to the suspension, before purging with nitrogen for photocatalytic reaction (see § 2.4.1). The platinum was then formed on the TiO_2 surface by starting the irradiation. In contrast with ex-situ deposition that imposes a TiO_2 drying step and may affect the specifications of TiO_2 (like surface area), this method has no effect on the specification of TiO_2.

2.3. Material characterization techniques

2.3.1. Scanning electron microscopy

Electron microscopy can provide a higher resolution and magnification in comparison to optical microscopy. Scanning electron microscopy (SEM) is an electron microscopy technique that is carried out by rastering an electron beam over the surface and then analyzing the secondary or backscattered yield. The section of sample that facing the detector appears brighter, making a difference with other surfaces.

In this work, to obtain a good SEM image, the samples were first sonicated to form separate particles. To do so, a 25 ppm suspension of the samples were prepared in ethanol and then were stirred and ultrasonicated using a Hielscher UP400S Ultrasonic Processor for 10 min. A drop of the prepared suspension was then placed on the sample holder using a micropipette and then the excess ethanol was partially adsorbed using a piece of filtration paper. The samples were then kept in the environment to dry overnight. As formation of electrical charge

in insulating materials under electron beam is a problem for this technique, all the samples were coated with a thin layer of gold and palladium using a Technic Hummer 2 machine, before conducting SEM measurements. It is worth mentioning that using water to make the sample suspension can cause difficulty during vacuuming the samples for this step. A JEOL JSM-840A device (Jeol Ltd., (Japan Electro Optic Laboratory)) equipped with Back-Scattered Electron (BSE) and Secondary Electron (SE) modes was used to perform SEM analysis. The schematic of SEM sample preparation and analysis procedure is shown in Figure 2.9.

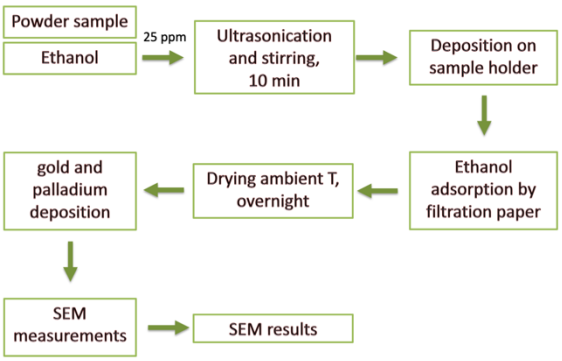

Figure 2.9. The schematic of SEM sample preparation and analysis procedure.

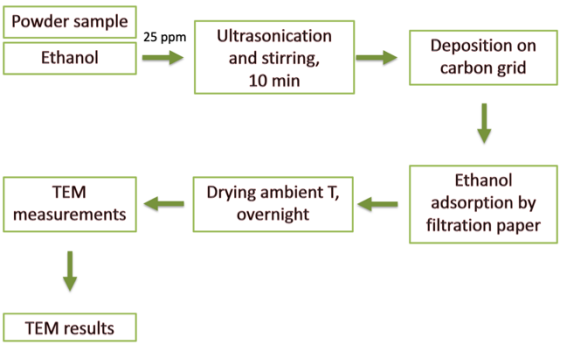

Figure 2.10. The schematic of TEM sample preparation and analysis procedure.

2.3.2. Transmission Electron Microscopy

As SEM analysis cannot usually provide a high resolutions of nanoparticles, TEM images were captured to have a higher accuracy. The main difference between SEM and TEM is that SEM measures the contrast that formed because of topology and composition of surface, however, TEM provides two-dimensional projected image.

In order to detach the particles before TEM analysis and avoid overlapping the particles in TEM images, the samples were detached before analysis. In this regard, a 25 ppm suspension of the samples was prepared using ethanol and then sonicated by a Hielscher UP400S Ultrasonic Processor under magnetic stirring for 10 min. One drop of the prepared suspension was taken using a micropipette while was under magnetic stirring and placed on a carbon grid. The excess ethanol was then adsorbed using a piece of filtration paper and left in the environment during night to dry. The TEM analysis was performed using a JEOL JEM 1230

operated with a 120 kV accelerating voltage, equipped with a lanthanum hexaboride (LaB_6) thermionic emission source and a Gatan dual-view multiscan camera. Figure 2.10 provides the schematic of TEM sample preparation and analysis procedure.

2.3.3. X-ray diffraction

X-ray diffraction (XRD) analysis method takes advantage of analyzing the elastic scattering of X-ray photons by atoms in periodic lattice [206]. XRD is one of the most common characterization techniques for research and development on catalyst synthesis that provides different information such as type of crystalline phases, different polymorph of crystalline phase, content of different polymorphs, and the size of crystals. As XRD is limited to analyze the samples with a crystalline phase, amorphous phases cannot be analyzed properly.

X-ray diffraction (XRD) of the samples was collected using a Bruker SMART APEXII X-ray diffractometer equipped with a Cu Kα radiation source (λ= 1.5418 Å) in the scan range of 2θ=10−80º, step size of 0.02, and count time of 1.2 s. After performing XRD experiments, the data was analyzed to find the types of crystalline phase, the polymorphs of crystalline phase, the crystal size, and anatase over rutile ratio. The type of crystalline phase and polymorphs were found by comparing peak position using the software library. The percentage of rutile phase in the samples was calculated based on Eq. (2–1) [207].

$$\%Rutile = \frac{1}{\left[1 + 0.8(I_A / I_B)\right]} \times 100 \qquad (2–1)$$

where I_A and I_B are the intensities of anatase (101) and rutile (110) reflections, respectively. The Scherrer equation [208] was incorporated to find the average Anatase (101) and Rutile (110) particle sizes.

2.3.4. BET

Specific surface area and pore size distribution of materials can be studied using physisorption isotherm analysis. The physisorption isotherm analysis is based on the plot of the amount of gas adsorbed on the surface of material versus relative pressure (P/P0) in the equilibrium at a constant temperature. Different theories were introduced to calculate the surface area of porous materials using physisorption isotherm, Brunauer-Emmett-Teller (BET) theory is one of the most common ones.

In this work, the surface area of prepared materials was analyzed by physical adsorption of nitrogen gas on the surface and then calculating the amount of gas adsorbed by assuming a monomolecular layer adsorption. Before starting the adsorption of nitrogen, the samples were degassed at 120 °C for 4 h to remove physiosorbed gases or water vapor. A Micrometrics TRISTAR 3000 instrument was used to perform the physisorption isotherm analysis and calculate the BET surface area of the prepared samples.

2.3.5. Thermal gravimetric analysis

Thermal gravimetric analysis (TGA) is a technique that analyzes the variation of mass of sample during a heating cycle. This technique can detect the changes in the sample as a result of different phenomena such as dehydration, decomposition and oxidation/reduction as a function of time and temperature. In a TGA graph, the vertical axis is typically the change of weight in percentage and horizontal axis is usually time or temperature.

In this work, the TGA experiments were conducted using a Q5000IR equipped with a furnace and an analytical balance. For each experiment, 10 mg of sample was analyzed under 25 ml/min of air flow by increasing the temperature from 50 to 700 ºC with a heating ramp of 10 ºC/min. The amount of weight loss was then recorded and analyzed to find the required temperature to burn out the templates and assess the template content of the prepared samples. The derivation of weight loss was also calculated and analyzed to analyze the peaks related to weight loss during the TGA.

2.3.6. Fourier Transform Infrared Spectroscopy

Vibrational spectroscopy is a technique that analyses the interaction between electromagnetic radiation and nuclear vibrations to inspects the molecular structure. By irradiating a molecule with a range of infrared electromagnetic waves, the wave that its frequency matches the vibrational frequency of the molecule is adsorbed. By adsorbing the infrared electromagnetic wave, an electron of molecule is excited and then releases the energy through recombination, causing the scattering of light. Analyzing the adsorbed and scattered light by a molecule helps in examination of the structure of molecule. This technique can be used to analyze the molecular structure of gas, liquid, and solid samples.

In this work, Fourier transform infrared spectroscopy (FTIR) was performed to analyze the available functional groups on the surface of the prepared carbon sphere. In addition, the quality of CNT functionalization was assessed by comparing the functional groups available on the surface of pristine and functionalized CNT. The FTIR spectrum of carbon sphere sample was taken by a FTS-45 infrared spectrophotometer. To do so, first a mixture of 0.1 wt% sample with KBr was prepared and then was ground to form a homogenous mixture. The mixture was then used to make an almost clear pellet. The obtained pellet was used to measure the FTIR spectrum of the sample by the infrared spectrophotometer. The FTIR spectrum of the pristine and functionalized CNT samples was measured using a Thermo Nicolet Magna-850 spectrometer that was equipped with a Golden Gate® ATR accessory.

2.4. Photocatalytic experiments

2.4.1. Photocatalytic slurry experiments

2.4.1.1. Sample preparation

To prepare the sample for photocatalytic slurry experiments, 10 ml gas-tight reaction cells that were equipped with open-top screw caps and septa were employed. The total amount of 5 ml (for hydrogen production) or 10 ml (for cyclohexanone production) of liquid was added into the reaction cells. For hydrogen production experiments, a defined solution of glycerol or ethanol were prepared in distilled water and used as the hydrogen source. Pure cyclohexanol was used for cyclohexanone production. The required amount of photocatalyst was added into another vial containing distilled water and sonicated in ice bath by a Hielscher UP400S Ultrasonic Processor for 5 min to separate the agglomerated photocatalyst particles. Pt/TiO_2 (P25), TiO_2 (prepared by hydrothermal, aqueous phase sol−gel, or alcoholic phase sol−gel methods), TiO_2/CS (prepared by hydrothermal or alcoholic phase sol−gel methods), or TiO_2/CNT (prepared by hydrothermal, aqueous phase sol−gel, or alcoholic phase sol−gel methods) were utilized for the hydrogen production tests and TiO_2 (Hombikat) was used for the cyclohexanone production experiments. For the hydrogen production experiments conducted based on in-situ photodeposition of platinum, a required amount of hexachloroplatinic acid solution in distilled water was introduced into the vials by a micropipette. For the hydrogen production experiments at acidic or basic pH, the pH of solution was adjusted by adding required amount of 0.1 M NaOH or HCl solutions using a

micropipette. A Mettler Toledo SevenEasy pH Meter as well as VWR Chemicals pH Test Strips were used to measure pH. The volume of suspensions was then adjusted at 5 ml by adding required amount of deionized water. The suspensions were then purged with a nitrogen flow to remove the dissolved oxygen. For the cyclohexanone production experiments, the suspensions were purged with an oxygen flow to saturate. For all the experiments, the suspension was mixed for at least 15 min in the dark to ensure the adsorption of substrates on the surface of the catalyst, before starting the illumination.

2.4.1.2. Photocatalytic reaction

To start photocatalytic reactions, the reaction cells were exposed under radiation in a photoreactor. The photoreactor was made of an isolated box to protect the environment from UV radiation. The box was made of aluminum to reflect the UV radiation and not only increase the intensity of light towards the reaction cells, but also provide a uniform irradiation intensity in the box. Required number of 20 W Black-Ray® mercury tubes (365 nm) were employed to provide the UV radiation. The spectral chart of the employed mercury tubes is presented in Figure 2.11. The box was equipped with a cooling fan to transfer ambient air into the box and keep its temperature constant and around the environment. A Thermo-ScientificTM CimarecTM 15 position magnetic stirrer was used to provide a constant 500 rpm mixing during the experiments. The intensity of light was assured to be similar in different positions of the magnetic stirrer. A picture of gas-tight reaction cells on the multi-position magnetic stirrer and under UV radiation inside the aluminum box is illustrated in Figure 2.12. At the end of hydrogen production experiments, 500 or 250 µL of the gas phase product was sampled using a gas tight syringe or GC standard sampling tube and then analyzed. For cyclohexanone production experiments, 1 ml of the product was sampled by a syringe and filtered through a 0.45 µm Sarstedt syringe filtration unit to separate the photocatalyst. The solution was then introduced into a 1.5-ml vial and analyzed by HPLC to measure the amount of generated cyclohexanone. The photocatalytic experiments were repeated to ensure the accuracy of the results and an average was reported. Some experiments were performed in the absence of light or photocatalyst to ensure the photocatalytic nature of the reaction. The schematic of photocatalytic slurry experiments procedure is shown in Figure 2.13.

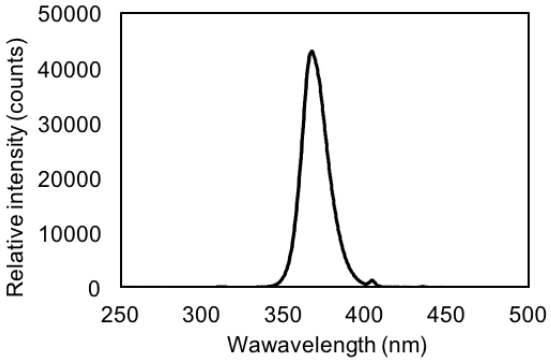

Figure 2.11. The spectral chart of the employed mercury tubes.

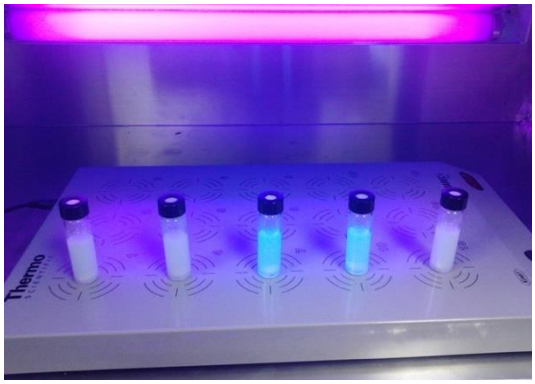

Figure 2.12. A picture of gas-tight reaction cells on the multi-position magnetic stirrer and under UV radiation inside aluminum box.

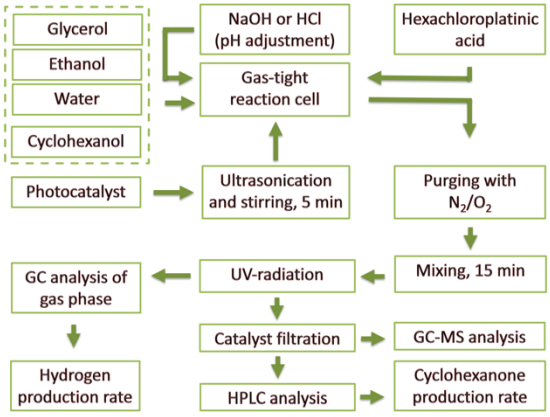

Figure 2.13. The schematic of photocatalytic slurry experiments procedure.

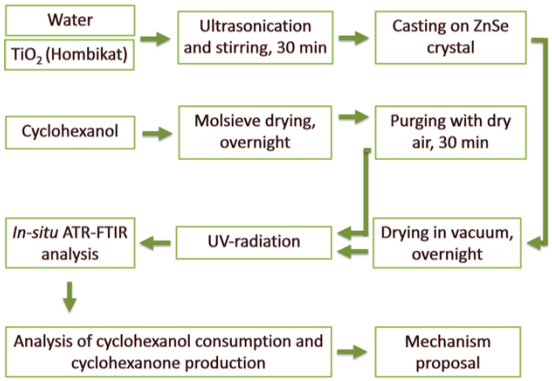

Figure 2.14. The schematic of photocatalytic film experiments procedure.

2.4.2. Photocatalytic film experiments and *in-situ* analysis

2.4.2.1. Sample preparation

In order to perform an *in-situ* ATR-FTIR analysis of photocatalytic experiments, the reaction should be performed on a film of photocatalyst. The schematic of photocatalytic film experiments procedure is presented in Figure 2.14. Hombikat TiO_2 photocatalyst was deposited on a ZnSe ATR crystal for this purpose. Deposition of other photocatalysts such as P25 or Sigma-Aldrich anatase TiO_2 was not successful as formed a nonuniform film. A 3 gL^{-1} of hombikat photocatalyst suspension in water was prepared and then ultrasonicated using a 35 kHz Elmasonic ultrasonic bath for 30 min to separate the agglomerated TiO_2

particles. Afterwards, 1.5 ml of the sonicated suspension was taken by a syringe and poured on the crystal and dried in dark at ambient temperature overnight inside a vacuumed desiccator. A picture of TiO_2 casted ZnSe ATR crystal is presented in Figure 2.15. To prepare cyclohexanol for the experiments (i) traces of water was removed by exposing it into a Molsieve (type 4A) overnight, and (ii) it was then oxygen saturated by purging with 10 ml/min flow of dry air for 30 min.

2.4.2.2. Photocatalytic reaction

The photocatalytic film experiments were performed to monitor the deformation of cyclohexanol and generation of cyclohexanone based on ATR-FTIR spectroscopic analysis. At the beginning of experiment, a spectrum was recorded and saved as background for adsorption. The prepared cyclohexanol was then deposited on the photocatalyst casted film. After saturation of the catalyst, another spectrum was recorded and used as background for photocatalytic experiments. The UV irradiation was then triggered to start the experiments. The employed UV lamp had the light intensity of 9×10^{-9} Enistein.cm^{-2} with a wavelength centered at 375 nm. During the experiments, the reaction was monitored based on *in-situ* ATR−FTIR spectroscopy.

Figure 2.15. A picture of TiO_2 casted ZnSe ATR crystal for *in-situ* ATR−FTIR spectroscopy.

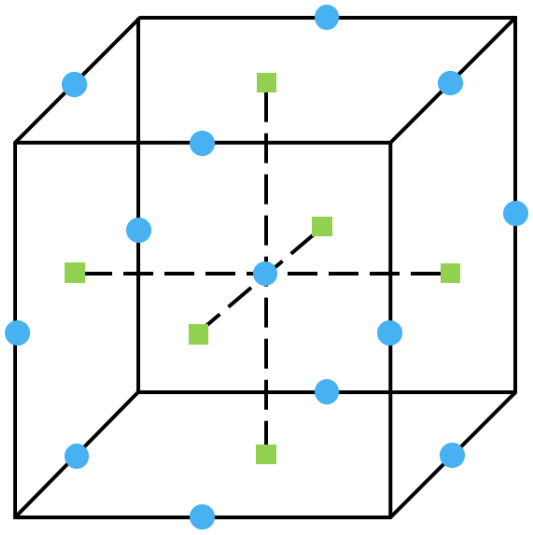

Figure 2.16. A three dimensional representation of Box-Behnken (blue circles) and face-centered (green squares) designs for three factors..

2.5. Product analysis

2.5.1. Gas chromatography

After performing the photocatalytic slurry experiments for hydrogen production, the gas phase product was analyzed using a gas chromatograph (GC). An Agilent Technologies 7820A GC was employed for the analysis. The GC was equipped with an HP-Molesieve column (Agilent) and a TCD detector. Nitrogen used as the carrier gas for the analysis. The retention time of hydrogen was obtained by injection of a pure hydrogen gas to GC. A calibration curve was then developed using the samples with defined hydrogen content in nitrogen. The peak area of these samples was plotted versus the percentage of hydrogen to develop a calibration curve. After analysis of the products, the obtained surface area of the corresponding peaks to hydrogen was then analyzed using the obtained calibration curve to find the percentage of hydrogen in the product.

2.5.2. High-pressure liquid chromatography

After conducting photocatalytic the slurry experiments of cyclohexanone production, the liquid product was analyzed by high-pressure liquid chromatography (HPLC) to find the amount of cyclohexanone in the product. A LC-30AD Shimadzu device was employed for these analyses. The HPLC device was equipped with DGU-20A5 degasser, SIL-20A XR autosampler, and RID-10A detector. An Ultra C18 3μm column (150×4.5 mm) and a solution containing 50% acetonitrile in water were used as stationary and mobile phases, respectively. The rate of mobile phase fixed to 0.3 ml/min and 1 μl of liquid sample was injected for each analysis. LabSolutions software was employed to calculate the surface area behind the cyclohexanone peak and then calculate the cyclohexanone percentage by a calibration curve. The retention time of cyclohexanone was obtained by injection of a standard cyclohexanone sample. The calibration curve was developed by injection of cyclohexanone solutions in cyclohexanol and then plotting the surface area of the corresponding peak versus cyclohexanone percentage.

2.5.3. In-situ ATR-FTIR

In-situ ATR−FTIR spectroscopy was employed to analyze the photocatalytic film experiments. A VERTEX 70 Bruker FTIR spectrometer was used to perform the

spectroscopic analysis. At the beginning of photocatalytic film experiments, a spectra was recorded as an average of 64 scans and saved as adsorption background. The prepared cyclohexanol was then poured on the photocatalyst casted film. A spectra was then recorded each minute as an average of 32 scans to follow the adsorption of cyclohexanol on the photocatalyst. After catalyst saturation (constant intensity of cyclohexanol bands) another spectrum was recorded at and used as background for photocatalytic reactions. To monitor the photocatalytic experiments, one spectrum was recorded per minute from 700-4000 cm^{-1} with a resolution of 4 cm^{-1}. The average of 32 scans was recorded as the spectra during the photocatalytic experiments.

2.6. Design of experiments

2.6.1. Box-Behnken design

The experiments were designed based of the design of experiments approach to minimize the number of required tests for training the developed models. Box-Behnken design of experiment was employed to conduct the experiments for validation of the statistical and kinetic models developed to predict the rate of hydrogen production. A three dimensional representation of Box-Behnken design (blue circles) for three factors are depicted in Figure 2.16. The number and type of the independent variables were selected based on the literature review and the results of earlier steps of this work. The experimental ranges were first obtained according to preliminary experiments and then defined in three levels (coded as -1, 0, +1). The experiments designed for four and three independent variables comprises of 29 (including five center points) and 15 (including three center points) sets of experiments, respectively.

2.6.2. Face-centered design

To assess the validity of the developed kinetic mode, other experiments were defined based on face-centered design. A three dimensional representation of face-centered design (green squares) for three factors are illustrated in Figure 2.16. In this regard, 6 sets of experiments were defined in three levels of independent variables (coded as −1, 0, and +1). This design plays a significant role in the statistical design of experiments as its points are located on the center of each cube face (the cube is considered as the space of variation of the three operating

parameters). As the points of the face-centered experimental design have the highest distance from the points of the Box-Behnken design, validation of the model that developed based on the later design, with the former design, can ensure its validity in the entire range.

2.6.3. Full factorial design

A full factorial design can be used for a system with at least two independent variables. In this design, the independent variables take on all possible combinations of the defined levels. As the number of combinations in a full factorial design may be too high to be logistically feasible, usually a factorial fractional design is usually employed. In this work, a full factorial design was used for a system with two independent variables in three levels. Accordingly, nine (3^2) experiments were defined based on this design.

2.7. Model development

2.7.1. Statistical modelling

2.7.1.1. Response Surface Methodology model

The experimental results that obtained based on Box-Behnken design were used to develop a Response Surface Methodology (RSM) model. Accordingly, Eq. (2–2) (a second-order polynomial equation) was employed to model the amount of hydrogen produced from glycerol as a function of four independent variables which coded as A to D.

$$Y = \beta_0 + \beta_1 A + \beta_2 B + \beta_3 C + \beta_4 D + \beta_{12} AB + \beta_{13} AC + \beta_{14} AD + \beta_{23} BC + \beta_{24} BD + \beta_{34} CD + \beta_{11} A^2 + \beta_{22} B^2 + \beta_{33} C^2 + \beta_{44} D^2 \quad (2\text{–}2)$$

where Y represents the amount of produced hydrogen, β_0 is the interception coefficient, β_1, β_2, β_3, and β_4 represent the coefficients of the independent variables, β_{11}, β_{22}, β_{33}, and β_{44} are the quadratic terms, and β_{12}, β_{13}, β_{14}, β_{23}, β_{24}, and β_{34} represent the interaction coefficients [156]. After conducting the experiments, the amounts of produced hydrogen for different experiments (designed based on Box-Behnken) was used in Design-Expert® software (10.0.2.0 Stat-Ease, Inc. Minneapolis, USA) to find the value of model coefficients. The analysis of variance (ANOVA) was also performed by this software.

2.7.1.2. Artificial Neural Network model

Artificial Neural Network (ANN) is a modelling technique that is inspired by biological neural networks. This technique benefits from some simple and non-linear models [194]. In this work, ANN modelling method was employed to predict the amount produced hydrogen as a function of four operating parameters. In this regards, a three-layer feed-forward neural network was first developed and then trained by back-propagation gradient-descendent algorithm. The result of experiments which were conducted based on Box-Behnken experimental design were used for the model training. The experimental data were randomly distributed into three groups containing 23, 3, and 3 points and employed for train, test and validation, respectively. The training data was used to update the model weights and biases via Levenberg–Marquardt algorithm and then the test data was employed to assess the generalization ability of the trained network. To avoid overfitting, the error of validation data was monitored during the training process. A hyperbolic tangent sigmoid function and two linear functions were employed as transfer functions for hidden, input, and output layers, respectively. Four and one neurons were considered for the input and output layers, respectively. Different topologies were tested in order to establish the optimal number of neurons of the hidden layer; it was observed that the number of neurons is between 2 and 10. Each topology was repeated 10 times to prevent random correlation due to random initialization of the weights and biases [209].

2.7.2. Kinetic modelling

After proposal of the reaction mechanism even through literature review (for hydrogen production) or ATR-FTIR analysis (for cyclohexanone production), the individual steps of chemical reactions were obtained. The rate of each individual step was then acquired as a function of the adsorbed concentration of the substrates. On the other hand, the concentration of adsorbed substrates was calculated using the concentration of substrates in the solution. The rate of obtained chemical reactions were employed to develop a kinetic model. A rate equation was finally acquired to predict the rate of chemical generation as a function of different operating parameters such as light intensity and time (for hydrogen and cyclohexanone production) as well as substrate concentration and catalyst loading (for hydrogen production). The value of kinetic parameters was then optimized using GA method.

2.8. Model optimization and analysis

2.8.1. RSM model optimization

After development of the RSM model, it was optimized to find the maximum amount of produced hydrogen as well as the value of operating parameters that are corresponding to the maximized value. Design-Expert® software (10.0.2.0 Stat-Ease, Inc. Minneapolis, USA) was employed for the optimization. In this regard, the range of independent variables were limited to the range of defined experiments and the aim of optimization was defined to maximize the response (the amount of produced hydrogen).

2.8.2. ANN model optimization (GA method)

The developed ANN model is composed of a set of non-linear equations that cannot be optimized by conventional methods. Genetic Algorithm (GA) method was therefore employed to optimize the developed ANN model. GA uses a robust optimization procedure that mimics the natural selection process. The global optimizing capability of GA is more powerful in comparison with other heuristic optimization approaches [210]. Matlab® R2017a software was used to perform GA optimization. In this regard, a primary population containing 50 individuals with uniform distribution was first randomly created. A stochastic universal sampling was utilized as selection function, and the rank function was considered as fitness scaling function. 80% and 15% of individuals of each generation were produced from crossover and mutation of the former generation, respectively, and 5% of the population was selected as elites to guarantee survival of the next generation. Gaussian and scattered functions were employed as the mutation and crossover functions, respectively.

2.8.3. Kinetic parameter estimation (GA method)

After the development of kinetic model, the experimental data that obtained based on the Box-Behnken (for hydrogen production model) or the Full Factorial (for cyclohexanone production model) designs were used to find the value of kinetic parameters. In this regards, GA optimization was employed to estimate the value of kinetic parameters to have the best fitting of model prediction to experimental data. The process of GA optimization was the same as the previous section.

2.8.4. Garson's method analysis

Garson's method was used to obtain the relative importance of the operating parameters on the amount of produced hydrogen (response). In this regard, Eq. (2–3) was employed to find the relative importance using the connection weights of the developed ANN model [211, 212]:

$$I_j = \frac{\sum_{m=1}^{m=N_h}\left(\left(\left|W_{jm}^{ih}\right| \Big/ \sum_{k=1}^{k=N_i}\left|W_{km}^{ih}\right|\right)\times\left|W_{mn}^{ho}\right|\right)}{\sum_{k=1}^{k=N_i}\left\{\sum_{m=1}^{m=N_h}\left(\left(\left|W_{km}^{ih}\right| \Big/ \sum_{k=1}^{k=N_i}\left|W_{km}^{ih}\right|\right)\times\left|W_{mn}^{ho}\right|\right)\right\}} \quad (2–3)$$

where I_j represents the relative importance of the j^{th} input variable on the response, W is the connection weight, and N_i and N_h are the numbers of input and hidden neurons, respectively. The superscripts 'i', 'h' and 'o' refer to input, hidden and output layers, and the subscripts 'k', 'm' and 'n' denote input, hidden and output neurons, respectively.

2.8.5. Statistical analysis

After calculating the amount of product generation, the model predictions were statistically compared with the current experimental data to analyze the accuracy of the model. This statistical comparison was conducted in terms of the coefficient of determination (R^2), adjusted coefficient of determination (R^2_{adj}), root mean squared error (*RMS*), mean absolute error (*MAE*), and absolute average deviation (*AAD*). The following equations were used for these analyses:

$$R^2 = 1 - \sum_{i=1}^{n}\left(\frac{(y_{i,cal} - y_{i,\exp})^2}{(y_{ave,\exp} - y_{i,\exp})^2}\right) \quad (2–4)$$

$$R^2_{adj} = 1 - \left[(1-R^2)\frac{n-1}{n-K-1}\right] \quad (2–5)$$

$$RMS = \sqrt{\frac{\sum_{i=1}^{n}\left(y_{i,cal} - y_{i,\exp}\right)^2}{n}} \tag{2–6}$$

$$MAE = \frac{\sum_{i=1}^{n}\left|y_{i,cal} - y_{i,\exp}\right|}{n} \tag{2–7}$$

$$AAD = \left\{\frac{\sum_{i=1}^{n}\left(\left|y_{i,cal} - y_{i,\exp}\right| / y_{i,cal}\right)}{n}\right\} \times 100 \tag{2–8}$$

where $y_{i,cal}$, $y_{i,exp}$ and $y_{ave,exp}$ refer to the model predictions, the experimental data, and the arithmetic mean of all of the experimental data, respectively. Moreover, n and K are the number of data points and independent variables. The model predictions are well predicted when R^2 is closer to 1, R^2_{adj} is closer to R^2, and *RMS*, *MAE*, and *AAD* are closer to zero.

Based on the literature review, most of the research in this field concentrated on the synthesis of photocatalysts and feasibility of photocatalytic reaction. However, this field suffers from the lack of optimization of operating parameters. On the other hand, it is challenging to develop a consensus on the optimum value of operating parameters because of considerable differences and contradictions. These conflicts may be due to the use of an OVAT approach that neglects the influence of interaction effects. By applying powerful RSM and ANN models, the interaction effect of operating parameters can be analyzed.

This chapter concerns the development of ***RSM and ANN models*** to evaluate *individual and* interaction effects *of operating parameters for photocatalytic* ***hydrogen*** *production from* ***glycerol****. The ANN model was then used for process optimization using GA method and find the optimum value of operating parameters, as well as the rate of hydrogen production.*

Chapter 3 : Photocatalytic valorization of glycerol to hydrogen: Optimization of operating parameters by artificial neural network

Résumé

Le glycérol est un résidu important de la production de biodiesel à partir de la biomasse. La valorisation photocatalytique du glycérol en hydrogène est une approche intéressante du point de vue du développement durable. Cette étude examine les effets individuels et les effets d'interaction des principaux paramètres opératoires du processus de production d'hydrogène photocatalytique, à partir du glycérol à l'aide d'un photocatalyseur Pt/TiO_2. Quatre paramètres opératoires (pourcentage de glycérol, catalyseur, et Pt (co-catalyseur), ainsi que pH) ont été sélectionnés comme variables indépendantes et la quantité d'hydrogène produite a été considérée comme la variable dépendante (réponse). Les expériences ont été menées sur le modèle Box-Behnken. Des modèles de « Réseau de neurones artificiels » (*Artificial Neural Network*) ainsi qu'une « Méthode des surfaces de réponses » (*Response Surface Methodology*) ont été développés sur la base d'une approche de conception expérimentale visant à prédire la production d'hydrogène. La capacité prédictive des deux modèles a été comparée sur la base de R^2, R^2_{adj}, RMS, MAE et AAD. Le modèle de Réseau de neurones artificiels, s'avérant plus précis et fiable, a donc été utilisé pour l'optimisation de la production d'hydrogène et l'investigation paramétrique. L'analyse des résultats a montré que les paramètres opératoires peuvent également influer sur la valeur optimale de chacun. L'augmentation du pourcentage de glycérol déplace les valeurs optimales de pourcentage de catalyseur, de pourcentage de Pt et de pH vers des valeurs plus élevées; cependant, le pourcentage de Pt a un effet négligeable sur les valeurs optimales des autres paramètres. De plus, le pourcentage de catalyseur et le pH n'ont pas d'effet sur la valeur optimale du pourcentage de glycérol, mais l'augmentation de chacun de ces deux paramètres réduit les valeurs optimales du pourcentage de glycérol et du Pt. L'algorithme génétique ainsi que le modèle du réseau de neurones artificiels ont également été utilisés pour l'optimisation et il a été constaté que l'optimum global du système était de 50% de glycérol (v/v), une masse

de catalyseur de 3,9 g/L, 3,1% de Pt et un pH de 4,5. Enfin, la méthode de Garson a été utilisée pour obtenir l'importance relative de chaque variable dans le système. Cette analyse a révélé que la variation du pourcentage de glycérol avait peu d'effet sur la quantité d'hydrogène produite contrairement au pourcentage de catalyseur dont l'impact est le plus important.

Abstract

Glycerol is a considerable byproduct of biodiesel production from biomass. Photocatalytic glycerol valorization to hydrogen is an attractive approach from the sustainable development point of view. This study investigates the individual and interaction effects of main operating parameters of the photocatalytic hydrogen production process from glycerol using Pt/TiO_2 photocatalyst. Four key operating parameters (i.e. glycerol%, catalyst loading, Pt% and pH) were selected as independent variables, and the amount of produced hydrogen was considered as the dependent variable (response). Experiments were conducted based on the Box-Behnken design. Response surface methodology (RSM) and Artificial Neural Network (ANN) models were developed based on the experimental design approach to predict hydrogen production. The predictive capacity of the two models was compared based on R^2, R^2_{adj}, *RMS*, *MAE* and *AAD*. The ANN model was found more accurate and reliable, and it was therefore employed for the optimization of H_2 production and parametric investigation. Analysis of the results showed that the operating parameters can also influence each other's optimum value. Increasing glycerol% shifts the optimum values of catalyst loading, Pt%, and pH to higher values; however, Pt% has a negligible effect on the optimum values of the other parameters. Moreover, the catalyst loading and pH have no effect on the optimum value of glycerol%, but the increase of each of these two parameters reduces the optimum value of glycerol% and Pt%. The Genetic Algorithm along with the ANN model were also utilized for the optimization and it was found that the overall optimum of the system was 50% glycerol (v/v), 3.9 g/L catalyst loading, 3.1% Pt, and pH 4.5. Finally, Garson's method was employed to obtain the relative importance of each variable in the system. This analysis revealed that the variation of glycerol% and catalyst loading had, respectively, the least and the most effect on the amount of produced hydrogen.

3.1. Introduction

In recent years, global energy crises have led to the development of renewable energies like biodiesel and hydrogen [213]. Due to abundance of water on earth, water splitting using solar light driven photocatalysts is a promising alternative for future energy production. Despite vast research in this area, still more studies are required to increase the efficiency of the photocatalysis process. One the other hand, the price of glycerol, one of the biodiesel byproducts, has decreased significantly due to overproduction [18]. Valorization of sustainable glycerol to green fuels is therefore another promising alternative for future energy production. In addition, investigation of glycerol photo-reforming can assist with clarifying the mechanisms of photocatalysis. This knowledge is also beneficial to increase insight into water photo-splitting as well as glycerol photo-conversion to valuable liquid products.

TiO_2 is the most common photocatalyst which benefits from advantages like very high photocatalyst activity, low cost, suitable chemical and thermal stability, and low toxicity [164, 171]. These advantages make TiO_2 a promising photocatalyst; however, more research is required to achieve an economically viable hydrogen production process on an industrial scale. One of the most efficient techniques to increase the photocatalytic activity of TiO_2 is incorporating metals or metal oxides as co-catalysts [173]. The presence of co-catalysts could provide hydrogen reaction sites, favor the charge separation reaction, trap photo-generated electrons and extend light absorption toward the visible range [214].

Among the metals used as co-catalysts in the photocatalytic glycerol conversion to hydrogen, like Pt [33, 74, 76, 78, 80, 82-84, 86, 89-91, 93, 95, 165], Cu [90, 91, 96, 97, 99-101, 104, 105, 115, 116, 126], Au [86, 89, 107, 108, 110, 165], Pd [41, 86, 89, 165], Ni [32, 105, 113, 165], Co [112, 165], Ag [111, 165], Mn [165], Cr [165], and W [165], Pt is the one most commonly used. Fu *et al.* [215] found that Pt decorated photocatalysts exhibited the highest hydrogen production rate and the photocatalytic activity decreased in the order of Pt>Au>Pd>Rh>Ag>Ru. In another work, Pt was found to be the most active co-catalyst for hydrogen production by investigating the vast range of Pt, Pd, Ir, Au, Ru, Rh, and Ni [216]. Recently, López- Tenllado *et al.* [86] reported the order of Pt>Pd>Au for propan-2-ol and Pt≈Au>Pd for glycerol photocatalytic valorization to hydrogen.

Although there is much research on the synthesis of photocatalyst and feasibility of hydrogen production from glycerol, this field suffers from the lack of optimization of operating parameters. On the other hand, it is very challenging to develop a consensus on the optimum value of operating parameters due to significant differences and contradictions in previous work [15]. These conflicts may be attributed to the application of a 'one-variable-at-a-time' approach and to a disregard for the interaction effect of the parameters [152].

To assess the interaction effect of various operating parameters, a comprehensive model is required. Response Surface Methodology (RSM) and Artificial Neural Networks (ANN) are two useful modeling methods that can be applied for complex processes like photocatalytic hydrogen production because they do not require knowledge about the fundamentals of the photocatalytic process [193]. RSM is a statistical method to design experiments, develop a model, investigate effects of parameters, assess the interaction effect of the parameters, and optimize the desired responses [70, 151]. ANN was inspired by biological neural networks taking advantage of some simple and non-linear models [194]. The Genetic Algorithm (GA) can be further employed to optimize the output of ANN models. GA utilizes a robust optimization procedure that mimics the process of natural selection, and its global optimizing capability is more powerful in comparison with other heuristic optimization methods [210].

To the best of our knowledge, a single statistical analysis on glycerol conversion to hydrogen has been reported to date. Bastos *et al.* [130] examined the glycerol valorization to hydrogen using a simple factorial design statistical model. The critical point which was obtained corresponded to a minimum, *i.e.*, no optimization could be performed using this model. On the other hand, there is no publication in this field using other powerful methods such as RSM or ANN. Moreover, no statistical analysis study was found on the optimization of glycerol valorization to hydrogen using a TiO_2 based photocatalyst (as the most common photocatalyst).

Herein, we investigated individual and interaction effects of four key operating parameters (including catalyst loading, Pt%, glycerol%, and pH) on the photocatalytic glycerol valorization to hydrogen rate using Pt/TiO_2. Two approaches of RSM and ANN were employed to model the process, and their predictive ability for photocatalytic hydrogen production reactions was compared. Moreover, GA was applied to optimize the response of

the ANN model. Finally, the level of influence of each operating parameter on the amount of produced hydrogen was calculated.

3.2. Materials and methods

3.2.1. Materials

The commercial TiO_2 Aeroxide P25 (≥99.5%) photocatalyst was provided by Evonik Industries. Hexachloroplatinic acid (IV) ($H_2PtCl_6 \cdot 6H_2O$, ≥37.50% Pt) was obtained from Sigma–Aldrich to be used as the platinum precursor. Glycerol (≥99.5%) and ethyl alcohol (99.99%) were supplied by Caledon and Commercial Alcohols, respectively. pH adjustment was made using NaOH (≥97%) and HCl (36.5-38.0%) which were purchased from VWR. Milli-Q water was utilized in the synthesis of photocatalysts.

3.2.2. Preparation of Pt/TiO_2 photocatalyst

Platinum deposition on TiO_2 was performed based on the photo-deposition method [83]. Briefly, a suspension of 1 g TiO_2 and 120 ml ethyl alcohol solution (10%) was sonicated for 30 min using a Hielscher UP400S Ultrasonic Processor. Hexachloroplatinic acid solution in water was then added to the suspension in order to obtain Pt loadings of 0.02, 2.51, and 5 wt%. The mixture was purged with nitrogen for 15 min to remove the oxygen present in the mixture. A photoreactor equipped with four 20 W Black-Ray® mercury tubes (365 nm) was used to perform the photocatalytic experiments. The irradiation was maintained for 3 hours under continuous nitrogen flow and constant 500 rpm magnetic stirring in all experiments. Finally, the Pt/TiO_2 material was filtered, washed and dried overnight at 110 °C.

3.2.3. Photocatalyst characterization

Powder X-ray diffraction (XRD) patterns of the prepared samples were obtained using a Bruker SMART APEXII X-ray diffractometer equipped with Cu Kα radiation source (λ = 1.5418 Å). The patterns were measured from 2θ= 10–80° at a step of 0.02° and a scan rate of 1.2 min^{-1}. The Anatase:Rutile ratio of the samples was calculated using Eq. (3–1) [217]:

$$\%Rutile = \frac{1}{\left[1 + 0.8(I_A / I_B)\right]} \times 100 \quad (3\text{–}1)$$

where I_A and I_B are, respectively, the intensities of anatase (101) and rutile (110) reflections. TEM images were collected using a JOEL JEM 1230 operated an accelerating voltage of 120 kV. To prepare the samples for the analysis, they were dispersed in water and sonicated using a Hielscher UP400S Ultrasonic Processor and then placed on carbon coated copper TEM grids.

3.2.4. Hydrogen production experiments

The photocatalytic hydrogen production experiments were carried out in gas-tight Pyrex reaction cells using the prepared photocatalysts. In each experiment, predetermined amounts of glycerol, water, and photocatalyst (Table 3.2) were introduced into the cells. After sonication of the suspensions for 5 min to ensure proper dispersion of photocatalysts, the pH was adjusted using NaOH and HCl solutions. The volume of suspensions was ensured to be kept at 5 ml. Before irradiation, the reaction cells were purged with nitrogen (20 ml/min) for 15 min to remove oxygen and stirred in the dark for 20 min to allow the adsorption of glycerol on the catalyst surface. The cells were then irradiated with a light intensity of 1600 μW/cm^2 in a photoreactor equipped with four 20 W Black-Ray® mercury tubes. The spectral chart of the mercury tubes is illustrated in Figure 3.1. During the experiments, the mixtures were maintained at constant 500 rpm magnetic stirring using Thermo-Scientific™ Cimarec™ 15-Position magnetic stirrer. The temperature of the reactor was maintained around ambient (25°C) using a cooling fan. The photocatalytic reactions were assessed after illumination of the samples for 4 h. To measure the amount of produced hydrogen in the photocatalytic reactions, 0.5 ml of gas headspace was sampled from the cells using a gas tight syringe with valve and injected to a Hewlett Packard HP 5890 gas chromatograph (GC) equipped with TCD detector, carboxen-1010 capillary column, and nitrogen carrier gas. Three replicate runs were performed to ensure the accuracy of the results. To ensure that no hydrogen was produced in the absence of illumination, a sample was also analyzed without the use of UV irradiation.

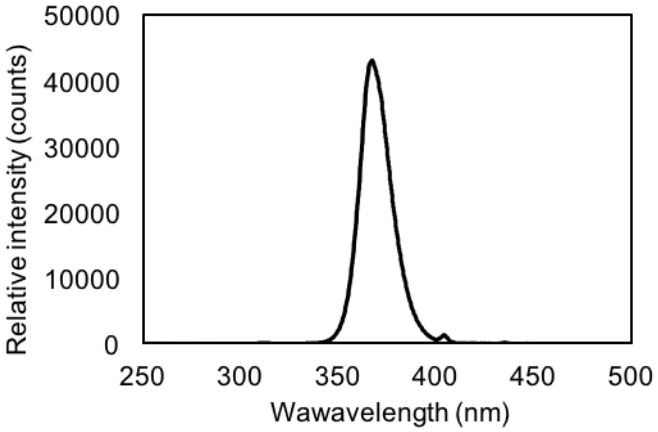

Figure 3.1. The spectral chart of the employed mercury tubes.

Table 3.1. Experimental ranges and levels of variables for hydrogen production experiments.

Variables	-1	0	+1
Glycerol% (A, v/v)	0.5	25.25	50
Catalyst loading (B, g/L)	0.05	2.525	5
Pt% (C, wt%)	0.02	2.51	5
Initial pH of solution (D)	2	7	12

Table 3.2. The box-behnken design of experiment along with actual and predicted values of the produced hydrogen.

Run #	Independent variables				Produced hydrogen[1]								
					Experimental			ANN			RSM		
	Glycerol % (v/v)	Catalyst loading (g/l)	Pt% (wt%)	pH	Yield	µmol g^{-1} hr^{-1}	µmol	Yield	µmol g^{-1} hr^{-1}	µmol	Yield	µmol g^{-1} hr^{-1}	µmol
1	0.50	2.525	2.51	2	0.4211	2851	144	0.4385	2970	150	0.4327	2931	148
2	0.50	2.525	0.02	7	0.3625	2455	124	0.3654	2475	125	0.3567	2416	122
3	0.50	0.050	2.51	7	0.0819	28000	28	0.0409	14000	14	0.0906	31000	31
4	0.50	5.000	2.51	7	0.6169	2110	211	0.6139	2100	210	0.5584	1910	191
5	0.50	2.525	5.00	7	0.5321	3604	182	0.5496	3723	188	0.4707	3188	161
6	0.50	2.525	2.51	12	0.1666	1129	57	0.1841	1248	63	0.2719	1842	93
7	25.25	2.525	0.02	2	0.0060	2040	103	0.0059	2040	103	0.0066	2257	114
8	25.25	0.050	2.51	2	0.0014	25000	25	0.0012	22000	22	0.0015	26000	26
9	25.25	5.000	2.51	2	0.0156	2690	269	0.0151	2610	261	0.0155	2670	267
10	25.25	2.525	5.00	2	0.0133	4554	230	0.0134	4594	232	0.0138	4733	239
11	25.25	0.050	0.02	7	0.0016	28000	28	0.0017	30000	30	0.0005	10000	10
12	25.25	5.000	0.02	7	0.0084	1450	145	0.0085	1480	148	0.0088	1530	153
13	25.25	2.525	2.51	7	0.0148	5050	255	0.0145	4970	251	0.0143	4891	247
14	25.25	2.525	2.51	7	0.0143	4891	247	0.0145	4970	251	0.0143	4891	247
15	25.25	2.525	2.51	7	0.0146	5010	253	0.0145	4970	251	0.0143	4891	247
16	25.25	2.525	2.51	7	0.0137	4693	237	0.0145	4970	251	0.0143	4891	247
17	25.25	2.525	2.51	7	0.0141	4812	243	0.0145	4970	251	0.0143	4891	247
18	25.25	0.050	5.00	7	0.0032	56000	56	0.0034	60000	60	0.0034	60000	60
19	25.25	5.000	5.00	7	0.0141	2430	243	0.0143	2480	248	0.0158	2730	273
20	25.25	2.525	0.02	12	0.0043	1485	75	0.0034	1188	60	0.0039	1347	68
21	25.25	0.050	2.51	12	0.0008	14000	14	0.0009	17000	17	0.0001	2000	2
22	25.25	5.000	2.51	12	0.0076	1320	132	0.0076	1320	132	0.0068	1170	117
23	25.25	2.525	5.00	12	0.0071	2416	122	0.0067	2317	117	0.0064	2218	112

24	50.00	2.525	2.51	2	0.0075	5050	255	0.0074	5030	254	0.0068	4594	232
25	50.00	2.525	0.02	7	0.0035	2396	121	0.0033	2297	116	0.0037	2535	128
26	50.00	0.050	2.51	7	0.0013	44000	44	0.0019	67000	67	0.0019	65000	65
27	50.00	5.000	2.51	7	0.0077	2630	263	0.0077	2640	264	0.0076	2610	261
28	50.00	2.525	5.00	7	0.0081	5386	272	0.0077	5228	264	0.0076	5149	260
29	50.00	2.525	2.51	12	0.0031	2079	105	0.0025	1723	87	0.0033	2257	114

[1]amount of hydrogen in 3.5 mL of gas headspace after 4 hours.

3.2.5. Design and analysis of experiments

3.2.5.1 Box-Behnken experimental design

The Box-Behnken experimental design was employed for the design of the experiment to evaluate the effect of four operating parameters, i.e., glycerol% (v/v%), catalyst loading (g/L), Pt% (wt%) and pH, which are respectively labeled A to D. These selected parameters were considered as the independent variables and the amount of produced hydrogen (μmol) after 4 h of irradiation was selected as the dependent variable (response). The experimental ranges were obtained based on preliminary experiments, as presented in Table 3.1. Accordingly, 29 sets of tests (including five center points) were defined for these four independent variables in three levels (coded as -1, 0, +1), as shown in Table 3.2. These data sets were then used to develop the RSM and ANN models.

3.2.5.2. RSM model

For RSM, a second-order polynomial equation (Eq. 3–2)) was obtained to model the amount of produced hydrogen as a function of the four independent variables mentioned above (A to D).

$$Y = \beta_0 + \beta_1 A + \beta_2 B + \beta_3 C + \beta_4 D + \beta_{12} AB + \beta_{13} AC + \beta_{14} AD + \beta_{23} BC + \beta_{24} BD + \beta_{34} CD + \beta_{11} A^2 + \beta_{22} B^2 + \beta_{33} C^2 + \beta_{44} D^2 \quad (3\text{–}2)$$

where Y is the amount of produced hydrogen (response), β_0 represents the interception coefficient, β_1, β_2, β_3, and β_4 are the coefficients of the independent variables, β_{11}, β_{22}, β_{33}, and β_{44} are the quadratic terms, and β_{12}, β_{13}, β_{14}, β_{23}, β_{24}, and β_{34} are the interaction coefficients [156]. Moreover, the analysis of variance (ANOVA) and optimization of produced hydrogen in the reaction were performed by Design-Expert® software (10.0.2.0 Stat-Ease, Inc. Minneapolis, USA).

3.2.5.3. ANN model

For ANN, a three-layer feed-forward neural network was developed and trained by back-propagation gradient-descendent algorithm. The obtained experimental data were randomly classified into three sets containing 23, 3, and 3 data to be employed for train, test and validation, respectively. Training data sets were used for updating weights and biases via Levenberg–Marquardt algorithm and the test data were utilized to evaluate the generalization ability of the trained network. Moreover, the error of validation data was supervised during training to avoid overfitting [218]. A hyperbolic tangent sigmoid function and two linear functions were used as

transfer functions for the neurons in the hidden layer and the neurons in the input and output layers, respectively. The input and output layers had 4 and 1 neurons, respectively. To determine the optimal number of neurons in the hidden layer, different topologies were examined during which the number of neurons varied between 2 and 10. Each topology was repeated 10 times to prevent random correlation because of random initialization of the weights and biases [209].

To evaluate the performance of the networks, the coefficient of determination (R^2), adjusted coefficient of determination (R^2_{adj}), root mean squared error (*RMS*), mean absolute error (*MAE*) and absolute average deviation (*AAD*) were calculated based on Eqs. (3–3)-(3–7). These parameters were also utilized to compare RSM and ANN models.

$$R^2 = 1 - \sum_{i=1}^{n} \left(\frac{(y_{i,cal} - y_{i,\exp})^2}{(y_{ave,\exp} - y_{i,\exp})^2} \right) \tag{3–3}$$

$$R^2_{adj} = 1 - \left[(1 - R^2) \frac{n-1}{n-K-1} \right] \tag{3–4}$$

$$RMS = \sqrt{\frac{\sum_{i=1}^{n} \left(X_{i,cal} - X_{i,\exp} \right)^2}{n}} \tag{3–5}$$

$$MAE = \frac{\sum_{i=1}^{n} \left| X_{i,cal} - X_{i,\exp} \right|}{n} \tag{3–6}$$

$$AAD = \left\{ \frac{\sum_{i=1}^{n} \left(\left| X_{i,cal} - X_{i,\exp} \right| / X_{i,cal} \right)}{n} \right\} \times 100 \tag{3–7}$$

where n represents the number of data points, K is the number of input variables, $X_{i,cal}$, $X_{\mathrm{i,exp}}$, and $X_{\mathrm{ave,exp}}$ are the response of predicted, experimental and arithmetic mean of all experimental data, respectively.

3.2.5.4. Genetic Algorithm

GA optimization procedure was employed to optimize the ANN model. A primary population of 50 individuals with uniform distribution was randomly created to initialize the optimization procedure. A stochastic universal sampling was used as selection function, and the rank function was employed as fitness scaling function. In each generation, 80% and 15% of individuals were produced from crossover and mutation of the previous generation, respectively, and 5% of the population was chosen as elites and was guaranteed to survive to the next generation. Gaussian and scattered functions were used as the mutation and crossover functions respectively.

3.2.5.5. Garson's method

Garson's method was employed to obtain the level of influence of variables on the response. This method is based on Eq. (3–8) which uses the connection weights of the neural network [211, 212]:

$$I_j = \frac{\sum_{m=1}^{m=N_h}\left(\left(\left|W_{jm}^{ih}\right| \Big/ \sum_{k=1}^{k=N_i}\left|W_{km}^{ih}\right|\right)\times\left|W_{mn}^{ho}\right|\right)}{\sum_{k=1}^{k=N_i}\left\{\sum_{m=1}^{m=N_h}\left(\left(\left|W_{km}^{ih}\right| \Big/ \sum_{k=1}^{k=N_i}\left|W_{km}^{ih}\right|\right)\times\left|W_{mn}^{ho}\right|\right)\right\}} \quad (3–8)$$

where I_j refers to the relative importance of the j^{th} input variable on the response, W represents the connection weights, and N_i and N_h refer to the numbers of input and hidden neurons, respectively. The superscripts 'i', 'h' and 'o' denote input, hidden and output layers, and the subscripts 'k', 'm' and 'n' are related to input, hidden and output neurons, respectively.

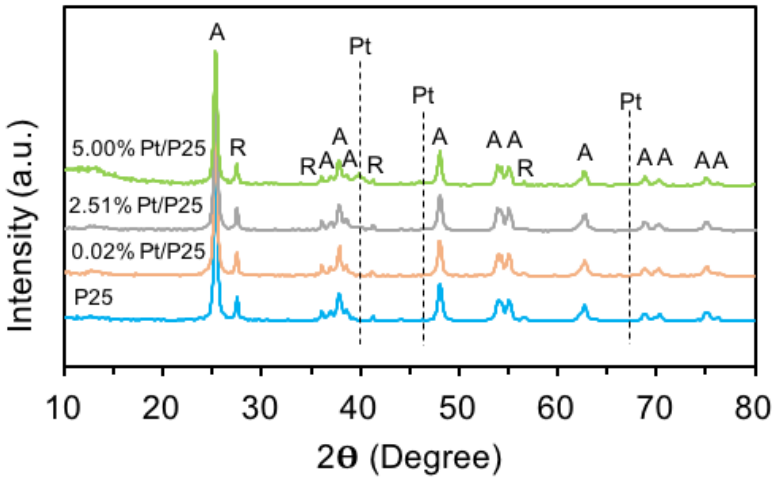

Figure 3.2 XRD patterns of the photocatalyst samples with different platinum loadings.

3.3. Results and discussion

3.3.1. Characterization of the prepared samples

XRD patterns of the prepared samples with different platinum loadings are presented in Figure 3.2. It demonstrates that in all TiO_2 samples, the peaks related to Anatase and Rutile phases of TiO_2 remained intact after platinum deposition. Pt (111) reflection at $2\theta=39.84^{o}$, which is characteristic of the face-centered cubic (fcc) structure of platinum [219], obviously grew at 5% of Pt. Regarding the Pt (200) and Pt (220) reflections at $2\theta=46.32^{o}$ and 67.54^{o}, only a slight shoulder can be observed for the sample loaded with 5% Pt [220]. Table 3.3 presents some characteristics for the prepared samples. The Scherrer equation [208] was employed to estimate the average Anatase (101) and Rutile (110) particle sizes which were found to be ca. 20 and 30 nm for all particles, respectively. The Anatase:Rutile ratio in TiO_2 was calculated based on the peak heights of Anatase (101) and Rutile (110) reflections [217], and was 1:6 for all of prepared samples. Similar particle sizes and phase ratios of TiO_2 particles confirm that the Pt photo-deposition process did not affect the size and crystal structure of the TiO_2 samples.

Table 3.3. Characteristics of the prepared photocatalyst samples.

Photocatalyst	Anatase crystal size (nm)	Rutile crystal size (nm)	Rutile fraction (wt%)
P25	20	31	16
2.51% Pt/P25	19	30	17
5% Pt/P25	20	33	18
0.02% Pt/P25	20	28	16

The morphology of the prepared sample was studied, and the deposition of platinum particles on TiO_2 was checked by TEM. Figure 3.3 clearly displays deposited Pt particles on TiO_2 as black dots for the 5.00% Pt/P25 sample. Based on this figure, the average size of the particles was around 25 nm, and the mean metal nanoparticle size was around 2 nm, which is in the range of previous studies [33, 84, 89].

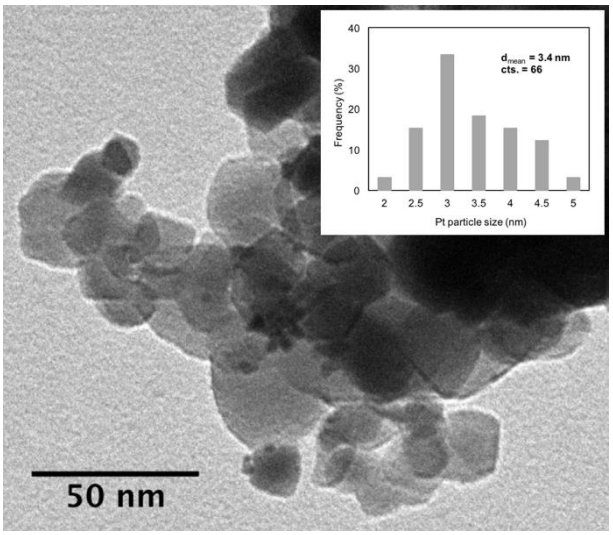

Figure 3.3. TEM images of 5.00% Pt/P25 photocatalyst sample.

3.3.2. Experimental hydrogen production results

29 sets of experiments were performed based on Box-Behnken design to study the effect of the four operating parameters mentioned above on the amount of produced hydrogen. For this purpose, the range of glycerol% (v/v%), catalyst loading (g/L), Pt% (wt%) and pH were 0.5-50%, 0.05-5 g/L, 0.02-5%, and 2-12. The experimental design and obtained results are summerized in Table 3.2. These experimental data were utilized to implement the RSM and ANN models.

The yield of produced hydrogen after 4 hours of experiments was calculated based on Eq. (3–9) and the results are presented in Table 3.2. As can be seen, the yield is greater at lower initial

glycerol concentrations and among the designed experiments, the maximum yield (0.6169) corresponds to catalyst loading = 5 g/L, Pt% = 2.51, glycerol% = 0.5 and pH = 7.

$$Yield = \frac{\mu mol\ produced\ H_2}{\mu mol\ glycerol\ fed} \quad (3–9)$$

3.3.3. Modeling

3.3.3.1. ANN model

Several networks with a different number of neurons in the hidden layer were evaluated to find the best configuration based on the minimum *RMS*. The neural network including a hidden layer with four neurons (architecture of 4-4-1) was found to be the most appropriate network structure to model the photocatalytic process. The predictions of the amount of produced hydrogen by the ANN model are listed in Table 3.2. The representation of predicted values versus experimental data (Figure 3.4) shows a good predictive ability of the current ANN model. As seen in Table 3.4, the R^2 value of 0.9913 for the ANN model is in good agreement with the adjusted R^2_{adj} of 0.9800. The high value of R^2 denotes that the current ANN model is suitable for the prediction of this system. Furthermore, the small values of *RMS* (8.1706), *MAE* (5.9310) and *AAD* (8.1147) demonstrate that the developed ANN model has good approximation and generalization characteristics.

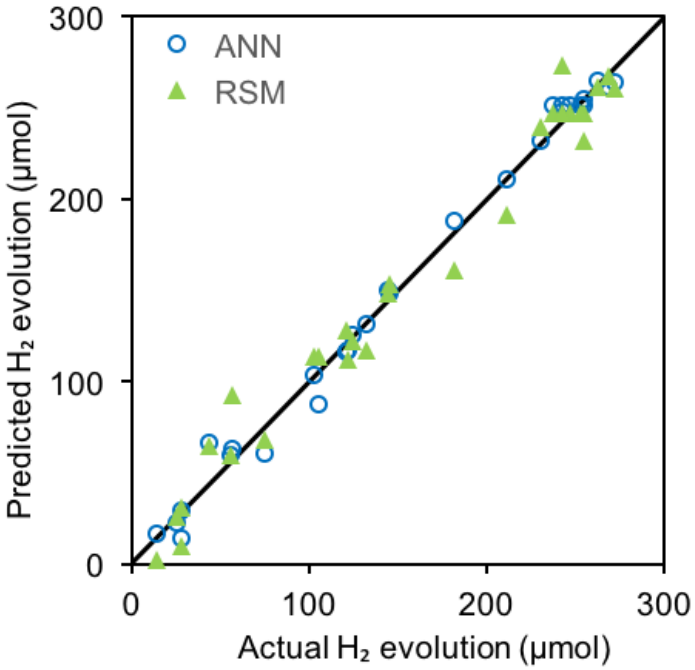

Figure 3.4. The actual amount of produced hydrogen versus the predicted values by ANN and RSM models.

Table 3.4. Comparison of the predictive capacity of ANN and RSM models.

Parameter	RSM	ANN
R^2	0.9748	0.9913
$R^2_{adj.}$	0.9419	0.9800
RMS	13.9692	8.1706
AAD	14.1436	8.1147
MAE	10.8621	5.9310

3.3.3.2. RSM model

An empirical second-order polynomial equation was obtained based on RSM:

$$Y = -190 + 3.34A + 106B + 49.0C + 42.7D + 0.150AB + 0.377AC - 0.126AD + 2.86BC \quad (3\text{–}10)$$
$$- 2.55BD - 1.61CD - 0.0540A^2 - 12.5B^2 - 7.46C^2 - 2.69D^2$$

where *Y* represents the amount of produced hydrogen (µmol) and *A*, *B*, *C*, and *D* are, respectively, glycerol% (v/v%), catalyst loading (g/L), Pt% (wt%), and pH. The predicted values of produced hydrogen based on the current RSM model are presented in Table 3.2. The R^2, adjusted R^2_{adj}, *RMS*, *MAE*, and *AAD* of the developed RSM model which are presented in Table 3.4, show good

approximation and generalization characteristics for this model. To find the combination accuracy of the coefficients, the current model (Eq. (3–10)) was statistically investigated by ANOVA. This analysis showed that the p-value of the model is lower than 0.0001 which confirms that the model is adequate with more than 99% significance level. The predicted values by the developed RSM model are compared with the experimental data in Figure 3.4. As can be seen, although the fitting capability of the RSM model is very good, it is not as suitable as the ANN model.

3.3.3.3. Comparison of ANN and RSM models

The predicted values obtained from the ANN and RSM models and the corresponding accuracies and prediction capabilities of these two models (based on the values of R^2, R^2_{adj}, *RMS*, *AAD*, and *MAE*) are given in Table 3.2 and Table 3.4, respectively. As it can be inferred, R^2 of ANN model is closer to 1 compared to RSM model and R^2_{adj} of ANN model is in closer agreement with the corresponding R^2. Furthermore, the value of *RMS* obtained for ANN is closer to zero compared to the RSM model. Moreover, *AAD* corresponding to ANN is around twice less compared to RSM. Table 3.4 suggests that both models are suitable to predict this photocatalytic system. However, the ANN model is superior for both data fitting and predictive performance. While RSM is limited by a second order polynomial, ANN is a more reliable modeling technique to represent the nonlinearities of this system. Thus, in the forthcoming subsections, the performance of the photocatalytic process is assessed based on the ANN model.

3.3.4. Effects and optimum of operating parameters

The response surface plots of the amount of produced hydrogen as functions of six pairs of the independent variables (*i.e.* glycerol%, catalyst loading, Pt%, and pH) are depicted in Figure 3.5. In all the plots, the values of the two parameters that are not varied in each graph have been fixed at the average of their ranges. Thus, these six surface plots pass through the average point of the system (catalyst loading=2.525 g/L, Pt%=2.51, glycerol%=25 and pH=7), where the amount of produced hydrogen is around 251 μmol. To compare the interaction of operating parameters more easily and their influence on the optimum value of other parameters, the two-dimensional representations of the response surfaces of Figure 3.5 are also shown in Figure 3.6-Figure 3.9. Similarly to Figure 3.5, the two factors which are not presented in each of these four diagrams have been considered equal to the average of their ranges.

In the following subsections, the effects of the four operation parameters on the amount of produced hydrogen are discussed, as well as the effect of these parameters on the optimum value of other parameters.

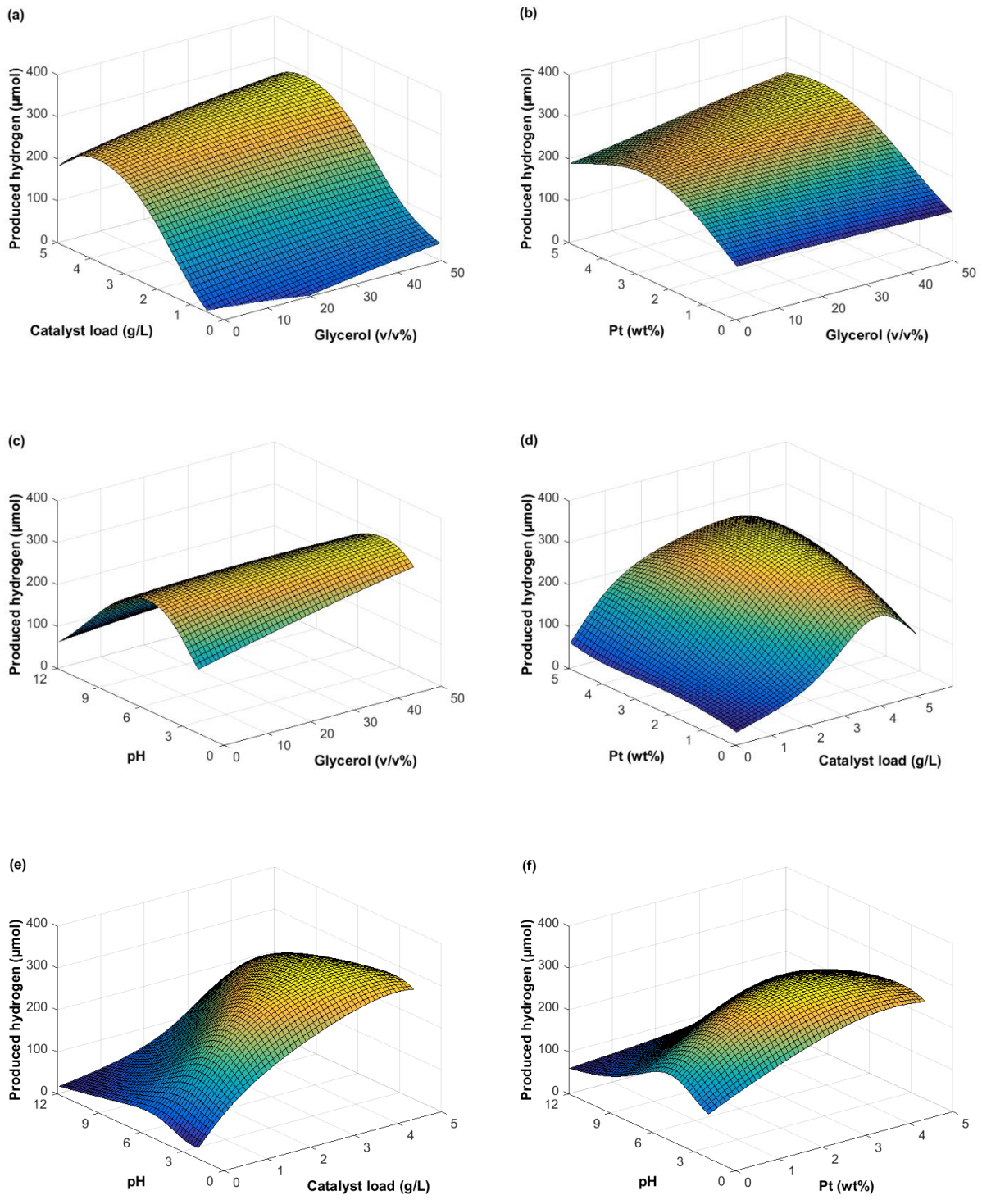

Figure 3.5. Response surface plots of the amount of produced hydrogen as a function of (a) catalyst loading and glycerol%, (b) Pt% and glycerol%, (c) pH and glycerol%, (d) Pt and catalyst loading, (e) pH and catalyst loading, and (f) pH and Pt%. In all figures, the values of the two parameters not included in the graphs were considered equal to the average of their ranges.

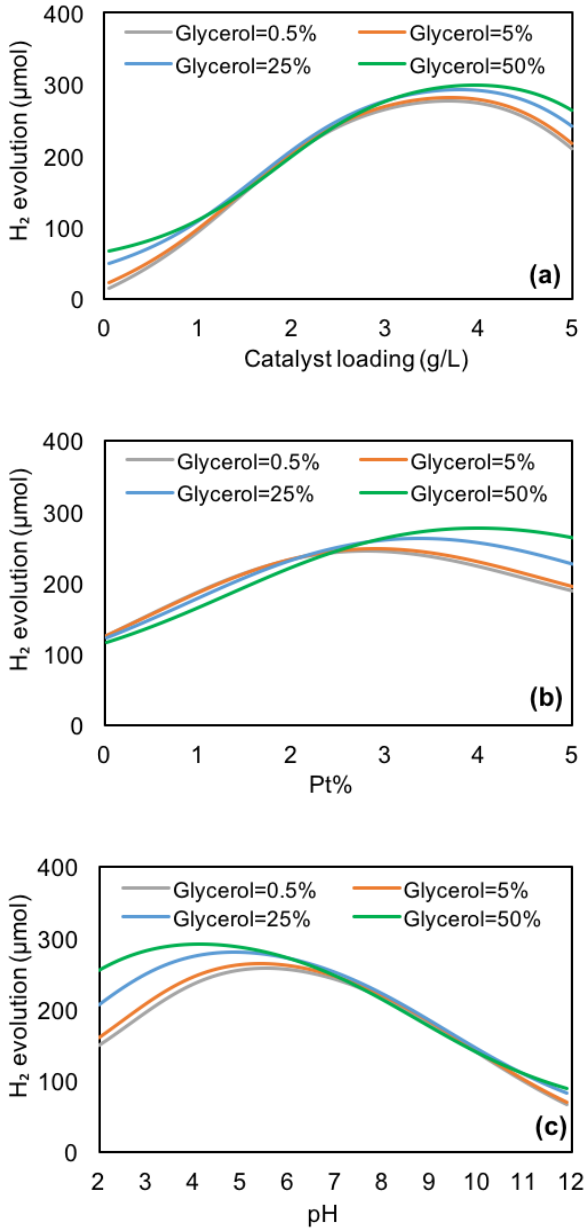

Figure 3.6. Effect of glycerol% on the amount of production H_2 as well as the optimum value of (a) catalyst loading, (b) Pt%, and (c) pH.

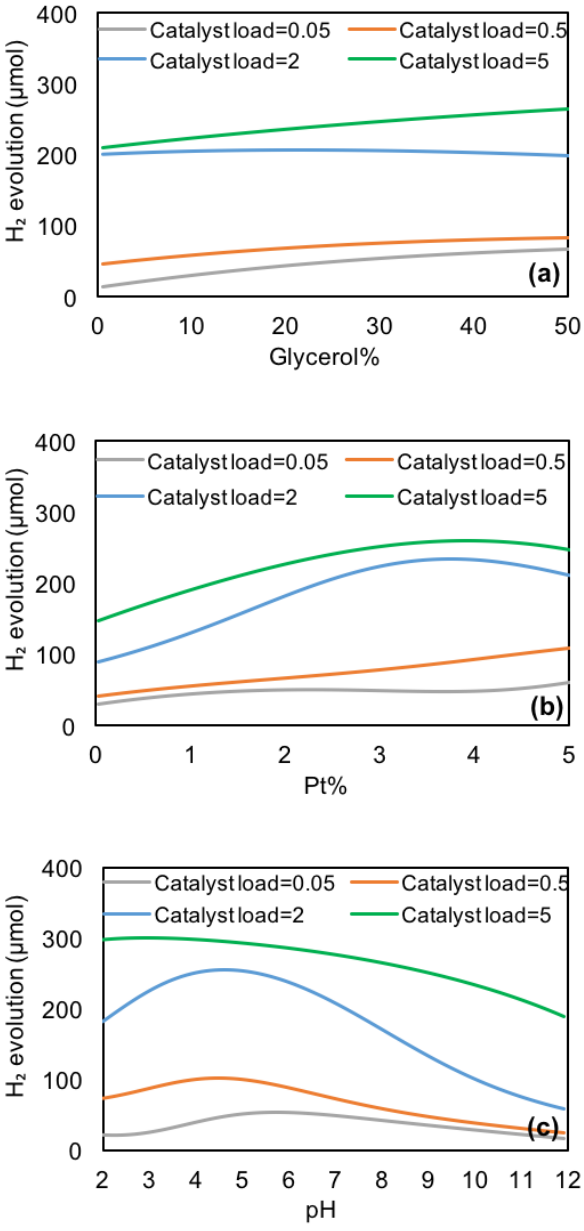

Figure 3.7. Effect of catalyst loading on the amount of produced H_2 as well as the optimum value of (a) glycerol%, (b) Pt%, and (c) pH.

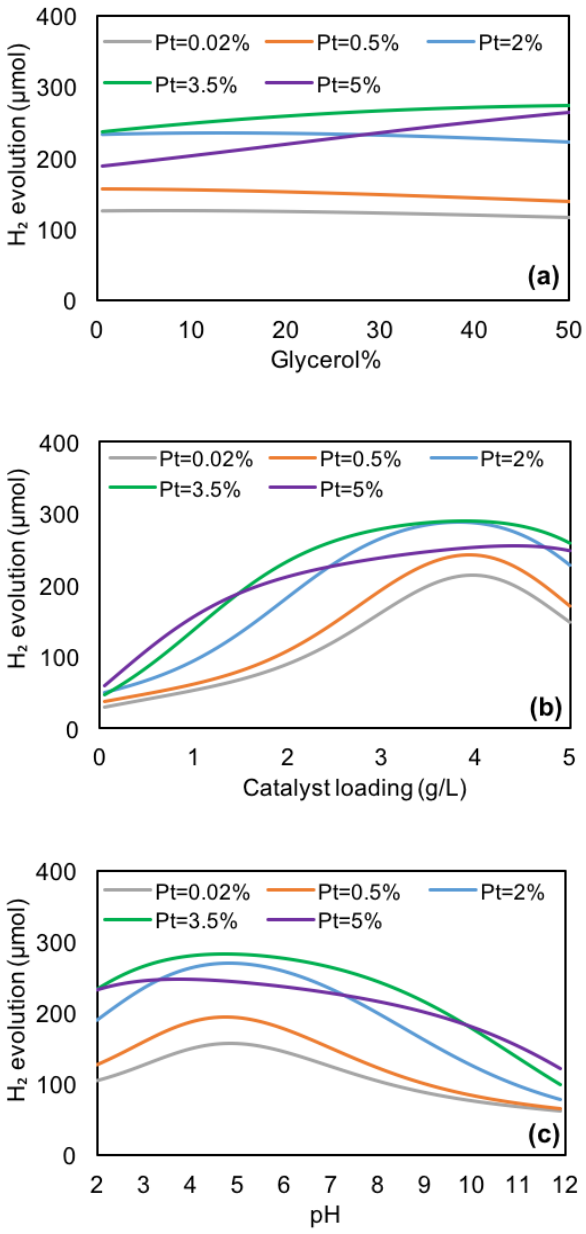

Figure 3.8. Effect of Pt% on the amount of produced H_2 as well as the optimum value of (a) glycerol%, (b) catalyst loading, and (c) pH.

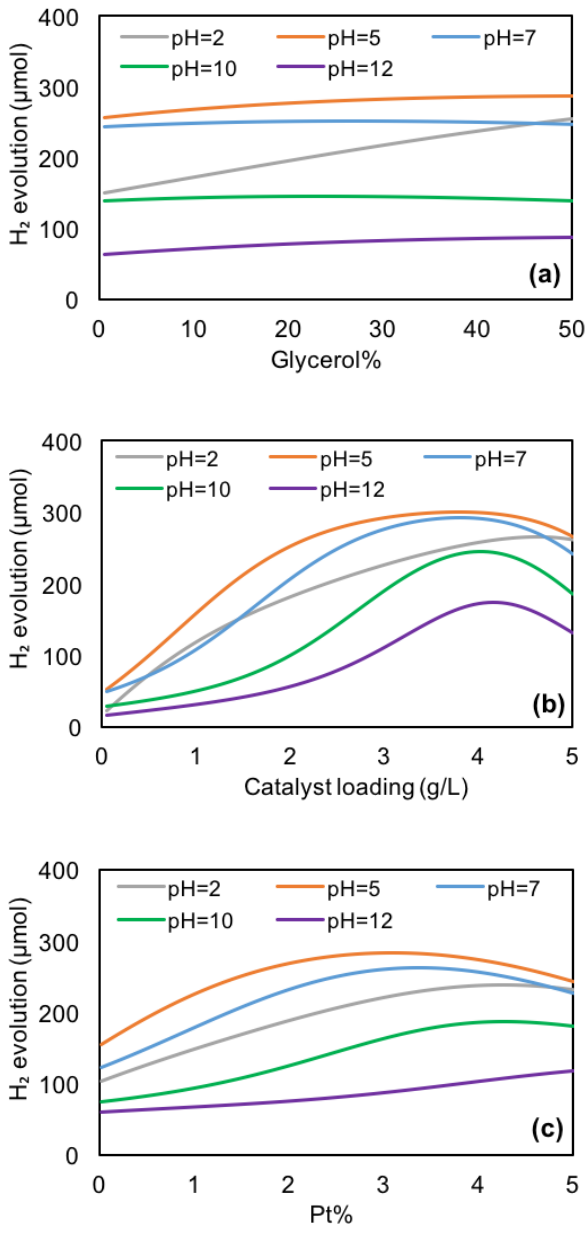

Figure 3.9. Effect of pH on the amount of produced H_2 as well as the optimum value of (a) glycerol%, (b) catalyst loading, and (c) Pt%.

3.3.4.1. Glycerol concentration

Figure 3.5a-c illustrate that the amount of produced hydrogen is slightly enhanced by increasing glycerol%, even though the enhancement is not considerable, and increasing glycerol% from 0.5 to 50% enhances the amount of produced hydrogen to only around 61%. Improvement of the

amount of produced hydrogen by increasing glycerol% can be due to easier access of the photocatalyst to the glycerol molecule [101].

Enhancement of the amount of produced hydrogen by increasing glycerol% agrees with existing literature. In the case of using Pt/TiO_2 for hydrogen production from glycerol, Daskalaki and Kondarides [74] reported that the amount of produced hydrogen was enhanced by increasing glycerol concentration from 0.073 to 7.93%. In another work conducted with the same photocatalyst but larger glycerol concentrations, it was found that the amount of produced hydrogen reached a plateau at high concentrations (up to 29.2%) [80]. Based on Figure 3.5a-c, the optimum value of glycerol% is 50%, which can be considered in agreement with the 45% [95] and 53.6% [148] values reported as optimum glycerol% using TiO_2 photocatalyst.

Other than the amount of produced hydrogen, glycerol% could affect the optimum value of other parameters. According to Figure 3.5a-c (and also Figure 3.6), increasing glycerol% from 0.5 to 50% shifts the optimum catalyst loading from 3.75 to 3.95, the optimum Pt% from 2.75% to 4%, and the optimum pH from 4.4 to 6.4. By increasing glycerol%, the rate of oxidation half reaction increases, and further catalyst loading or Pt% provides more reaction sites for reduction half reaction.

3.3.4.2. Catalyst loading

The effect of catalyst loading on the amount of produced hydrogen can be seen in Figure 3.5a, d, and e. Analysis of these surface plots reveals that the amount of produced hydrogen could be enhanced up to 8.1 times by the optimization of catalyst loading. Moreover, these surface plots show that catalyst loading around 4 g/L is optimal. Observation of an optimum value for catalyst loading may be due to the fact that, in a low amount of catalyst loading, a significant portion of radiated photons may transmit out of the photoreactor [158]. On the other hand, a high amount of catalyst loading may result in the tendency towards agglomeration of catalyst particles, thus rendering a part of the catalyst surface unavailable for photon absorption [157]. Other authors [74, 112, 221, 222] have also reported an optimum value of catalyst loading in the photocatalytic hydrogen production reactions. The predictive accuracy of the developed model was compared to the experimental data given by Daskalaki and Kondarides [74], the only observed work in the literature on the investigation of hydrogen production from glycerol using Pt/TiO_2 with different catalyst loading. The evaluation of this research shows that in the experimental conditions

(0.0027% of glycerol, 0.5% of Pt%, and pH of 7) given in [74], the optimum value of the catalyst loading that was predicted by the current ANN model is 2.7 g/L, which agrees very well with the reported optimum value of 2.7 g/L (based on their experimental data). This comparison confirms the accuracy of the developed model and its predictive ability in a wide range of parameters. It also suggests that the model based on ANN is a powerful tool for optimizing this kind of complex process.

Figure 3.5a, d, and e, also represent the effect of catalyst loading on the optimum value of the other three independent variables (see Figure 3.7 for more clarity). These figures imply that the catalyst loading has no effect on the optimum value of glycerol%, as the maximum amount of hydrogen is produced at 50% glycerol for all the catalyst loadings. However, by increasing the catalyst loading from 0.05 to 5 g/L, the optimum Pt% decreases from 5% to 3.9%. The reason for this observation could be due to the fact that at high catalyst loadings sufficient platinum particles are accessible to play the role of reaction site, and excessive Pt% makes a barrier against absorption of light by semiconductor and also prevents facile access of substrates to the semiconductor surface [145]. In addition, by increasing catalyst loading from 0.05 to 5 g/L, the optimum value of pH decreases from 5.7 to 3.5. This decrease could be attributed to supply of more reaction sites at higher catalyst loading, to convert higher concentration of hydronium ions (which are available at lower pH values) to hydrogen [147].

3.3.4.3. Pt%

It can be observed from Figure 3.5b, d and f that hydrogen production hit a peak around 3-4% of platinum. The amount of produced hydrogen could increase up to 2.1 fold by the optimization of Pt%. As platinum plays the role of a photo-generated electron trap, it improves the charge separation of electron-hole and decreases the rate of recombination [223]. Thus, the amount of produced hydrogen is enhanced by increasing Pt% due to higher accessibility of platinum surface sites. Notwithstanding this, after the optimum point, addition of more platinum decreases the rate of photocatalytic reaction due to some issues such as light shielding and impeding access of substrate to semiconductor surface [145].

Observation of optimum values of co-catalyst agrees with previous research. For Pt-decorated TiO_2, optimum percentages of 2 [74] and 2.1 [224] were reported. In addition, in the case of using

glycerol as hydrogen source, 1 [112], 2 [113] and 2.5 [96] percent of co-catalyst were obtained as optimum.

The influence of Pt% on the optimum value of the other three parameters could be discussed using Figure 3.5b, d and f (see also Figure 3.8). These figures suggest that Pt% has insignificant effects on the optimum values of glycerol%, catalyst loading, and pH which are around 50%, 4 g/L and 5, respectively.

3.3.4.4. pH

By analyzing Figure 3.5c, d and f, it can be found that the amount of produced hydrogen could be enhanced up to 3.5 times by pH optimization. Moreover, these figures show that by changing pH from highly acidic solution to around 5, the amount of produced hydrogen increases; however, further growth of pH toward basic decreases the amount of produced hydrogen. Glycerol is adsorbed through hydrogen bonding with the surface hydroxyl groups of the photocatalyst (which are in the form of TiOH) [225]. The surface charge of the photocatalyst is neutral and glycerol could be adsorbed more conveniently around the point of zero charge (pH of 6.25 for P25 [80]). However, acidic solution causes agglomeration of P25 particles. On the other hand, in caustic solution, higher concentration of OH bonding leads to UV screening of photocatalyst [80]. Figure 3.5c, d, and f, as well as Figure 3.9 clarify the effect of pH on the optimum values of other operating parameters. Based on these figures, pH does not affect the optimum value of glycerol%. Conversely, decreasing pH from 12 to 5 shifts the optimum value of catalyst loading and Pt% respectively from 3.8 to 4.15 g/L and 3.1 to 5%. Variations of optimum catalyst loading and Pt% in different pH values could be attributed to the fact that a portion of surface active sites are not accessible in catalyst particles which agglomerate due to acidic pH [226]; thus, more catalyst loading or platinum is required to provide the necessary reaction sites. Furthermore, pH affects the electrokinetic potential of platinum particles and changes its capacity to trap photo-generated electrons and its adsorption of hydronium ions [147].

3.3.5. Overall optimization using GA

To find the maximum value of produced hydrogen and associated optimum operating parameters, the obtained ANN model was utilized as the fitness function in the optimization procedure based on GA. In the GA method, the population of the individual solutions was modified iteratively and the ANN model was employed to find the best generation in each iteration. Then the chosen

generation was utilized to produce the next generation by reproduction, mutation and crossover (more detail about GA procedure can be found in [227]). The optimized values of hydrogen production and four operating parameters based on GA are summarized in Table 3.5. The optimum values of glycerol%, catalyst loading, Pt%, and pH were found to be respectively 50%, 3.9 g/L, 3.1%, and 4.5.

The ANN model predicted that 311 µmol of hydrogen will be produced in optimum conditions achieved by GA, which is very close to the 321 µmol obtained by experiments in these conditions and consequently, it confirms the accuracy of the model (see Table 3.5). Moreover, experimental data of the rate of produced hydrogen during 4 hours in optimum conditions is represented in Figure 3.10. As can be seen, the amount of produced hydrogen increased exponentially during the experiment.

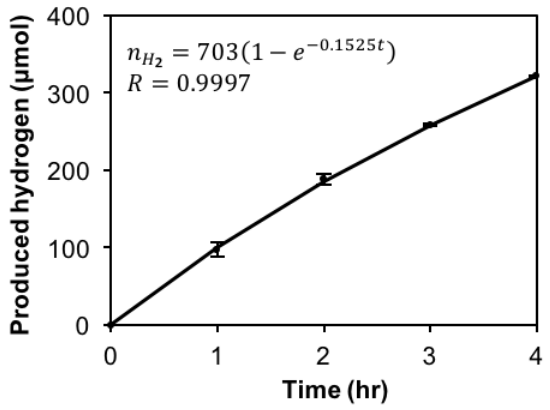

Figure 3.10. The rate of produced hydrogen during 4 hours at the optimum condition obtained by GA.

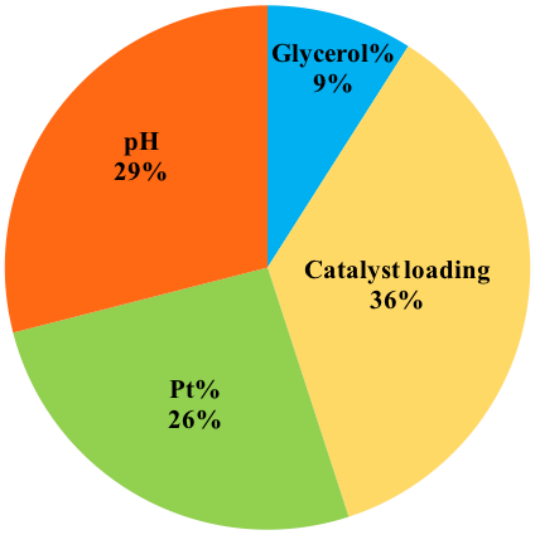

Figure 3.11. The percentage relative importance of operating parameters in the current photocatalytic hydrogen production reaction.

Table 3.5. The optimized value of hydrogen production and the four operating parameters based on GA.

Parameter	Produced hydrogen (µmol)		Glycerol% (v/v)	Catalyst loading (g/L)	Pt% (wt%)	pH
	Experimental	ANN model				
Optimized value	321	311	50	3.9	3.1	4.5

3.3.6. Relative importance of the operating parameters

Garson's method (which uses the neural network weights matrix) was utilized to obtain the level of influence of each input variable on the response. Table 3.6 shows the connection weight values (neural network weights matrix) for the developed model. The relative importance of input variables computed by Eq. (3–8) is illustrated in Figure 3.11. The results indicate that glycerol% and catalyst loading are, respectively, the least and most influential operating parameters with 9% and 36% effect on the amount of produced hydrogen. Moreover, the importance of Pt% and pH are approximately the same. This observation reveals that the amount of produced hydrogen is not significantly affected by the concentration of the glycerol, as this parameter does not control the reaction rate. On the other hand, the highest dependency of the amount of produced hydrogen to catalyst loading shows that the photocatalytic phenomenon is the main route for hydrogen production. This observation is in accordance with the 8.1 times enhancement of the amount of produced hydrogen by optimization of catalyst loading as represented in Figure 3.5.

Table 3.6. Connection weights between input and hidden layers (W^{ih}) as well as between hidden and output layers (W^{ho}).

	W^{ih}				W^{ho}
Neuron	Glycerol%	Catalyst loading	Pt%	pH	
1	0.4245	0.7942	0.779	2.2713	0.8999
2	-0.1613	1.8853	1.1621	-1.4580	0.9778
3	-0.4451	-0.4102	1.1537	0.3641	-0.7347
4	-0.1986	2.4042	-0.7028	0.6537	-0.9891

3.4. Conclusion

In this study, we investigated the interaction effects of key operating parameters in the photocatalytic glycerol valorization to hydrogen process using Pt/TiO_2 photocatalyst. Four operating parameters of glycerol%, catalyst loading, Pt%, and pH were selected as independent

variables, and the value of produced hydrogen was considered as the response. The experiments were performed based on Box-Behnken experimental design. Two techniques of RSM and ANN were employed to model the process, and the obtained experimental data were utilized to train the models. Afterward, the optimization and predictive ability of these models were compared based on R^2, R^2_{adj}, RMS, MAE and AAD. This comparison revealed that the ANN-based model is more accurate and reliable; thus it was employed for the optimization and parametric investigation. Optimization of the ANN model was performed by the GA approach and it was found that the highest amount of hydrogen could be produced at the condition of 50% glycerol (v/v), 3.9 g/L catalyst loading, 3.1% Pt, and pH of 4.5. Garson's method was employed to obtain the relative importance of each operating parameter in the response. This analysis revealed that glycerol% and catalyst loading are, respectively, the least and most influential parameters on the amount of produced hydrogen. Moreover, analysis of the effect of operating parameters showed that, in addition to affecting the amount of produced hydrogen, they could affect the optimum values of other parameters.

Briefly, interaction effect analysis of the results showed that:

- Increasing glycerol% shifts the optimum value of catalyst loading, Pt% and pH to higher values.
- Catalyst loading has no effect on the optimum value of glycerol%; however, the optimum values of Pt% and pH decrease by increasing catalyst load.
- Pt% has insignificant effects on the optimum values of glycerol%, catalyst loading, and pH.
- pH does not affect the optimum value of glycerol%; however, decreasing pH shifts the optimum catalyst loading and Pt% to higher values.

*In the previous chapter, a **statistical** study was performed on photocatalytic valorization of glycerol to hydrogen and the most important operating parameters were identified.*

*In the following chapter, a **kinetic** study was performed for photocatalytic production of **hydrogen** from **glycerol** and **ethanol**. All kinetic models for the photocatalytic valorization of alcoholic wastes available in the literature are all based on L-H model. Their limitation come from the fact that they are only function of substrate concentration. Therefore, they are not suitable for a comprehensive modelling of photocatalytic processes. On the other hand, the intrinsic kinetic models available in the literature have been developed for gas phase photocatalytic reactions. Because the photocatalytic reactions are interesting to be performed at ambient temperature and pressure and the alcoholic wastes are in liquid phase in these conditions, the development of a comprehensive kinetic model for liquid phase photocatalysis is essential to analyze the valorization of alcoholic wastes.*

Chapter 4 : An intrinsic kinetic model for liquid phase photocatalytic hydrogen production

Résumé

Une étude cinétique a été réalisée pour décrire la production photocatalytique d'hydrogène en phase liquide. Un mécanisme de réaction et un modèle cinétique ont été proposés pour prédire le taux de production d'hydrogène en fonction de l'intensité de la lumière, de la pourcentage de catalyseur, de la concentration de substrat et du temps. Pour évaluer la capacité du modèle proposé, le glycérol et l'éthanol ont été choisis comme sources d'hydrogène (substrats). Les données expérimentales réalisées dans les différentes conditions opératoires, basées sur la conception expérimentale Box-Behnken, ont été utilisées pour former le modèle cinétique développé, optimiser les paramètres à l'aide d'algorithmes génétiques et en vérifier la précision. L'analyse confirme la validité du modèle dans les différentes conditions opératoires. En outre, la capacité du modèle à prédire le taux de production d'hydrogène pour d'autres substrats, photocatalyseurs et conditions opératoires ont été confirmées en comparant les prédictions du modèle aux données expérimentales de la littérature.

Abstract

A kinetic study was accomplished to describe the photocatalytic production of hydrogen in liquid phase. A reaction mechanism and a kinetic model were proposed to predict the rate of hydrogen production which is a function of light intensity, catalyst loading, substrate concentration, and time. To assess the capability of the proposed model, glycerol and ethanol were selected as representative hydrogen sources (substrates). The experimental data performed under different operating conditions, based on Box-Behnken experimental design, were used to train the developed kinetic model, optimize the parameters using genetic algorithms and check its accuracy. The analysis confirms the validity of the model under different operating conditions. In addition, the ability of the model to predict the rate of hydrogen production for other substrates, photocatalysts and operating conditions was confirmed by comparing model predictions with experimental data from literature.

4.1. Introduction

Renewable hydrogen is considered as a promising energy source of the future [228]. Different techniques such as thermal [229], biological [230], photoelectrochemical [231], and photocatalytic [232, 233] can be followed for hydrogen production. Photoelectrochemical and photocatalytic techniques take advantage of utilizing renewable solar energy, and operating at ambient temperature and atmospheric pressure [54]. Photocatalytic approach can be more attractive as not only the photolysis occurs in the homogeneous phase, but also no expensive transparent electrodes and directional illumination are required [234].

Photocatalytic reactions have been considered as a promising alternative for future chemical conversion, since the discovery of water photolysis on a TiO_2 electrode by Fujishima and Honda [64]. Titanium-based photocatalysts are the most recognized [164, 235-237] and alternative photocatalysts are not still reliable due to issues such as their stability, cost, toxicity, availability, and activity under full solar spectrum [238]. Deposition of cocatalysts on semiconductor is one of the best-known approaches to increase the efficiency of photocatalysts [173] and platinum is the most common cocatalyst for hydrogen production [239]. Platinum can provide reaction sites for hydrogen production, enhance charge separation, and trap photo-excited electrons [214]. Most of previous works considered the deposition of around 1% Pt on TiO_2 for hydrogen production [33, 75, 84, 93, 95]. However, Daskalaki *et al.* reported that 2% Pt is the optimum value for hydrogen production from glycerol [74] and 0.5% Pt was considered as optimum in another work[78]. For other metals used as cocatalysts, such as Cu [99, 100, 104], Au [108], Co [112], Ni [113] , and Ag [111], the optimum amount was around 1%.

Although photocatalytic processes seem promising for sustainable development, more research is essential to enhance their efficiency toward economically-viable processes. Other than enhancement of photocatalyst efficiency, the process should be optimized by a reliable model. Notwithstanding this, the fundamentals of photocatalytic processes are not yet found comprehensively to obtain a reliable kinetic model. Therefore, most of the corresponding models have been only developed based on the statistical analysis of experimental data [130, 150, 190-192, 240].

A limited number of kinetic studies have been performed for gas-phase photocatalytic hydrogen generation from substrates such as carbon dioxide and water vapor [241] as well as alcohols [203].

Nevertheless, regarding photocatalytic hydrogen production in liquid phase of substrates (hydrogen sources), all of the observed studies simply used the Langmuir-Hinshelwood (L-H) model (Eq. (4–1)) to develop their kinetic models [98, 195-202].

$$r_{H_2} = k_s \frac{\mathrm{K_s}[Sub]}{1 + \mathrm{K_s}[Sub]} \qquad (4–1)$$

In Eq. (4–1) , r_{H_2} , k_s , $\mathrm{K_s}$, and $[Sub]$ represent the rate of hydrogen production, reaction rate constant, adsorption coefficient of substrate on the photocatalyst surface, and concentration of substrate, respectively. In fact, L-H-based models estimated the rate of substrate transformation, it was simply assumed that the rate of hydrogen production varied similar to the rate of substrate transformation, and kinetic parameters (i.e., constants of Eq. (4–1)) were calculated to find the rate of hydrogen production [98, 195-202]. As a result, the kinetic parameters calculated in previous works are only valid under the specific conditions in which the experiments were performed. Moreover, the L-H based models are practically limited because they are only a function of substrate concentration or a rate equation was not developed. Therefore, the L-H based models can only be applied when the effect of substrate concentration is dominant. However, in our previous work [150], we showed that the substrate concentration could have the least effect on the rate of hydrogen production. Consequently, the available L-H-based models are not suitable for a comprehensive modelling of photocatalytic production of hydrogen.

To the best knowledge of authors, there is no work on intrinsic kinetic model for the photocatalytic production of hydrogen in liquid phase. As the photocatalytic reactions are interesting because they are performed at ambient temperature and pressure, and most of the prospective hydrogen sources are in liquid phase, it seems vital to develop a powerful kinetic model for photocatalytic production of hydrogen in liquid phase.

To obtain the kinetic parameters, most of the previous works on photocatalytic hydrogen production followed the ‘one-variable-at-a-time’ (OVAT) approach. As OVAT overlooks interaction effect of variables, it is not a reliable approach for the optimization of the constants of a multivariable model [152, 156]. To overcome this issue, the statistical design of experiment can be used as a novel approach that considers the interaction effect of variables and minimizes the number of required experiments [70].

On the other hand, it is expected that the treatment of biodiesel wastewater will soon be a significant issue due to the fast growth of biodiesel industries [242, 243]. The overproduction of glycerol, a significant component of biodiesel wastewater, has led to a glut and a significant decrease in its price during recent years [22, 244, 245]. Instead of the traditional treatment of wastewater and degradation of pollutants, their valorization to valuable compounds is a smart approach. Therefore, photocatalytic valorization of glycerol to hydrogen seems to be a promising process from both environmental protection and energy development points of views. Ethanol is another renewable source of hydrogen that can be produced through fermentation of sugars.

This work proposes a novel kinetic model for the photocatalytic production of hydrogen in liquid phase. As the developed model is not based on L-H, it has more flexibility and can predict the rate of hydrogen production as a function of multiple parameters like substrate concentration, catalyst loading, light intensity, and time. In this regard, a reaction mechanism was proposed and the rate expressions were defined based on the proposed mechanism. Then, an intrinsic kinetic model was developed to predict the rate of hydrogen production as a function of the four abovementioned parameters. To evaluate the ability of the proposed model, glycerol and ethanol were selected as representative substrates, a series of experiments were designed (according to Box-Behnken design), and the value of kinetic parameters were optimized using the genetic algorithm (GA). In addition, two other series of experiments were designed and carried out to check the validity of the suggested kinetic model based on face-centered and random designs. The model predictions were also compared with various data from literature to assess the ability of the proposed model in the prediction of the hydrogen production rate in different conditions (other substrates, photocatalysts, and ranges of operating parameters). Finally, the predictions of the proposed model were compared with those obtained using the L-H model.

4.2. Materials and methods

4.2.1. Materials

Glycerol (≥99.7%) and ethanol (99.99%) were obtained from VWR and Commercial Alcohols, respectively. Aeroxide P25 photocatalyst (≥99.5%) was provided by Evonik Industries and used as TiO_2 source. Hexachloroplatinic acid (IV) ($H_2PtCl_6 \cdot 6H_2O$, ≥37.50% Pt) was purchased from Sigma–Aldrich and used as platinum precursor.

4.2.2. Pt/TiO_2 preparation

Pt/TiO_2 photocatalyst was prepared using the photo-deposition technique [246]. In the beginning, the suspension of TiO_2 in water was ultrasonicated using a Hielscher UP400S Ultrasonic Processor to detach the agglomerated TiO_2 particles. Afterward, the required amount of the platinum precursor (to make 1% platinum loading on TiO_2) as well as ethyl alcohol (which plays the role of sacrificial agent in the photo-deposition process) were added to the suspension. After 15 min of purging the suspension by nitrogen gas (to remove the dissolved oxygen), it was irradiated using four 20 W Black-Ray® mercury tubes (λ_{max}=365 nm) for 3 hr, while the suspension was being purged. The platinum deposited TiO_2 was filtered through centrifugation at 5,000 rpm and rinsed with deionized water three times. Finally, the obtained sample was dried at 110 ˚C overnight.

4.2.3. Photocatalyst characterization

To assess the properties of the prepared photocatalyst, the sample was analyzed with X-ray diffraction (XRD) and TEM. XRD patterns of the prepared sample as well as pristine TiO_2 were collected by a Bruker SMART APEXII X-ray diffractometer equipped with a Cu Kα radiation source (λ = 1.5418 Å). The measurement range was 2θ = 10–80˚ with a step size of 0.02˚ and a scan rate of 1.2 min^{-1}. Anatase over Rutile ratio was calculated based on the method described by Ding et al.[207]. TEM image of the platinum deposited sample was captured using a JOEL JEM 1230 device operated at an accelerating voltage of 120 kV.

4.2.4. Photocatalytic hydrogen production

Photocatalytic hydrogen production experiments were performed in 10 ml vials equipped with open-top screw caps and septa. In the experiments, 5 ml solutions of predefined percentages of glycerol or ethanol were prepared in Mili-Q water, based on Table 4.1-4.5. Afterward, the required amounts of prepared photocatalyst were added and the suspensions were ultrasonicated using a Hielscher UP400S Ultrasonic Processor for 15 min. After purging the vials for 15 min with 20 mL/min of nitrogen gas, they were stirred in the dark for 20 min to complete glycerol adsorption on the surface of photocatalyst. Thermo-Scientific™ Cimarec™ 15-Position magnetic stirrer was used to have a continuous 500 rpm mixing. A cooling fan was employed to ventilate the box reactor and keep its temperature around ambient. The vials were irradiated with 20 W Black-Ray® mercury tubes (λ_{max}=365 nm) as required based on Table 4.1-4.5. To find the average rate of hydrogen production at 1, 2, 3, and 4 hr, 250 µL of the gas headspace product was collected by a gastight

syringe at pre-defined time intervals and analyzed with an Agilent Technologies 7820A gas chromatograph (GC) equipped with TCD and FID detectors, HP-Molesieve and HP-PLOT columns (Agilent), and nitrogen carrier gas. At least three replicate experiment were performed for each data set to assure the accuracy of results.

Table 4.1. The values of independent variables obtained based on the Box-Behnken design (for the model development) and corresponding average rate of hydrogen production in various times based on the experiments and kinetic model for glycerol.

Run #	Independent variables			Rate of hydrogen production (µmol/h)							
				t=1 h		t=2 h		t=3 h		t=4 h	
	Light intensity (µW/ cm^2)	Catalyst loading (g/l)	Glycerol % (v/v)	Experiment	Kinetic model	Experiment	Kinetic model	Experiment	Kinetic model	Experiment	Kinetic model
1	400	1.55	1	36	36	25	24	21	16	10	11
2	400	0.1	15.5	17	18	12	12	11	8	4	6
3	400	3	15.5	71	69	54	47	36	32	17	22
4	400	1.55	30	58	54	40	37	32	25	14	17
5	800	0.1	1	10	14	8	10	7	7	5	4
6	800	3	1	52	56	38	38	28	26	14	17
7	800	0.1	30	18	22	17	15	14	10	8	7
8	800	3	30	78	85	54	57	37	39	29	26
9	800	1.55	15.5	55	64	47	43	28	29	16	20
10	800	1.55	15.5	66	64	41	43	38	29	17	20
11	800	1.55	15.5	62	64	45	43	29	29	22	20
12	1200	1.55	1	52	48	34	32	23	22	16	15
13	1200	0.1	15.5	21	24	20	16	16	11	9	7
14	1200	3	15.5	102	93	58	63	37	43	29	29
15	1200	1.55	30	77	72	43	49	33	33	29	22

Table 4.2. The values of independent variables obtained according to the face-centered design (for the model validation) and corresponding average rate of hydrogen production in various times based on the experiments and kinetic model for glycerol.

Run #	Independent variables			Rate of hydrogen production (µmol/h)							
				t=1 h		t=2 h		t=3 h		t=4 h	
	Light intensity ($\mu W/cm^2$)	Catalyst loading (g/l)	Glycerol % (v/v)	Experiment	Kinetic model	Experiment	Kinetic model	Experiment	Kinetic model	Experiment	Kinetic model
1	400	1.55	15.5	60	53	39	36	30	24	12	17
2	800	3.00	15.5	86	84	50	57	42	38	24	26
3	800	0.10	15.5	18	21	13	14	13	10	5	7
4	800	1.55	30.0	65	65	47	44	32	30	17	20
5	800	1.55	1.0	47	43	32	29	22	20	13	13
6	1200	1.55	15.5	72	71	44	48	40	33	26	22

Table 4.3. The values of independent variables obtained based on the Box-Behnken design (for the model development) and corresponding average rate of hydrogen production in various times based on the experiments and kinetic model for ethanol.

Run #	Independent variables			Rate of hydrogen production (µmol/h)							
				t=1 h		t=2 h		t=3 h		t=4 h	
	Light intensity (µW/ cm^2)	Catalyst loading (g/l)	Glycerol % (v/v)	Experiment	Kinetic model	Experiment	Kinetic model	Experiment	Kinetic model	Experiment	Kinetic model
1	400	1.55	1	6	6	8	6	7	6	3	6
2	400	0.1	15.5	4	7	8	7	8	7	4	7
3	400	3	15.5	13	17	21	17	18	17	19	17
4	400	1.55	30	15	15	17	15	14	15	17	14
5	800	0.1	1	6	5	4	5	6	5	3	5
6	800	3	1	12	13	16	13	16	13	15	13
7	800	0.1	30	15	13	14	13	16	13	15	13
8	800	3	30	31	34	35	33	34	33	35	32
9	800	1.55	15.5	24	27	24	27	29	26	28	26
10	800	1.55	15.5	27	27	28	27	24	26	24	26
11	800	1.55	15.5	25	27	24	27	26	26	23	26
12	1200	1.55	1	16	16	17	16	15	15	16	15
13	1200	0.1	15.5	20	19	21	18	18	18	15	18
14	1200	3	15.5	43	47	46	46	43	46	44	45
15	1200	1.55	30	43	41	42	40	40	40	39	39

Table 4.4. The values of independent variables obtained according to the face-centered design (for the model validation) and corresponding average rate of hydrogen production in various times based on the experiments and kinetic model for ethanol.

Run #	Independent variables			Rate of hydrogen production (µmol/h)							
				t=1 h		t=2 h		t=3 h		t=4 h	
	Light intensity (µW/cm^2)	Catalyst loading (g/l)	Glycerol % (v/v)	Experiment	Kinetic model	Experiment	Kinetic model	Experiment	Kinetic model	Experiment	Kinetic model
1	400	1.55	15.5	11	14	13	14	15	14	15	14
2	800	3.00	15.5	29	33	31	32	31	32	29	31
3	800	0.10	15.5	13	13	16	13	14	13	16	12
4	800	1.55	30.0	26	28	29	28	25	27	31	27
5	800	1.55	1.0	10	11	13	11	13	11	12	10
6	1200	1.55	15.5	37	39	41	39	36	38	36	38

Table 4.5. The values of independent variables obtained according to random function of Matlab® and corresponding average rate of hydrogen production based on the experiments and kinetic model for glycerol and ethanol.

Run #	Independent variables				Rate of hydrogen production (µmol/h)			
					Glycerol		Ethanol	
	Light intensity (µW/cm2)	Catalyst loading (g/l)	Glycerol % (v/v)	t (h)	Experiment	Kinetic model	Experiment	Kinetic model
1	800	1.79	26.01	1.56	53	55	26	29
2	400	1.94	11.50	2.33	33	34	23	24
3	400	2.21	4.927	2.49	31	32	26	28
4	800	2.55	7.49	3.61	53	55	45	46
5	1200	2.76	17.01	1.36	77	78	15	17
6	400	2.68	18.82	2.84	29	32	16	15
7	800	1.54	6.43	2.88	24	29	13	14
8	400	1.53	7.07	3.60	21	19	13	13

4.2.5. Design of experiments

The value of kinetic parameters was calculated using the experiments performed according to the Box-Behnken design. Light intensity (μW/cm^2), catalyst loading (g/L), and glycerol% (v/v) were defined as three independent variables, labeled A-C, respectively (see Table 4.6). In addition, rate of hydrogen production (μmol/h) was selected as dependent variable. Based on preliminary experiments, the range of independent variables were selected as shown in Table 4.6. According to the Box-Behnken design, 15 sets of experiments (including three center points) were performed in three levels (coded as −1, 0, and +1), as illustrated in Table 4.1 and Table 4.3.

Moreover, to assess the validity of the developed model, two sets of experiments, one based on the face-centered design (Table 4.2 and Table 4.4) and another randomly designed (Table 4.5), were performed and utilized to define validation experiments. For the face-centered design of validation experiments, 6 sets of experiments were defined in three levels (coded as −1, 0, and +1) of independent variables, as shown in Table 4.2 and Table 4.4. The random experiments defined based on random function of Matlab® (8 sets) are shown in Table 4.5. A graphical representation of Box-Behnken and face-centered designs for three factors is depicted in Figure 2.16 to provide a three dimensional insight of the above-mentioned statistical designs.

Table 4.6. Experimental ranges and levels of variables for hydrogen production experiments.

Variables	-1	0	+1
Light intensity (A, μW/cm^2)	400	800	1200
Catalyst loading (B, g/L)	0.1	1.55	3
Glycerol% (C, v/v)	1	15.5	30

4.2.6. Genetic algorithm

GA optimization technique was used to optimize the kinetic parameters. For the GA optimization, 200 individuals were selected as population size and the individuals were randomly distributed for each generation. Constraint dependent was selected as creation function to create the initial population. Rank function was selected for the fitness scaling and the raw scores were scaled according to the rank of each individual. To choose the parents for subsequent generation, stochastic uniform function was taken as the selection function.

Five percent of the individuals were considered as elite count to generate the children of a new generation and guarantee the survival of next generation. In addition, 80% and 20% of the next generation were produced by crossover and mutation, respectively. Constraint dependent functions were selected for both crossover and mutation.

4.3. Proposed reaction mechanism

Photocatalytic hydrogen production from a substrate involves several parallel reactions. A series of elementary steps should be considered to study the mechanism of these reactions. These steps are as follows:

i. Photocatalytic reaction is triggered by the adsorption of a photon of light (which possesses enough energy) on a photocatalyst, to promote an electron from a filled valence to an empty conduction band. Because of the electron migration, a hole forms on the valence band:

$$Photocatalyst + h\upsilon \rightarrow e^{-} + h^{+} \quad (4–2)$$

ii. The pair of photo-generated species can recombine and release heat (Eq.(4–3)), especially in the absence of an electron scavenger.

$$e^{-} + h^{+} \rightarrow Heat \quad (4–3)$$

iii. Substrate and water adsorb competitively on the surface of the semiconductor in an equilibrium state:

$$Sub + S \leftrightarrow Sub_{ads} \quad (4–4)$$

$$H_2O + S \leftrightarrow H_2O_{ads} \quad (4–5)$$

where S represents a vacant surface site.

iv. The oxidation reaction occurs on the surface of semiconductor and both substrate and water can act as electron donor species. In this regard, the adsorbed substrate can react with the photo-generated holes directly (Eq. (4–6)) or indirectly (Eqs. (4–7) and

(4–8), and produce H^+_{ads} and liquid products. The direct and indirect routes can be called hole-mediated and radical-mediated, respectively.

$$Sub_{ads} + h^+ \rightarrow LP_{ads} + H^+_{ads} \quad (4–6)$$

$$H_2O_{ads} + h^+ \rightarrow {}^{\bullet}OH_{ads} + H^+_{ads} \quad (4–7)$$

$$Sub_{ads} + {}^{\bullet}OH_{ads} \rightarrow LP_{ads} + H_2O_{ads} \quad (4–8)$$

where LP_{ads} represents liquid products. It should be pointed out that it is assumed that the liquid products do not participate in subsequent reactions to produce further proton or the amount of hydrogen produced from liquid products is negligible in comparison to its production from glycerol. This assumption is reasonable as the amount of generated liquid products during a limited reaction time is negligible in comparison to the amount of the primary substrate [150].

v. The formed liquid products desorb from the photocatalyst surface to the balk and leave free vacant surface site (for the substrate or water adsorption):

$$LP_{ads} \rightarrow LP \quad (4–9)$$

vi. The photo-generated electron competes with the substrate to react with the adsorbed hydroxyl radical according to Eq. (4–10). As no oxygen exists to react with the formed hydroxide, it can transfer the electron back to the photocatalyst and convert to hydroxyl radical. This reaction could assist in decreasing the rate of recombination.

$${}^{\bullet}OH_{ads} + e^- \leftrightarrow OH^-_{ads} \quad (4–10)$$

vii. In the absence of reactive oxygen species, the produced H^+_{ads} has a high tendency to react with photo-generated electrons. In the presence of a cocatalyst, this reaction mostly occurs on cocatalyst surface acting as photocathode, reducing protons to hydrogen [69]:

$$2H^{+}_{ads} + 2e^{-} \rightarrow H_2 \quad (4\text{–}11)$$

4.4. Kinetic model development

The reaction rate expressions can be derived according to the described reaction mechanism. In the presence of an active cocatalyst, reaction (4–11) is very fast and does not control the overall reaction rate [69]. Therefore, the rate of hydrogen production can be expressed according to the rate of proton generation:

$$r_{H_2} = \frac{1}{2} \times r_{H^+} = \frac{1}{2} \times \frac{dH^+}{dt} \quad (4\text{–}12)$$

On the other hand, the rate of proton generation can be achieved based on Eqs. (4–6) and (4–7). In the resulting equation (Eq. (4–13)), the reaction rates with respect to the concentration of adsorbed species are shown as m^{th} and n^{th} orders. It is worth mentioning that reactions (4–6) and (4–7) may not be elementary as they can follow different pathways and steps. In these reactions, the proton is first trapped by the substrate or water, and then a H^+ is released [247]. The released H^+ adsorbs on the surface of catalyst in the next step.

$$\frac{dH^+}{dt} = k_6[Sub_{ads}]^m[h^+] + k_7[H_2O_{ads}]^n[h^+] \quad (4\text{–}13)$$

By considering $k_6[Sub_{ads}]^m[h^+] \gg k_7[H_2O_{ads}]^n[h^+]$ assumption [194] which means that the rate of direct substrate reaction with photo-generated holes is much higher than its rate of indirect reaction, Eq. (4–13) transformed to (4–14):

$$\frac{dH^+}{dt} = k_6[Sub_{ads}]^m[h^+] \quad (4\text{–}14)$$

As the adsorbed substrate and water are in equilibrium with the bulk, their concentration can be obtained based on Eqs. (4–4) and (4–5) as follows:

$$[Sub_{ads}] = K_4[Sub][S] \quad (4\text{–}15)$$

$$[H_2O_{ads}] = K_5[H_2O][S] \quad (4–16)$$

where K_4 and K_5 are equilibrium constants.

The initial concentration of vacant surface sites is constant and can be represented with Eq. (4–17):

$$[S_0] = [S_{act}] + [S_{dec}] \quad (4–17)$$

where $[S_{act}]$ and $[S_{dec}]$ represent the concentration of active and deactivated vacant surface sites, respectively at arbitrary time of t. In fact, it is considered that the active surface sites are composed of the vacant surface sites and the surface sites occupied by adsorbed water and the substrate:

$$[S_{act}] = [S] + [H_2O_{ads}] + [Sub_{ads}] \quad (4–18)$$

The active surface sites can be deactivated during the process based on Eq. (4–19):

$$[S_{act}] \rightarrow [S_{dec}] \quad (4–19)$$

The photocatalyst deactivation usually occurs because of the accumulation of partially oxidized intermediates or products on the active sites [82, 248, 249]. A kinetic study performed by Cao et al. on the deactivation process showed that its rate is first order [159]. Therefore, the concentration of deactivated surface sites can be calculated as follows:

$$[S_{dec}] = [S_0] \times \left(1 - \exp(-k_{dec} t)\right) \quad (4–20)$$

where k_{dec} is the first-order rate constant of the active surface sites deactivation and t represents time.

As the number of vacant surface sites is directly dependent on the amount of available catalyst, $[S_0]$ is a function of the catalyst loading. Extensive addition of catalyst would cause catalyst agglomeration, which makes parts of surface sites inaccessible [150]. Li *et al.* showed that the catalyst loading can significantly affect the average particle size and

consequently, its agglomeration [250]. Therefore, the number of vacant surface sites can be formulated like Eq. (4–21) where the concentration of initial active surface sites increases linearly by increasing the catalyst loading if p=1, and the effect of catalyst agglomeration can be considered using a non-linear function when p<1.

$$[S_0] = k_{cat}[Cat]^p \tag{4–21}$$

where $[Cat]$ represents the catalyst loading. k_{cata} and p can be a function of substrate type, as it affects the intermediates formation and adsorption on the catalyst surface during the reaction. The chemical nature of the adsorbed species can influence the catalyst agglomeration by changing the surface charge of catalyst and electrostatic surface potential [251].

By substituting Eqs. (4–15), (4–16), (4–18), (4–20), (4–21), and in Eq. (4–17), the concentration of vacant surface sites can be represented as below:

$$[S] = \frac{k_{cat}[Cat]^p \exp(-k_{dec}t)}{1 + K_4[Sub] + K_5[H_2O]} \tag{4–22}$$

Since the solution is a binary aqueous mixture (of water and the substrate), the water concentration in the bulk can be calculated as a function of the substrate concentration as follows:

$$[H_2O] = \frac{\rho_w}{M_w}\left(1 - \frac{M_{Sub}}{\rho_{Sub}}\right)[Sub] \tag{4–23}$$

where ρ and M represent density and molecular weight, respectively, and subscripts w and Sub represent water and substrate, respectively. Accordingly, Eq. (4–22) can be simplified as follow, based on Eq. (4–23).

$$[S] = \frac{k_{cat}[Cat]^p \exp(-k_{dec}t)}{1 + \left(K_4 + K_5\frac{\rho_w}{M_w} - K_5\frac{\rho_w}{M_w}\frac{M_{Sub}}{\rho_{Sub}}\right)[Sub]} \tag{4–24}$$

The rate of reaction (4–2) is a function of the light intensity and concentration of photocatalyst [194, 252]. At high light intensities, it is possible that all of the photons are not adsorbed and efficiently used to trigger a reaction. Moreover, extensive catalyst loading causes nonuniform reaching of the photons to the bulk [157]. These undesirable effects can be taken into account in Eq. (4–25) when q<1 and l<1:

$$r_2 = k_2[Cat]^q(\phi I)^l \tag{4–25}$$

where I represents light intensity, ϕ is quantum efficiency, and q and l are constants.

Recombination of the electron and hole (Eq. (4–3)) is an important step [253] whose rate can be considered as:

$$r_3 = k_3[e^-][h^+] \tag{4–26}$$

In a steady state condition, it can be assumed that the concentration of photo-generated holes equals that of photo-generated electrons [254], then:

$$r_3 = k_3[h^+]^2 \tag{4–27}$$

The concentration of photo-induced holes is almost fixed during the reaction in the steady state condition [254]. Consequently, the concentration of holes can be calculated as follows:

$$\frac{d[h^+]}{dt} = k_2[Cat]^q(\phi I)^l - k_3[h^+]^2 - k_6[Sub_{ads}]^m[h^+] - k_7[H_2O_{ads}]^n[h^+] = 0 \tag{4–28}$$

While the charge carriers recombine as fast as 10^{-9} s, the adsorbed species make reaction occur in the range of 10^{-8}- 10^{-3} s [65, 173]. Thus, recombination of photo-generated species is a rate determining step and the assumptions of $k_3[h^+]^2 >> k_6[Sub_{ads}]^m[h^+]$ and $k_3[h^+]^2 >> k_7[H_2O_{ads}]^n[h^+]$ are valid, especially for the case of hydrogen production that no reactive oxygen species are present to increase adsorbed species reaction rate [254, 255]. It means that recombination rate of photo-generated species is higher than trapping of hole by the substrate and water. As a result, the concentration of photo-generated holes can be calculated by solving the differential equation (4–28):

$$[h^+]=\sqrt{\frac{k_2[Cat]^q(\phi I)^l}{k_3}} \tag{4–29}$$

As it can be seen, the concentration of holes in the valance band is a function of the catalyst loading, light intensity, and intrinsic properties of photocatalyst (ϕ).

The rate of hydrogen production can then be obtained by substituting Eqs.(4–14), (4–15), (4–24), and (4–29) in Eq. (4–12):

$$r_{H_2}=\frac{1}{2}\times\sqrt{\frac{k_2}{k_3}}k_6K_4^mk_{cat}^m\phi^{l/2}[Cat]^{mp+q/2}I^{l/2} \times\left(\frac{[Sub]}{1+\left(K_4+K_5\frac{\rho_w}{M_w}-K_5\frac{\rho_w}{M_w}\frac{M_{Sub}}{\rho_{Sub}}\right)[Sub]}\right)^m \exp(-mk_{dec}t) \tag{4–30}$$

Eq. (4–30), can be simplified to Eq. (4–31) considering $\alpha=\frac{1}{2}\times\sqrt{\frac{k_2}{k_3}}k_6K_4^mk_{cat}^m\phi^{l/2}$, $\beta=mp+q/2$, $\gamma=l/2$, $\delta=K_4+K_5\frac{\rho_w}{M_w}-K_5\frac{\rho_w}{M_w}\frac{M_{Sub}}{\rho_{Sub}}$, $\varepsilon=m$, and $\zeta=-mk_{dec}$ as equation constants.

$$r_{H_2}=\alpha[Cat]^\beta I^\gamma\left(\frac{[Sub]}{1+\delta[Sub]}\right)^\varepsilon\exp(\zeta t) \tag{4–31}$$

The developed model (Eq. (4–31)) is a multiplication of different terms, each representing an independent variable and can be simply used to predict the effect of each independent variable on the rate. In other words, as each term is independent of other terms, the equation can be simplified to be only a function of one or more desired operating parameters. On the other hand, the kinetic parameters in Eq. (4–31) are completely independent as none of them can be defined as a function of other parameters and each kinetic parameter presents a combination effect of independent variables.

In Eq. (4–31), $[Cat]^{\beta}$ is the term related to the effect of catalyst load and shows that the rate of hydrogen production increases as a power function with respect to the catalyst load. Pseudo-exponent of catalyst load, β, is function of (i) the exponent of adsorbed substrate concentration (m) in calculation of the proton generation reaction rates (Eq. (4–13)), (ii) the exponent of catalyst loading (p) in calculation of the concentration of initial active surface (Eq. (4–21)), and (iii) the exponent of catalyst loading (q) in calculation of the rate of excited electron-hole pair generation (Eq. (4–25)). The term I^{γ} is related to the effect of light intensity on the rate of hydrogen production. Pseudo-exponent of light intensity, γ, is a function of the exponent of light intensity (l) in calculation of the rate of excited electron-hole pair generation (Eq. (4–25)). The term $\left(\frac{[Sub]}{1+\delta[Sub]}\right)^{\varepsilon}$ is the L-H term which is modified by the factor of ε. The value of ε is equal to the exponent of adsorbed substrate concentration (m) in calculation of proton generation reaction rates (Eq. (4–13)). The term $\exp(\zeta t)$ is corresponding to the deactivation of catalyst, where ζ <0 and is a function of the exponent of adsorbed substrate concentration (m) in calculation of proton generation reaction rates (Eq. (4–13)) and the first-order rate constant of the active surface sites deactivation (k_{dec}) in calculation of the concentration of deactivated surface sites (Eq. (4–20)).

In comparison to the L-H-based model which presents the rate of hydrogen production as a function of the substrate concentration only, Eq. (4–31) is a function of further parameters of catalyst loading, light intensity, and time. Eq. (4–31) correctly predicts zero reaction rate for [Cat] = 0, I = 0, [Sub] = 0, and t = 0. Therefore, this model can be appropriate for parametric study and optimization of photocatalytic production of hydrogen in liquid phase.

4.5. Results and discussion

4.5.1. Photocatalyst characterization

XRD patterns of the prepared Pt/TiO_2 as well as pristine TiO_2 are presented in Figure 4.1. The average Anatase (101) and Rutile (110) crystal sizes of both of the samples were estimated to be around 20 and 30 nm, respectively, using the Scherrer equation [158, 256]. By considering the peak heights of Anatase (101) and Rutile (110) reflections [207], it was revealed that around 15% of each sample is composed of Rutile crystals. Approximately

equal crystal size and Rutile percentage in the composition also confirms that platinum deposition had no effect on the characteristics of the semiconductor. TEM image of the prepared Pt/TiO_2 was captured and presented in Figure 4.2. As Figure 4.2 confirms, platinum is deposited on TiO_2 in the form of black dots. Based on the particle size analysis of around 50 particles (extracted from TEM images), the particle size of around 87.5% of the particles were around 20 nm (15-25 nm) and the other 12.5% were about 30 nm (25-35 nm). This analysis illustrates that each particle is generally composed of only one crystal.

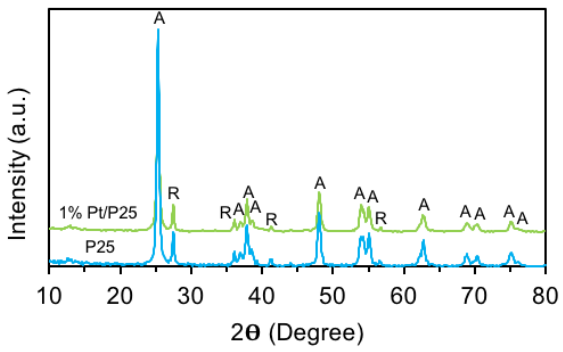

Figure 4.1. XRD pattern of the prepared Pt/TiO2 photocatalyst.

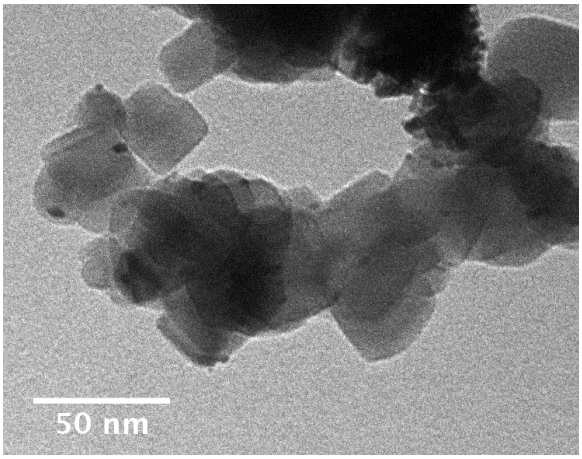

Figure 4.2. TEM image of the prepared sample.

4.5.2. Evaluating the accuracy of the present model

To check the validity of Eq. (4–31), the kinetic constants were calculated for glycerol and ethanol (as representative substrates) and model predictions were compared with experimental data. Employing traditional gradient based algorithms to find optimized values of kinetic parameters (in this nonlinear structure) can cause getting trapped in local optima. Thus, the optimized values of kinetic parameters were obtained by GA according to the procedure described in section 2.6, and the results are presented in Table 4.7. For these calculations, the results of designed experiments based on Box-Behnken (Table 4.1 and Table 4.3) were used. Finally, using the optimized kinetic constants, the Eq. (4–31) was converted to Eqs. (4–32) and (4–33) for glycerol and ethanol, respectively.

$$r_{H_2} = 266[Cat]^{0.400} I^{0.265} \left(\frac{[Glycerol]}{1+4.25[Glycerol]} \right)^{2.04} \exp(-0.390t) \qquad (4–32)$$

$$r_{H_2} = 14.7[Cat]^{0.271} I^{0.907} \left(\frac{[Ethanol]}{1+3.74[Ethanol]} \right)^{4.15} \exp(-0.0135t) \quad (4\text{–}33)$$

Table 4.7. The optimized values of the proposed kinetic parameters for the hydrogen production.

Kinetic parameter	Glycerol	Ethanol
α [1]	266	14.7
β	0.400	0.271
γ	0.265	0.907
δ ($\frac{l}{\mu mol}$)	4.25	3.74
ε	2.04	4.15
ξ ($\frac{1}{h}$)	-0.390	-0.0135

[1] In general, the unit of α is $\frac{(\mu\text{mol})^{1-\epsilon}.\text{cm}^{-2\gamma+3\beta+3\epsilon}}{g^{\beta}.\mu\text{W}^{\gamma}.h}$.

The values of hydrogen production rate predicted using Eqs. (4–32) and (4–33) (for the Box-Behnken points) are presented in Table 4.1 and Table 4.3, and the diagrams of the dispersion of hydrogen production rate (Box-Behnken points) for glycerol and ethanol are represented in Figure 4.3a and Figure 4.4a, respectively. As it can be seen, the present model has a good ability to predict the hydrogen production rate. It is worth mentioning that some experiments were performed in the absence of photocatalyst/UV illumination and the lack of hydrogen production proved the photocatalytic nature of reactions.

To statistically assess the developed models, their predictions (based on Box-Behnken design) were compared with the experimental data in terms of R^2, R^2_{adj}, *RMS*, *AAD*, and *MAE*. These values are presented in Table 4.8. Accordingly, it can be found that R^2 values are close enough to 1 and R^2_{adj} values are close to the corresponding R^2. Additionally, the values of *RMS*, *AAD*, and *MAE* are properly close to zero. Thus, it can be inferred that the developed model is appropriately fitted to the experimental data of both glycerol and ethanol.

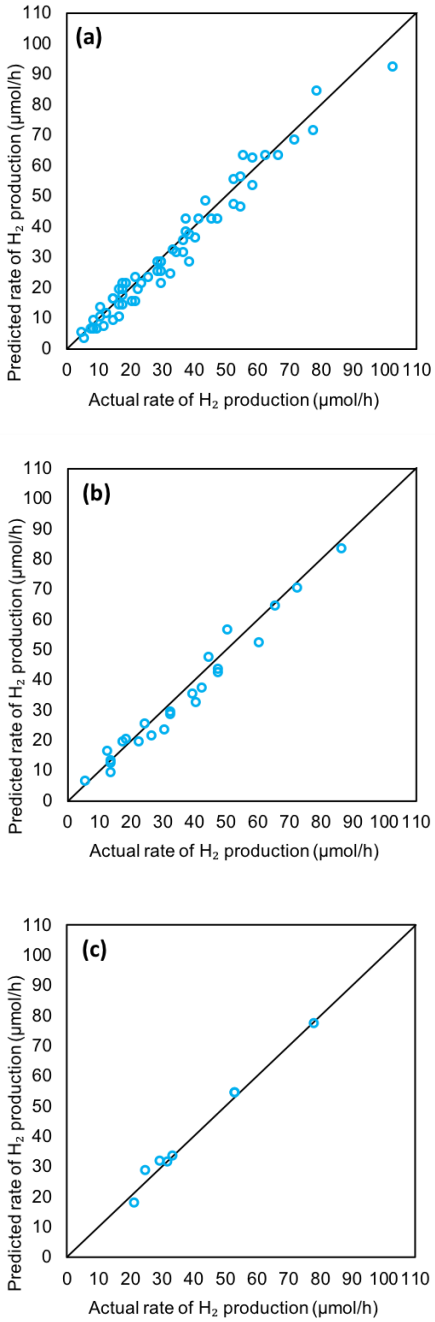

Figure 4.3. The experimental rate of hydrogen production versus the theoretical rate predicted by the proposed kinetic model based on (a) Box-Behnken design (model development), (b) face-centered design (model validation), and (c) random design (model validation) obtained for glycerol.

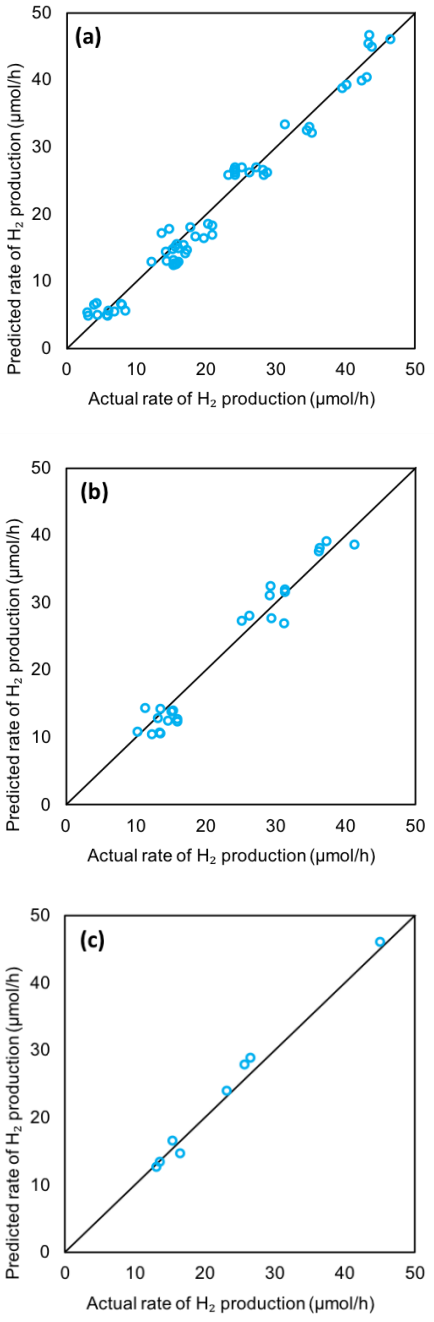

Figure 4.4. The experimental rate of hydrogen production versus the theoretical rate predicted by the proposed kinetic model based on (a) Box-Behnken design (model development), (b) face-centered design (model validation), and (c) random design (model validation) obtained for ethanol.

Figure 4.3a, Figure 4.4a and Table 4.8 show a good fitting of the current model on the experimental data for glycerol and ethanol which were designed according to Box-Behnken

design and utilized to obtain model constants. However, as the model was developed based on a logical and general procedure and the experiments were defined according to a statistical design of experiment, the developed model is expected to be valid in the entire rang defined in Table 4.6. To ensure the validity of the current model in other points, the obtained predictions for glycerol and ethanol (Eqs. (4–32) and (4–33)) assessed in face-centered and random design points. The face-centered points play a significant role in the statistical design of experiments as they are located on the center of each cube face (where the cube is considered as the space of variation of the three operating parameters, see Figure 2.16). In the current work, these points can ensure the validity of the developed model for the entire range, as the face-centered experimental design points have the highest distance from the Box-Behnken design points. In this regard, the experiments based on face-centered design were carried out according to Table 4.2 and Table 4.4 for glycerol and ethanol, respectively. To check the validity of the models in other levels defined in the experimental design range (Table 4.6), additional experiments were selected randomly according to random function of Matlab® for glycerol and ethanol (Table 4.5).

To check the validity of the developed model based on face-centered and random experimental data, the corresponding diagrams of dispersion obtained for glycerol and ethanol are presented in Figure 4.3b-c and Figure 4.4b-c. As it is obvious, these diagrams of dispersion also confirm that the developed model has a good prediction. In addition, for the statistical analysis of the goodness of fit, the values of R^2, R^2_{adj}, *RMS*, *AAD*, and *MAE* were calculated for glycerol and ethanol (Table 4.8). As it can be inferred, R^2 values for both face-centered (0.966 and 0.948 for glycerol and ethanol, respectively) and random (0.978 and 0.971 for glycerol and ethanol, respectively) designs are close to 1. Moreover, R^2_{adj} values obtained for face-centered (0.919 and 0.878 for glycerol and ethanol, respectively) and random (0.901 and 0.867 for glycerol and ethanol, respectively) designs are in close agreement with the corresponding R^2. Furthermore, the small values of *RMS*, *AAD*, and *MAE*, verify the good approximation and generalization characteristics of the developed models. Comparison between the R^2 of optimization and validation data (Table 4.8) reveals that they are in a very good agreement; thus, the measured kinetic parameters are accurate and the number of experimental data used to calculate the value of kinetic parameters is sufficient.

Table 4.8. Statistical analysis of comparison between the kinetic model predictions and the experimental data designed based on Box-Behnken, face-centered and random experimental design of glycerol and ethanol.

Parameter	*Glycerol*			*Ethanol*		
	Box-Behnken	***face-centered***	***random***	***Box-Behnken***	***face-centered***	***random***
R^2	0.964	0.966	0.978	0.973	0.948	0.971
R^2_{adj}	0.925	0.919	0.901	0.943	0.878	0.867
RMS	3.93	3.80	2.60	2.08	2.22	1.69
AAD	12.8	12.6	1.00	12.3	4.10	0.855
MAE	3.16	3.25	0.285	1.79	0.794	0.191

4.5.3. Model validation with data from literature

The rate of hydrogen production using Pt/TiO_2 obtained in this work was first compared with experimental data from literature to ensure that they are in the same order [74, 150], thus proving the proper performance of the prepared catalyst. The predictions of the proposed model were then compared with literature data to validate the model. In the present work, the experiments used to validate the proposed model were performed using Pt/TiO_2 as photocatalyst, and glycerol or ethanol as substrate, and were designed in the range shown in Table 4.6. To assess the ability of the present model to predict the rate of hydrogen production for other substrates, photocatalysts, and ranges of the independent variables, the predictions of Eq. (4–31) were compared with other sets of experimental data from literature and the results are presented in Table 4.9. The first two columns of this table show the type of substrate and photocatalyst used in each work. Based on the type of investigated operating parameter in each work, a kinetic model is developed according to Eq. (4–31) and presented in the third column. The value of kinetic parameters for each kinetic model was optimized using GA and based on the experimental data in each work. Finally, the agreement between model predictions and the literature experimental data were evaluated and R^2 values are presented in Table 9. For example, Fan et al. [257] reported the experimental data of the rate of hydrogen production from methanol using TiO_2/RGO. Therefore, a kinetic model was developed as a function of substrate concentration, and other parameters (photocatalyst load, light intensity, and time) in Eq. (4–31) were combined with α as they were constant. Finally, the kinetic parameters (α, δ, and ε) were calculated using the experimental data and R^2 value

was found to be 0.999. In brief, according to Table 4.9, the experimental data from the literature also confirm the validity of proposed model as all R^2 values are close to 1.

Table 4.9. The values of kinetic parameters and R^2 obtained for the present model based on the experimental data from literature for different substrates, photocatalysts and operating conditions.

Substrate	Photocatalyst	Independent parameters[1]	R^2	Ref
Methanol	TiO_2/RGO	*Sub*	0.999	[257]
Methanol	CuO/TiO_2	*Sub*	0.937	[258]
Methanol	Au/TiO_2	*I*	0.980	[259]
Methanol	Pt/TiO_2 (P25)	*I*	0.906	[260]
	Pt/TiO_2 (P25HT)		0.998	
	Pt/TiO_2 (Hombikat)		0.999	
Ethanol	Au/TiO_2	*I, Sub*	0.986	[202]
Glycerol	Pt/TiO_2	*Sub*	0.910	[84]
Glycerol	Pt/TiO_2	*Cat, t*	0.987	[74]
Ammonium sulfite	Pt/ZnSe-CdS	*Cat, I*	0.916	[261]
Cellulose	Pt/TiO_2	*Cat, Sub*	0.930	[221]
Swine sewage	Pt/TiO_2	*Cat*	0.943	[222]

[1]Parameter whose effect was evaluated and which is found in the kinetic model: *Cat* (catalyst loading), *I* (light intensity), *Sub* (substrate concentration), *t* (time).

According to Table 4.9, the present model has a good ability for predicting the rate of hydrogen production not only from alcohols such as glycerol, ethanol, and methanol, but even other kind of substrates such as ammonium sulfite, cellulose, and swine sewage. Moreover, it can be inferred that other than TiO_2 (including homemade, P25 and Hombicat,), this model is valid for Z-scheme (Pt/ZnSe-CdS) and composite (TiO_2/RGO) photocatalysts. In addition, by considering the list of photocatalysts presented in Table 9, this model has a good prediction accuracy for the photocatalysts decorated by other cocatalysts such as CuO and Au. On the other hand, the validation of Eq. (4–31) with experimental data from literature shows the proposed model can have a very good accuracy in wide ranges of catalyst loading, substrate concentration, and light intensity.

4.5.4. Comparison of the present and L-H based models

As mentioned above, regarding photocatalytic production of hydrogen from substrates in liquid phase, all of the observed studies used the L-H model to develop their kinetic models [98, 195-202]. Therefore, the capability of the proposed model and its advantages over previous models can be assessed by comparing the predicted rates of the present and L-H-

based models with a series of experimental data. As the L-H model is just a function of the substrate, this comparison was done at three glycerol concentrations and different times. In these experiments, light intensity and catalyst loading were set to average values of the investigated range, i.e., 800 $\mu W/cm^2$ and 1.5 g/L, respectively.

The results of this comparison for glycerol (rate of hydrogen production versus time) are presented in Figure 4.5. It can be seen that the proposed model predictions and experimental values are in very good agreement with R^2 of 0.954, 0.985, and 0.9879 for 1%, 15.5%, and 30% of glycerol concentration, respectively. However, the L-H-based model cannot be fitted acceptably to the experimental data and the corresponding R^2 values were found to be -0.2653, -0.0836, and 0.0475, respectively. Comparison of these R^2 values proves the advantage of the current intrinsic kinetic model over L-H-based models. It is worth mentioning that light intensity and catalyst loading are considered fixed. The variability of these parameters makes deviations of L-H-model prediction from the experimental values more significant.

Thus, the obtained results imply that the developed intrinsic kinetic model has a good capability to predict the rate of hydrogen production as a function of catalyst loading, light intensity, glycerol concentration, and time. This observation shows that the proposed reaction mechanism and the assumptions made to develop the intrinsic kinetic model are valid.

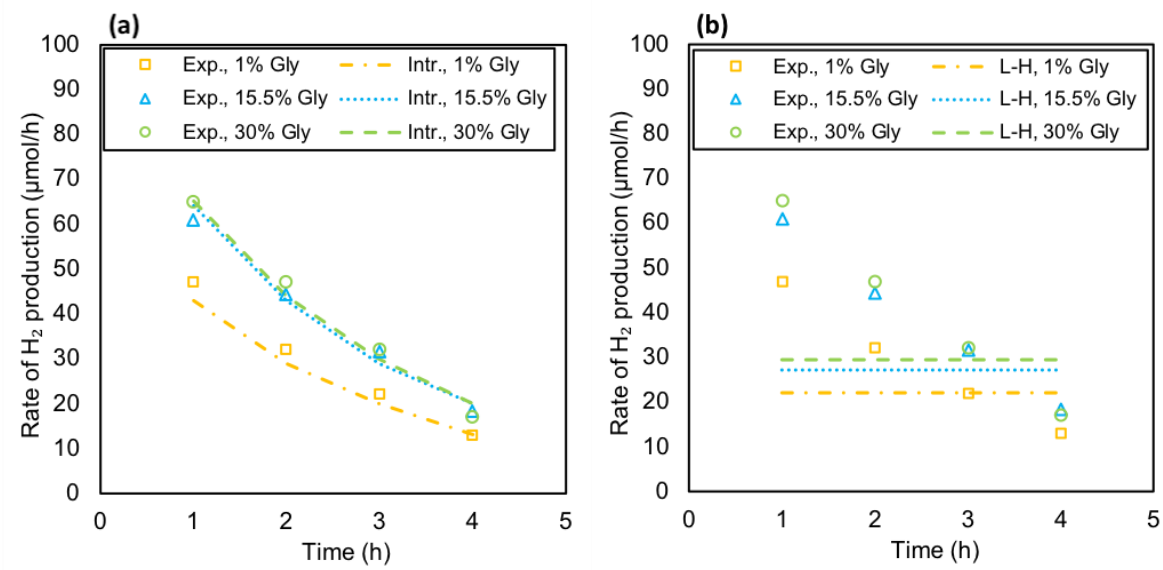

Figure 4.5. Comparison between the predictions by (a) the proposed intrinsic model and (b) L-H model, for glycerol volume percent of 30%, 15.5%, and 1%. The light intensity and catalyst loading were set at 800 µW/cm^2 and 1.5 g/L, respectively. Exp: experimental data, Intr: intrinsic kinetic model prediction, and L-H: L-H model prediction.

4.5.5. Kinetic parameter analysis

According to Eqs. (4–32) and (4–33), the values of power for catalyst loading and light intensity were obtained at 0.400 and 0.271 for glycerol and 0.265 and 0.907, respectively. Therefore, the assumptions made in Eqs. (4–21) and (4–25) are valid and those reactions are not first order in respect to catalyst loading and light intensity. In addition, ξ value for glycerol is -0.390 which indicates that the rate of hydrogen production from this substrate reduces rapidly with time, as photocatalyst deactivates rapidly during glycerol conversion, which is consistent with other experimental data [150]. However, ξ value for ethanol is close to zero which shows the rate of hydrogen production is almost fixed, and the photocatalyst remains active for this substrate. Based on the value of ζ in Eqs. (4–32) and (4–33), the values of k_{dec} (which is the first-order rate constant of the catalyst surface sites deactivation, see Eq. (4–19)) were calculated at 0.191 and 00.00451 for glycerol and ethanol, respectively. This shows that the catalyst deactivation rate was low during ethanol reaction. The deactivation of catalyst can be analysed from the experimental data given in Tables 1-4. As can be clearly seen, the rate of hydrogen production decreases because of catalyst deactivation for glycerol, but a limitted catalyst deactivation can be observed in the case of ethanol in the same time

scale. There are also experimental evidences in the literature that prove that photocatalyst deactivation indeed occurs for glycerol photoreforming [86], but in the case of ethanol the catalyst remains active for a longer time [262]. The higher deactivation of Pt/TiO_2 during the photocoversion of glycerol, compared to ethanol, is in line with previous research [82] and can be attributed to the formation of intermediates/products, which irreversibly adsorbed on the catalyst active sites [263].

Gas and liquid products generated during glycerol and ethanol conversion were analyzed by GC. Other than hydrogen, carbon dioxide and methane were also detected in the gas phase for both ethanol and glycerol. In the liquid phase, only acetaldehyde and formaldehyde were detected for ethanol. In the case of glycerol, other than these products, acrolein, glyceraldehyde, and hydroxyacetone were also found. Previous studies on photocatalytic conversion of glycerol and ethanol also reported the presence of similar products [80, 97, 140, 149, 176, 178, 183, 264-267].

The value of ε in the present model for glycerol and ethanol were obtained 2.04 and 4.15, respectively. Consequently, they are almost twice and three times the corresponding power in L-H-based models where ε is considered 1. This fact also shows simple L-H models cannot appropriately predict the behavior of this reaction.

4.6. Conclusion

In this work, an intrinsic kinetic model was developed for the photocatalytic production of hydrogen in liquid phase. To this end, a mechanism was suggested and rate expressions were obtained based on the suggested mechanism. To develop the kinetic model, some effective novelties were taken into account, such as:

- the rate of hydrogen production as a function of proton reduction step (not L-H based);
- the rate of hydrogen production as a function of catalyst loading, light intensity, and time;
- the deactivation of active surface sites of the photocatalyst;
- the effect of catalyst loading on both of photon and reactant adsorption;

- the rate of substrate reaction as i^{th} order in respect to substrate concentration to find its order;

To optimize the kinetic parameters by using the GA, glycerol and ethanol were considered as representative substrates, and the experiments were designed in different operating conditions based on Box-Behnken experimental design. To assure the validity of the developed model, model predictions were assessed with two other series of experiments which were designed according to face-centered and random designs. The model's goodness of fit with all series of the experiments were statistically analyzed in terms of R^2, R^2_{adj}, *RMS*, *AAD*, and *MAE*, and very good agreement was found between the model and experimental data. Moreover, the ability of the model to predict the rate of hydrogen production for other substrates, photocatalysts, and ranges of operating parameters was confirmed by comparing model predictions with the experimental data from literature. Finally, the predicted rates of hydrogen production with the present and L-H-based models were compared with experimental data. The results clearly confirmed the advantages of the developed model compared to L-H model. These results show that the proposed mechanism and developed kinetic model are valid for photocatalytic production of hydrogen in liquid phase and the proposed assumptions are valid. Although the present model proved its validity in the range of designed experiments (i.e. light intensity of 400-1200 $\mu W/cm^2$, catalyst loading of 0.1-3 g/L, glycerol% of 1-30%, and reaction time of 1-4 h), the validation of the model with different data from literature clearly showed that the proposed model can also be applied with a very good accuracy in a wider ranges of the above-mentioned operating parameters.

In conclusion, the present approach and the resulting rate expression are appropriate for use in various future works to determine and analyze the rate of hydrogen production using other substrates and photocatalysts.

Following the results of the relative importance of the operating parameters (Chapter 3), the catalyst loading was found to be one of the most effective parameter. Therefore, composite photocatalysts can be a suitable alternative that can offer the reduction of the amount of photocatalyst consumption together with the enhancement of the photocatalytic activity.

In the following chapter, ***carbon nanotube*** *and* ***carbon sphere*** *were incorporated in TiO_2@CT composites and then used for photocatalytic* ***hydrogen*** *production from* ***glycerol****. Incorporation of biobased carbonaceous templates for preparation of TiO_2@CT composites is a sustainable alternative to improve the photocatalytic activity of TiO_2. CNT and CS are two well-known CTs with unique structural, chemical, thermal, and electrical properties, well suited for TiO_2@CT composites preparation. The research conducted on photocatalytic activity of TiO_2@CT composites for valorization of alcoholic waste has shown either positive effect of CNT and CS in photocatalytic enhancement, or insignificant effect of CTs. Therefore, a thorough investigation of TiO_2@CT composites is essential to clarify the roles of CTs in the enhancement of photocatalytic activity.*

Chapter 5 : Effects of carbon nanotube and carbon sphere templates in TiO_2 composites for photocatalytic hydrogen production

Résumé

L'incorporation des composants carbonés (CT) dans les composites de TiO_2 constitue une alternative prometteuse pour augmenter l'activité photocatalytique du TiO_2. Dans ce travail, les effets de l'incorporation des nanotubes de carbone (*carbon nanotubes*) et des sphères de carbone (*carbon spheres*) dans les composites de TiO_2 ont été étudiés et le rôle de ces CT en tant que matrice, cocatalyseur et adsorbant a été étudié. À cette fin, trois méthodes différentes ont été utilisées pour former une couche de TiO_2 sur la CT: sol-gel en phase alcoolique, sol-gel en phase aqueuse et hydrothermal. Le rôle de la CT en tant que matrice a été examiné par l'analyse morphologique des composites préparés. Les rôles de co-catalyseur et d'adsorbant de la CT ont été étudiés en fonction de la production photocatalytique d'hydrogène à partir de glycérol. Il est intéressant de noter que l'incorporation de CNT dans un composite de TiO_2 peut environ doubler le taux de production d'hydrogène (i) en l'absence de Pt ou (ii) à faible concentration en glycérol. En conséquence, il a été conclu qu'en plus d'être une matrice, le nanotubes de carbone peut jouer deux rôles importants en tant que cocatalyseur et adsorbant.

Abstract

Incorporation of carbonaceous templates (CT) into TiO_2 composites is a promising alternative to increase the photocatalytic activity of TiO_2. In this work, the effects of carbon sphere (CS) and carbon nanotube (CNT) incorporation (as CT) in TiO_2 composites were thoroughly investigated and the roles of these CTs as template, cocatalyst, and adsorbent were studied. To this end, three different methods were utilized to form a layer of TiO_2 on the CT: alcoholic phase sol−gel, aqueous phase sol−gel, and hydrothermal. The role of CT as template was examined through morphology analysis of the prepared composites. The cocatalyst and adsorbent roles of CT were investigated based on photocatalytic hydrogen production from glycerol. Interestingly, it was found that the incorporation of CNT into TiO_2 composite can approximately double the rate of hydrogen production (i) in the absence of Pt or (ii) at low glycerol concentration. Accordingly, it was concluded that in addition to being a template, the CNT can play two important roles as cocatalyst and adsorbent.

5.1. Introduction

Glycerol is a byproduct of biodiesel production from biomass [59]. Because of glycerol overproduction, its price in the market has decreased significantly in the past years, setting it up as a promising renewable feedstock [268, 269]. Photocatalytic valorization of biobased glycerol to hydrogen is an alternative to today's critical energy, environmental, and sustainability issues [229, 270]. Photocatalysis is currently being considered as a promising technique with many applications, such as renewable energy production and treatment of environmental pollution. Although TiO_2 is the most prominent photocatalyst and has attracted the most attention in photocatalysis research, it still suffers from low efficiency [173, 271]. Utilization of a carbonaceous template (CT) incorporated composite to enhance the photocatalytic activity of TiO_2 has been widely investigated in recent years [66, 272]. Incorporation of biobased carbonaceous templates to prepare TiO_2@CT composites is an effective and sustainable approach [273, 274].

The discovery of fullerenes in 1985 drew tremendous attention to the application of carbon (nano)materials in contemporary research [275]. For instance, since the discovery of carbon nanotube (CNT) in 1991 [276], its applications in different fields, including catalysis, have been extensively studied. As the most well-known one-dimensional carbonaceous material with unique structural, chemical, thermal, and electrical properties [277], CNT can be used in many applications such as preparation of TiO_2 composites [175, 278]. Carbon sphere (CS) is another carbonaceous material that has a long history, but has especially gained a lot of attention in the past decade. CS benefits from the advantages of both carbon materials and spherical colloids that provide it with remarkable characteristics such as uniform geometry, good liquidity, controllable porosity, surface functionality, adjustable particle size distribution, and excellent chemical and thermal stability[279, 280]. These characteristics suggest CS as a promising CT for photocatalytic applications.

To prepare a TiO_2@CT composite, simple mechanical mixing of presynthesized semiconductors and CT may not enhance the photocatalytic activity [281]. Thus, to have an intimate contact between semiconductor and CT, the semiconductor should be synthesized in the presence of CT [282]. Sol−gel and hydrothermal methods are the most common approaches for the preparation of carbonaceous TiO_2 composites [66, 278]. In the synthesis,

the thermal treatment is important because it affects the crystallinity, particle sintering, and electronic interphase interaction between TiO_2 and CT [283].

Several studies have been performed on the photocatalytic activity of TiO_2 and CT composites for hydrogen generation [284-287]. Although many of them indicated the effectiveness of CNT and CS in photocatalytic activity, some showed that they may not be beneficial in specific cases [66, 288]. Leary *et al*. [66] conducted a comprehensive literature review on the effect of carbonaceous materials on the enhancement of TiO_2 photocatalytic activity and concluded that the first challenge in further exploitation of synergistic effects of carbonaceous materials is a better understanding of the fundamentals of enhancement of photocatalytic activity using carbonaceous materials as well as controlling the synthesis method conditions.

CTs can play different roles, such as support, cocatalyst, and adsorbent [289]. First, as a support, CTs are promising materials available in different 0D, 1D, 2D, and 3D allotropes [290]. This vast variety provides the opportunity of TiO_2 formation in different shapes such as nanotube, sphere, sheet, and nanodiamond. Second, CTs can also play the role of cocatalyst as they possess conjugated π electrons that can accelerate the transfer of photogenerated electrons from conduction band to H_2 production active sites [291]. Considering the new approach of using low-cost earth-abundant metals or metal free materials [292], CTs are promising cheap, abundant, stable, and nontoxic cocatalysts. Third, the high adsorption capacity of CTs reveals the effectiveness of CT incorporation as adsorbent in TiO_2 composites, as CTs not only increase the concentration of the substrate on the surface of photocatalyst but even enhance the product selectivity [290]. To the best of our knowledge, no study has focussed on the individual effects and roles of CTs in photocatalytic hydrogen production.

In this context, the aim of the present work is to perform a thorough comparative study on carbonaceous TiO_2 composites to explore the individual roles of CTs as template, cocatalyst, and adsorbent. The analysis was performed using different (i) carbonaceous material (CS and CNT), (ii) synthesis methods (hydrothermal, alcohol phase sol−gel, and aqueous phase sol−gel), and (iii) calcination temperatures (300−800 ºC). The role of CT as template was examined through the morphology analysis of the prepared composites. The synergistic

functions of CT and Pt during photocatalytic hydrogen production reactions were evaluated to investigate the effect of CT as cocatalyst. Finally, the adsorbent role of CT was assessed by comparing the amount of hydrogen produced in the presence or absence of CT.

5.2. Experimental section

5.2.1. Materials

Graphistrength C100 multiwalled CNT (≥90%,10−15 nm diameter, 5−10 walls, 1−10 μm length [293]) was kindly provided by ARKEMA and functionalized as described below. Titanium (IV) isopropoxide (TTIP, ≥98%) and titanium (IV) n-butoxide (TBOT, ≥99%) were obtained from Acros Organics. Glycerol (≥99.7%), acetic acid (≥99.7%), ethyl alcohol (99.99%), and 2-propanol (≥99.9%) were purchased from VWR Analytical, Caledon, Commercial Alcohols, and Fisher Scientific, respectively. Nitric acid (68.0−70.0%), sulfuric acid (95.0−98.0%), and hydrochloric acid (36.5−38.0%) were acquired from Anachemia. Benzyl alcohol (≥99%) and D−(+)−glucose anhydrous (≥99%) were bought from Alfa Aesar. Hexachloroplatinic acid (IV) ($H_2PtCl_6 \cdot 6H_2O$, ≥37.50% Pt) was purchased from Sigma-Aldrich. Potassium bromide (≥99%) of Oakwood Chemicals brand was used to make pellets for Fourier transform infrared (FT-IR) analysis.

Table 5.1. List of the prepared samples.

nomenclature	template	synthesis method	calcination temperature (ºC)
TiO_2@CS_HT_CN	CS	hydrothermal	noncalcined
TiO_2@CS_HT_C300	CS	hydrothermal	300
TiO_2@CS_HT_C400	CS	hydrothermal	400
TiO_2@CS_HT_C500	CS	hydrothermal	500
TiO_2@CS_HT_C600	CS	hydrothermal	600
TiO_2@CS_HT_C800	CS	hydrothermal	800
TiO_2@CNT_HT_CN	CNT	hydrothermal	noncalcined
TiO_2@CNT_HT_C300	CNT	hydrothermal	300
TiO_2@CNT_HT_C400	CNT	hydrothermal	400
TiO_2@CNT_HT_C500	CNT	hydrothermal	500
TiO_2@CNT_HT_C600	CNT	hydrothermal	600
TiO_2@CNT_HT_C800	CNT	hydrothermal	800
TiO_2_HT_C400	templateless	hydrothermal	400
TiO_2@CNT_ALSG_C400	CNT	alcohol phase sol−gel	400
TiO_2@CS_ALSG_C400	CS	alcohol phase sol−gel	400
TiO_2_ALSG_C400	templateless	alcohol phase sol−gel	400
TiO_2@CNT_AQSG_C400	CNT	aqueous phase sol−gel	400
TiO_2_AQSG_C400	templateless	aqueous phase sol−gel	400

5.2.2. Sample preparation

5.2.2.1. Nomenclature

The prepared samples were coded as a string with three elements: TiO_2@A_B_C*X* (Table 5.1). A represents the type of template employed (CS or CNT). When no template was used during the synthesis, only the type of semiconductor (TiO_2) is mentioned. B represents the synthesis method: HT for hydrothermal, ALSG for alcoholic phase sol−gel, and AQSG for aqueous phase sol−gel. C*X* represents the calcination temperature, X=300-800 ºC (CN denotes a noncalcined sample).

5.2.2.2. CS preparation

The CS template was prepared using glucose as a sustainable carbon source based on the method described in other work [204]. Briefly, 36 g of glucose was dissolved in 200 mL deionized water and kept at room temperature under 30 min of stirring. Then, the solution was transferred into a 460-mL autoclave and kept at 180 ºC for 18 h. The formed brownish carbon sphere particles were filtered and washed with distilled water 3 times using a centrifuge. Finally, the sample was dried at 80 ºC for 24 h. Through all the synthesis methods, 5% CS [294] was used to prepare TiO_2@CS composite.

5.2.2.3. Functionalization of CNT

To attach TiO_2 particles on the surface of CT, oxygen-containing groups such as hydroxyl, carboxyl, carbonyl, and epoxy are required on the surface to provide nucleation sites and play the role of anchor toward the reagents [205]. Because of the absence of these groups in the case of pristine CNT, functionalization is typically essential. An acid treatment was therefore performed to functionalize the CNT and remove the catalytic metal residues and amorphous carbon [295]. The pristine CNT was first washed with 32 wt % HCl at 70 ºC for 12 h in a round-bottom flask equipped with a condenser [296]. The sample was then washed with deionized water and kept at boiling temperature in a 10 M nitric acid solution for 3 h [283]. It is worth mentioning that the functionalized CNT using a mixture of H_2SO_4:HNO_3 = 3:1 (volume ratio) was not found effective because of extensive damage to the CNT structure and low recovery. After being cooled, the sample was filtered under vacuum and rinsed several times by deionized water to reach the neutral pH of the filtrate. The prepared sample was dried in an oven at 80 ºC for 16 h. Approximately 9% weight loss was observed during the acid treatment process. All the TiO_2@CNT composites were prepared with 20% CNT[66, 297]; however, samples containing 1% CNT were also prepared and used only to analyze the adsorbent role of CNT.

5.2.2.4. Hydrothermal synthesis

To prepare composites by hydrothermal synthesis, the required amount of TTIP was added to propanol (solvent) and BA (linking agent) with the volume ratio of TTIP:BA:PrOH equal to 10:17.5:150. After 30 min of continuous stirring, CT (CS or HCl-treated CNT which were prepared as described in sections 3.2.2.2 and 3.2.2.3, respectively) was added to the solution

and sonicated in an ice bath for 1 h; the solution was covered to prevent alcohol evaporation and moisture absorption. The as-obtained suspension was transferred to a 460 mL Teflon-lined stainless-steel autoclave and heated in an oven at 180 ºC for 48 h. After formation of titanium on the CT, the brownish/black product was harvested by centrifugation. A washing process involving three cycles of centrifugation, washing, and redispersion in ethanol was then performed. The resulting composite was dried at 90 ºC overnight and calcined in air atmosphere for 2 h. For comparison purposes, the above-mentioned procedure was repeated without the addition of CT.

5.2.2.5. Alcoholic phase sol−gel synthesis

The required amount of CT (CS or HCl-treated CNT) was added to ethanol, and the suspension was subjected to ultrasonication for 1 h. Then, BA and water were added to the suspension and mixed for 30 min (solution A). Separately, TBOT was dissolved in ethanol by mixing for 30 min (solution B). Solution B was added dropwise into solution A with the rate of 30 mL/h using a syringe pump to obtain a TBOT:BA:H_2O:EtOH molar ratio of 1:5:5:100. After ultrasonication, the mixture remained under stirring for 1 h to completely hydrolyze the titanium precursor. The formed suspension was subjected to 3 cycles of centrifugation and washing and subsequently dried at 90 ºC overnight. The obtained powder was calcined at 400 ºC for 2 h (heating ramp of 5 ºC min^{-1}). Templateless TiO_2 was also prepared according to the procedure mentioned above without addition of CT for comparison purposes.

5.2.2.6. Aqueous phase sol−gel synthesis

The aqueous phase sol−gel synthesis was done according to our previous research [158, 171]. Briefly, a beaker containing glacial acetic acid was placed in an ice bath to freeze. TTIP was added and mixed under magnetic stirring for 30 min. The beaker was covered by a layer of parafilm to avoid moisture absorption or acid evaporation. After deionized water was slowly injected using a syringe pump (pumping rate of 30 mL/h), the nitric acid-treated CNT was added to the solution and ultrasonicated in the ice bath under magnetic mixing for 1 h. The obtained suspension was subsequently kept under stirring for 2 h to let TTIP completely hydrolyze. The mixture was sonicated again in the ice bath for 15 min and aged at room temperature in the absence of light for 24 h. Then, the suspension was gelated at 75 ºC

overnight and dried at 120 ºC for 2 h. The dried gel was ground into a fine powder and calcined in air at 400 ºC (heat ramp of 5 ºC/min). Templateless TiO_2 was also prepared according to the same procedure, but without employing CT.

5.2.3. Characterization techniques

The structure and morphology of the prepared samples were analyzed by a scanning electron microscopy (SEM) using JEOL JSM-840A device. Transmission electron microscopy (TEM) images of the samples were captured using a JEOL JEM 1230 operated with a 120 kV accelerating voltage. For SEM and TEM, a 25 ppm suspension of the samples in ethanol was sonicated to detach the agglomerated particles, and the analyses were performed after drying. Particle size analyses were performed using multiple SEM and TEM images. X-ray diffraction (XRD) was collected for $2\theta=10-80^{o}$ on a Bruker SMART APEXII X-ray diffractometer equipped with a Cu Kα radiation source (λ= 1.5418 Å). The percentage of rutile phase in the samples was calculated based on Eq. (5–1) [207].

$$\%Rutile = \frac{1}{\left[1+0.8(I_A / I_B)\right]} \times 100 \qquad (5–1)$$

where I_A and I_B represent the intensities of anatase (101) and rutile (110) reflections, respectively.

Thermogravimetry and differential thermal analyses (TG/DTA) of the prepared samples were carried out on a TGA Q5000IR from 50 to 700 ºC with a heating ramp of 10 ºC/min and air flow of 25 mL/min. For BET measurements using a Micrometrics TRISTAR 3000 instrument, the samples were dried for 4 h at 120 ºC to remove the adsorbed water. FT-IR spectrum was taken using an FTS 45 infrared spectrophotometer with the KBr pellet technique. ATR-FTIR absorption spectra were measured by a Thermo Nicolet Magna-850 spectrometer device and a Golden Gate® ATR accessory.

5.2.4. Photocatalytic hydrogen production

For each experiment, an aqueous solution containing 10% glycerol (which is the average glycerol content in biodiesel production wastes) and 1 g/L catalyst was introduced in 10 mL vials. To investigate the effect of glycerol concentration, some tests were also performed for 1% and 50%. The required amount of platinum (Pt) precursor solution in deionized water

was added to form 1 wt% Pt as cocatalyst on the surface of the photocatalyst. The final volume of the suspension was adjusted to 5 mL using deionized water. Before starting the experiments, each of the following steps was performed for 15 min: (a) ultrasonication by a Hielscher UP400S Ultrasonic Processor to detach the agglomerated catalyst, (b) purging with 20 mL/min flow of nitrogen to remove oxygen, and (c) mixing the suspension to ensure the adsorption of glycerol on the surface of the catalyst. The photocatalytic hydrogen production experiments were done at ambient temperature by starting irradiation using four Black-Ray 20 W mercury tubes (365 nm). A Thermo-Scientific^{TM} Cimarec^{TM} 15 position magnetic stirrer was utilized to have a uniform 500 rpm mixing during photocatalytic experiments. Pt was deposited on the photocatalyst at the beginning of the photocatalytic reaction based on in situ photodeposition method [84]. The amount of hydrogen produced by each of the prepared samples was measured by analyzing 250 µL of the product gas headspace after 4 h of irradiation, using an Agilent Technologies 7820A gas chromatograph (GC). The GC equipped with an HP-Molesieve column (Agilent) and TCD detector used nitrogen as the carrier gas. The experiments were performed in triplicate, and a mean value is reported. Some experiments were done in the absence of light and photocatalyst to be certain of the photocatalytic nature of the reaction. Some tests were also performed using a pure template, and no photocatalytic activity was observed.

5.3. Results and discussion

5.3.1. Morphology analysis

The structure and morphology of TiO_2 nanoparticles formed on the CT were investigated based on SEM and TEM analyses (Figure 5.1 and Figure 5.2).

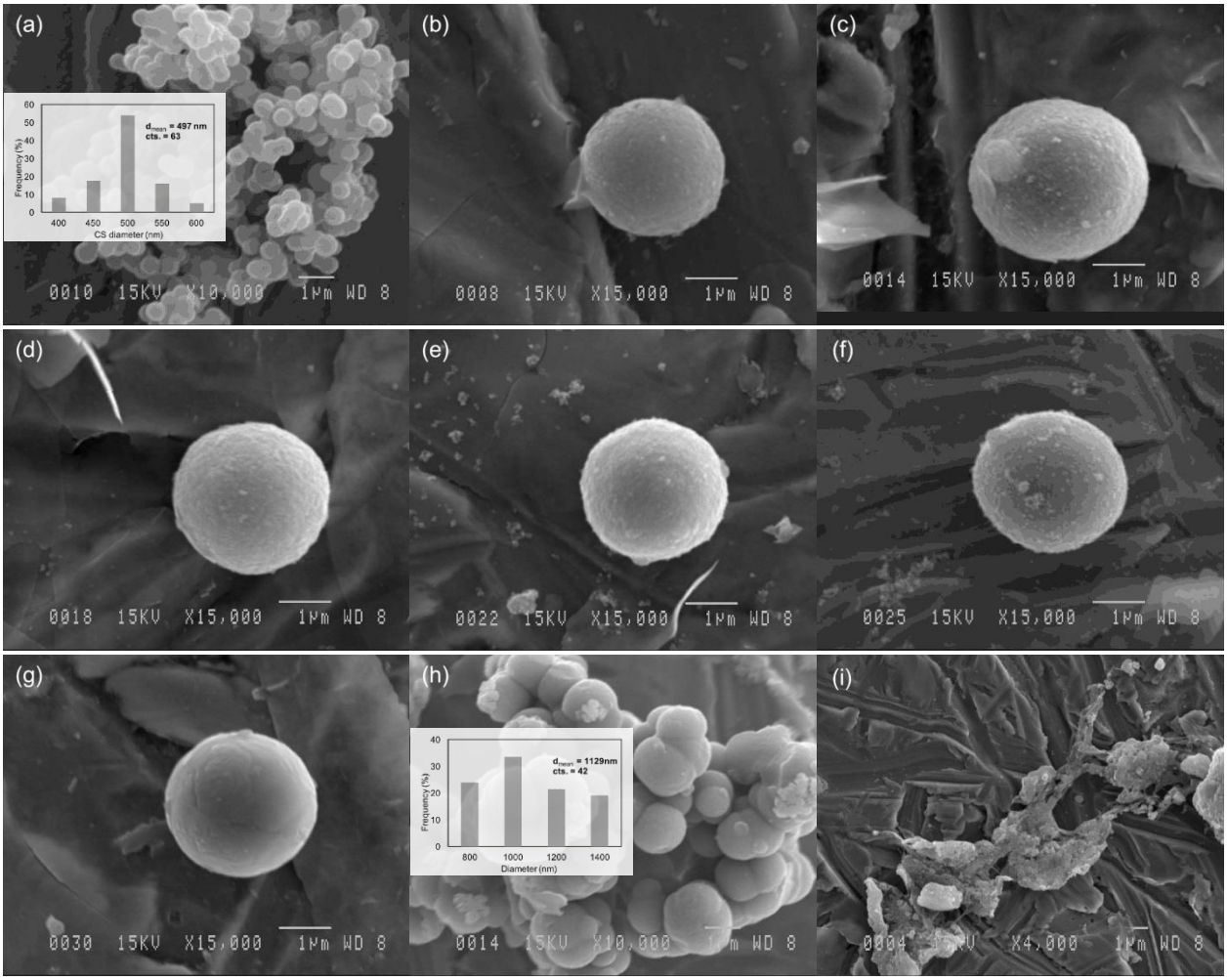

Figure 5.1. SEM images of (a) as-prepared CS, (b) TiO_2@CS_HT_CN, (c) TiO_2@CS_HT_C300, (d) TiO_2@CS_HT_C400, (e) TiO_2@CS_HT_C500, (f) TiO_2@CS_HT_C600, (g) TiO_2@CS_HT_C800, (h) TiO_2@CS_ALSG_C400, and (i) TiO_2@CNT_AQSG_C400.

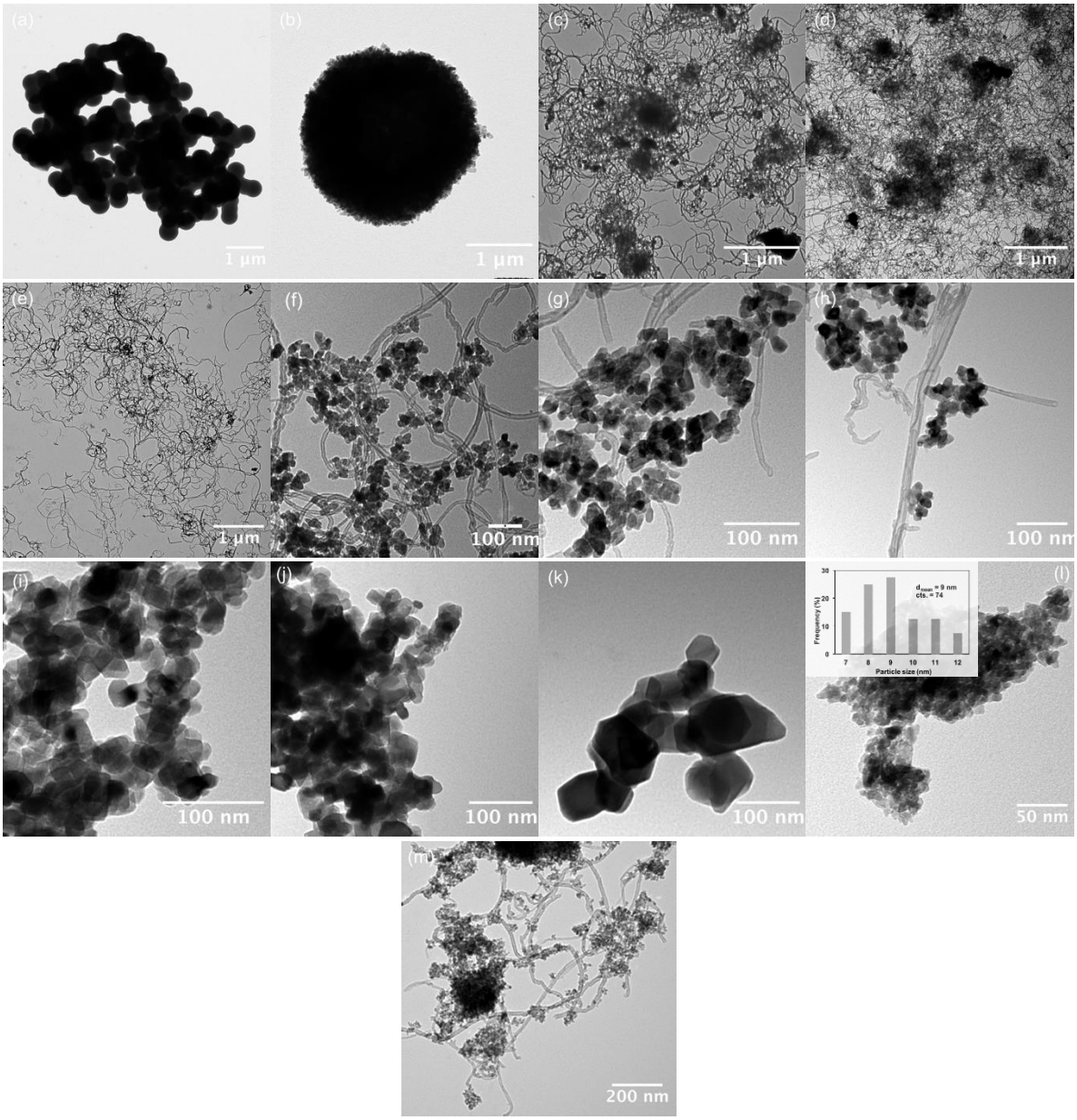

Figure 5.2. TEM images of (a) as-prepared CS, (b) TiO_2@CS_HT_CN, (c) pristine CNT, (d) HCl-treated CNT, (e) HCl- and HNO_3 -treated CNT, (f) TiO_2@CNT_HT_CN, (g) TiO_2@CNT_HT_300, (h) TiO_2@CNT_HT_400, (i) TiO_2@CNT_HT_500, (j) TiO_2@CNT_HT_600, (k) TiO_2@CNT_HT_800, (l) TiO_2_AQSG_C400, and (m) TiO_2@CNT_AQSG_C400.

As can be seen from the SEM image of as-prepared CS (Figure 5.1a), the spheres have almost uniform spherical morphology and no broken *CS* is observed. On the basis of the TEM image of as-prepared CS (Figure 5.2a), the spheres are not uniformly formed through the entire bulk. This tendency to accretion is common in the CS with less than 1000 nm diameter [298]. Indeed, the size distribution histogram of CS depicted in the inset of Figure 5.1a reveals diameters between 400 and 600 nm, with an average value of 497 nm.

Figure 5.1b−g depicts the SEM of *TiO_2 samples prepared on CS by hydrothermal method* and calcined at different temperatures. A spherical morphology with a particle diameter of around 3 µm can be seen for all samples. The surface of the spheres is rough, suggesting that they may be formed by nanocrystalline flakes. This assumption was proved by the TEM image of the spherical TiO_2 surface (Figure 5.2b). Although the samples calcined at different temperatures show a similar spherical shape, the effect of increasing calcination temperature on the sintering can be seen on the surface. For instance, the surface roughness of the spheres calcined at 800 ºC is evidently reduced compared to those calcined at the lower temperature (Figure 5.1c−g), in agreement with the obtained BET result (Table 5.2). Nevertheless, almost no noticeable change in the sphere diameter is observed, which is consistent with the work done by Bakardjieva et al. [299]. This observation suggests that the modification of the structure of the samples prepared on CS (through carbon sphere removal by burning, transformation of amorphous phase to anatase and anatase to rutile, and sintering) did not affect the sphere diameter but predominantly influenced the morphology of the carbon sphere surface.

Figure 5.1h depicts the SEM image and the spherical size distribution of the *TiO_2 samples grown on the CS using the alcoholic phase sol−gel method*. By considering the shape of CS (Figure 5.1a), it can be seen in Figure 5.1h that the TiO_2 particles formed uniformly on the surface of CS and formed in the shape of CS. The diameter of particles is distributed between 800 and 1400 nm, and the average diameter is 1129 nm. Thus, the average diameter is almost doubled in comparison to CS.

The TEM images of the *pristine, HCl-treated, and HCl and HNO_3 treated CNT* samples are shown in Figure 5.2c−e. As can be seen, the pristine CNT is a network of curved entanglements and intertwined strands, with some intense black agglomerates that can be organic and metallic impurities. HCl treatment had no significant effect on the morphology of the CNT; however, the treatment by HNO_3 caused opening of the CNT bundles and shortening of the length of strands that facilitate the CNT access by the TiO_2 particles [300]. Moreover, in comparison to the pristine and acid treated CNT, acid-treatment successfully eliminated the impurities (as confirmed by TGA results).

TEM analysis of *TiO_2 samples formed on the CNT by hydrothermal method* (Figure 5.2f−k) illustrates the formation of TiO_2 nanoparticle clusters with an intimate bound along the side walls as well as the ends of CNT. Similar results have been previously obtained on TiO_2@CNT composites [301-304]. As seen in Figure 5.2f−h, the TiO_2 nanoparticles distributed between the bundles and the CNT are able to hinder the agglomeration of TiO_2 particles. FT-IR analysis of CNT also confirmed the formation of functional groups on the surface of CNT as a result of the functionalization process. These functional groups provided nucleation sites and played the role of anchor during formation of TiO_2 nanoparticles on the CNT surface. The diameter of CNT bundles is around 10−15 nm, confirming that the functionalization and sample preparation had no effect on CNT diameter. The CNT is burned out in the samples calcined at 500 ºC or higher, in agreement with the TGA results. Even after burning the CNT templates, the TiO_2 particles have almost retained their interconnected structure (Figure 5.2i,j). From TEM images, the average particle size of the samples prepared by the hydrothermal method on CNT and calcined at 300, 400, 500, 600, and 800 ºC was calculated to be around 18, 19, 20, 22, and 58 nm, respectively. The increase of particle size can be attributed to the agglomeration of particles as well as the conversion of anatase to rutile. The particle size of the samples calcined at 300−600 ºC is very close to the crystallite size calculated from XRD results (Table 5.2). However, the particle size of the sample calcined at 800 ºC is higher than its crystalline size, suggesting that each particle is composed of more than one crystal.

The TEM image of the *templateless TiO_2 sample produced by aqueous phase sol−gel method* shows the agglomeration of nanoscale particles with the average particle size of 9 nm (Figure 5.2l). However, in the presence of CNT, the TiO_2 particles are successfully distributed between CNT strands (Figure 5.2m). Because of the use of acetic acid in the synthesis method, the CNT template agglomerates because of shifting CNT zeta potential toward zero at low pH [305]. The agglomeration of CNT leads to an accumulation of TiO_2 particles which can also be seen in the corresponding SEM image (Figure 5.1i). It is worth mentioning that the stability of the prepared functionalized CNT template in water was evaluated in different pH and only at basic pH did it remain dispersed after several days. This observation confirms that the functionalized CNT agglomerated during synthesis with the aqueous phase sol−gel method.

Table 5.2. Physicochemical properties and the rate of hydrogen production of different samples.

Sample	BET surface area (m^2/g)	Polymorph (%)		Crystallite size (nm)		H_2 production ($\mu mol\ g^{-1}\ hr^{-1}$)
		anatase	rutile	anatase	rutile	
CS	5.7					
CNT HCl treated	251.2					
CNT HCl and HNO_3 treated	296.4					
TiO_2@CS_HT_CN	66.1					
TiO_2@CS_HT_C300	77.3	100	0	14		795
TiO_2@CS_HT_C400	45.8	100	0	16		3210
TiO_2@CS_HT_C500	41.6	100	0	18		3000
TiO_2@CS_HT_C600	11.8	100	0	25		1210
TiO_2@CS_HT_C800	1.3	0	100		45	965
TiO_2@CNT_HT_CN	103.5					
TiO_2@CNT_HT_C300	104.4	100	0	13		50
TiO_2@CNT_HT_C400	90.2	100	0	14		350
TiO_2@CNT_HT_C500	51.6	100	0	17		830
TiO_2@CNT_HT_C600	42.1	100	0	21		265
TiO_2@CNT_HT_C800	6.4	25	75	36	44	45
TiO_2_HT_C400	66.0	100	0	13		1145
TiO_2@CNT_ALSG_C400	100.8	100	0	14		580
TiO_2@CS_ALSG_C400	2.7	100	0	19		545
TiO_2_ALSG_C400	7.3	100	0	27		670
TiO_2@CNT_AQSG_C400	194.9	100	0	9		4360
TiO_2_AQSG_C400	133.1	100	0	9		4790

5.3.2. XRD patterns

The XRD patterns of the samples prepared by hydrothermal and sol−gel methods are presented in Figure 5.3. Panels a and b of Figure 5.3, show the XRD pattern of the samples prepared on the CS and CNT, respectively, by hydrothermal method and calcined at different temperatures. No crystalline impurities are detected in the prepared samples. The crystallinity is enhanced by increasing the calcination temperature. The samples calcined at 300-600 ºC demonstrate the characteristic XRD pattern of anatase phase and all the corresponding

characteristic planes (JCPDS no.: 01-084-1286) are clearly exhibited at 2θ = 25.3 (101), 36.9 (103), 37.8 (004), 38.6 (112), 48.0 (200), 53.9 (105), 55.0 (211), 62.1 (213), 62.7 (204), 68.8 (116), 70.25 (220), 74.1 (107), 75.0 (215), and 76.0 (301). The high intensity of characteristic diffraction peaks exhibits the high degree of crystallinity and low resistance of electron transport [205].

The phase transformation of the samples prepared on the CNT by the hydrothermal method from anatase to rutile was observed by calcination at 800 ºC, according to results reported in the literature [306]. The TiO_2@CNT_HT_C800 sample is composed of a mixture of anatase and rutile phases, while the anatase phase was completely transformed to rutile phase in the case of the TiO_2@CS_HT_C800. The characteristic planes of the rutile phase at 2θ = 27.5 (110), 36.1 (101), 39.2 (200), 41.2 (111), 44.0 (210), 54.3 (211), 56.6 (220), 62.6 (002), 64.0 (310), 69.0 (301), 69.7 (112), 72.5 (311), 76.5 (202), and 79.8 (212) are in good agreement with the standard rutile spectrum (JCPDS no.: 01-088-1175).

The XRD pattern of the samples prepared by sol−gel methods is depicted in Figure 5.3c. As expected, all samples are composed of pure anatase. The CT incorporation increased the crystallinity of the sample prepared by the aqueous sol−gel method but decreased it in the case of the alcoholic sol−gel method.

The values of anatase crystallite size, rutile crystallite size, anatase%, and rutile% are presented in Table 5.2. The crystallite size of the prepared samples was estimated by the Scherrer equation [207] and the anatase:rutile ratio of the samples containing both phases was predicted according to the peak heights of anatase (101) and rutile (110) reflections [256]. Accordingly, TiO_2@CS_HT_C800 is composed of pure rutile, TiO_2@CNT_HT_C800 is made of 25% anatase and 75% rutile , and all the other samples are pure anatase. Figure 5.4 illustrates the effect of the calcination temperature on the crystallite size of the samples prepared on CT using the hydrothermal method. As can be seen, the crystallite size increases by increasing the calcination temperature. For the case of TiO_2@CNT sample, increasing the calcination temperature from 300 to 800 ºC led to 2.8 times increase of the anatase crystallite size. It can also be inferred from Figure 5.4 that the calcination temperature has almost the same effect on the crystallite size of the samples formed on the CS or CNT templates. However, the CS assisted the transformation of anatase to rutile at 800 ºC, as in contrast with

the sample formed on the CNT, no anatase phase was observed for the TiO_2@CS_HT_C800 sample. For the case of TiO_2@CNT_HT_C800 sample, the rutile crystallite size is 20% larger than the anatase crystallite size.

According to Table 5.2, the incorporation of CT has no effect on the crystallite size of the sample prepared by the aqueous phase sol−gel method. A comparison of the crystallite size of the samples prepared by the hydrothermal method on the CT and calcined at 400 ºC with the templateless TiO_2 sample synthesized by the same method shows that the incorporation of CT slightly increases the crystallite size. Only for the case of alcoholic phase sol−gel method does employing the CT decrease the crystallite size. The crystallite size of the TiO_2@CS_ALSG_C400 and TiO_2@CNT_ALSG_C400 samples is 19 and 14 nm, respectively, which are approximately 1.5 and 2 times lower than the crystallite size of the TiO_2_ALSG_C400 sample. Among all the samples prepared on the CT, TiO_2@CNT_AQSG_C400 has the lowest crystallite size of 9 nm. This value is the same as the particle size obtained based on the TEM image (Figure 5.2g−k) and shows that each particle is formed by one crystal.

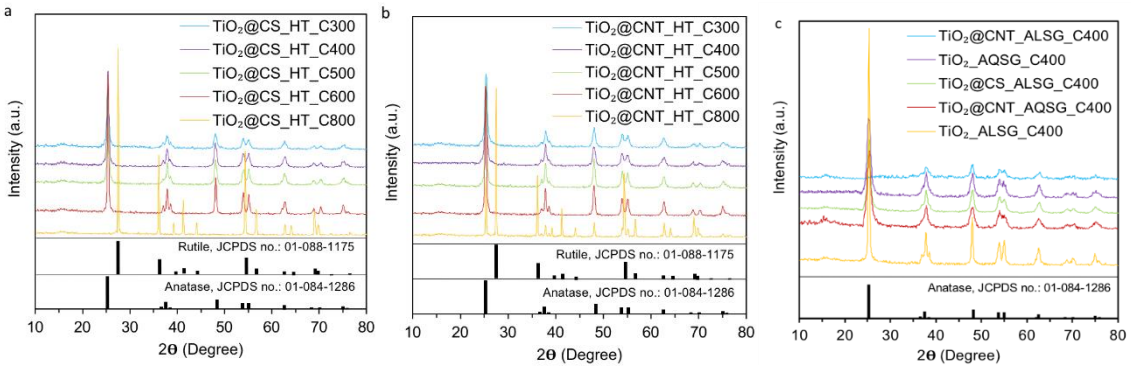

Figure 5.3. XRD patterns of the composites synthesized on (a) CS template by hydrothermal method, (b) CNT template by hydrothermal method, and (c) CS and CNT templates by sol−gel method.

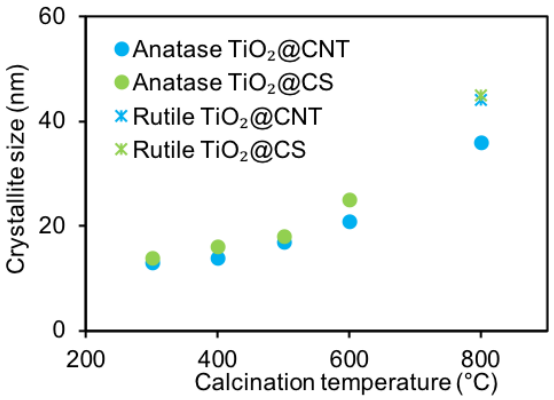

Figure 5.4. Effect of calcination temperature on the crystallite size of samples prepared on CS and CNT using hydrothermal method.

5.3.3. BET analysis

The surface area of the prepared samples is presented in Table 5.2 and Figure 5.5. Compared to CS (5.7 m^2/g), the HCl-treated CNT sample has a high surface area of 251.2 m^2/g, and it increases to 296.4 m^2/g by further treatment with HNO_3. Moreover, the calcination of TiO_2@CS_HT_CN at 300 ºC increased it by around 17%. This increase in surface area may be attributed to the burning of organic impurities (as their presence is confirmed by the TGA results) that block the pores, their presence being proved by TGA (Figure 5.6b). However, further increase in the calcination temperature decreases the surface area progressively because of the sintering of TiO_2 particles (see Figure 5.5) [306]. According to Table 5.2, the BET surface area of TiO_2@CS_HT_C800 and TiO_2@CNT_HT_C800 decreased to 1.3 and 6.4 m^2/g, respectively. This behavior suggests that the materials are drastically agglomerated and the active sites are located in the interagglomerate pores [299]. For TiO_2@CNT_HT_CN,

the calcination at 300 ºC has no significant effect on the surface area; however, the presence of CNT reduces the sintering effect in comparison with the sample prepared on the CS template. The decrease of surface area of the TiO_2@CS_HT material from 500 ºC (41.6 m^2/g) to 400 ºC (45.8 m^2/g) is not significant. This observation may be attributed to the combined effect of the increase of porosity due to burning of the carbonaceous templates between 400 and 500 ºC (as confirmed by the TGA results) and the sintering at higher temperatures. Similar behavior was also observed in the case of TiO_2@CNT_HT between 500 and 600 ºC, corresponding to the CNT burning temperature.

The surface area of TiO_2 (templateless) as well as TiO_2@CS and TiO_2@CNT (CT-based) samples prepared in the same conditions (hydrothermal method and calcination at 400 ºC) was found to be 66.0, 45.8, and 90.2 m^2/g, respectively. This could be explained by the analysis of these materials after performing TGA. Figure 5.6d,i reveals that TiO_2@CS_HT_C400 corresponds to pure TiO_2, but 60% of the initial CNT in TiO_2@CNT_HT_C400 still remained unburned (TiO_2@CNT_HT_C400 contains 12% CNT). By considering the surface area of CTs (see Table 5.2) and their amount in the above-mentioned materials, it can be concluded that the utilization of CS and CNT (as CT) in TiO_2 composites respectively reduced the surface area of TiO_2 around 30% and increased its surface area about 17%.

Comparing the samples synthesized by the alcoholic phase sol−gel method reveals that the surface areas of TiO_2_ALSG_C400, TiO_2@CS_ALSG_C400, and TiO_2@CNT_ALSG_C400 are 7.3, 2.7, and 100.8 m^2/g, respectively. Thus, for the hydrothermal method, the incorporation of the CS template leads to a decrease of surface area. However, as TiO_2@CNT_ALSG_C400 contains 20% CNT (with a surface area of 296.4 m^2/g), it can be concluded that using this template enhanced the surface area of TiO_2 in the sample 5.7 fold.

By comparing the materials prepared using different methods, the sample prepared by the aqueous phase sol−gel on CNT method exhibits the highest surface area. The surface areas of TiO_2_AQSG_C400 and TiO_2@CNT_AQSG_C400 are 133.1 and 194.9 m^2/g, respectively. As this increase corresponds to the surface area of the CNT contained in the

sample (20%), it seems that the utilization of the CNT as CT in the aqueous phase sol−gel method has almost no effect on the surface area of TiO_2 in the composite.

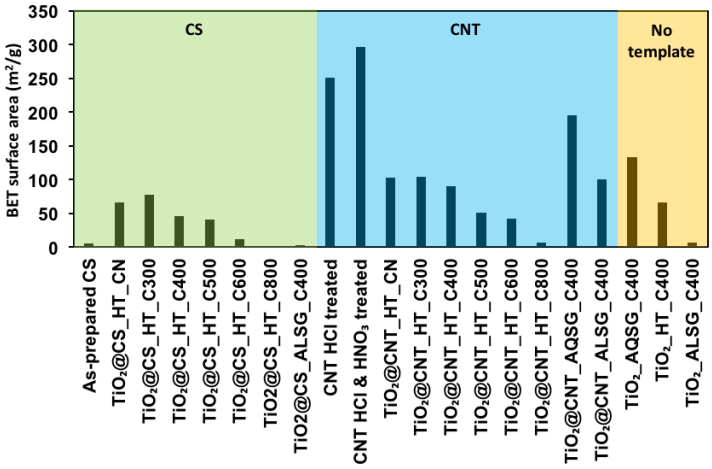

Figure 5.5. BET surface area of samples prepared without and with carbonaceous template (CS or CNT).

5.3.4. TGA analysis

TGA was performed on CT and the samples containing template to analyze the required temperature to burn out the template and evaluate the template content in the samples. For the CS template (Figure 5.6a), less than 2% weight loss is observed at 200 ºC, most probably because of the adsorbed water [307]. The broad peaks ranging from 250 to 550 ºC correspond to the gradual burning of the CS template. The peak at around 300 ºC may be attributed to the presence of amorphous carbon. It is well-known that CT can have different burning temperatures due to the burning of amorphous carbon or the presence of different diameters or sites[308]. TGA analysis demonstrates the high purity of CS.

The TGA results of TiO_2-coated CS samples, noncalcined or calcined at 300 or 400 ºC, are given in Figure 5.6b−d. TiO_2@CS_HT_NC demonstrated a broad peak, which began at around 250 ºC, while TiO_2@CS_HT_C300 started to burn at 300 ºC, as the less stable compounds have already burned during calcination at 300 ºC. According to Figure 5.6a−c, the template burned faster in the samples containing TiO_2, as it can catalyze the reaction [309]. For TiO_2@CS_HT_NC, the presence of TiO_2 did not shift the shoulder related to amorphous carbon (around 300 ºC) to lower temperatures, indicating that the amorphous carbon may not be in contact with TiO_2 and is located inside CS. For TiO_2@CS_HT_C300,

5.6% weight loss related to CS burning is close to 5% CS content, confirming the complete hydrolysis of the titanium precursor during the hydrothermal synthesis. All the template burned out by calcination at 400 ºC, where less than 2% weight loss is related to the adsorbed water (Figure 5.6d).

According to Figure 5.6e, the HCl-treated CNT template illustrates 96% weight loss in the range of 450−650 ºC, which is related to the combustion of the CNT template. The sample weight is stable after 650 ºC, indicating that all the template is burned out. In the case of HCl- and HNO_3 -treated CNT template, around 5% gradual weight loss is observed between 100 and 400 ºC. Moreover, CNT starts to burn at lower temperatures, indicating that the HNO_3 treatment has partly affected the CNT structure and produced some defects (Figure 5.6f). At the end of TGA analysis of the pristine CNT (not shown), HCl-treated CNT (Figure 5.6e), and HCl- and HNO_3 -treated CNT (Figure 5.6f), 7.3, 3.0, and 1.0% of the initial sample remained unburned, respectively. This behavior shows that both HCl and HNO_3 treatments help to remove impurities. By considering this 7.3% initial sample remaining from TGA and taking into account the weight loss of pristine CNT during acid treatment (9%), it can be concluded that around 1.7% of the organic compounds in the pristine CNT removed during acid treatment can be attributed to the amorphous carbon.

The TGA analysis of the TiO_2@CNT_HT_CN sample (Figure 5.6g) reveals that the amorphous carbon and the compounds formed during the hydrothermal treatment are removed between 300 and 430 ºC, followed by removal of the CNT template in the range of 430−660 ºC. In addition, a weight loss of 19% is observed for the peak corresponding to CNT burning, which is very close to the 20% CNT content in the sample. Moreover, the TiO_2 catalyzes the CNT burning and decreases the burning temperature up to 430 ºC. Both TiO_2@CNT_HT_C300 and TiO_2@CNT_HT_C400 (Figure 5.6h,i) show that the burning of CNT occurs between 350 and 655 ºC; the weight loss being 19.5% and 12%, respectively. By considering the 20% CNT content of the samples, this observation demonstrates that the sample calcined at 400 ºC lost around 40% of the containing CNT template during calcination. As expected, no burning of organic compounds is observed for TiO_2@CNT_HT_C500, indicating that no template remained after the calcination at 500 ºC (Figure 5.6j).

The TGA analysis of the TiO_2@CS_ALSG_C400 sample (Figure 5.6k) shows around 3% weight loss before 400 ºC, which can be attributed to the removal of the adsorbed water, followed by CS burning between 400 and 550 ºC. The 6.3% weight loss corresponding to the CS burning is close to the 5% CS content. The TGA analysis of TiO_2@CNT_ALSG_C400 is similar to that of TiO_2@CNT_HT_C400, and both samples lost around 5% of their CNT during calcination at 400 ºC because of the catalyzing effect of TiO_2. Nevertheless, 19% weight loss of TiO_2@CNT_AQSG_C400 in the temperature range of 400−700 ºC shows that the material has not lost the containing CNT during the calcination at 400 ºC. In all the TGA graphs of Figure 5.6, the appearance of the exothermic peaks shows that the oxidative decomposition is the cause of the weight loss.

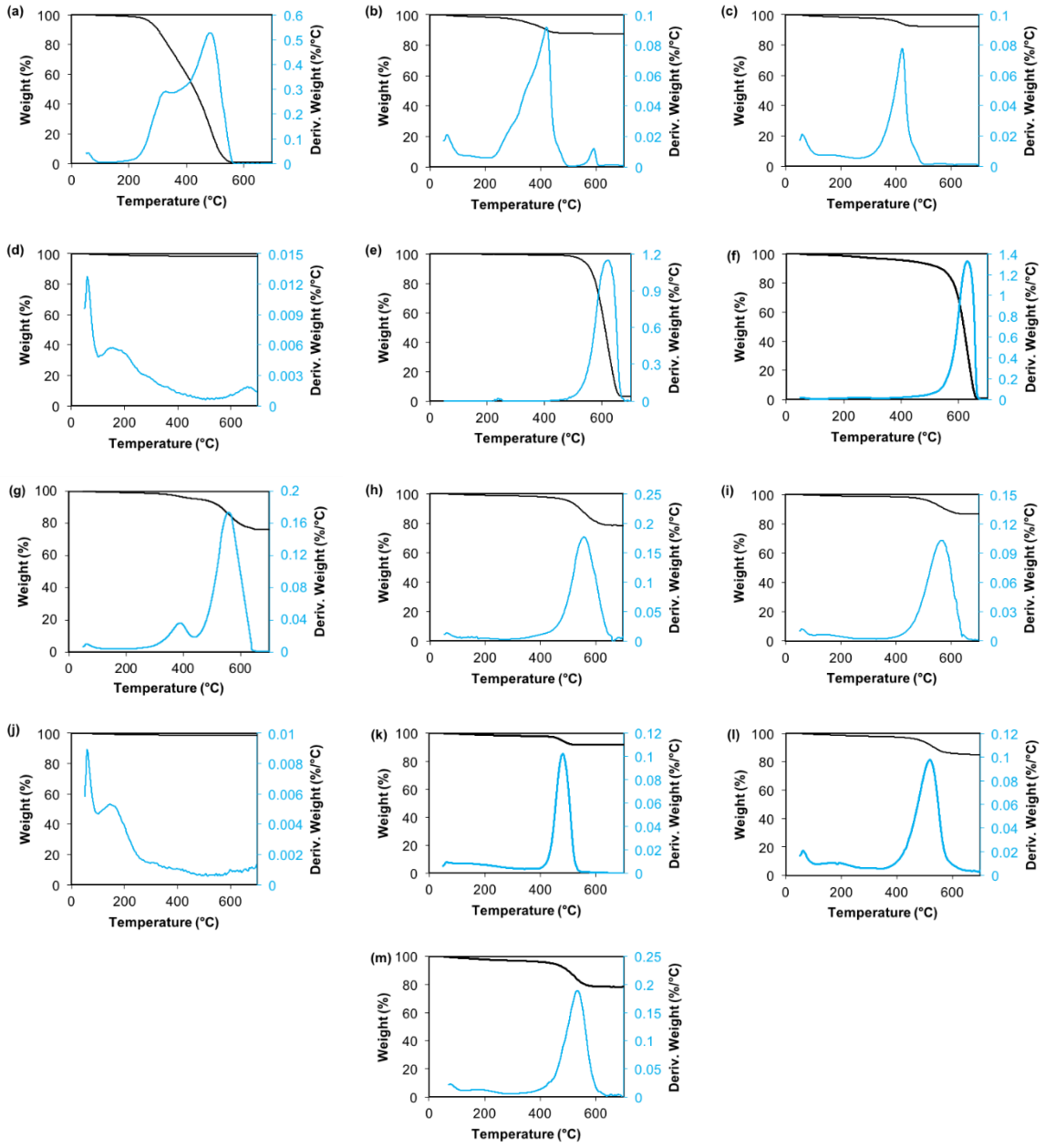

Figure 5.6. Thermogravimetric analysis curves of (a) as-prepared CS, (b) TiO_2@CS_HT_CN, (c) TiO_2@CS_HT_C300, (d) TiO_2@CS_HT_C400, (e) HCl-treated CNT, (f) HCl- and HNO_3 -treated CNT, (g) TiO_2@CNT_HT_CN, (h) TiO_2@CNT_HT_C300, (i) TiO_2@CNT_HT_C400, (j) TiO_2@CNT_HT_C500, (k) TiO_2@CS_ALSG_C400, (l) TiO_2@CNT_ALSG_C400, and (m) TiO_2@CNT_AQSG_C400.

5.3.5. FT-IR analysis

FT-IR technique was used to investigate the chemical structure of the prepared samples. The infrared ATR spectrum of the as-synthesized CS is shown in Figure 5.7a. The bands at 799 and 2980 can be assigned to the aromatic C–H out-of-plane bending vibrations [310], and

stretching vibrations [311], respectively, illustrating the occurrence of aromatization during the hydrothermal treatment. The broad and interconnected peaks from 1000 to 1400 can be attributed to the C–O vibration in highly conjugated, aromatic, or other chemical structures [311]. The band at 1680 corresponds to the stretching of carbon−carbon double bonds [288]. The IR-absorption bands at 1704 can be attributed to the main stretching bands of the C=O group [288], suggesting the formation of carboxylic acid groups on the surface of CS. The very intense band between 2300 and 2400 belongs the O=C=O asymmetric stretching vibration of the adsorbed carbon dioxide [311]. The broad band which appears in the 3000−3700 range can be attributed to the stretching vibrations of OH group as well as the physisorbed water [282]. As can be seen, C–O is the predominant oxygen-containing functional group on the CS surface.

To examine the success of CNT functionalization, the FT-IR spectra of functionalized and pristine CNT samples are compared in Figure 5.7b. The band appearing at 651 may be attributed to the remained metallic impurities, whose presence was proved by TGA (Figure 5.6f). The broad and intense band at 1158 belongs to the C–C–O ring and C–C–C asymmetric groups [312]. The band peaking at 1560 can be assigned to the C=C bond vibration in the aromatic ring [283]. Moreover, the stretching vibration band of the carbonyl (C=O) and carboxyl (C(=O)OH) groups can be seen at 1652 and 1699, respectively. By comparing the FT-IR spectra of functionalized and pristine CNT, it can be inferred that the CNT sample was successfully functionalized in order to assist the formation of TiO_2 on the CNT surface.

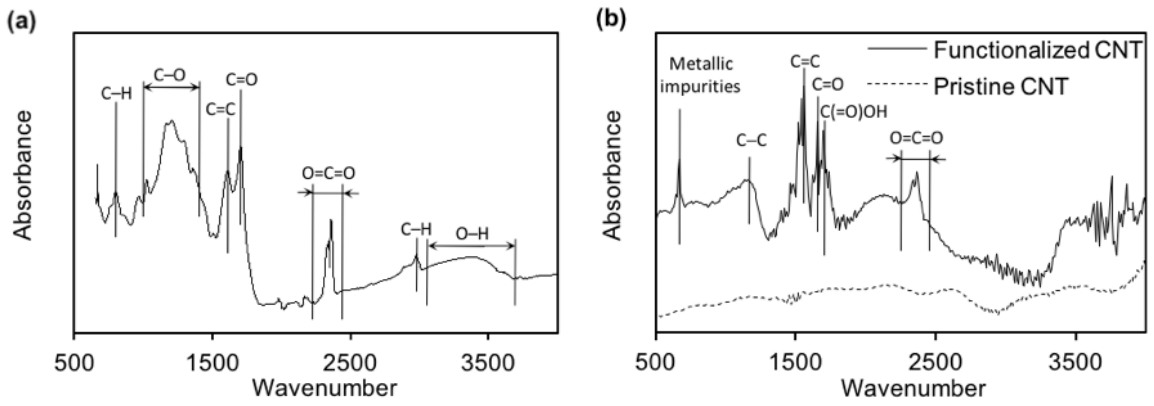

Figure 5.7. (a) Infrared ATR spectrum of as-synthesized CS and (b) FT-IR spectra of pristine and functionalized CNT.

5.3.6. Photocatalytic hydrogen production

The photocatalytic activity of the prepared samples was examined based on the rate of hydrogen production, and the results are presented in Table 5.2. Accordingly, the samples prepared by aqueous sol−gel method (TiO_2@CNT_AQSG_C400 and TiO_2_AQSG_C400) illustrate the highest photocatalytic activity. On the other hand, TiO_2@CNT_HT samples calcined at 300 and 800 ºC illustrate the lowest photocatalytic activity. By associating the rate of hydrogen production with the sample characterization results, it can be seen that the samples which present simultaneously high surface area (Table 5.2) and high crystallinity (Figure 5.3) demonstrate high photocatalytic activities. Higher crystallinity results in a decrease of crystal defects, which leads to a lower recombination rate of photoinduced species [313]. Although TiO_2_ALSG_C400 and TiO_2@CS_ALSG_C400 samples were crystallized considerably (Figure 5.3c), the hydrogen production was not significant because of their low surface area (7.3 and 2.7 m^2/g, respectively, according to Table 5.2). On the other hand, despite the relatively high surface area of the TiO_2@CNT_ALSG_C400 sample (100.8), the rate of hydrogen production was low as a result of a low crystallinity (Figure 5.3c).

To investigate thoroughly the effect of CT incorporation during the catalyst preparation on the rate of hydrogen production by each of the prepared catalysts, the results were compared based on CT effectiveness ratio and are depicted in Figure 5.8. The CT effectiveness ratio was defined as follows:

$$CT\ effectiveness\ ratio = \frac{Produced\ hydrogen\ by\ sample\ synthesized\ on\ CT\ (mol)}{Produced\ hydrogen\ by\ templateless\ sample\ (mol)} \quad (5\text{–}2)$$

The highest amount of hydrogen produced by the templateless sample which was prepared by the same method was considered the denominator for these calculations.

The results of hydrogen produced by the samples synthesized on CS and CNT templates are illustrated in Figure 5.8. The red line corresponds to a CT effectiveness ratio of 1. Larger values (greater than 1) denote the positive effect of CT incorporation on the rate of hydrogen production. Accordingly, no significant enhancement was observed for the composites prepared on CT (CS and CNT) by sol−gel methods (aqueous phase and alcoholic phase).

The catalyst synthesized on the CS by the hydrothermal method followed by calcination at 400 ºC shows the best results, leading to an increase of the rate of hydrogen production 2.8 times in comparison to the sample prepared in the same conditions but without CS. For the case of CNT incorporation by hydrothermal synthesis, the highest effectiveness ratio corresponds to the calcination temperature of 500 ºC. According to BET (Figure 5.5) and XRD (Figure 5.3a-b) data, both surface area and crystallinity are appropriate to the calcination temperatures corresponding to optimum hydrogen production. At the lower and higher calcination temperatures corresponding to optimum hydrogen production, respectively, the crystallinity and surface area considerably decrease. On the basis of TGA results (Figure 5.6), the samples where no template remained in the samples after calcination (TiO_2@CS_HT_C400 and TiO_2@CNT_HT_C500) lead to the highest hydrogen production.

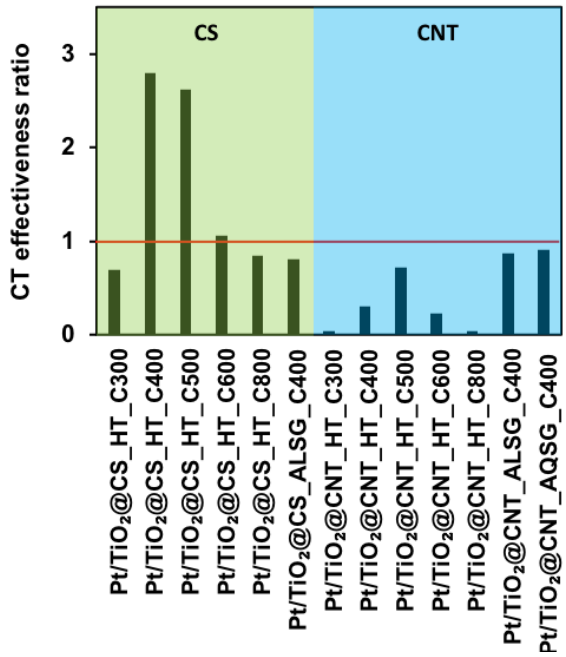

Figure 5.8.Effect of carbonaceous template incorporation on the enhancement of hydrogen production. CT effectiveness ratio is defined by Eq. (5–2) and the red line corresponds to the material without CT incorporation. Experimental conditions: 10% glycerol, 1% Pt, and 1 g/L catalyst.

Figure 5.8 illustrates that all the samples prepared on the CNT have an effectiveness ratio less than 1. To explore the reason for this behavior, some supplementary experiments were performed using the templateless TiO_2 and TiO_2@CNT materials prepared by aqueous phase sol−gel method, whose application led to the production of the highest amount of hydrogen (see Table 5.2). These experiments were performed in the presence and absence of Pt as cocatalyst. For this investigation, the Pt effectiveness ratio is defined as follows:

$$Pt\ effectiveness\ ratio = \frac{Produced\ hydrogen\ by\ platinum\ deposited\ sample\ (mol)}{Produced\ hydrogen\ by\ sample\ without\ platinum\ (mol)} \quad (5–3)$$

Figure 5.9 illustrates the Pt effectiveness ratio for the templateless TiO_2, TiO_2@CNT, and TiO_2@CS samples prepared by the sol−gel method. According to this figure, Pt deposition on the surface of samples led to a Pt effectiveness ratio of around 13 for the TiO_2 and TiO_2@CS samples, while for the TiO_2@CNT sample this value is almost halved. Additionally, the CT effectiveness ratios for the samples prepared on CS and CNT in the presence and absence of Pt are depicted in Figure 5.10. This figure shows that only in the

case of the TiO_2@CNT sample and in the absence of Pt could CT incorporation double the rate of hydrogen production. In other words, no positive effect was observed in the case of the TiO_2@CS sample, which can be justified by the fact that all CS was burned during calcination at 400 ºC (Figure 5.6d). It can be inferred from Figure 5.9 and Figure 5.10 that both CNT and Pt have a positive effect on the rate of hydrogen production; however, the effect of Pt is around 6.5 times higher. The addition of CNT can improve the rate of hydrogen production, but this enhancement is not synergistic with the positive effect of Pt. This behavior can be explained by considering the electron-transfer mechanism during the photocatalytic process. The CNT can scavenge the photogenerated electrons because its work function (4.3−5.1 eV [314]) is greater than the conduction band energy level of TiO_2 (4.21 eV [315]). On the other hand, the work function of Pt is in the range of 5.6−5.9 eV [316] and greater than the work function of CNT, indicating the facile electron transfer from CNT to Pt. Thus, in the presence of both of CNT and Pt, the reduction of protons to hydrogen does not occur on CNT and only Pt plays the role of cocatalyst. As the results of hydrogen production demonstrated that the positive effect of Pt and CNT are not synergistic, it could be concluded that a role of CNT is to act as the cocatalyst. The conduction band edge of CNT is lower compared to TiO_2 [317]; thus, the photogenerated electrons can be transferred to CNT as a cocatalyst. On the other hand, CNT can rapidly transfer the electrons to the reaction sites as it possesses an excellent electrical conductivity and electron storage capacity [318]. The high electron affinity of CNT decreases the chance of electron and hole recombination, thus enhancing the rate of hydrogen production [319].

As mentioned above, the former experiments were performed using a glycerol concentration of 10% (typical content in the biodiesel wastes). To check the effect of CNT as adsorbent, additional photocatalytic experiments were also performed at very high (50%) and low (1%) glycerol concentration. For these experiments, the aqueous phase sol−gel synthesized TiO_2 and TiO_2@CNT samples were used. As can be seen in Figure 5.11, the CNT effectiveness ratio is around 1 at higher glycerol concentrations (10 and 50%). The CNT effectiveness ratio is doubled at the low glycerol concentration of 1%. These results suggest that the amount of adsorbed glycerol on the surface of the templateless sample was not sufficient at low glycerol concentrations and that this shortage controls the rate of reaction (as the adsorption step can be the predominant in the process for this condition). In this case, the adsorbent role of CNT

is influential. The CNT increases the glycerol concentration on the surface of catalyst by the adsorption of glycerol molecules. It should be noted that additional experiments performed at 1% glycerol concentration and lower CNT content (1%) led to similar results (not shown). We can conclude that even 1% of CNT is sufficient to play the role of adsorbent. It is worth mentioning that the trend illustrated in Figure 5.11 was not observed for the catalyst formed on CS. This can be justified by the fact that CS is not present in the sample because it was burnt out (Figure 5.6d).

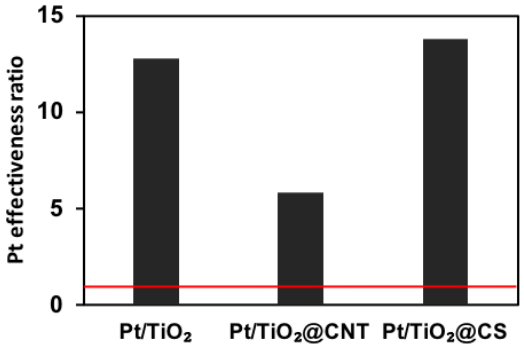

Figure 5.9. Effect of Pt deposition on the enhancement of hydrogen production rate in the presence of templateless TiO_2, TiO_2@CNT, and TiO_2@CS. Pt effectiveness ratio is defined in Eq. (5–3) and the red line corresponds to the material without Pt incorporation (Pt effectiveness ratio = 1). Experimental conditions: 10% glycerol, 1% Pt, and 1 g/L catalyst.

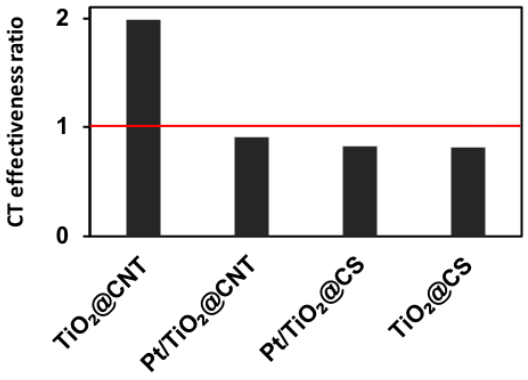

Figure 5.10. Effect of CNT incorporation on the enhancement of the hydrogen production rate, with and without Pt deposition. CT effectiveness ratio is defined in Eq. (5–2) and the red line corresponds to the material without CT incorporation (CT effectiveness ratio = 1). Experimental conditions: 10% glycerol, 1% Pt, and 1 g/L catalyst.

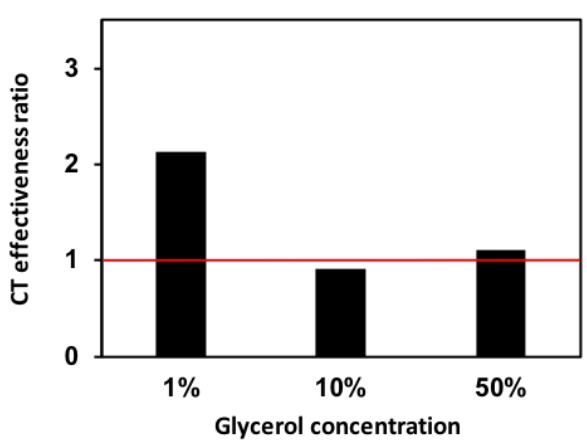

Figure 5.11. Effect of glycerol concentration on the enhancement of the hydrogen production rate using an aqueous phase sol−gel prepared TiO_2@CNT sample. CT effectiveness ratio is defined in Eq. (5–2) and the red line corresponds to the material without CNT incorporation (CT effectiveness ratio = 1). Experimental conditions: 1% Pt, and 1 g/L catalyst.

5.4. Conclusion

In this work, the effects of incorporating CS and CNT as CT for the preparation of TiO_2 composites were investigated, and the roles of CTs as support, cocatalyst, and adsorbent were examined. To evaluate the effect of incorporating CT and preparation methods thoroughly, hydrothermal and sol−gel (alcoholic phase and aqueous phase) methods were utilized to form a layer of TiO_2 on both CTs, as well as to synthesize TiO_2 samples without CT. The synthesized samples were characterized by SEM, TEM, XRD, BET analysis, TGA, and FT-IR. The analysis of the results revealed the following:

- TiO_2 nanoparticles were uniformly distributed on the surface of the carbon sphere (average diameter of CS around 1.1 µm for the alcoholic phase sol−gel method and 3 µm for the hydrothermal method).
- TiO_2 formation on the CNT was not uniform; however, CNTs could hinder the agglomeration of TiO_2 particles.
- Incorporation of CNT could significantly increase the composite surface area; however, no positive effect was observed regarding CS.
- Increasing the calcination temperature had similar effects on the enlargement of the crystallite size of TiO_2 particles formed on both CS and CNT.

Concerning the effects of incorporating CTs on the photocatalytic activity of the prepared samples, the following conclusions can be drawn:

- The highest amount of hydrogen production corresponded to the synthesis conditions that simultaneously lead to high crystallinity and high surface area.
- The incorporation of CS during the hydrothermal preparation of TiO_2 followed by calcination at 400 ºC had the highest enhancement (2.8 times) compared to the other samples.
- Using Pt and CNT individually enhanced photocatalytic activity 13- and 2-fold, respectively.
- CNT has proved to have the role of cocatalyst in the TiO_2 composite, but the incorporation of CNT was not found to have a positive effect in the presence of Pt as cocatalyst (their effects were not synergistic).
- The adsorbent role of CNT was revealed to be considerable only at low substrate concentrations.

Accordingly, this work contributes to the existing knowledge regarding the roles of CTs because (i) the morphology analysis of the prepared composites showed that CT can play the role of template, (ii) the analysis of synergistic effects of CT and Pt during the photocatalytic reaction revealed the role of CT as cocatalyst, and (iii) comparing photocatalytic experiments in the presence and absence of CT indicated the effective role of CT as adsorbent.

*In Chapter 4, a kinetic study was performed on the photocatalytic oxidation of alcoholic wastes (**glycerol** and **ethanol**) to **hydrogen** and a kinetic model was developed to predict the rate of hydrogen production.*

*In the following chapter, a **kinetic** study is performed on the photocatalytic selective oxidation of alcoholic waste (**cyclohexanol**) to generate a liquid product (**cyclohexanone**). Photocatalytic generation of liquid chemicals is of interest because it can achieve higher selectivity in comparison to conventional thermal processes. Because the photocatalytic processes operate at ambient temperature and atmospheric pressure, the synthesis of sensitive liquid chemicals by photocatalysis method is a promising approach as well. As lignin-sourced cyclohexanol is a biobased alcohol, its photocatalytic valorization to cyclohexanone for subsequent generation of caprolactam is a promising process to produce bioplastics.*

Chapter 6 : Selective photocatalytic oxidation of cyclohexanol to cyclohexanone: a spectroscopic and kinetic study

Résumé

La conversion photocatalytique du cyclohexanol en cyclohexanone peut constituer une approche durable pour la production ultérieure de bioplastiques. Dans ce travail, des études spectroscopiques et cinétiques ont été effectuées sur l'oxydation photocatalytique du cyclohexanol en cyclohexanone. L'analyse in situ ATR-FTIR de la réaction photocatalytique a révélé que le cyclohexanol peut être converti sélectivement en cyclohexanone et qu'un mécanisme réactionnel basé sur différentes étapes allant de la séparation des charges à la formation de molécules de cyclohexanone a été proposé. Le mécanisme actuel a été utilisé pour développer un modèle cinétique et prédire le taux de production de cyclohexanone. Les expériences photocatalytiques ont été réalisées selon un plan factoriel complet à trois niveaux et le taux de production de cyclohexanone a été déterminé par analyse HPLC. Les résultats ont été utilisés pour déterminer les paramètres cinétiques (à l'aide d'un algorithme génétique) et valider le modèle. Les analyses spectroscopiques (ATR-FTIR) et chromatographiques (HPLC et CPG-MS) ont confirmé une excellente sélectivité de la cyclohexanone et prouvé que l'approche photocatalytique pouvait constituer une alternative prometteuse pour la production de cyclohexanone.

Abstract

In this work, spectroscopic and kinetic studies were performed on photocatalytic oxidation of cyclohexanol to cyclohexanone. The photocatalytic experiments were performed according to a three-level full factorial design and the rate of cyclohexanone production was determined by HPLC analysis. *In situ* ATR-FTIR analysis of the photocatalytic reaction revealed that cyclohexanol can be selectively converted to cyclohexanone, without the formation of significant amounts of carbonates and carboxylates. A reaction mechanism based on different steps from charge separation to cyclohexanone molecule formation is proposed. The results were utilized to determine the kinetic parameters (with the help of genetic algorithm) and validate the model. The developed kinetic model illustrates that the rate of cyclohexanone production increases as a power function with respect to the light intensity and decreases as an exponential function with respect to time. An excellent selectivity of cyclohexanone was confirmed by spectroscopic and chromatographic studies. This study demonstrates that photocatalysis can be a promising technology for formation of cyclohexanone from cyclohexanol.

6.1. Introduction

In the recent years, great attention has been paid to photocatalytic conversion of chemicals for the purpose of their elimination [171, 320-324] or as a smart approach of synthesis [81, 150, 233, 325-327]. In principle, photocatalytic synthesis can lead to higher selectivity in comparison to conventional oxidation processes [328, 329]. As photocatalytic processes operate at moderate conditions, photocatalytic synthesis of temperature or pressure sensitive products is a particular point of interest.

Caprolactam is an important monomer feedstock for nylon-6 production and it is estimated that around 90% of caprolactam is produced from cyclohexanone [39]. In addition to caprolactam, cyclohexanol is used for production of adipic acid (for nylon-6,6 production) or as solvent for resins, lacquers, dyes, and insecticides [330]. Production of caprolactam requires high temperatures and elevated pressures implying high energy consumption [40]. As cyclohexanol can be sustainably produced from lignin [14], the photocatalytic production of cyclohexanone from cyclohexanol and subsequent conversion to caprolactam can be a sustainable approach for the production of nylon-6 [331].

In our previous work on photocatalytic production of cyclohexanone from cyclohexane, a mixture of cyclohexanone and cyclohexanol was detected as final product [332]. It was revealed that strongly adsorbed intermediates further oxidize to carboxylates and cause catalyst deactivation [333]. The selectivity to cyclohexanone is a key factor in the transformation of cyclohexanol [334-336]. A higher cyclohexanone purity increases the process efficiency by reducing energy consumption [42].

In this context, our aim was to explore the possibility to produce cyclohexanone from cyclohexanol with high selectivity, and to minimize catalyst deactivation as caused by carboxylate formation. In particular, a mechanistic and kinetic study was performed on the photocatalytic production of cyclohexanone from cyclohexanol using a TiO_2-based photocatalyst. In this regard, an *in situ* ATR−FTIR (attenuated total reflectance−Fourier transform infrared) analysis was employed, as a feasible technique for real time mechanistic understanding of the photocatalytic reaction and analysis of formed molecules. A mechanism was proposed for the formation of cyclohexanone and a kinetic model was developed to predict the rate of cyclohexanone production as a function of light intensity and time. The

photocatalytic experiments were performed according to a three-level full factorial design, which permitted (i) the calculation of kinetic parameters based on the genetic algorithm (GA) method and (ii) the model validation. To the best of our knowledge, no work on detailed kinetic evaluation of photocatalytic oxidation of cyclohexanol is available in the open literature.

6.2. Experimental

6.2.1. Materials

Cyclohexanol (99.0%), cyclohexanone (≥99.0%) and anatase TiO_2 (≥99.7%) were obtained from Sigma Aldrich. Hombikat UV-100 TiO_2 (100% anatase) was provided by Sachtleben Chemie GmbH and used as photocatalyst. TiO_2 Aeroxide P25 (≥99.5%) was provided by Evonik Industries. HPLC-grade acetonitrile (≥99.8%) was purchased from VWR.

6.2.2. TiO_2 film preparation

In order to choose the best TiO_2 for the film preparation, different TiO_2 samples such as Hombikat, P25, and Sigma-Aldrich anatase were first tested. It was found that only the Hombikat TiO_2 film was uniformly formed on the ZnSe ATR crystal and is thus suitable for *in situ* ATR−FTIR analysis. Therefore, the Hombikat sample with a surface area of 337 m^2/g and a primary particle size of approximately 5 nm was used to prepare a TiO_2 film for the *in situ* ATR−FTIR analysis [337]. Thin films of TiO_2 on ZnSe ATR crystals were prepared from a 3 g/L photocatalyst suspension. Suspensions were prepared using Milli-Q water. After ultrasonication for 30 min in a 35 kHz Elmasonic ultrasonic bath to to de-agglomerate the TiO_2 particles, 1.5 mL of the prepared suspension was drop-casted on the crystal and dried overnight inside a vacuumed desiccator at ambient temperature.

6.2.3. *In situ* ATR−FTIR analysis

The transformation of cyclohexanol was analyzed using *in situ* ATR−FTIR spectroscopy. A VERTEX 70 Bruker FTIR spectrometer was employed for the spectroscopic analysis. A scheme of the employed setup is shown elsewhere [333]. The experiments were conducted using pure cyclohexanol instead of aqueous solutions to avoid the interference of cyclohexanol bands with intensive OH bands that appear in the presence of water. Prior to the start of each experiment, traces of water were removed from cyclohexanol overnight

using a Molsieve (type 4A). Cyclohexanol was then oxygen saturated by purging with a 10 mL/min flow of dry air for 30 min. After depositing oxygen saturated cyclohexanol on the photocatalyst containing crystal (preparation described in Section 6.2.2), a spectrum was recorded at equilibrium adsorption and used as background. The photocatalytic transformation was initiated by irradiating 9×10^{-9} mol·(cm^2·s) of UV light with a wavelength centered at 375 nm. During illumination, one spectrum per minute was recorded from 700-4000 cm^{-1} with a resolution of 4 cm^{-1}. The spectra of background and photocatalytic reactions were averaged using 64 and 32 scans, respectively.

6.2.4. Photocatalytic experiments

The photocatalytic reactions for production of cyclohexanone were carried out in pyrex slurry- reaction cells. In each experiment, 10 ml of cyclohexanol and 1 g/L of TiO_2 photocatalyst were introduced into the cells and sonicated for 15 min to de-agglomerate the photocatalyst particles. Before starting irradiation, the cells were purged with pure oxygen for 15 min to ensure saturation of the suspension. The cells were stirred in the dark for 20 min for complete adsorption of cyclohexanol on the photocatalyst surface. Afterwards, the cells were irradiated with required number of 20 W Black-Ray® mercury tubes to provide 400, 800, or 1200 μW/cm^2 of light intensity. During the experiments, the cells were kept under 500 rpm magnetic stirring. A cooling fan was used to keep the temperature of the reaction cells around ambient during the reaction. The cells were radiated for 4, 7, and 10 days to transform cyclohexanol to cyclohexanone. At the end of experiment, 1 mL of suspension was filtered through a 0.45 μm Sarstedt syringe filtration unit into 1.5-mL vials and analyzed by HPLC to measure the amount of formed cyclohexanone. The experiments were repeated to ensure the accuracy of the results.

6.2.5. HPLC method

HPLC measurements were performed using a LC-30AD Shimadzu device equipped with a DGU-20A5 degasser, SIL-20A XR autosampler, and RID-10A detector. An Ultra C18 3 μm column (150×4.5 mm) with a mobile phase containing 50% acetonitrile in water was used for the analysis. In each analysis, 1 μL of sample was injected into the mobile phase with a 0.3 mL/min flow rate. LabSolutions software was used to analyze the data and calculate the

amount of formed cyclohexanone. The actual concentration was calculated using appropriate calibration data.

6.2.6. Design of experiments

To evaluate the proposed model, photocatalytic experiments were designed based on the design of experiment approach [156]. These experiments were conducted according to a three-level full factorial design. Light intensity ($\mu W/cm^2$) and time (day) were defined as independent variables, labeled A and B (see Table 6.1). The range of independent variables was obtained based on preliminary experiments. The rate of cyclohexanone production was defined as the dependent variable (response). As demonstrated in Tables 6.1 and 6.2, nine sets of experiments were conducted in three levels and coded as −1, 0, and +1.

Table 6.1. Experimental ranges and levels of independent variables for photocatalytic experiments performed using slurry photoreactor.

Variables	-1	0	+1
Light intensity (A, $\mu W/cm^2$)	400	800	1200
Time (B, day)	4	7	10

6.2.7. Genetic algorithm (GA)

GA is a powerful method for solving optimization problems and takes advantage of a robust optimization procedure. It is inspired by the process of natural selection and its global optimizing capacity is more powerful than other heuristic optimization approaches [210]. In this work, the GA optimization method was used to determine the kinetic parameters. 200 individuals were selected and randomly distributed for each generation. Constraint dependent, rank, and stochastic uniform functions were selected as creation, fitness scaling, and selection functions, respectively. To generate new generations, 5% of the individuals were selected as elite count. Moreover, crossover and mutation were employed to generate respectively 80% and 20% of the subsequent generation. Constraint-dependent functions were considered for crossover and mutation.

Table 6.2. Values of independent variables obtained based on three-level full factorial design and corresponding rates of cyclohexanone production.

Run #	Independent variables		Rate of cyclohexanone production (mmol/day)	
	Light intensity (μW/ cm^2)	Time (day)	Experiment	Kinetic model
1	400	4	5.1	5.1
2	400	7	3.1	3.2
3	400	10	2.2	2.1
4	800	4	6.5	6.2
5	800	7	3.7	4.0
6	800	10	2.3	2.6
7	1200	4	7.0	7.0
8	1200	7	4.3	4.5
9	1200	10	3.2	2.9

6.2.8. Statistical analysis

The predicted rates of cyclohexanone production by the proposed kinetic model were statistically compared with the experimental values to evaluate the accuracy of the model. This statistical comparison was performed in terms of the coefficient of determination (R^2), adjusted coefficient of determination (R^2_{adj}), root mean squared error (*RMS*), mean absolute error (*MAE*), and absolute average deviation (*AAD*). In this regard, the following expressions were employed for the analysis:

$$R^2 = 1 - \sum_{i=1}^{n} \left(\frac{(y_{i,cal} - y_{i,\exp})^2}{(y_{ave,\exp} - y_{i,\exp})^2} \right) \quad (6\text{–}1)$$

$$R^2_{adj} = 1 - \left[(1 - R^2) \frac{n-1}{n-K-1} \right] \quad (6\text{–}2)$$

$$RMS = \sqrt{\frac{\sum_{i=1}^{n}\left(y_{i,cal} - y_{i,\exp}\right)^2}{n}} \quad (6–3)$$

$$MAE = \frac{\sum_{i=1}^{n}\left|y_{i,cal} - y_{i,\exp}\right|}{n} \quad (6–4)$$

$$AAD = \left\{\frac{\sum_{i=1}^{n}\left(\left|y_{i,cal} - y_{i,\exp}\right| / y_{i,cal}\right)}{n}\right\} \times 100 \quad (6–5)$$

where $y_{i,cal}$, $y_{i,exp}$ and $y_{ave,exp}$ are the predicted and experimental rates of cyclohexanone production, and the arithmetic mean of all of the experimental data, respectively. In addition, n and K represent the number of data points and independent variables. A better fit is achieved when R^2 is closer to 1, R^2_{adj} is closer to R^2, and *RMS*, *MAE*, and *AAD* are closer to zero.

6.3. Mechanistic and kinetic study

6.3.1. Mechanism of cyclohexanol conversion

A reaction mechanism was proposed for the production of cyclohexanone from cyclohexanol based on different steps, from charge separation to cyclohexanone molecule formation (k_i and K_i represent the reaction constant and equilibrium constant, respectively):

- Photocatalytic conversion of cyclohexanol to cyclohexanone initiates by the generation of an electron and hole pair as a result of absorbance of a photon of light by photocatalyst:

$$Photocatalyst + h\nu \xrightarrow{k_6} e^- + h^+ \quad (6–6)$$

- The photo-generated species tend to recombine rapidly and release heat [253]:

$$e^- + h^+ \xrightarrow{k_7} Heat \quad (6–7)$$

- The cyclohexanol molecule adsorbs on the active catalyst surface sites:

$$C_6H_{11}-OH+S \underset{}{\overset{K_8}{\rightleftarrows}} C_6H_{11}-OH_{ads} \quad (6\text{–}8)$$

where *S* represents a free active reaction site.

- The photo-generated hole can be scavenged by the adsorbed cyclohexanol to release a proton.

$$C_6H_{11}-OH_{ads}+h^+ \xrightarrow{k_9} C_6H_{11}-O^{\bullet}_{ads}+H^+ \quad (6\text{–}9)$$

- The photo-generated electron can react with oxygen to generate a superoxide radical, as the liquid phase is saturated with oxygen:

$$O_2+e^- \xrightarrow{k_{10}} O_2^- \quad (6\text{–}10)$$

The photo-generated superoxide radical and proton react in a series of reactions according to Eqs. (6–11)-(6–15) to generate hydrogen peroxide [266]:

$$O_2^- + H^+ \xrightarrow{k_{11}} HO_2^{\bullet} \quad (6\text{–}11)$$

$$HO_2^{\bullet} + HO_2^{\bullet} \xrightarrow{k_{12}} H_2O_2 + O_2 \quad (6\text{–}12)$$

$$HO_2^{\bullet} + O_2^- \xrightarrow{k_{13}} HO_2^- + O_2 \quad (6\text{–}13)$$

$$HO_2^{\bullet} + e^- \xrightarrow{k_{14}} HO_2^- \quad (6\text{–}14)$$

$$HO_2^- + H^+ \xrightarrow{k_{15}} H_2O_2 \quad (6\text{–}15)$$

- The generated hydrogen peroxide converts to hydroxyl radical either by adsorption of a photon of light or reaction with a photo-generated electron:

$$H_2O_2 + h\upsilon \xrightarrow{k_{16}} 2^{\bullet}OH \quad (6\text{–}16)$$

$$H_2O_2 + e^- \xrightarrow{k_{17}} {}^{\bullet}OH + OH^- \quad (6\text{–}17)$$

Other than direct reaction of cyclohexanol with a photo-generated hole (Eq.(6–9)), cyclohexanol can also react with hydroxyl radicals:

$$C_6H_{11}-OH_{ads}+^{\bullet}OH \xrightarrow{k_{18}} C_6H_{11}-O^{\bullet}_{ads}+H_2O \quad (6\text{–}18)$$

Finally, hydroxyl radical reacts with cyclohexanol radicals (generated either by reactions (6–9) or Eq. (6–18)) to produce cyclohexanone and water and re-establish the reaction site:

$$C_6H_{11}-O^{\bullet}_{ads}+^{\bullet}OH \xrightarrow{k_{19}} C_6H_{10}=O+H_2O+S \quad (6\text{–}19)$$

In brief, based on the proposed mechanism, the cyclohexanol molecule releases two protons to produce cyclohexanone in two steps (reactions (6–9) and (6–19) or (6–18) and (6–19), depending on the path of the oxidation) and the generated protons indirectly react with the dissolved oxygen through Eqs. (6–10) to (6–17) to eventually form a water molecule (Eqs. (6–18) and/or (6–19)).

6.3.2. Kinetic model development

The kinetic model was developed based on the proposed mechanism (see Section 3.1). According to Eq. (6–19), the production rate of cyclohexanone (r_{Cnon}) can be calculated as:

$$r_{Cnon}=\frac{d[C_6H_{10}\text{=O}]}{dt}=k_{19}[C_6H_{11}-O^{\bullet}_{ads}][^{\bullet}OH] \quad (6\text{–}20)$$

where [X] represents the concentration of X.

Assuming that the concentration of $C_6H_{11}-O^{\bullet}_{ads}$ radicals is constant during the reaction, the variation rate of $[C_6H_{11}-O^{\bullet}_{ads}]$ is zero:

$$\frac{dC_{C_6H_{11}-O^{\bullet}}}{dt}=k_9[C_6H_{11}-OH_{ads}][h^+]+k_{18}[C_6H_{11}-OH_{ads}][^{\bullet}OH] \quad (6\text{–}21)$$
$$-k_{19}[C_6H_{11}-O^{\bullet}_{ads}][^{\bullet}OH]=0$$

Accordingly, $[C_6H_{11}-O^{\bullet}_{ads}]$ can be calculated as follows:

$$[C_6H_{11}-O^{\bullet}_{ads}]=\frac{(k_9[h^+]+k_{18}[^{\bullet}OH])[C_6H_{11}-OH_{ads}]}{k_{19}[^{\bullet}OH]} \quad (6\text{–}22)$$

By considering that the rate of direct photocatalytic conversion of cyclohexanol (reaction with photogenerated holes) is much higher than the rate of its indirect photocatalytic conversion (reaction with $^{\bullet}OH$ radicals generated in the photocatalytic process) [194], Eq. (6–22) can be simplified to Eq. (6–23):

$$[C_6H_{11}-O^{\bullet}_{ads}]=\frac{k_9[h^+][C_6H_{11}-OH_{ads}]}{k_{19}[^{\bullet}OH]} \quad (6–23)$$

The concentration of adsorbed cyclohexanol can be determined based on Eq. (6–8) as follows:

$$[C_6H_{11}-OH_{ads}]=K_8[C_6H_{11}-OH][S] \quad (6–24)$$

where [S] represents the concentration of reaction sites and K_8 is the equilibrium constant of Eq. (6–8). The total concentration of reaction sites is constant during the reaction and can be defined as:

$$[S_0]=[S_{act}]+[S_{dec}] \quad (6–25)$$

where $[S_{act}]$ and $[S_{dec}]$ correspond to the active and deactivated reaction sites, respectively. The active reaction sites are composed of free sites and sites occupied by cyclohexanol.

$$[S_{act}]=[S]+[C_6H_{11}-OH_{ads}] \quad (6–26)$$

The active reaction sites deactivate according to Eq. (6–27). By assuming the deactivation as a first order reaction, the concentration of active reaction sites can be expressed by Eq. (6–28):

$$[S_{act}]\rightarrow[S_{dec}] \quad (6–27)$$

$$[S_{dec}]=[S_0]\times(1-\exp(-k_{dec}t)) \quad (6–28)$$

where k_{dec} represents the first-order rate constant of active site deactivation and t is the reaction time. As the number of reaction sites depends on the catalyst concentration in the reaction media, $[S_0]$ is a function of catalyst loading:

$$[S_0] = a[Cat]^b \tag{6–29}$$

where [*Cat*] represents the catalyst loading and *a* and *b* are constants. *b* should be equal or lower than 1 to take into account the possible agglomeration of catalyst [150].

The concentration of free reaction sites can be obtained by substituting Eqs. (6–24), (6–26), (6–28), and (6–29), in Eq. (6–25) as follows:

$$[S] = \frac{a[Cat]^b \exp(-k_{dec}t)}{1 + K_8[C_6H_{11} - OH]} \tag{6–30}$$

The rate of reaction (6–6) is a function of catalyst loading and light intensity [252, 338]:

$$r_1 = k_6[Cat]^q(\phi I)^l \tag{6–31}$$

where *q* and *l* are constants and *φ* is quantum efficiency. *q* and *l* are the orders of reaction with respect to the catalyst load and light intensity, respectively.

The rate of the reaction (6–7) can be expressed by Eq. (6–32), considering the equality between the concentrations of photo-generated (i) electrons and (ii) holes [254]:

$$r_2 = k_7[h^+]^2 \tag{6–32}$$

The concentration of photo-generated holes can be considered as constant [254], as a result:

$$\frac{d[h^+]}{dt} = k_6[Cat]^q(\phi I)^l - k_7[h^+]^2 - k_9[h^+][C_6H_{11} - OH] = 0 \tag{6–33}$$

As the rate of photogenerated species recombination is very fast [254, 255], by assuming $k_7[h^+]^2 >> k_9[h^+][C_6H_{11} - OH]$, the concentration of photo-generated holes can be calculated as follows:

$$[h^+] = \sqrt{\frac{k_6[Cat]^q(\phi I)^l}{k_7}} \tag{6–34}$$

By substituting Eqs. (6–23), (6–24), (6–30), and (6–34) in Eq. (6–20), the rate of cyclohexanone production can be obtained as follows:

$$r_{Cnon} = \alpha I^{\beta} \exp(\gamma t) \tag{6–35}$$

where $\alpha = \dfrac{a\sqrt{k_6 / k_7}\, k_9 K_8 \phi^{l/2} [C_6H_{11}-OH][Cat]^{b+q/2}}{1 + K_8[C_6H_{11}-OH]}$, $\beta = l/2$, and $\gamma = -k_{dec}$. Eq. (6–35) determines the rate of cyclohexanone production as a function of light intensity and time, and this rate equation can be easily used in practice. In Eq. (6–35), I^{β} is the term related to the effect of light intensity (β is the pseudo-exponent of light intensity). It shows that the rate of cyclohexanone production increases as a power function with respect to the light intensity. The term $exp(\gamma t)$ is related to the deactivation of photocatalyst, where γ depends on the first-order rate constant of the active surface sites deactivation (k_{dec}, Eq. (6–28)).

6.4. Results

6.4.1. ATR−FTIR analysis

ATR−FTIR analysis during the photocatalytic reaction was performed to *experimentally investigate the cyclohexanone production and confirm the proposed reaction mechanism.* The obtained spectra in the wavenumber range between 1000 and 4000 cm^{-1} for the time range of 0-200 min are depicted in Figure 6.1a. The spectra of adsorbed cyclohexanol on the TiO_2 surface (in dark condition) were considered as reference for this measurement. To find the IR bands of cyclohexanol and cyclohexanone, ATR−FTIR measurements were performed using pure cyclohexanol and 1% dissolved cyclohexanone in cyclohexanol in the absence of light (Figure 6.1b). According to Figure 6.1b, the main cyclohexanol bands are located at 1030, 1065, 1366, 1449, 2855, and 2929 cm^{-1}. An obvious indicative band of cyclohexanone is positioned at 1713 cm^{-1}, which is attributed to the C=O stretching vibration of cyclohexanone. As can be seen in Figure 6.1a, negative bands related to cyclohexanol appeared during illumination, representing cyclohexanol transformation. In addition, two positive bands appeared at 1713 and 3390 cm^{-1}. The band at 1713 cm^{-1} is attributed to cyclohexanone (as suggested by Figure 6.1b) and confirms the transformation of cyclohexanol to cyclohexanone during the photocatalytic reaction. In addition, the observed

band at 3390 cm^{-1} is related to OH stretching vibrations of water (as suggested by Figure 6.1b). These results confirm the accuracy of the proposed mechanism in which cyclohexanol is directly converted into cyclohexanone and water (no intermediates were detected), cf. to the Eqs. (6–18) and (6–19).

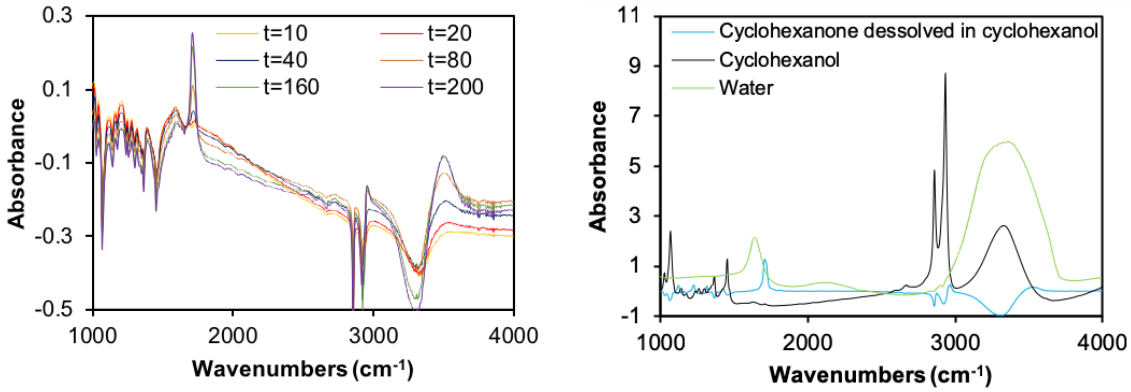

Figure 6.1. ATR−FTIR spectra of (a) cyclohexanol photooxidation in the range of 1000 and 4000 cm^{-1} for 200 min of reaction time, (b) spectra of respectively 1% cyclohexanone dissolved in cyclohexanol, cyclohexanol, and water.

In addition, the heights of the bands observed at 1713 and 3390 cm^{-1} were analyzed and the results are presented in Figure 6.2a and b, respectively. The height of the bands increases continuously, demonstrating continuous formation of cyclohexanone and water. In both cases, a maximum in the production rate can be observed. Compared to cyclohexanone formation, the maximum rate of water formation occurred at earlier times, suggesting that the desorption of water from the catalyst surface occurred prior to cyclohexanone desorption (Eq. (6–19)). Interestingly, bands that could be assigned to deactivating species such as carbonates and carboxylates, which are abundant in experiments where cyclohexane is oxidized [339], did not develop significantly, suggesting that the catalyst surface is less sensitive to deactivation during oxidation of cyclohexanol as compared to oxidation of cyclohexane. This may be attributed to the fact that cyclohexanol oxidation to cyclohexanone can occur in two steps (reactions (6–9) and (6–19) or (6–18) and (6–19). However, the formation of a double bond between oxygen and cyclohexane (for cyclohexanone generation) is a complex process that occurs in several steps, thus increasing the chances of the formation of deactivating species as side products [340].

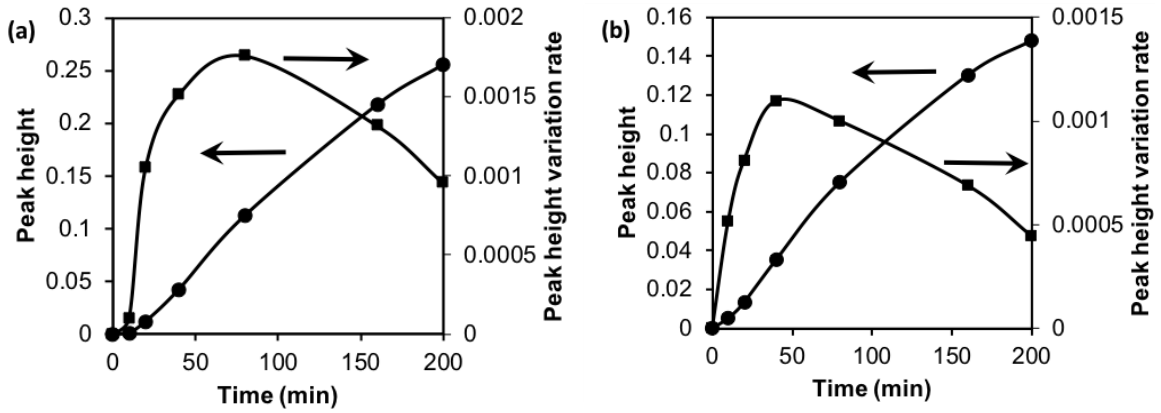

Figure 6.2. Time profiles of product formation obtained from peak deconvolution at (a) 1713 cm^{-1} (cyclohexanone) and (b) 3390 cm^{-1} (water).

6.4.2. Evaluation of the proposed kinetic model accuracy

To *evaluate the accuracy of the proposed kinetic model*, photocatalytic experiments were performed in a slurry photoreactor based on three-level full factorial experimental design. The rate of cyclohexanone production was measured by HPLC analysis of the products and the results are presented in 6.2.7. Genetic algorithm (GA)

GA is a powerful method for solving optimization problems and takes advantage of a robust optimization procedure. It is inspired by the process of natural selection and its global optimizing capacity is more powerful than other heuristic optimization approaches [210]. In this work, the GA optimization method was used to determine the kinetic parameters. 200 individuals were selected and randomly distributed for each generation. Constraint dependent, rank, and stochastic uniform functions were selected as creation, fitness scaling, and selection functions, respectively. To generate new generations, 5% of the individuals were selected as elite count. Moreover, crossover and mutation were employed to generate respectively 80% and 20% of the subsequent generation. Constraint-dependent functions were considered for crossover and mutation.

Table 6.2. It is worth mentioning that the detection of cyclohexanone as final product was also verified by GC-MS (data not shown here). In agreement with the spectroscopic data, an excellent (almost 100%) selectivity of cyclohexanone (H_2O free basis) was confirmed.

The kinetic parameters of Eq. (6–35) (Table 6.3) were calculated based on the experimental data (6.2.7. Genetic algorithm (GA)

GA is a powerful method for solving optimization problems and takes advantage of a robust optimization procedure. It is inspired by the process of natural selection and its global optimizing capacity is more powerful than other heuristic optimization approaches [210]. In this work, the GA optimization method was used to determine the kinetic parameters. 200 individuals were selected and randomly distributed for each generation. Constraint dependent, rank, and stochastic uniform functions were selected as creation, fitness scaling, and selection functions, respectively. To generate new generations, 5% of the individuals were selected as elite count. Moreover, crossover and mutation were employed to generate respectively 80% and 20% of the subsequent generation. Constraint-dependent functions were considered for crossover and mutation.

Table 6.2) and GA (as described in section 6.2.7). For this purpose, the experimental values of cyclohexanol production rate obtained at different light intensities and times (6.2.7. Genetic algorithm (GA)

GA is a powerful method for solving optimization problems and takes advantage of a robust optimization procedure. It is inspired by the process of natural selection and its global optimizing capacity is more powerful than other heuristic optimization approaches [210]. In this work, the GA optimization method was used to determine the kinetic parameters. 200 individuals were selected and randomly distributed for each generation. Constraint dependent, rank, and stochastic uniform functions were selected as creation, fitness scaling, and selection functions, respectively. To generate new generations, 5% of the individuals were selected as elite count. Moreover, crossover and mutation were employed to generate respectively 80% and 20% of the subsequent generation. Constraint-dependent functions were considered for crossover and mutation.

Table 6.2) were substituted into Eq. (6–35) and the kinetic parameters (α, β, and γ) were then estimated using a MATLAB code, prepared based on the described GA method. Based on the values of β (0.2993) and γ (-0.1482), the order of reaction (6–6) with respect to the light intensity, l, is equal to 0.5986 ($\beta = l/2$) and the constant of site deactivation (k_{dec}) is 0.1482 ($\gamma = -k_{dec}$).

Table 6.3. The values of kinetic parameters of the proposed kinetic model.

Kinetic parameter	Value
α	1.521
β	0.2994
γ	-0.1482

Figure 6.3 presents a three-dimensional graphical representation of the model predictions as a function of light intensity and time. It was observed that the rate of cyclohexanone production enhances by increasing the intensity of light, but decreases as a function of time. Figure 6.4 (diagram of dispersion) and Table 6.4 (parameters of the statistical analysis, as described in section 6.2.8) show the very good agreement between the predicted cyclohexanone production rates and experimental data. Data from Table 6.4 (R^2 close to 1, R^2_{adj} close to R^2, and *RMS*, *AAD*, and *MAE* close to zero) demonstrate the capability of the proposed model to predict the rate of cyclohexanone formation very well. Accordingly, Figure 6.4 and Table 6.4 confirm that the effects of light intensity and time can be modeled as power and exponential functions with a high accuracy. Modeling of the effect of light intensity and time is of high interest because these two parameters are known as the most effective in photocatalytic reactions [15, 140].

These results demonstrate that photocatalysis can be a promising technology for the production of cyclohexanone from cyclohexanol, not only for the excellent selectivity of cyclohexanone, but because of a low catalyst deactivation in comparison to cyclohexane conversion to cyclohexanone, due to avoiding the formation of significant amounts of carbonates and carboxylates. Nevertheless, further extensive work still needs to be done to enhance the rate of reaction, for eventual industrial implementation of this technology.

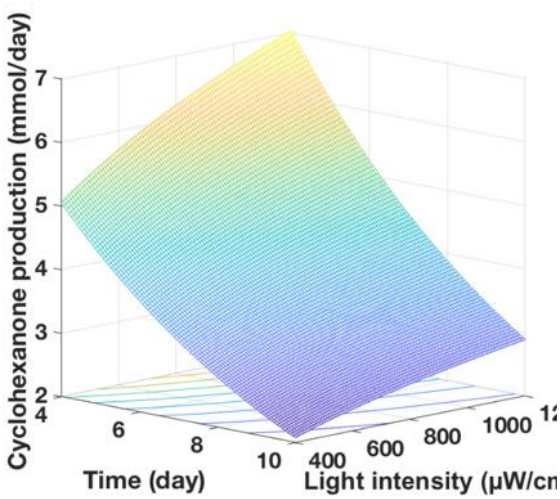

Figure 6.3. Three dimensional model prediction of the cyclohexanone production rate as a function of light intensity and time.

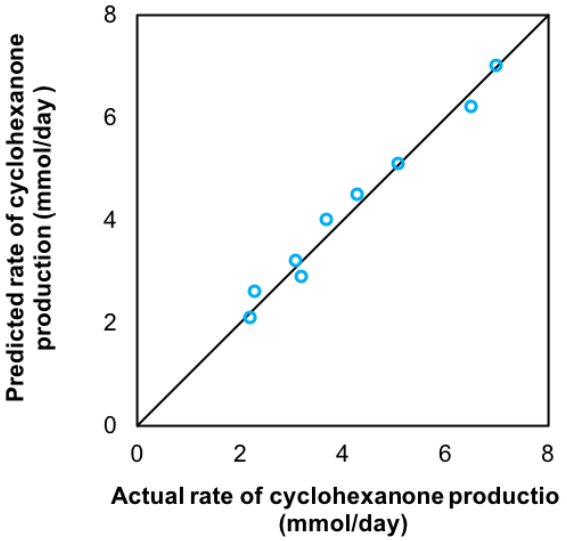

Figure 6.4. Comparison between the kinetic model predictions of cyclohexanone production rate with the obtained experimental results.

Table 6.4. Statistical comparison between the kinetic model predictions and experimental data.

Parameter	Value
R^2	0.9825
$R^2_{adj.}$	0.9537
RMS	0.2160
AAD	0.7927
MAE	0.0267

6.5. Conclusion

In this work, spectroscopic and kinetic studies were performed on the photocatalytic cyclohexanone production from cyclohexanol. *In situ ATR-FTIR* analysis of the photocatalytic reaction was employed to investigate this process, and revealed that the oxidation of surface bound cyclohexanol is highly selective without the formation of significant amounts of carbonates and carboxylates. A kinetic model was then developed (based on the present mechanism) to predict the rate of cyclohexanone production. The comparison between the experimental data and the kinetic model developed showed that the effects of light intensity and time can be modeled as power and exponential functions,

respectively. Both spectroscopic and chromatographic analyses demonstrated an excellent selectivity of cyclohexanone, and it proved that the photocatalytic approach could be a promising alternative for production of cyclohexanone from cyclohexanol.

General conclusions and future outlook

1. General conclusions

The main goal of this thesis was to study the photocatalytic valorization of biobased alcoholic wastes (glycerol, ethanol and cyclohexanol) to value-added green products (hydrogen and cyclohexanone). For "glycerol to hydrogen", the individual and interaction effect of operating parameters were studied using kinetic and statistical models and the process was optimized using GA method. Moreover, the role of CT (CNT and CS) in carbonaceous TiO_2 composite photocatalysts was investigated. For "cyclohexanol to cyclohexanone", the mechanism of photocatalytic reaction was examined by an *in-situ* analysis of reaction path.

First, the photocatalytic glycerol valorization to hydrogen was studied to find (i) the optimum values of the key operating parameters, (ii) the interaction effects of operating parameters, (iii) the optimal hydrogen production rate, and (iv) the relative importance of operating parameters. In this regard, ANN and RSM models were developed to predict the rate of hydrogen production as a function of glycerol%, catalyst loading, Pt%, and pH. The comparison of these models revealed that the ANN-based model is more accurate and reliable; thus it was employed for the optimization and parametric analysis. The developed ANN model was then optimized by the GA approach and it was found that the highest amount of hydrogen could be produced with 50% glycerol (v/v), 3.9 g/L catalyst loading, 3.1% Pt, and pH of 4.5. Finally, the relative importance of the operating parameters was analyzed using Garson's method and it was revealed that glycerol% and catalyst loading are the least and most influential parameters in hydrogen production, respectively (Chapter 3).

Second, a kinetic study was carried out to describe the photocatalytic production of hydrogen in liquid phase. A reaction mechanism and a kinetic model were proposed to predict the rate of hydrogen production as a function of light intensity, catalyst loading, substrate concentration, and time. The capability of the proposed model was confirmed based on the results of experiments conducted using glycerol and ethanol as representative biobased hydrogen sources. The ability of the model to predict the rate of hydrogen production for other substrates, photocatalysts, and ranges of operating parameters was confirmed by comparing model predictions with the experimental data from literature. Accordingly, it was

concluded that the present approach is appropriate to determine the rate of hydrogen production using other substrates and photocatalysts in various future works (Chapter 4).

Third, carbonaceous TiO_2 composites were developed using CNT and CS (as CT) and their role as template, cocatalyst, and adsorbent was studied. The role of CT as template was examined through morphology analysis of the prepared composites. It was found that TiO_2 nanoparticles were uniformly distributed on the surface of the CS. The formation of TiO_2 on the CNT was not uniform, however, CNTs could hinder the agglomeration of TiO_2 particles. The cocatalyst and adsorbent roles of CT were investigated based on photocatalytic experiments of hydrogen production from glycerol. Interestingly, it was found that the incorporation of CNT in TiO_2 composite can approximately double the rate of hydrogen production (i) in the absence of Pt or (ii) at low glycerol concentration. Accordingly, it was concluded that in addition to being a template, the CNT can play two important roles as cocatalyst and adsorbent (Chapter 5).

Forth, spectroscopic and kinetic studies were performed on selective photocatalytic oxidation of cyclohexanol (as another biobased alcohol) to cyclohexanone. A reaction mechanism based on different steps from charge separation to cyclohexanone molecule formation was proposed and *in-situ* ATR-FTIR analysis during the photocatalytic reaction was performed to confirm it. A kinetic model was developed to predict the rate of cyclohexanone production as a function of light intensity and time. The photocatalytic experiments performed in a slurry reactor allowed the determination of the kinetic parameters using the genetic algorithm method and helped validate the model. Both spectroscopic and chromatographic analyses confirmed a high selectivity of cyclohexanone, proving that the photocatalytic approach can be a promising alternative for the production of cyclohexanone (Chapter 6).

In summary, the results of this thesis show that photocatalysis is a promising alternative to valorize biobased alcoholic wastes to value-added products. The investigated processes meet the requirements of green chemistry as (i) solar can be the source of energy, (ii) the feedstocks are biobased (iii) the oxidant is oxygen or water (iv) operating pressure is atmospheric, (v) operating temperature is ambient, and (vi) process is catalytic.

2. Future outlooks

The results obtained in this thesis open several opportunities for future research in this area.

- The results of this thesis showed that glycerol can be valorized to hydrogen as a prospective green energy source in the future. As glycerol possesses three hydroxyl groups, it has a great potential to be valorized into a vast range of liquid products. Accordingly, studding the valorization of glycerol to value-added liquid products is an interesting subject for further research.
- In this research work, the photocatalytic valorization of glycerol, ethanol and cyclohexanol were studied. The valorization of other biobased alcohols (like methanol) using the photocatalytic process is a good study subject.
- In this work, pure glycerol was used for photocatalytic valorization experiments. It is of interest to study the effect of impurities in crude glycerol (obtained as a byproduct of biodiesel production process) on the rate of photocatalytic reaction and the selectivity of products.
- In the current research study, only hydrogen was measured in the gas phase and analyzed during the valorization of alcohols experiments. Analysis of gas phase to find the generation rate of other products (such as CH_4, CO, CO_2) is beneficial.
- The pH affects different aspects of the photocatalytic reaction, and according to relative importance analysis of the parameters, pH is one of the most important operating parameters. Therefore, development of a kinetic model that can predict the effect of pH on the photocatalytic processes is an interesting area of future research.
- As the results showed that CNT can effectively play the role of adsorbent, functionalization of CNT with specific functional groups for the purpose of (i) having affinity to adsorb specific intermediates/products and (ii) changing the path of reaction and the distribution of products is an interesting area of research.

References

[1] R.W. Griffin, Fundamentals of management, Cengage Learning, (2013).
[2] P. René, L'économique et le vivant, Payot,, (1979).
[3] A. Scerri, P. James, Accounting for sustainability: combining qualitative and quantitative research in developing 'indicators' of sustainability, International Journal of Social Research Methodology, 13 (2010) 41-53.
[4] F. White, L. Stallones, J.M. Last, Global public health: ecological foundations, Oxford University Press, (2013).
[5] L.R. Kahle, E. Gurel-Atay, Communicating sustainability for the green economy, ME Sharpe, (2013).
[6] K. Kristianova, E. Putrova, K. Gecova, Landscape architecture for architects-teaching landscape architecture in the architecture and urbanism study programmes, Global journal of engineering education, 19 (2017) 60-65.
[7] R. Lal, Feeding 11 billion on 0.5 billion hectare of area under cereal crops, Food and Energy Security, 5 (2016) 239-251.
[8] P. Imhof, J.C. van der Waal, Catalytic process development for renewable materials, John Wiley & Sons, (2013).
[9] D.L. Klass, Biomass for renewable energy, fuels, and chemicals, Elsevier, (1998).
[10] C.S.K. Lin, L.A. Pfaltzgraff, L. Herrero-Davila, E.B. Mubofu, S. Abderrahim, J.H. Clark, A.A. Koutinas, N. Kopsahelis, K. Stamatelatou, F. Dickson, Food waste as a valuable resource for the production of chemicals, materials and fuels. Current situation and global perspective, Energy Environ. Sci., 6 (2013) 426-464.
[11] M.J. Climent, A. Corma, S. Iborra, Conversion of biomass platform molecules into fuel additives and liquid hydrocarbon fuels, Green Chemistry, 16 (2014) 516-547.
[12] D.M. Alonso, J.Q. Bond, J.A. Dumesic, Catalytic conversion of biomass to biofuels, Green Chemistry, 12 (2010) 1493-1513.
[13] J.P. Diebold, A review of the chemical and physical mechanisms of the storage stability of fast pyrolysis bio-oils, National Renewable Energy Lab., Golden, CO (US), 1999.
[14] Y.-x. Yu, X. Ying, T.-j. Wang, Q. Zhang, X.-h. Zhang, X. Zhang, In-situ hydrogenation of lignin depolymerization model compounds to cyclohexanol, Journal of Fuel Chemistry and Technology, 41 (2013) 443-447.
[15] A.V. Puga, Photocatalytic production of hydrogen from biomass-derived feedstocks, Coordin. Cem. Rev., 315 (2016) 1-66.
[16] M.R. Monteiro, C.L. Kugelmeier, R.S. Pinheiro, M.O. Batalha, A. da Silva César, Glycerol from biodiesel production: Technological paths for sustainability, Renew. Sust. Energ. Rev., 88 (2018) 109-122.
[17] T. Werpy, G. Petersen, Top value added chemicals from biomass: volume I--results of screening for potential candidates from sugars and synthesis gas, National Renewable Energy Lab., Golden, CO (US), 2004.
[18] D. Sun, Y. Yamada, S. Sato, W. Ueda, Glycerol hydrogenolysis into useful C_3 chemicals, Appl. Catal. B:Environ., 193 (2016) 75-92.
[19] I. Iliuta, H.R. Radfarnia, M.C. Iliuta, Hydrogen Production by Sorption-Enhanced Steam Glycerol Reforming: Sorption Kinetics and Reactor Simulation, AIChE Journal, 59 (2013) 2105-2118.
[20] T.A. Ngo, M.-S. Kim, S.J. Sim, High-yield biohydrogen production from biodiesel manufacturing waste by Thermotoga neapolitana, Int. J. Hydrogen Energy, 36 (2011) 5836-5842.
[21] M. Stelmachowski, M. Marchwicka, E. Grabowska, M. Diak, A. Zaleska, The Photocatalytic Conversion of (Biodiesel Derived) Glycerol to Hydrogen-A Short Review and Preliminary Experimental Results Part 1: A Review, J Adv Oxid Technol, 17 (2014) 167-178.

[22] C.A.G. Quispe, C.J.R. Coronado, J.A. Carvalho Jr, Glycerol: Production, consumption, prices, characterization and new trends in combustion, Renew. Sust. Energ. Rev., 27 (2013) 475-493.
[23] P. Bondioli, Overview from oil seeds to industrial products: Present and future oleochemistry, Journal of Synthetic Lubrication, 21 (2005) 331-343.
[24] M. Ayoub, A.Z. Abdullah, Critical review on the current scenario and significance of crude glycerol resulting from biodiesel industry towards more sustainable renewable energy industry, Renew. Sust. Energ. Rev., 16 (2012) 2671-2686.
[25] J.M. Clomburg, R. Gonzalez, Anaerobic fermentation of glycerol: a platform for renewable fuels and chemicals, Trends in biotechnology, 31 (2013) 20-28.
[26] D. Samul, K. Leja, W. Grajek, Impurities of crude glycerol and their effect on metabolite production, Annals of Microbiology, 64 (2014) 891-898.
[27] H.W. Tan, A.R.A. Aziz, M.K. Aroua, Glycerol production and its applications as a raw material: A review, Renew. Sust. Energ. Rev., 27 (2013) 118-127.
[28] S.J. Sarma, S.K. Brar, E.B. Sydney, Y. Le Bihan, G. Buelna, C.R. Soccol, Microbial hydrogen production by bioconversion of crude glycerol: A review, Int. J. Hydrogen Energy, 37 (2012) 6473-6490.
[29] M.S. Ardi, M.K. Aroua, N.A. Hashim, Progress, prospect and challenges in glycerol purification process: a review, Renew. Sust. Energ. Rev., 42 (2015) 1164-1173.
[30] R.A.D. Arancon, C.S.K. Lin, K.M. Chan, T.H. Kwan, R. Luque, Advances on waste valorization: new horizons for a more sustainable society, Energy Science & Engineering, 1 (2013) 53-71.
[31] J.H. Clark, F.E.I. Deswarte, The biorefinery concept—an integrated approach, Introduction to chemicals from biomass, Wiley, Chichester, United Kingdom2008, pp. 1-18.
[32] R. Liu, H. Yoshida, S.-i. Fujita, M. Arai, Photocatalytic hydrogen production from glycerol and water with NiO_x/TiO_2 catalysts, Appl. Catal. B:Environ., 144 (2014) 41-45.
[33] X. Fu, X. Wang, D.Y.C. Leung, Q. Gu, S. Chen, H. Huang, Photocatalytic reforming of C_3-polyols for H_2 production: part (I). Role of their OH groups, Appl. Catal. B:Environ., 106 (2011) 681-688.
[34] P.U. Okoye, B.H. Hameed, Review on recent progress in catalytic carboxylation and acetylation of glycerol as a byproduct of biodiesel production, Renew. Sust. Energ. Rev., 53 (2016) 558-574.
[35] S. Bagheri, N.M. Julkapli, W.A. Yehye, Catalytic conversion of biodiesel derived raw glycerol to value added products, Renew. Sust. Energ. Rev., 41 (2015) 113-127.
[36] A.V. Puga, A. Forneli, H. García, A. Corma, Production of H_2 by ethanol photoreforming on Au/TiO_2, Advanced Functional Materials, 24 (2014) 241-248.
[37] H. Lu, J. Zhao, L. Li, L. Gong, J. Zheng, L. Zhang, Z. Wang, J. Zhang, Z. Zhu, Selective oxidation of sacrificial ethanol over TiO 2-based photocatalysts during water splitting, Energy Environ. Sci., 4 (2011) 3384-3388.
[38] G. Yang, R. Cang, L.-Q. Shen, F. Xue, H. Huang, Z.-G. Zhang, Expanding the substrate scope of phenylacetone monooxygenase from Thermobifida fusca towards cyclohexanone by protein engineering, Catal. Commun., 119 (2019) 159-163.
[39] J. Ritz, H. Fuchs, H. Kieczka, W.C. Moran, "Caprolacatam" in Ullmann's Encyclopedia of Industrial Chemis, Wiley VCH, Weinheim, Germany, (2005).
[40] W.B. Fisher, J.F. Van Pepper, M. Grayson, Kirk-Othner Encyclopedia of Chemical Technology, 3rd ed., Wiley, New York, 1979.
[41] H. Bahruji, M. Bowker, P.R. Davies, L.S. Al-Mazroai, A. Dickinson, J. Greaves, D. James, L. Millard, F. Pedrono, Sustainable H_2 gas production by photocatalysis, J. Photoch. Photobio., A, 216 (2010) 115-118.
[42] B. Srinivas, K. Lalitha, P.A.K. Reddy, G. Rajesh, V.D. Kumari, M. Subrahmanyam, B.R. De, Cyclohexanol dehydrogenation over Cu-loaded TiO_2 photocatalyst under solar illumination, Res. Chem.Intermed., 37 (2011) 1069-1086.
[43] X. Li, S. Shinoda, Y. Saito, Photocatalytic liquid-phase dehydrogenation of cyclohexanol with rhodium porphyrin complex, Journal of molecular catalysis, 49 (1989) 113-119.

[44] A. Brandner, K. Lehnert, A. Bienholz, M. Lucas, P. Claus, Production of biomass-derived chemicals and energy: chemocatalytic conversions of glycerol, Topics in Catalysis, 52 (2009) 278-287.
[45] C.H. Zhou, J.N. Beltramini, Y.X. Fan, G.Q. Lu, Chemoselective catalytic conversion of glycerol as a biorenewable source to valuable commodity chemicals, Chem Soc Rev, 37 (2008) 527-549.
[46] M.S. Yancheshmeh, H.R. Radfarnia, M.C. Iliuta, High temperature CO 2 sorbents and their application for hydrogen production by sorption enhanced steam reforming process, Chem. Eng. J., 283 (2016) 420-444.
[47] H.R. Radfarnia, M.C. Iliuta, Hydrogen production by sorption-enhanced steam methane reforming process using CaO-Zr/Ni bifunctional sorbent–catalyst, Chemical Engineering and Processing: Process Intensification, 86 (2014) 96-103.
[48] H. Balat, E. Kırtay, Hydrogen from biomass – Present scenario and future prospects, Int. J. Hydrogen Energy, 35 (2010) 7416-7426.
[49] N.H. Tran, G.S.K. Kannangara, Conversion of glycerol to hydrogen rich gas, Chem. Soc. Rev., 42 (2013) 9454-9479.
[50] D. Panepinto, S. Fiore, G. Genon, M. Acri, Thermal valorization of sewer sludge: Perspectives for large wastewater treatment plants, J. Clean. Prod., 137 (2016) 1323-1329.
[51] A. Bosmans, I. Vanderreydt, D. Geysen, L. Helsen, The crucial role of Waste-to-Energy technologies in enhanced landfill mining: a technology review, J. Clean. Prod., 55 (2013) 10-23.
[52] R.R. Singhania, A.K. Patel, G. Christophe, P. Fontanille, C. Larroche, Biological upgrading of volatile fatty acids, key intermediates for the valorization of biowaste through dark anaerobic fermentation, Bioresource technology, 145 (2013) 166-174.
[53] S. Diener, N.M.S. Solano, F.R. Gutiérrez, C. Zurbrügg, K. Tockner, Biological treatment of municipal organic waste using black soldier fly larvae, Waste and Biomass Valorization, 2 (2011) 357-363.
[54] J.C. Colmenares, R. Luque, Heterogeneous photocatalytic nanomaterials: prospects and challenges in selective transformations of biomass-derived compounds, Chem. Soc. Rev., 43 (2014) 765-778.
[55] X. Fan, R. Burton, Y. Zhou, Glycerol (Byproduct of Biodiesel Production) as a Source for Fuels and Chemicals Mini Review, The Open Fuels & Energy Science Journal, 3 (2010).
[56] W. Wang, Thermodynamic analysis of glycerol partial oxidation for hydrogen production, Fuel processing technology, 91 (2010) 1401-1408.
[57] X. Wang, S. Li, H. Wang, B. Liu, X. Ma, Thermodynamic analysis of glycerin steam reforming, Energy Fuels, 22 (2008) 4285-4291.
[58] I. Iliuta, M.C. Iliuta, P. Fongarland, F. Larachi, Integrated aqueous-phase glycerol reforming to dimethyl ether synthesis—A novel allothermal dual bed membrane reactor concept, Chem. Eng. J., 187 (2012) 311-327.
[59] I. Iliuta, M.C. Iliuta, Biosyngas production in an integrated aqueous-phase glycerol reforming/chemical looping combustion process, Ind. Eng. Chem. Res., 52 (2013) 16142-16161.
[60] R. Liguori, V. Faraco, Biological processes for advancing lignocellulosic waste biorefinery by advocating circular economy, Bioresource technology, 215 (2016) 13-20.
[61] M. Mohajerani, M. Mehrvar, F. Ein-Mozaffari, Photoreactor design and CFD modelling of a UV/H_2O_2 process for distillery wastewater treatment, Can. J. Chem. Eng., 90 (2012) 719-729.
[62] B.A. Pinaud, J.D. Benck, L.C. Seitz, A.J. Forman, Z. Chen, T.G. Deutsch, B.D. James, K.N. Baum, G.N. Baum, S. Ardo, Technical and economic feasibility of centralized facilities for solar hydrogen production via photocatalysis and photoelectrochemistry, Energy Environ. Sci., 6 (2013) 1983-2002.
[63] G. Ciamician, The photochemistry of the future, Science, 36 (1912) 385-394.
[64] A. Fujishima, K. Honda, Electrochemical Photolysis of Water at a Semiconductor Electrode, Nature, 238 (1972) 37-38.

[65] M. Hilgendorff, V. Sundström, Dynamics of electron injection and recombination of dye-sensitized TiO_2 particles, Phys. Chem. B., 102 (1998) 10505-10514.
[66] R. Leary, A. Westwood, Carbonaceous nanomaterials for the enhancement of TiO_2 photocatalysis, Carbon, 49 (2011) 741-772.
[67] K. Maeda, K. Teramura, D. Lu, T. Takata, N. Saito, Y. Inoue, K. Domen, Photocatalyst releasing hydrogen from water, Nature, 440 (2006) 295-295.
[68] S.Y. Reece, J.A. Hamel, K. Sung, T.D. Jarvi, A.J. Esswein, J.J.H. Pijpers, D.G. Nocera, Wireless solar water splitting using silicon-based semiconductors and earth-abundant catalysts, Science, 334 (2011) 645-648.
[69] P. Panagiotopoulou, E.E. Karamerou, D.I. Kondarides, Kinetics and mechanism of glycerol photo-oxidation and photo-reforming reactions in aqueous TiO_2 and Pt/TiO_2 suspensions, Catal. Today, 209 (2013) 91-98.
[70] M.M. Mohammadi, M. Vossoughi, M. Feilizadeh, D. Rashtchian, S. Moradi, I. Alemzadeh, Effects of electrophoretic deposition parameters on the photocatalytic activity of TiO_2 films: optimization by response surface methodology, Colloids Surf. A: Physicochem. Eng. Asp., 452 (2014) 1-8.
[71] B. Ohtani, Preparing articles on photocatalysis-beyond the illusions, misconceptions, and speculation, Chemistry letters, 37 (2008) 216-229.
[72] N.L. Reddy, K. D Praveen, M.V. Shankar, Co-catalyst free Titanate Nanorods for improved Hydrogen production under solar light irradiation, Journal of Chemical Sciences, 128 (2016) 649-656.
[73] K. Manukumar, G. Nagaraju, D.P. Kumar, M.J.J.o.M.S.M.i.E. Shankar, Facile ionothermal synthesis of TiO_2 nanorods for photocatalytic H_2 generation, 30 (2019) 1076-1083.
[74] V.M. Daskalaki, D.I. Kondarides, Efficient production of hydrogen by photo-induced reforming of glycerol at ambient conditions, Catal. Today, 144 (2009) 75-80.
[75] K. Majrik, Z. Pászti, L. Korecz, L. Trif, A. Domján, G. Bonura, C. Cannilla, F. Frusteri, A. Tompos, E.J.M. Tálas, Study of $PtOx/TiO_2$ Photocatalysts in the Photocatalytic Reforming of Glycerol: The Role of Co-Catalyst Formation, 11 (2018) 1927.
[76] N. Fu, G. Lu, Hydrogen Evolution Over Heteropoly Blue-Sensitized Pt/TiO_2 Under Visible Light Irradiation, Catalysis Letters, 127 (2008) 319-322.
[77] D.I. Kondarides, V.M. Daskalaki, A. Patsoura, X.E. Verykios, Hydrogen Production by Photo-Induced Reforming of Biomass Components and Derivatives at Ambient Conditions, Catalysis Letters, 122 (2007) 26-32.
[78] N. Fu, G. Lu, Photo-catalytic H_2 evolution over a series of Keggin-structure heteropoly blue sensitized Pt/TiO_2 under visible light irradiation, Appl. Surf. Sci., 255 (2009) 4378-4383.
[79] J. Gunlazuardi, E.L.J.I.J.o.H.E. Dewi, Enhanced photocatalytic activity of Pt deposited on titania nanotube arrays for the hydrogen production with glycerol as a sacrificial agent, 42 (2017) 24014-24025.
[80] M. Li, Y. Li, S. Peng, G. Lu, S. Li, Photocatalytic hydrogen generation using glycerol wastewater over Pt/TiO_2, Frontiers of Chemistry in China, 4 (2009) 32-38.
[81] V.M. Daskalaki, P. Panagiotopoulou, D.I. Kondarides, Production of peroxide species in Pt/TiO_2 suspensions under conditions of photocatalytic water splitting and glycerol photoreforming, Chem. Eng. J., 170 (2011) 433-439.
[82] A. Beltram, I. Romero-Ocaña, J. Josè Delgado Jaen, T. Montini, P. Fornasiero, Photocatalytic valorization of ethanol and glycerol over TiO_2 polymorphs for sustainable hydrogen production, Appl. Catal. A: Gen., 518 (2016) 167-175.
[83] E.P. Melián, C.R. López, D.E. Santiago, R. Quesada-Cabrera, J.A.O. Méndez, J.M.D. Rodríguez, O.G. Díaz, Study of the photocatalytic activity of Pt-modified commercial TiO_2 for hydrogen production in the presence of common organic sacrificial agents, Appl. Catal. A: Gen., 518 (2016) 189-197.

[84] X. Jiang, X. Fu, L. Zhang, S. Meng, S. Chen, Photocatalytic reforming of glycerol for H_2 evolution on Pt/TiO_2: fundamental understanding the effect of co-catalyst Pt and the Pt deposition route, J. Mater. Chem. A, 3 (2015) 2271-2282.
[85] P. Ribao, M.A. Esteves, V.R. Fernandes, M.J. Rivero, C.M. Rangel, I.J.I.J.o.H.E. Ortiz, Challenges arising from the use of TiO_2/rGO/Pt photocatalysts to produce hydrogen from crude glycerol compared to synthetic glycerol, (2018).
[86] F.J. López-Tenllado, J. Hidalgo-Carrillo, V. Montes, A. Marinas, F.J. Urbano, J.M. Marinas, L. Ilieva, T. Tabakova, F. Reid, A comparative study of hydrogen photocatalytic production from glycerol and propan-2-ol on M/TiO_2 systems (M= Au, Pt, Pd), Catal. Today, 280 (2016) 58-64.
[87] K. Bednarczyk, M. Stelmachowski, M.J.E.P. Gmurek, S. Energy, The Influence of Process Parameters on Photocatalytic Hydrogen Production, (2018).
[88] T.W. Seadira, G. Sadanandam, T. Ntho, C.M. Masuku, M.S.J.A.C.B.E. Scurrell, Preparation and characterization of metals supported on nanostructured TiO_2 hollow spheres for production of hydrogen via photocatalytic reforming of glycerol, 222 (2018) 133-145.
[89] Z.H.N. Al-Azri, W.-T. Chen, A. Chan, V. Jovic, T. Ina, H. Idriss, G.I.N. Waterhouse, The roles of metal co-catalysts and reaction media in photocatalytic hydrogen production: Performance evaluation of M/TiO_2 photocatalysts (M=Pd, Pt, Au) in different alcohol–water mixtures, J. Catal., 329 (2015) 355-367.
[90] M. Jung, J.N. Hart, D. Boensch, J. Scott, Y.H. Ng, R. Amal, Hydrogen evolution via glycerol photoreforming over Cu–Pt nanoalloys on TiO_2, Appl. Catal. A: Gen., 518 (2016) 221-230.
[91] D.W. Skaf, N.G. Natrin, K.C. Brodwater, C.R. Bongo, Comparison of photocatalytic hydrogen production from glycerol and crude glycerol obtained from biodiesel processing, Catalysis letters, 142 (2012) 1175-1179.
[92] N. Luo, Z. Jiang, H. Shi, F. Cao, T. Xiao, P. Edwards, Photo-catalytic conversion of oxygenated hydrocarbons to hydrogen over heteroatom-doped TiO_2 catalysts, Int. J. Hydrogen Energy, 34 (2009) 125-129.
[93] M.R. Pai, A.M. Banerjee, S.A. Rawool, A. Singhal, C. Nayak, S.H. Ehrman, A.K. Tripathi, S.R. Bharadwaj, A comprehensive study on sunlight driven photocatalytic hydrogen generation using low cost nanocrystalline Cu-Ti oxides, Solar Energy Materials and Solar Cells, 154 (2016) 104-120.
[94] S.A. Rawool, M.R. Pai, A. Banerjee, R. Bapat, C. Nayak, A.J.I.J.o.H.E. Tripathi, Lab scale optimization of various factors for photocatalytic hydrogen generation over low cost Cu0. 02Ti0. 98O2-δ photocatalyst under UV/Visible irradiation and sunlight, 43 (2018) 1271-1284.
[95] Slamet, D. Tristantini, Valentina, M. Ibadurrohman, Photocatalytic hydrogen production from glycerol–water mixture over Pt-N-TiO_2 nanotube photocatalyst, International Journal of Energy Research, 37 (2013) 1372-1381.
[96] K. Lalitha, G. Sadanandam, V.D. Kumari, M. Subrahmanyam, B. Sreedhar, N.Y. Hebalkar, Highly Stabilized and Finely Dispersed Cu_2O/TiO_2: A Promising Visible Sensitive Photocatalyst for Continuous Production of Hydrogen from Glycerol:Water Mixtures, Phys. Chem. C., 114 (2010) 22181-22189.
[97] T. Montini, V. Gombac, L. Sordelli, J.J. Delgado, X. Chen, G. Adami, P. Fornasiero, Nanostructured Cu/TiO_2 Photocatalysts for H_2 Production from Ethanol and Glycerol Aqueous Solutions, ChemCatChem, 3 (2011) 574-577.
[98] L. Clarizia, I. Di Somma, L. Onotri, R. Andreozzi, R. Marotta, Kinetic modeling of hydrogen generation over nano-Cu(s)/TiO_2 catalyst through photoreforming of alcohols, Catal. Today, 281 (2017) 117-123.
[99] M. Zhang, R. Sun, Y. Li, Q. Shi, L. Xie, J. Chen, X. Xu, H. Shi, W. Zhao, High H_2 Evolution from Quantum Cu (II) Nanodot-doped 2D Ultrathin TiO_2 Nanosheets with Dominant Exposed {001} Facets for Reforming Glycerol with Multiple Electron Transport Pathways, Phys. Chem. C., 120 (2016) 10746-10756.

[100] D.P. Kumar, M.V. Shankar, M.M. Kumari, G. Sadanandam, B. Srinivas, V. Durgakumari, Nano-size effects on CuO/TiO_2 catalysts for highly efficient H_2 production under solar light irradiation, Chemical Communications, 49 (2013) 9443-9445.
[101] A. Petala, E. Ioannidou, A. Georgaka, K. Bourikas, D.I. Kondarides, Hysteresis phenomena and rate fluctuations under conditions of glycerol photo-reforming reaction over CuO_x/TiO_2 catalysts, Appl. Catal. B:Environ., 178 (2015) 201-209.
[102] M.O. Segovia-Guzmán, M. Román-Aguirre, J.Y. Verde-Gomez, V.H. Collins-Martínez, G. Zaragoza-Galán, V.H.J.C.T. Ramos-Sánchez, Green Cu_2O/TiO_2 heterojunction for glycerol photoreforming, (2018).
[103] K.K. Mandari, J.Y. Do, A.K.R. Police, M.J.A.C.B.E. Kang, Natural solar light-driven preparation of plasmonic resonance-based alloy and core-shell catalyst for sustainable enhanced hydrogen production: Green approach and characterization, 231 (2018) 137-150.
[104] D. Praveen Kumar, N. Lakshmana Reddy, M. Mamatha Kumari, B. Srinivas, V. Durga Kumari, B. Sreedhar, V. Roddatis, O. Bondarchuk, M. Karthik, B. Neppolian, M.V. Shankar, Cu_2O-sensitized TiO_2 nanorods with nanocavities for highly efficient photocatalytic hydrogen production under solar irradiation, Solar Energy Materials and Solar Cells, 136 (2015) 157-166.
[105] F.K. Chong, E. Nurlaela, B.K. Dutta, Impact of glycerol as scavenger for solar hydrogen production from water, International Journal of Energy and Environment, (2014) 19-26.
[106] S. Ibrahim, Y. Cheng, D. Zhao, M.A.J.I.J.o.H.E. Nadeem, A new insight for photocatalytic hydrogen production by a Cu/Ni based cyanide bridged polymer as a co-catalyst on titania support in glycerol water mixture, 44 (2019) 2508-2518.
[107] W.-T. Chen, A. Chan, Z.H.N. Al-Azri, A.G. Dosado, M.A. Nadeem, D. Sun-Waterhouse, H. Idriss, G.I.N. Waterhouse, Effect of TiO_2 polymorph and alcohol sacrificial agent on the activity of Au/TiO_2 photocatalysts for H_2 production in alcohol–water mixtures, J. Catal., 329 (2015) 499-513.
[108] A.G. Dosado, W.-T. Chen, A. Chan, D. Sun-Waterhouse, G.I.N. Waterhouse, Novel Au/TiO_2 photocatalysts for hydrogen production in alcohol–water mixtures based on hydrogen titanate nanotube precursors, J. Catal., 330 (2015) 238-254.
[109] W.-T. Chen, A.G. Dosado, A. Chan, D. Sun-Waterhouse, G.I.J.A.C.A.G. Waterhouse, Highly reactive anatase nanorod photocatalysts synthesized by calcination of hydrogen titanate nanotubes: Effect of calcination conditions on photocatalytic performance for aqueous dye degradation and H2 production in alcohol-water mixtures, 565 (2018) 98-118.
[110] M. Bowker, P.R. Davies, L.S. Al-Mazroai, Photocatalytic Reforming of Glycerol over Gold and Palladium as an Alternative Fuel Source, Catalysis Letters, 128 (2008) 253-255.
[111] D.P. Kumar, N.L. Reddy, M. Karthik, B. Neppolian, J. Madhavan, M.V. Shankar, Solar light sensitized p-Ag_2 O/n-TiO_2 nanotubes heterojunction photocatalysts for enhanced hydrogen production in aqueous-glycerol solution, Solar Energy Materials and Solar Cells, 154 (2016) 78-87.
[112] G. Sadanandam, K. Lalitha, V.D. Kumari, M.V. Shankar, M. Subrahmanyam, Cobalt doped TiO_2: A stable and efficient photocatalyst for continuous hydrogen production from glycerol: Water mixtures under solar light irradiation, Int. J. Hydrogen Energy, 38 (2013) 9655-9664.
[113] S.-i. Fujita, H. Kawamori, D. Honda, H. Yoshida, M. Arai, Photocatalytic hydrogen production from aqueous glycerol solution using NiO/TiO_2 catalysts: Effects of preparation and reaction conditions, Appl. Catal. B:Environ., 181 (2016) 818-824.
[114] N. Lakshmana Reddy, K.K. Cheralathan, V. Durga Kumari, B. Neppolian, S.J.A.S.C. Muthukonda Venkatakrishnan, Engineering, Photocatalytic reforming of biomass derived crude glycerol in water: a sustainable approach for improved hydrogen generation using $Ni(OH)_2$ decorated TiO_2 nanotubes under solar light irradiation, 6 (2018) 3754-3764.
[115] V. Gombac, L. Sordelli, T. Montini, J.J. Delgado, A. Adamski, G. Adami, M. Cargnello, S. Bernal, P. Fornasiero, CuO_x–TiO_2 Photocatalysts for H_2 Production from Ethanol and Glycerol Solutions, The Journal of Physical Chemistry A, 114 (2009) 3916-3925.

[116] R. Bashiri, N.M. Mohamed, C.F. Kait, S. Sufian, Hydrogen production from water photosplitting using Cu/TiO_2 nanoparticles: Effect of hydrolysis rate and reaction medium, Int. J. Hydrogen Energy, 40 (2015) 6021-6037.
[117] S. Taylor, M. Mehta, A. Samokhvalov, Production of Hydrogen by Glycerol Photoreforming Using Binary Nitrogen–Metal-Promoted N-M-TiO_2 Photocatalysts, ChemPhysChem, 15 (2014) 942-949.
[118] M. MamathaKumari, D. Praveen Kumar, P. Haridoss, V. DurgaKumari, M.V. Shankar, Nanohybrid of titania/carbon nanotubes – nanohorns: A promising photocatalyst for enhanced hydrogen production under solar irradiation, Int. J. Hydrogen Energy, 40 (2015) 1665-1674.
[119] M.J.I.J.o.H.E. Tahir, La-modified TiO_2/carbon nanotubes assembly nanocomposite for efficient photocatalytic hydrogen evolution from glycerol-water mixture, 44 (2019) 3711-3725.
[120] M. Umer, M. Tahir, M.U. Azam, M.M.J.A.S.S. Jaffar, Metals free MWCNTs@ TiO_2@ MMT heterojunction composite with MMT as a mediator for fast charges separation towards visible light driven photocatalytic hydrogen evolution, 463 (2019) 747-757.
[121] N.R. Reddy, M.M. Kumari, K. Cheralathan, M.J.i.j.o.h.e. Shankar, Enhanced photocatalytic hydrogen production activity of noble metal free MWCNT-TiO_2 nanocomposites, 43 (2018) 4036-4043.
[122] N.-T. Nguyen, D.-D. Zheng, S.-S. Chen, C.-T. Chang, C.-M. Ma, N.-C. Nguyen, H.-T. Nguyen, S.-S. Hsiao, S.-Y.J.J.o.n. Kang, nanotechnology, Effects of Different Sacrificial Agents and Hydrogen Production from Wastewater by Pt-Graphene/TiO_2, 18 (2018) 3563-3570.
[123] H.Y. Hafeez, S.K. Lakhera, P. Karthik, M. Anpo, B.J.A.S.S. Neppolian, Facile construction of ternary $CuFe_2O_4$-TiO_2 nanocomposite supported reduced graphene oxide (rGO) photocatalysts for the efficient hydrogen production, 449 (2018) 772-779.
[124] H.Y. Hafeez, S.K. Lakhera, S. Bellamkonda, G.R. Rao, M. Shankar, D. Bahnemann, B.J.i.j.o.h.e. Neppolian, Construction of ternary hybrid layered reduced graphene oxide supported g-C_3N_4-TiO_2 nanocomposite and its photocatalytic hydrogen production activity, 43 (2018) 3892-3904.
[125] G. Sadanandam, L. Zhang, M.S.J.J.o.R. Scurrell, S. Energy, Enhanced photocatalytic hydrogen formation over Fe-loaded TiO_2 and g-C_3N_4 composites from mixed glycerol and water by solar irradiation, 10 (2018) 034703.
[126] S.G. Babu, R. Vinoth, D.P. Kumar, M.V. Shankar, H.-L. Chou, K. Vinodgopal, B. Neppolian, Influence of electron storing, transferring and shuttling assets of reduced graphene oxide at the interfacial copper doped TiO_2 p–n heterojunction for increased hydrogen production, Nanoscale, 7 (2015) 7849-7857.
[127] G. Marcì, E. García-López, V. Vaiano, G. Sarno, D. Sannino, L.J.C.T. Palmisano, Keggin heteropolyacids supported on TiO_2 used in gas-solid (photo) catalytic propene hydration and in liquid-solid photocatalytic glycerol dehydration, 281 (2017) 60-70.
[128] C. Wang, X. Cai, Y. Chen, Z. Cheng, X. Luo, S. Mo, L. Jia, P. Lin, Z.J.C.E.J. Yang, Improved hydrogen production from glycerol photoreforming over sol-gel derived TiO_2 coupled with metal oxides, 317 (2017) 522-532.
[129] M. de Oliveira Melo, L.A. Silva, Visible light-induced hydrogen production from glycerol aqueous solution on hybrid Pt–CdS–TiO_2 photocatalysts, J. Photoch. Photobio., A, 226 (2011) 36-41.
[130] S.A.L. Bastos, P.A.L. Lopes, F.N. Santos, L.A. Silva, Experimental design as a tool to study the reaction parameters in hydrogen production from photoinduced reforming of glycerol over CdS photocatalyst, Int. J. Hydrogen Energy, 39 (2014) 14588-14595.
[131] J.J. Wang, Z.J. Li, X.B. Li, X.B. Fan, Q.Y. Meng, S. Yu, C.B. Li, J.X. Li, C.H. Tung, L.Z. Wu, Photocatalytic Hydrogen Evolution from Glycerol and Water over Nickel-Hybrid Cadmium Sulfide Quantum Dots under Visible-Light Irradiation, ChemSusChem, 7 (2014) 1468-1475.
[132] S. Manchala, L.R. Nagappagari, S.M. Venkatakrishnan, V.J.i.j.o.h.e. Shanker, Facile synthesis of noble-metal free polygonal Zn2TiO4 nanostructures for highly efficient photocatalytic hydrogen evolution under solar light irradiation, 43 (2018) 13145-13157.

[133] S. Peng, M. Ding, T. Yi, Z. Zhan, Y. Li, Photocatalytic hydrogen evolution and decomposition of glycerol over $Cd_{0.5}Zn_{0.5}S$ solid solution under visible light irradiation, Environ Prog Sustain, 35 (2016) 141-148.
[134] P.A.L. Lopes, A.J.S. Mascarenhas, L.A. Silva, Sonochemical synthesis of $Cd_{1-x}Zn_xS$ solid solutions for application in photocatalytic reforming of glycerol to produce hydrogen, J Alloy Compd, 649 (2015) 332-336.
[135] T.P. Lyubina, D.V. Markovskaya, E.A. Kozlova, V.N. Parmon, Photocatalytic hydrogen evolution from aqueous solutions of glycerol under visible light irradiation, Int. J. Hydrogen Energy, 38 (2013) 14172-14179.
[136] D. Bao, P. Gao, X. Zhu, S. Sun, Y. Wang, X. Li, Y. Chen, H. Zhou, Y. Wang, P. Yang, ZnO/ZnS Heterostructured Nanorod Arrays and Their Efficient Photocatalytic Hydrogen Evolution, Chem-Eur J, 21 (2015) 12728-12734.
[137] H.X. Sang, X.T. Wang, C.C. Fan, F. Wang, Enhanced photocatalytic H_2 production from glycerol solution over ZnO/ZnS core/shell nanorods prepared by a low temperature route, Int. J. Hydrogen Energy, 37 (2012) 1348-1355.
[138] C.-J. Chang, Y.-G. Lin, H.-T. Weng, Y.-H.J.A.S.S. Wei, Photocatalytic hydrogen production from glycerol solution at room temperature by ZnO-ZnS/graphene photocatalysts, 451 (2018) 198-206.
[139] S. Liu, X. Wang, K. Wang, R. Lv, Y. Xu, ZnO/ZnS–PdS core/shell nanorods: synthesis, characterization and application for photocatalytic hydrogen production from a glycerol/water solution, Appl. Surf. Sci., 283 (2013) 732-739.
[140] T. Jedsukontorn, V. Meeyoo, N. Saito, M. Hunsom, Route of glycerol conversion and product generation via TiO_2-induced photocatalytic oxidation in the presence of H_2O_2, Chem. Eng. J., 281 (2015) 252-264.
[141] J.C. Colmenares, R. Luque, Heterogeneous photocatalytic nanomaterials: prospects and challenges in selective transformations of biomass-derived compounds, Chem Soc Rev, 43 (2014) 765-778.
[142] K.K. Mandari, J.Y. Do, S.P. Vattikuti, A.K.R. Police, M.J.J.o.A. Kang, Compounds, Solar light response with noble metal-free highly active copper (II) phosphate/titanium dioxide nanoparticle/copper (II) oxide nanocomposites for photocatalytic hydrogen production, 750 (2018) 292-303.
[143] R. Reddy, U. Bhargav, M. Kumari, M.J.M.R.B. Shankar, Multiwalled carbon nanotubes in titania based nanocomposite as trap for photoexcitons for enhanced photocatalytic hydrogen production under solar light irradiation, 106 (2018) 271-275.
[144] P.M. Gharat, H. Pal, S.D.J.S.A.P.A.M. Choudhury, B. Spectroscopy, Photophysics and luminescence quenching of carbon dots derived from lemon juice and glycerol, 209 (2019) 14-21.
[145] L.S. Al-Mazroai, M. Bowker, P. Davies, A. Dickinson, J. Greaves, D. James, L. Millard, The photocatalytic reforming of methanol, Catal. Today, 122 (2007) 46-50.
[146] M. Bowker, D. James, P. Stone, R. Bennett, N. Perkins, L. Millard, J. Greaves, A. Dickinson, Catalysis at the metal-support interface: exemplified by the photocatalytic reforming of methanol on Pd/TiO_2, J. Catal., 217 (2003) 427-433.
[147] T. Sreethawong, T. Puangpetch, S. Chavadej, S. Yoshikawa, Quantifying influence of operational parameters on photocatalytic H_2 evolution over Pt-loaded nanocrystalline mesoporous TiO_2 prepared by single-step sol–gel process with surfactant template, J Power Sources, 165 (2007) 861-869.
[148] C.R. López, E.P. Melián, J.A. Ortega Méndez, D.E. Santiago, J.M. Doña Rodríguez, O. González Díaz, Comparative study of alcohols as sacrificial agents in H_2 production by heterogeneous photocatalysis using Pt/TiO_2 catalysts, J. Photoch. Photobio., A, 312 (2015) 45-54.
[149] C. Minero, A. Bedini, V. Maurino, Glycerol as a probe molecule to uncover oxidation mechanism in photocatalysis, Appl. Catal. B:Environ., 128 (2012) 135-143.

[150] M.R. Karimi Estahbanati, M. Feilizadeh, M.C. Iliuta, Photocatalytic valorization of glycerol to hydrogen: Optimization of operating parameters by artificial neural network, Appl. Catal. B:Environ., 209 (2017) 483-492.
[151] M. Feilizadeh, M. Rahimi, S.M. Zakeri, N. Mahinpey, M. Vossoughi, M. Qanbarzadeh, Individual and interaction effects of operating parameters on the photocatalytic degradation under visible light illumination: Response surface methodological approach, Can. J. Chem. Eng., (2017).
[152] M. Feilizadeh, G. Mul, M. Vossoughi, E. coli inactivation by visible light irradiation using a Fe–Cd/TiO_2 photocatalyst: Statistical analysis and optimization of operating parameters, Appl. Catal. B:Environ., 168 (2015) 441-447.
[153] J. Choi, S.Y. Ryu, W. Balcerski, T.K. Lee, M.R. Hoffmann, Photocatalytic production of hydrogen on Ni/NiO/KNbO 3/CdS nanocomposites using visible light, Journal of Materials Chemistry, 18 (2008) 2371-2378.
[154] G. Zhang, Y. Xu, Polyoxometalate-mediated reduction of dichromate under UV irradiation, Inorganic Chemistry Communications, 8 (2005) 520-523.
[155] M.T. Pope, G.M. Varga Jr, Heteropoly blues. I. Reduction stoichiometries and reduction potentials of some 12-tungstates, Inorganic Chemistry, 5 (1966) 1249-1254.
[156] M. Feilizadeh, I. Alemzadeh, A. Delparish, M.R. Karimi Estahbanati, M. Soleimani, Y. Jangjou, A. Vosoughi, Optimization of operating parameters for efficient photocatalytic inactivation of Escherichia coli based on a statistical design of experiments, Water Sci. Technol., 71 (2015) 823-831.
[157] V.A. Sakkas, M.A. Islam, C. Stalikas, T.A. Albanis, Photocatalytic degradation using design of experiments: a review and example of the Congo red degradation, J. Hazard. Mater., 175 (2010) 33-44.
[158] S. Moradi, M. Vossoughi, M. Feilizadeh, S.M.E. Zakeri, M.M. Mohammadi, D. Rashtchian, A.Y. Booshehri, Photocatalytic degradation of dibenzothiophene using La/PEG-modified TiO_2 under visible light irradiation, Res. Chem.Intermed., 41 (2015) 4151-4167.
[159] L. Cao, Z. Gao, S.L. Suib, T.N. Obee, S.O. Hay, J.D. Freihaut, Photocatalytic oxidation of toluene on nanoscale TiO_2 catalysts: studies of deactivation and regeneration, J. Catal., 196 (2000) 253-261.
[160] Y. Zhang, N. Zhang, Z.-R. Tang, Y.-J. Xu, Identification of Bi2WO6 as a highly selective visible-light photocatalyst toward oxidation of glycerol to dihydroxyacetone in water, Chemical Science, 4 (2013) 1820.
[161] H.Y. Hafeez, S.K. Lakhera, P. Karthik, M. Anpo, B. Neppolian, Facile construction of ternary $CuFe_2O_4$-TiO_2 nanocomposite supported reduced graphene oxide (rGO) photocatalysts for the efficient hydrogen production, Appl. Surf. Sci., 449 (2018) 772-779.
[162] Y. Yao, F. Lu, Y. Zhu, F. Wei, X. Liu, C. Lian, S. Wang, Magnetic core–shell $CuFe_2O_4$@ C_3N_4 hybrids for visible light photocatalysis of Orange II, J. Hazard. Mater., 297 (2015) 224-233.
[163] L.A. Phillips, G.B. Raupp, Infrared spectroscopic investigation of gas—solid heterogeneous photocatalytic oxidation of trichloroethylene, Journal of molecular catalysis, 77 (1992) 297-311.
[164] M. Feilizadeh, A. Delparish, S.T. Bararpour, H.A. Najafabadi, S.M.E. Zakeri, M. Vossoughi, Photocatalytic removal of 2-nitrophenol using silver and sulfur co-doped TiO_2 under natural solar light, Water Sci. Technol., 72 (2015) 339-346.
[165] M. Stelmachowski, M. Marchwicka, E. Grabowska, M. Diak, A. Zaleska, The Photocatalytic Conversion of (Biodiesel Derived) Glycerol to Hydrogen-A Short Review and Preliminary Experimental Results Part 2: Photocatalytic Conversion of Glycerol to Hydrogen in Batch and Semi-batch Laboratory Reactors, J Adv Oxid Technol, 17 (2014) 179-186.
[166] Y. Huang, B. Long, M. Tang, Z. Rui, M.-S. Balogun, Y. Tong, H. Ji, Bifunctional catalytic material: an ultrastable and high-performance surface defect CeO2 nanosheets for formaldehyde thermal oxidation and photocatalytic oxidation, Appl. Catal. B:Environ., 181 (2016) 779-787.

[167] A. Castedo, A. Casanovas, I. Angurell, L. Soler, J. Llorca, Effect of temperature on the gas-phase photocatalytic H2 generation using microreactors under UVA and sunlight irradiation, Fuel, 222 (2018) 327-333.
[168] J. Nayak, S.N. Sahu, J. Kasuya, S. Nozaki, CdS–ZnO composite nanorods: synthesis, characterization and application for photocatalytic degradation of 3, 4-dihydroxy benzoic acid, Appl. Surf. Sci., 254 (2008) 7215-7218.
[169] Y. Ma, X. Wang, Y. Jia, X. Chen, H. Han, C. Li, Titanium Dioxide-Based Nanomaterials for Photocatalytic Fuel Generations, Chem. Rev., 114 (2014) 9987-10043.
[170] M.R. Hoffmann, S.T. Martin, W. Choi, D.W. Bahnemann, Environmental applications of semiconductor photocatalysis, Chem. Rev., 95 (1995) 69-96.
[171] M. Feilizadeh, M. Vossoughi, S.M.E. Zakeri, M. Rahimi, Enhancement of Efficient Ag–S/TiO_2 Nanophotocatalyst for Photocatalytic Degradation under Visible Light, Ind. Eng. Chem. Res., 53 (2014) 9578-9586.
[172] R. Marchand, L. Brohan, M. Tournoux, TiO_2(B) a new form of titanium dioxide and the potassium octatitanate $K_2Ti_8O_{17}$, Materials Research Bulletin, 15 (1980) 1129-1133.
[173] M.R. Gholipour, C.-T. Dinh, F. Béland, T.-O. Do, Nanocomposite heterojunctions as sunlight-driven photocatalysts for hydrogen production from water splitting, Nanoscale, 7 (2015) 8187-8208.
[174] T. Luttrell, S. Halpegamage, J. Tao, A. Kramer, E. Sutter, M. Batzill, Why is anatase a better photocatalyst than rutile-Model studies on epitaxial TiO_2 films, Sci. Rep., 4 (2014).
[175] K. Woan, G. Pyrgiotakis, W. Sigmund, Photocatalytic Carbon-Nanotube-TiO_2 Composites, Adv. Mater., 21 (2009) 2233-2239.
[176] V. Maurino, A. Bedini, M. Minella, F. Rubertelli, E. Pelizzetti, C. Minero, Glycerol transformation through photocatalysis: A possible route to value added chemicals, J Adv Oxid Technol, 11 (2008) 184-192.
[177] P. Montes-Navajas, M. Serra, A. Corma, H. Garcia, Contrasting photocatalytic activity of commercial TiO_2 samples for hydrogen generation, Catal. Today, 225 (2014) 52-54.
[178] V. Augugliaro, H.A.H. El Nazer, V. Loddo, A. Mele, G. Palmisano, L. Palmisano, S. Yurdakal, Partial photocatalytic oxidation of glycerol in TiO_2 water suspensions, Catal. Today, 151 (2010) 21-28.
[179] K.P. De Jong, Synthesis of solid catalysts, John Wiley & Sons2009.
[180] S. Martha, P. Chandra Sahoo, K.M. Parida, An overview on visible light responsive metal oxide based photocatalysts for hydrogen energy production, RSC Advances, 5 (2015) 61535-61553.
[181] S.M.E. Zakeri, M. Asghari, M. Feilizadeh, M. Vosoughi, A visible light driven doped TiO^ sub 2^ nanophotocatalyst: Preparation and characterization, International Journal of Nano Dimension, 5 (2014) 329.
[182] S. Nakabayashi, A. Fujishima, K. Honda, Experimental evidence for the hydrogen evolution site in photocatalytic process on Pt/TiO_2, Chem. Phys. Lett., 102 (1983) 464-465.
[183] B. Zhou, J. Song, H. Zhou, L. Wu, T. Wu, Z. Liu, B. Han, Light-driven integration of the reduction of nitrobenzene to aniline and the transformation of glycerol into valuable chemicals in water, RSC Adv., 5 (2015) 36347-36352.
[184] V. Žunič, M. Vukomanović, S.D. Škapin, D. Suvorov, J. Kovač, Photocatalytic properties of TiO_2 and TiO_2/Pt: a sol-precipitation, sonochemical and hydrothermal approach, Ultrasonics sonochemistry, 21 (2014) 367-375.
[185] M. Matsumura, S. Furukawa, Y. Saho, H. Tsubomura, Cadmium sulfide photocatalyzed hydrogen production from aqueous solutions of sulfite: effect of crystal structure and preparation method of the catalyst, The Journal of Physical Chemistry, 89 (1985) 1327-1329.
[186] D.V. Markovskaya, S.V. Cherepanova, A.A. Saraev, E.Y. Gerasimov, E.A. Kozlova, Photocatalytic hydrogen evolution from aqueous solutions of Na 2 S/Na 2 SO 3 under visible light irradiation on CuS/Cd 0.3 Zn 0.7 S and NizCd 0.3 Zn 0.7 S 1+ z, Chem. Eng. J., 262 (2015) 146-155.
[187] J.H. Bang, P.V. Kamat, Quantum dot sensitized solar cells. A tale of two semiconductor nanocrystals: CdSe and CdTe, ACS nano, 3 (2009) 1467-1476.

[188] J. Jasieniak, P. Mulvaney, From Cd-rich to Se-rich− the manipulation of CdSe nanocrystal surface stoichiometry, J. Am. Chem. Soc., 129 (2007) 2841-2848.
[189] L. Zhou, H. Zhang, H. Sun, S. Liu, M.O. Tade, S. Wang, W. Jin, Recent advances in non-metal modification of graphitic carbon nitride for photocatalysis: a historic review, Catalysis Science & Technology, 6 (2016) 7002-7023.
[190] R. Priya, S. Kanmani, Optimization of photocatalytic production of hydrogen from hydrogen sulfide in alkaline solution using response surface methodology, Desalination, 276 (2011) 222-227.
[191] M. Vaez, A. Zarringhalam Moghaddam, S. Alijani, Optimization and modeling of photocatalytic degradation of azo dye using a response surface methodology (RSM) based on the central composite design with immobilized titania nanoparticles, Ind. Eng. Chem. Res., 51 (2012) 4199-4207.
[192] H. Eskandarloo, A. Badiei, M.A. Behnajady, TiO_2/CeO_2 hybrid photocatalyst with enhanced photocatalytic activity: optimization of synthesis variables, Ind. Eng. Chem. Res., 53 (2014) 7847-7855.
[193] M. Antonopoulou, I. Konstantinou, Optimization and modeling of the photocatalytic degradation of the insect repellent DEET in aqueous TiO_2 suspensions, CLEAN–Soil, Air, Water, 41 (2013) 593-600.
[194] A.R. Amani-Ghadim, M.S.S. Dorraji, Modeling of photocatalyatic process on synthesized ZnO nanoparticles: Kinetic model development and artificial neural networks, Appl. Catal. B:Environ., 163 (2015) 539-546.
[195] G. Wu, T. Chen, W. Su, G. Zhou, X. Zong, Z. Lei, C. Li, H_2 production with ultra-low CO selectivity via photocatalytic reforming of methanol on Au/TiO_2 catalyst, Int. J. Hydrogen Energy, 33 (2008) 1243-1251.
[196] E.A. Kozlova, A.V. Vorontsov, Photocatalytic hydrogen evolution from aqueous solutions of organophosphorous compounds, Int. J. Hydrogen Energy, 35 (2010) 7337-7343.
[197] Y. Li, G. Lu, S. Li, Photocatalytic hydrogen generation and decomposition of oxalic acid over platinized TiO_2, Appl. Catal. A: Gen., 214 (2001) 179-185.
[198] Y. Li, Y. Xie, S. Peng, G. Lu, S. Li, Photocatalytic hydrogen generation in the presence of chloroacetic acids over Pt/TiO_2, Chemosphere, 63 (2006) 1312-1318.
[199] Y. Li, J. Wang, S. Peng, G. Lu, S. Li, Photocatalytic hydrogen generation in the presence of glucose over ZnS-coated $ZnIn_2S_4$ under visible light irradiation, Int. J. Hydrogen Energy, 35 (2010) 7116-7126.
[200] S.G. Lee, S. Lee, H.-I. Lee, Photocatalytic production of hydrogen from aqueous solution containing CN^- as a hole scavenger, Appl. Catal. A: Gen., 207 (2001) 173-181.
[201] S. Escobedo, B. Serrano, A. Calzada, J. Moreira, H. de Lasa, Hydrogen production using a platinum modified TiO_2 photocatalyst and an organic scavenger. Kinetic modeling, Fuel, 181 (2016) 438-449.
[202] A. Castedo, I. Uriz, L. Soler, L.M. Gandía, J. Llorca, Kinetic analysis and CFD simulations of the photocatalytic production of hydrogen in silicone microreactors from water-ethanol mixtures, Appl. Catal. B:Environ., 203 (2017) 210-217.
[203] G.L. Chiarello, D. Ferri, E. Selli, Effect of the CH_3 OH/H_2O ratio on the mechanism of the gas-phase photocatalytic reforming of methanol on noble metal-modified TiO_2, J. Catal., 280 (2011) 168-177.
[204] Y. Wang, W. Zhang, R. Li, W. Duan, B. Liu, Design of stable cage-like $CaO/CaZrO_3$ hollow spheres for CO_2 capture, Energy Fuels, 30 (2016) 1248-1255.
[205] J. Di, S. Li, Z. Zhao, Y. Huang, Y.A. Jia, H. Zheng, Biomimetic CNT@TiO_2 composite with enhanced photocatalytic properties, Chem. Eng. J., 281 (2015) 60-68.
[206] J.W. Niemantsverdriet, Spectroscopy in catalysis: an introduction, John Wiley & Sons, Weinheim, Germany, 2007.

[207] X.Z. Ding, X.H. Liu, Y.Z. He, Grain size dependence of anatase-to-rutile structural transformation in gel-derived nanocrystalline titania powders, J. Mater. Sci. Lett., 15 (1996) 1789-1791.
[208] J.W. Niemantsverdriet, Spectroscopy in Catalysis: An Introduction, Wiley2000.
[209] M. Zarei, A.R. Khataee, R. Ordikhani-Seyedlar, M. Fathinia, Photoelectro-Fenton combined with photocatalytic process for degradation of an azo dye using supported TiO_2 nanoparticles and carbon nanotube cathode: neural network modeling, Electrochimica Acta, 55 (2010) 7259-7265.
[210] B. Saha, P. Chowdhury, A.K. Ghoshal, Al-MCM-41 catalyzed decomposition of polypropylene and hybrid genetic algorithm for kinetics analysis, Appl. Catal. B:Environ., 83 (2008) 265-276.
[211] D.G. Garson, Interpreting neural network connection weights, (1991).
[212] A.R. Khataee, O. Mirzajani, UV/peroxydisulfate oxidation of CI Basic Blue 3: modeling of key factors by artificial neural network, Desalination, 251 (2010) 64-69.
[213] G. Corro, U. Pal, N. Tellez, Biodiesel production from Jatropha curcas crude oil using ZnO/SiO 2 photocatalyst for free fatty acids esterification, Appl. Catal. B:Environ., 129 (2013) 39-47.
[214] L. Clarizia, D. Spasiano, I. Di Somma, R. Marotta, R. Andreozzi, D.D. Dionysiou, Copper modified-TiO_2 catalysts for hydrogen generation through photoreforming of organics. A short review, Int. J. Hydrogen Energy, 39 (2014) 16812-16831.
[215] X. Fu, J. Long, X. Wang, D.Y.C. Leung, Z. Ding, L. Wu, Z. Zhang, Z. Li, X. Fu, Photocatalytic reforming of biomass: a systematic study of hydrogen evolution from glucose solution, Int. J. Hydrogen Energy, 33 (2008) 6484-6491.
[216] J. Greaves, L. Al-Mazroai, A. Nuhu, P. Davies, M. Bowker, Photocatalytic methanol reforming on Au/TiO_2 for hydrogen production, Gold Bulletin, 39 (2006) 216-219.
[217] X.-Z. Ding, X.-H. Liu, Y.-Z. He, Grain size dependence of anatase-to-rutile structural transformation in gel-derived nanocrystalline titania powders, J. Mater. Sci. Lett., 15 (1996) 1789-1791.
[218] A. Pasini, Artificial neural networks for small dataset analysis, Journal of thoracic disease, 7 (2015) 953.
[219] M.A. Shah, Growth of uniform nanoparticles of platinum by an economical approach at relatively low temperature, Scientia Iranica, 19 (2012) 964-966.
[220] C. Montero-Ocampo, J.R.V. Garcia, E.A. Estrada, Comparison of TiO_2 and TiO_2-CNT as cathode catalyst supports for ORR, Int. J. Electrochem. Sci, 8 (2013) 12780-12800.
[221] A. Speltini, M. Sturini, D. Dondi, E. Annovazzi, F. Maraschi, V. Caratto, A. Profumo, A. Buttafava, Sunlight-promoted photocatalytic hydrogen gas evolution from water-suspended cellulose: a systematic study, Photochem. Photobiol. Sci., 13 (2014) 1410-1419.
[222] A. Speltini, M. Sturini, F. Maraschi, D. Dondi, A. Serra, A. Profumo, A. Buttafava, A. Albini, Swine sewage as sacrificial biomass for photocatalytic hydrogen gas production: Explorative study, Int. J. Hydrogen Energy, 39 (2014) 11433-11440.
[223] A. Yamakata, T.-a. Ishibashi, H. Onishi, Kinetics of the photocatalytic water-splitting reaction on TiO_2 and Pt/TiO_2 studied by time-resolved infrared absorption spectroscopy, Journal of Molecular Catalysis A: Chemical, 199 (2003) 85-94.
[224] E.P. Melián, C.R. López, A.O. Méndez, O.G. Díaz, M.N. Suárez, J.M.D. Rodríguez, J.A. Navío, D.F. Hevia, Hydrogen production using Pt-loaded TiO_2 photocatalysts, Int. J. Hydrogen Energy, 38 (2013) 11737-11748.
[225] C. Kormann, D.W. Bahnemann, M.R. Hoffmann, Photolysis of chloroform and other organic molecules in aqueous titanium dioxide suspensions, Environ Sci Technol, 25 (1991) 494-500.
[226] M.H. Habibi, A. Hassanzadeh, S. Mahdavi, The effect of operational parameters on the photocatalytic degradation of three textile azo dyes in aqueous TiO_2 suspensions, J. Photoch. Photobio., A, 172 (2005) 89-96.
[227] S. Jacob, R. Banerjee, Modeling and optimization of anaerobic codigestion of potato waste and aquatic weed by response surface methodology and artificial neural network coupled genetic algorithm, Bioresource technology, 214 (2016) 386-395.

[228] C. Ziogou, D. Ipsakis, P. Seferlis, S. Bezergianni, S. Papadopoulou, S. Voutetakis, Optimal production of renewable hydrogen based on an efficient energy management strategy, Energy, 55 (2013) 58-67.
[229] M. Shokrollahi Yancheshmeh, H.R. Radfarnia, M.C. Iliuta, Sustainable Production of High-Purity Hydrogen by Sorption Enhanced Steam Reforming of Glycerol over CeO_2-Promoted $Ca_9Al_6O_{18}$–CaO/NiO Bifunctional Material, ACS Sustainable Chem. Eng., 5 (2017) 9774-9786.
[230] B. Wang, C. Zeng, K.H. Chu, D. Wu, H.Y. Yip, L. Ye, P.K. Wong, Enhanced biological hydrogen production from Escherichia coli with surface precipitated cadmium sulfide nanoparticles, Advanced Energy Materials, 7 (2017) 1700611.
[231] C.G. Morales-Guio, L. Liardet, M.T. Mayer, S.D. Tilley, M. Grätzel, X. Hu, Photoelectrochemical hydrogen production in alkaline solutions using Cu_2O coated with earth-abundant hydrogen evolution catalysts, Angewandte Chemie International Edition, 54 (2015) 664-667.
[232] M.R. Gholipour, F. Béland, T.-O. Do, Post-calcined carbon nitride nanosheets as an efficient photocatalyst for hydrogen production under visible light irradiation, ACS Sustainable Chem. Eng., 5 (2016) 213-220.
[233] M.R. Karimi Estahbanati, M. Feilizadeh, M. Shokrollahi Yancheshmeh, M.C. Iliuta, Effects of carbon nanotube and carbon sphere templates in TiO_2 composites for photocatalytic hydrogen production, Ind. Eng. Chem. Res., 58 (2019) 2770−2783.
[234] F.E. Osterloh, B.A. Parkinson, Recent developments in solar water-splitting photocatalysis, MRS bulletin, 36 (2011) 17-22.
[235] X. Meng, Z. Zhang, Experimental analysis of a photoreactor packed w ith Pd-$BiVO_4$-Coated glass beads, AIChE Journal, 5 (2018) 132-139.
[236] S.L. Chen, A.J. Wang, C.T. Hu, C. Dai, J.B. Benziger, Enhanced photocatalytic performance of nanocrystalline TiO_2 membrane by both slow photons and stop-band reflection of photonic crystals, AIChE Journal, 58 (2012) 568-572.
[237] M. Feilizadeh, F. Attar, N. Mahinpey, Hydrogen Peroxide-Assisted Photocatalysis under Solar Light Irradiation: Interpretation of Interaction Effects between an Active Photocatalyst and H_2O_2, Can. J. Chem. Eng., 97 (2019) 2009-2014.
[238] C.-C. Wang, J.-R. Li, X.-L. Lv, Y.-Q. Zhang, G. Guo, Photocatalytic organic pollutants degradation in metal–organic frameworks, Energy Environ. Sci., 7 (2014) 2831-2867.
[239] J.F. De Brito, F. Tavella, C. Genovese, C. Ampelli, M.V.B. Zanoni, G. Centi, S. Perathoner, Role of CuO in the modification of the photocatalytic water splitting behavior of TiO_2 nanotube thin films, Appl. Catal. B:Environ., 224 (2018) 136-145.
[240] S.T. Bararpour, M.R. Feylizadeh, A. Delparish, M. Qanbarzadeh, M. Raeiszadeh, M. Feilizadeh, Investigation of 2-nitrophenol solar degradation in the simultaneous presence of $K_2S_2O_8$ and H_2O_2: Using experimental design and artificial neural network, J. Clean. Prod., 176 (2018) 1154-1162.
[241] S.S. Tan, L. Zou, E. Hu, Kinetic modelling for photosynthesis of hydrogen and methane through catalytic reduction of carbon dioxide with water vapour, Catal. Today, 131 (2008) 125-129.
[242] T. Rajkhowa, G.B. Marin, J.W. Thybaut, A comprehensive kinetic model for Cu catalyzed liquid phase glycerol hydrogenolysis, Appl. Catal. B:Environ., 205 (2017) 469-480.
[243] A.N. Ardila, M.A. Sánchez-Castillo, T.A. Zepeda, A.L. Villa, G.A. Fuentes, Glycerol hydrodeoxygenation to 1, 2-propanediol catalyzed by CuPd/TiO_2-Na, Appl. Catal. B:Environ., 219 (2017) 658-671.
[244] O.A.Z. Sahraei, F. Larachi, N. Abatzoglou, M.C. Iliuta, Hydrogen production by glycerol steam reforming catalyzed by Ni-promoted Fe/Mg-bearing metallurgical wastes, Appl. Catal. B:Environ., 219 (2017) 183-193.
[245] O. Ali Zadeh Sahraei, F. Larachi, N. Abatzoglou, M.C. Iliuta, Hydrogen production by glycerol steam reforming catalyzed by Ni-promoted Fe/Mg-bearing metallurgical wastes, Appl. Catal. B:Environ., 219 (2017) 183-193.

[246] J.M. Herrmann, J. Disdier, P. Pichat, Photoassisted platinum deposition on TiO_2 powder using various platinum complexes, The Journal of Physical Chemistry, 90 (1986) 6028-6034.
[247] D. Brinkley, T. Engel, Photocatalytic dehydrogenation of 2-propanol on TiO_2 (110), Phys. Chem. B., 102 (1998) 7596-7605.
[248] M. Cargnello, A. Gasparotto, V. Gombac, T. Montini, D. Barreca, P. Fornasiero, Photocatalytic H_2 and Added-Value By-Products–The Role of Metal Oxide Systems in Their Synthesis from Oxygenates, European Journal of Inorganic Chemistry, 2011 (2011) 4309-4323.
[249] A. Patsoura, D.I. Kondarides, X.E. Verykios, Photocatalytic degradation of organic pollutants with simultaneous production of hydrogen, Catal. Today, 124 (2007) 94-102.
[250] G. Li, L. Lv, H. Fan, J. Ma, Y. Li, Y. Wan, X.S. Zhao, Effect of the agglomeration of TiO_2 nanoparticles on their photocatalytic performance in the aqueous phase, Journal of colloid and interface science, 348 (2010) 342-347.
[251] F. Loosli, P. Le Coustumer, S. Stoll, TiO_2 nanoparticles aggregation and disaggregation in presence of alginate and Suwannee River humic acids. pH and concentration effects on nanoparticle stability, Water Research, 47 (2013) 6052-6063.
[252] T. Hisatomi, T. Minegishi, K. Domen, Kinetic assessment and numerical modeling of photocatalytic water splitting toward efficient solar hydrogen production, Bull. Chem. Soc. Jpn., 85 (2012) 647-655.
[253] H. Park, H.-i. Kim, G.-h. Moon, W. Choi, Photoinduced charge transfer processes in solar photocatalysis based on modified TiO_2, Energy Environ. Sci., 9 (2016) 411-433.
[254] M. Fathinia, A. Khataee, S. Aber, A. Naseri, Development of kinetic models for photocatalytic ozonation of phenazopyridine on TiO_2 nanoparticles thin film in a mixed semi-batch photoreactor, Appl. Catal. B:Environ., 184 (2016) 270-284.
[255] D.W. Bahnemann, M. Hilgendorff, R. Memming, Charge carrier dynamics at TiO_2 particles: reactivity of free and trapped holes, Phys. Chem. B., 101 (1997) 4265-4275.
[256] J.W. Niemantsverdriet, Spectroscopy in catalysis: an introduction, John Wiley & Sons (2007).
[257] W. Fan, Q. Lai, Q. Zhang, Y. Wang, Nanocomposites of TiO_2 and reduced graphene oxide as efficient photocatalysts for hydrogen evolution, Phys. Chem. C., 115 (2011) 10694-10701.
[258] S. Xu, D.D. Sun, Significant improvement of photocatalytic hydrogen generation rate over TiO_2 with deposited CuO, Int. J. Hydrogen Energy, 34 (2009) 6096-6104.
[259] R. Reichert, Z. Jusys, R.J.r. Behm, Au/TiO_2 photo (electro) catalysis: the role of the Au cocatalyst in photoelectrochemical water splitting and photocatalytic H_2 evolution, Phys. Chem. C., 119 (2015) 24750-24759.
[260] T.A. Kandiel, R. Dillert, L. Robben, D.W. Bahnemann, Photonic efficiency and mechanism of photocatalytic molecular hydrogen production over platinized titanium dioxide from aqueous methanol solutions, Catal. Today, 161 (2011) 196-201.
[261] E.C. Vagia, N. Muradov, A. Kalyva, T. Ali, N. Qin, A.R. Srinivasa, K.E. Kakosimos, Solar hybrid photo-thermochemical sulfur-ammonia water-splitting cycle: Photocatalytic hydrogen production stage, Int. J. Hydrogen Energy, 42 (2017) 20608-20624.
[262] M. Tahir, Ni/MMT-promoted TiO2 nanocatalyst for dynamic photocatalytic H2 and hydrocarbons production from ethanol-water mixture under UV-light, Int. J. Hydrogen Energy, 42 (2017) 28309-28326.
[263] G. Colon, M.C. Hidalgo, J.A. Navıo, Photocatalytic deactivation of commercial TiO_2 samples during simultaneous photoreduction of Cr (VI) and photooxidation of salicylic acid, J. Photoch. Photobio., A, 138 (2001) 79-85.
[264] N.A. Hermes, A. Corsetti, eacute, M.A. Lansarin, Comparative Study on the Photocatalytic Oxidation of Glycerol Using ZnO and TiO_2, Chemistry Letters, 43 (2014) 143-145.
[265] D.S. Muggli, J.T. McCue, J.L. Falconer, Mechanism of the photocatalytic oxidation of ethanol on TiO_2, J. Catal., 173 (1998) 470-483.

[266] J. Chen, D.F. Ollis, W.H. Rulkens, H. Bruning, Photocatalyzed oxidation of alcohols and organochlorides in the presence of native TiO_2 and metallized TiO_2 suspensions. Part (II): photocatalytic mechanisms, Water Research, 33 (1999) 669-676.
[267] S. Carrettin, P. McMorn, P. Johnston, K. Griffin, C.J. Kiely, G.J. Hutchings, Oxidation of glycerol using supported Pt, Pd and Au catalysts, Phys. Chem. Chem. Phys., 5 (2003) 1329-1336.
[268] J.P. Tan, Z.K. Tee, W.N. Roslam Wan Isahak, B.H. Kim, A.J. Asis, J.M. Jahim, Improved fermentability of pretreated glycerol enhanced bioconversion of 1, 3-propanediol, Ind. Eng. Chem. Res., 57 (2018) 12565-12573.
[269] C. Xu, Q. Xu, A Novel Design for Simultaneous Production of Biodiesel and Glycerol Carbonate from Soybean Oil, Ind. Eng. Chem. Res., (2018).
[270] N.L. Reddy, S. Emin, V.D. Kumari, S. Muthukonda Venkatakrishnan, CuO Quantum Dots Decorated TiO_2 Nanocomposite Photocatalyst for Stable Hydrogen Generation, Ind. Eng. Chem. Res., 57 (2018) 568-577.
[271] B. Duan, Y. Zhou, C. Huang, Q. Huang, Y. Chen, H. Xu, S. Shen, Impact of Zr-Doped TiO_2 Photocatalyst on Formaldehyde Degradation by Na Addition, Ind. Eng. Chem. Res., 57 (2018) 14044-14051.
[272] N. Srisasiwimon, S. Chuangchote, N. Laosiripojana, T. Sagawa, TiO_2/Lignin-based Carbon Composited Photocatalysts for Enhanced Photocatalytic Conversion of Lignin to High Value Chemicals, ACS Sustainable Chem. Eng., (2018).
[273] W.-C. Chung, M.-B. Chang, Simultaneous generation of syngas and multiwalled carbon nanotube via CH_4/CO_2 reforming with spark discharge, ACS Sustainable Chem. Eng., 5 (2016) 206-212.
[274] F. Quan, J. Zhang, D. Li, Y. Zhu, Y. Wang, Y. Bu, Y. Qin, Y. Xia, S. Komarneni, D. Yang, Biomass as Template Leads to CdS@Carbon Aerogels for Efficient Photocatalytic Hydrogen Evolution and Stable Photoelectrochemical Cell, ACS Sustainable Chem. Eng., (2018).
[275] H.W. Kroto, J.R. Heath, S.C. O'Brien, R.F. Curl, R.E. Smalley, C60: Buckminsterfullerene, Nature, 318 (1985) 162.
[276] S. Iijima, Helical microtubules of graphitic carbon, Nature, 354 (1991) 56.
[277] R.H. Baughman, A.A. Zakhidov, W.A. De Heer, Carbon nanotubes--the route toward applications, Science, 297 (2002) 787-792.
[278] Q. Cao, Q. Yu, D.W. Connell, G. Yu, Titania/carbon nanotube composite (TiO_2/CNT) and its application for removal of organic pollutants, Clean Technol. Environ. Policy, 15 (2013) 871-880.
[279] J. Liu, N.P. Wickramaratne, S.Z. Qiao, M. Jaroniec, Molecular-based design and emerging applications of nanoporous carbon spheres, Nat. Mater., 14 (2015) 763.
[280] S. Li, A. Pasc, V. Fierro, A. Celzard, Hollow carbon spheres, synthesis and applications–a review, J. Mater. Chem. A, 4 (2016) 12686-12713.
[281] B.-S. Huang, F.-Y. Chang, M.-Y. Wey, An efficient composite growing N-doped TiO_2 on multi-walled carbon nanotubes through sol–gel process, J. Nanopart. Res., 12 (2010) 2503-2510.
[282] K. Dai, T. Peng, D. Ke, B. Wei, Photocatalytic hydrogen generation using a nanocomposite of multi-walled carbon nanotubes and TiO_2 nanoparticles under visible light irradiation, Nanotechnology, 20 (2009) 125603.
[283] C.G. Silva, M.J. Sampaio, R.R.N. Marques, L.A. Ferreira, P.B. Tavares, A.M.T. Silva, J.L. Faria, Photocatalytic production of hydrogen from methanol and saccharides using carbon nanotube-TiO_2 catalysts, Appl. Catal. B:Environ., 178 (2015) 82-90.
[284] A. Moya, A. Cherevan, S. Marchesan, P. Gebhardt, M. Prato, D. Eder, J.J. Vilatela, Oxygen vacancies and interfaces enhancing photocatalytic hydrogen production in mesoporous CNT/TiO_2 hybrids, Appl. Catal. B:Environ., 179 (2015) 574-582.
[285] Y. Haldorai, A. Rengaraj, J.-B. Lee, Y.S. Huh, Y.-K. Han, Highly efficient hydrogen production via water splitting using Pt@MWNT/TiO_2 ternary hybrid composite as a catalyst under UV–visible light, Synthetic Metals, 199 (2015) 345-352.

[286] J.B. Veluru, K.K. Manippady, M. Rajendiren, K.M. Mya, P.R. Rayavarapu, S.N. Appukuttan, R. Seeram, Photocatalytic hydrogen generation by splitting of water from electrospun hybrid nanostructures, Int. J. Hydrogen Energy, 38 (2013) 4324-4333.
[287] Y. Chen, J. Li, Z. Hong, B. Shen, B. Lin, B. Gao, Origin of the enhanced visible-light photocatalytic activity of CNT modified gC_3N_4 for H_2 production, Phys. Chem. Chem. Phys., 16 (2014) 8106-8113.
[288] N. Justh, L.P. Bakos, K. Hernádi, G. Kiss, B. Réti, Z. Erdélyi, B. Parditka, I.M. Szilágyi, Photocatalytic hollow TiO_2 and ZnO nanospheres prepared by atomic layer depositiondd, Sci. Rep., 7 (2017) 4337.
[289] S. Cao, J. Yu, Carbon-based H_2-production photocatalytic materials, J. Photochem. Photobiol., C, 27 (2016) 72-99.
[290] V. Georgakilas, J.A. Perman, J. Tucek, R. Zboril, Broad family of carbon nanoallotropes: classification, chemistry, and applications of fullerenes, carbon dots, nanotubes, graphene, nanodiamonds, and combined superstructures, Chem. Rev., 115 (2015) 4744-4822.
[291] X. Liu, P. Zeng, T. Peng, X. Zhang, K. Deng, Preparation of multiwalled carbon nanotubes/$Cd_{0.8}Zn_{0.2}S$ nanocomposite and its photocatalytic hydrogen production under visible-light, Int. J. Hydrogen Energy, 37 (2012) 1375-1384.
[292] J. Ran, J. Zhang, J. Yu, M. Jaroniec, S.Z. Qiao, Earth-abundant cocatalysts for semiconductor-based photocatalytic water splitting, Chem. Soc. Rev., 43 (2014) 7787-7812.
[293] T.P. McAndrew, P. Laurent, M. Havel, C. Roger, F. Ave, K. Prussia, Arkema graphistrength® multi-walled carbon nanotubes, Technical Proceedings of NSTI 2008, pp. 47-50.
[294] Q. Jiang, L. Li, J. Bi, S. Liang, M. Liu, Design and Synthesis of TiO_2 Hollow Spheres with Spatially Separated Dual Cocatalysts for Efficient Photocatalytic Hydrogen Production, Nanomaterials, 7 (2017) 24.
[295] B. Gao, G.Z. Chen, G.L. Puma, Carbon nanotubes/titanium dioxide ($CNTs/TiO_2$) nanocomposites prepared by conventional and novel surfactant wrapping sol–gel methods exhibiting enhanced photocatalytic activity, Appl. Catal. B:Environ., 89 (2009) 503-509.
[296] A.G. Osorio, I.C.L. Silveira, V.L. Bueno, C.P. Bergmann, $H_2SO_4/HNO_3/HCl$—functionalization and its effect on dispersion of carbon nanotubes in aqueous media, Appl. Surf. Sci., 255 (2008) 2485-2489.
[297] W. Wang, P. Serp, P. Kalck, J.L. Faria, Photocatalytic degradation of phenol on MWNT and titania composite catalysts prepared by a modified sol–gel method, Appl. Catal. B:Environ., 56 (2005) 305-312.
[298] A.A. Deshmukh, S.D. Mhlanga, N.J. Coville, Carbon spheres, Mater. Sci. Eng. R Rep., 70 (2010) 1-28.
[299] S. Bakardjieva, J. Šubrt, V. Štengl, M.J. Dianez, M.J. Sayagues, Photoactivity of anatase–rutile TiO_2 nanocrystalline mixtures obtained by heat treatment of homogeneously precipitated anatase, Appl. Catal. B:Environ., 58 (2005) 193-202.
[300] M. Cargnello, M. Grzelczak, B. Rodríguez-González, Z. Syrgiannis, K. Bakhmutsky, V. La Parola, L.M. Liz-Marzán, R.J. Gorte, M. Prato, P. Fornasiero, Multiwalled carbon nanotubes drive the activity of metal@oxide core–shell catalysts in modular nanocomposites, J. Am. Chem. Soc., 134 (2012) 11760-11766.
[301] M.M. Mohamed, G. Osman, K.S. Khairou, Fabrication of Ag nanoparticles modified TiO_2–CNT heterostructures for enhanced visible light photocatalytic degradation of organic pollutants and bacteria, J. Environ. Chem. Eng., 3 (2015) 1847-1859.
[302] J. Bao, Y. Dai, H. Liu, L. Yang, Photocatalytic removal of SO_2 over Mn doped titanium dioxide supported by multi-walled carbon nanotubes, Int. J. Hydrogen Energy, 41 (2016) 15688-15695.
[303] Y.-J. Xu, Y. Zhuang, X. Fu, New insight for enhanced photocatalytic activity of TiO_2 by doping carbon nanotubes: a case study on degradation of benzene and methyl orange, Phys. Chem. C., 114 (2010) 2669-2676.

[304] M. MamathaKumari, D.P. Kumar, P. Haridoss, V. DurgaKumari, M.V. Shankar, Nanohybrid of titania/carbon nanotubes–nanohorns: a promising photocatalyst for enhanced hydrogen production under solar irradiation, Int. J. Hydrogen Energy, 40 (2015) 1665-1674.
[305] E. Heister, C. Lamprecht, V. Neves, C. Tîlmaciu, L. Datas, E. Flahaut, B. Soula, P. Hinterdorfer, H.M. Coley, S.R.P. Silva, Higher dispersion efficacy of functionalized carbon nanotubes in chemical and biological environments, ACS Nano, 4 (2010) 2615-2626.
[306] D.A.H. Hanaor, C.C. Sorrell, Review of the anatase to rutile phase transformation, J. Mater. Sci., 46 (2011) 855-874.
[307] D.P. Subagio, M. Srinivasan, M. Lim, T.-T. Lim, Photocatalytic degradation of bisphenol-A by nitrogen-doped TiO_2 hollow sphere in a vis-LED photoreactor, Appl. Catal. B:Environ., 95 (2010) 414-422.
[308] P.M. Ajayan, T. Ichihashi, S. Iijima, Distribution of pentagons and shapes in carbon nano-tubes and nano-particles, Chem. Phys. Lett., 202 (1993) 384-388.
[309] D. Zhang, H. Fu, L. Shi, J. Fang, Q. Li, Carbon nanotube assisted synthesis of CeO_2 nanotubes, J. Solid State Chem., 180 (2007) 654-660.
[310] M. Li, W. Li, S. Liu, Hydrothermal synthesis, characterization, and KOH activation of carbon spheres from glucose, Carbohydr. Res., 346 (2011) 999-1004.
[311] B. Réti, G.I. Kiss, T. Gyulavári, K. Baan, K. Magyari, K. Hernadi, Carbon sphere templates for TiO_2 hollow structures: Preparation, characterization and photocatalytic activity, Catal. Today, 284 (2017) 160-168.
[312] Y. Liu, L. Gao, A study of the electrical properties of carbon nanotube-$NiFe_2O_4$ composites: effect of the surface treatment of the carbon nanotubes, Carbon, 43 (2005) 47-52.
[313] G. Tian, H. Fu, L. Jing, C. Tian, Synthesis and photocatalytic activity of stable nanocrystalline TiO_2 with high crystallinity and large surface area, J. Hazard. Mater., 161 (2009) 1122-1130.
[314] H. Ago, T. Kugler, F. Cacialli, W.R. Salaneck, M.S.P. Shaffer, A.H. Windle, R.H. Friend, Work functions and surface functional groups of multiwall carbon nanotubes, Phys. Chem. B., 103 (1999) 8116-8121.
[315] Y.K. Kim, H. Park, Light-harvesting multi-walled carbon nanotubes and CdS hybrids: application to photocatalytic hydrogen production from water, Energy Environ. Sci., 4 (2011) 685-694.
[316] W.M. Haynes, CRC handbook of chemistry and physics, CRC press2014.
[317] U. Mehmood, I.A. Hussein, K. Harrabi, M.B. Mekki, S. Ahmed, N. Tabet, Hybrid TiO_2–multiwall carbon nanotube (MWCNTs) photoanodes for efficient dye sensitized solar cells (DSSCs), Solar Energy Materials and Solar Cells, 140 (2015) 174-179.
[318] A. Kongkanand, P.V. Kamat, Electron storage in single wall carbon nanotubes. Fermi level equilibration in semiconductor–SWCNT suspensions, ACS nano, 1 (2007) 13-21.
[319] P. Du, L. Song, J. Xiong, N. Li, L. Wang, Z. Xi, N. Wang, L. Gao, H. Zhu, Dye-sensitized solar cells based on anatase TiO_2/multi-walled carbon nanotubes composite nanofibers photoanode, Electrochimica Acta, 87 (2013) 651-656.
[320] T. Zadi, A.A. Assadi, N. Nasrallah, R. Bouallouche, P.N. Tri, A. Bouzaza, M.M. Azizi, R. Maachi, D. Wolbert, Treatment of hospital indoor air by a hybrid system of combined plasma with photocatalysis: Case of trichloromethane, Chem. Eng. J., 349 (2018) 276-286.
[321] Y. Sheng, Z. Wei, H. Miao, W. Yao, H. Li, Y. Zhu, Enhanced organic pollutant photodegradation via adsorption/photocatalysis synergy using a 3D g-C_3N_4/TiO_2 free-separation photocatalyst, Chem. Eng. J., (2019) 287-294.
[322] Y. Boyjoo, H. Sun, J. Liu, V.K. Pareek, S. Wang, A review on photocatalysis for air treatment: From catalyst development to reactor design, Chem. Eng. J., 310 (2017) 537-559.
[323] X. Hu, X. Hu, Q. Peng, L. Zhou, X. Tan, L. Jiang, C. Tang, H. Wang, S. Liu, Y. Wang, Mechanisms underlying the photocatalytic degradation pathway of ciprofloxacin with heterogeneous TiO_2, Chem. Eng. J., (2019) DOI: https://doi.org/10.1016/j.cej.2019.122366.

[324] Z. Liu, Y. Zhang, L. Kong, L. Liu, J. Luo, B. Liu, Q. Zhou, F. He, D. Xu, Z. Wu, Preparation and preferential photocatalytic degradation of acephate by using the composite photocatalyst Sr/TiO_2-PCFM, Chem. Eng. J., (2019).
[325] Q. Li, Y. Xia, C. Yang, K. Lv, M. Lei, M. Li, Building a direct Z-scheme heterojunction photocatalyst by $ZnIn_2S_4$ nanosheets and TiO_2 hollowspheres for highly-efficient artificial photosynthesis, Chem. Eng. J., 349 (2018) 287-296.
[326] S. Zhu, W. Liao, M. Zhang, S. Liang, Design of spatially separated Au and CoO dual cocatalysts on hollow TiO_2 for enhanced photocatalytic activity towards the reduction of CO_2 to CH_4, Chem. Eng. J., 361 (2019) 461-469.
[327] J. Huang, Y. Cao, H. Wang, H. Yu, F. Peng, H. Zou, Z. Liu, Revealing active-site structure of porous nitrogen-defected carbon nitride for highly effective photocatalytic hydrogen evolution, Chem. Eng. J., 373 (2019) 687-699.
[328] A. Maldotti, A. Molinari, R. Amadelli, Photocatalysis with organized systems for the oxofunctionalization of hydrocarbons by O_2, Chem. Rev., 102 (2002) 3811-3836.
[329] Y. Zhang, R. Ciriminna, G. Palmisano, Y.-J. Xu, M. Pagliaro, Sol-gel entrapped visible light photocatalysts for selective conversions, RSC Advances, 4 (2014) 18341-18346.
[330] W.B. Fisher, J.F. VanPeppen, Cyclohexanol and cyclohexanone, Kirk-Othmer Encyclopedia of Chemical Technology, (2000).
[331] P. Anastas, N. Eghbali, Green chemistry: principles and practice, Chem. Soc. Rev., 39 (2010) 301-312.
[332] M.D. Hernández-Alonso, A.R. Almeida, J.A. Moulijn, G. Mul, Identification of the role of surface acidity in the deactivation of TiO_2 in the selective photo-oxidation of cyclohexane, Catal. Today, 143 (2009) 326-333.
[333] A.R. Almeida, J.A. Moulijn, G. Mul, In situ ATR-FTIR study on the selective photo-oxidation of cyclohexane over anatase TiO_2, Phys. Chem. C., 112 (2008) 1552-1561.
[334] J. Kou, C. Lu, J. Wang, Y. Chen, Z. Xu, R.S. Varma, Selectivity enhancement in heterogeneous photocatalytic transformations, Chem. Rev., 117 (2017) 1445-1514.
[335] F. Parrino, M. Bellardita, E.I. García-López, G. Marcì, V. Loddo, L. Palmisano, Heterogeneous photocatalysis for selective formation of high-value-added molecules: Some chemical and engineering aspects, ACS Catalysis, 8 (2018) 11191-11225.
[336] O.S. Mohamed, S.A. Ahmed, M.F. Mostafa, A.-M.A. Abdel-Wahab, TiO_2 nanoparticles-photocatalytic oxidation of selected cycloalkanols, Int J Photoenergy, (2008) 1-8, Article ID 205358.
[337] P. Du, J.A. Moulijn, G. Mul, Selective photo (catalytic)-oxidation of cyclohexane: effect of wavelength and TiO_2 structure on product yields, J. Catal., 238 (2006) 342-352.
[338] M.R. Karimi Estahbanati, M. Feilizadeh, M.C. Iliuta, An intrinsic kinetic model for liquid phase photocatalytic hydrogen production, AIChE J, DOI: https://doi.org/10.1002/aic.16724 (2019).
[339] J.T. Carneiro, T.J. Savenije, J.A. Moulijn, G. Mul, The effect of Au on TiO_2 catalyzed selective photocatalytic oxidation of cyclohexane, J. Photoch. Photobio., A, 217 (2011) 326-332.
[340] P. Boarini, V. Carassiti, A. Maldotti, R. Amadelli, Photocatalytic oxygenation of cyclohexane on titanium dioxide suspensions: Effect of the solvent and of oxygen, Langmuir, 14 (1998) 2080-2085.